

UNIVERSITE LILLE 1 – SCIENCES ET
TECHNOLOGIES

ECOLE DOCTORALE SCIENCES DE LA MATIERE, DU
RAYONNEMENT ET DE L'ENVIRONNEMENT

THESE

présentée par

Lishil SILVESTER

pour l'obtention du

TITRE DE DOCTEUR EN MOLECULES ET
MATIERE CONDENSEE

intitulée

**SYNTHESIS OF HIGHER ALCOHOLS FROM ETHANOL OVER
HYDROXYAPATITE-BASED CATALYSTS**

Soutenue **le 27 Février 2013** devant le jury d'examen :

Directeurs de thèse : **Franck DUMEIGNIL**, Professeur, Université Lille 1
Jean-François LAMONIER, Professeur, Université Lille 1

Rapporteurs : **François JEROME**, Directeur de Recherche CNRS, Université
de Poitiers
Guyène COSTENTIN, Chargée de Recherche CNRS,
Université Pierre et Marie Curie

Membres : **Christophe CALAIS**, Expert Researcher, ARKEMA
Carole LAMONIER, Professeur, Université Lille 1

Membre invité : **Rose-Noëlle VANNIER**, Professeur, Ecole Nationale
Supérieure de Chimie de Lille

Résumé

Dans un contexte mondial de demande croissante en énergie et d'une raréfaction des combustibles fossiles, la transformation de la biomasse en combustibles liquides est une alternative prometteuse car la biomasse est une source d'énergie renouvelable. L'éthanol et le butanol, alcools primaires les plus fréquemment rencontrés, peuvent être synthétisés à partir de la biomasse et utilisés (éthanol) ou envisagés d'être utilisés (butanol) comme biocarburants liquides. Le bio-butanol peut être obtenu selon plusieurs voies comme le procédé « Oxo », la fermentation « ABE » et la synthèse des alcools de « Guerbet ».

L'objectif de cette thèse était de développer des catalyseurs hétérogènes à base d'hydroxyapatite destinés à la transformation de l'éthanol en butanol et autres alcools supérieurs par la réaction de Guerbet. Des hydroxyapatites $[\text{Ca}_{10}(\text{PO}_4)_6(\text{OH})_2]$ ayant différents rapports Ca/P ont été synthétisées et caractérisées afin de déterminer leurs propriétés structurales, texturales et acido-basiques. Ces catalyseurs ont ensuite été testés dans la réaction de Guerbet en phase gazeuse. Une bonne corrélation a été trouvée entre les propriétés catalytiques des apatites et leurs propriétés acido-basiques. Les conditions expérimentales pour la réaction de Guerbet ont également pu être optimisées pour l'utilisation de ces catalyseurs. Suite à cette étude, d'autres apatites à base de strontium ont été synthétisées par substitutions partielle et totale du calcium. Une caractérisation fine des propriétés acido-basiques de ces solides a permis de montrer que la sélectivité pour les alcools de Guerbet atteignait un maximum pour une teneur donnée en strontium dans l'échantillon.

Keywords: Biomasse, combustibles liquides, l'éthanol, butanol, alcools supérieurs, réaction de Guerbet, hydroxyapatites, propriétés acido-basiques.

Abstract

The rapid worldwide increase in the consumption of fossil fuels to meet the energy demands suggests that time is not too far before depletion begins to adversely affect petroleum and natural gas resources. Transformation of biomass to liquid fuels will be one of the best alternatives because it is a renewable source. Ethanol and butanol are the most common primary alcohols that can be synthesized from biomass and they are used (ethanol) or being envisioned to be used (butanol) as liquid biofuels. Biobutanol with a higher molecular weight than ethanol has some additional advantages over ethanol. Biobutanol can be obtained through several routes like Oxo process, ABE fermentation and Guerbet alcohol synthesis.

The objective of this thesis is to develop hydroxyapatite-based heterogeneous catalysts and screen them in Guerbet reaction of ethanol to butanol and other higher alcohols. Hydroxyapatites $[\text{Ca}_{10}(\text{PO}_4)_6(\text{OH})_2]$ with different Ca/P ratios were synthesized and characterized to study the structural, textural and acid-base properties. These catalysts were then screened for gas phase reaction of ethanol and good correlation was found between the Guerbet reaction and acid-base properties of these apatite catalysts. Also we could optimize the experimental conditions suitable for Guerbet reaction.

Further strontium apatites were synthesized by varying the calcium and strontium content. After well characterization of acid-base properties of these solids, ethanol reaction was performed over these strontium apatite catalysts using the above optimized conditions. It was found that at a particular amount of strontium content, selectivity to Guerbet alcohols reached maximum.

Keywords: Biomass, biofuels, ethanol, butanol, higher alcohols, Guerbet reaction, hydroxyapatites, acid-base properties.

Acknowledgements

Firstly I would like to thank my supervisors Prof. Franck Dumeignil and Prof. Jean-François Lamonier to give me a chance to do my doctoral studies in their group. They gave me tremendous academic support and constant encouragement during the entire period of my PhD project.

I am grateful to Prof. Carole Lamonier and Prof. Rose-Nöelle Vannier for their great support and suggestions for the synthesis and deep characterization of the catalysts.

I also acknowledge Mickael Capron, Jérémy Faye and Pierre Miquel who helped me to learn more about the reactor and analytical setup and guided me whenever I faced problems related to the reactor setup. Thanks to Guillaume Tesquet and Fadime Hosoglu, my lab mates, for the friendly and relaxed atmosphere they were able to create inside the lab.

I thank my project partners Jean-Luc Dubois, Jean-Luc Couturier and Christophe Calais from ARKEMA for their valuable suggestions and scientific discussions that we have shared during the period of my PhD project. I also thank Eva Garrier and Matthieu Chatillon from NOVANCE who helped us to check the market value of the products obtained during the reaction.

I acknowledge also the reviewers of the Jury for evaluating my thesis even during their busy schedule.

I am thankful to Olivier Gardoll for helping me to perform the TGA/DTA and the TPD experiments which were very useful for my studies. I also acknowledge the help I have received from Nora Djelal and Laurence Burylo to perform XRD and SEM analyses.

Thanks to Arnaud Beaurain who performed the XPS analyses. I also thank Anne Sophie Mamede for the valuable LEIS experiments.

I would like to thank all my lab mates and my friends for their help, support and friendship which made my research fun and relaxing, without whom I would have been stressed during the time of PhD.

I would like to acknowledge the EUROpean multilevel integrated BIOREFinery design for sustainable biomass processing (EuroBioRef), the project under which the work has been carried out. The research leading to these results has received funding from the European Union Seventh Framework Programme (FP7/2007-2013) under grant agreement n°241718 EuroBioRef.

Big thanks to my Appachan (Father), Ammachi (Mother) and my lovely sisters, who loved, cared and supported me during the entire period of my studies. I dedicate this thesis to them.

Table of Contents

| | |
|---|-----------|
| General Introduction..... | 5 |
| Chapter 1 Bibliography..... | 9 |
| 1.1 Need for Renewable energy resources | 9 |
| 1.2 Biomass and Biorefinery concept | 11 |
| 1.2.1 Biomass | 11 |
| 1.2.2 The Biorefinery concept | 13 |
| 1.3 Production of chemicals and fuel energy from Biomass | 17 |
| 1.3.1 Dimethyl ether..... | 18 |
| 1.3.2 Biodiesel (FAME)..... | 19 |
| 1.3.3 Methyl-tert-butyl-ether (MTBE) and Ethyl-tert-butylether (ETBE)..... | 20 |
| 1.3.4 Primary alcohols | 21 |
| 1.3.4.1 Bioethanol | 21 |
| 1.3.4.2 Biobutanol | 25 |
| 1.4 Guerbet reaction | 28 |
| 1.4.1 Mechanism of Guerbet reaction..... | 29 |
| 1.4.2 Catalysts employed for the Guerbet reaction..... | 30 |
| 1.4.2.1 Homogeneous catalysts | 30 |
| 1.4.2.2 Heterogeneous solid metal + liquid co-catalysts | 32 |
| 1.4.2.3 Monofunctional two component heterogeneous catalysts | 32 |
| 1.4.2.4 Heterogeneous one component multifunctional catalysts..... | 33 |
| 1.5 Hydroxyapatites (HAPs) | 35 |
| 1.5.1 Synthesis of hydroxyapatites | 35 |
| 1.5.1.1 Dry chemical methods | 35 |
| 1.5.1.2 Wet chemical methods..... | 36 |
| Hydrothermal synthesis | 36 |
| Sol-gel method..... | 37 |
| Precipitation..... | 37 |
| 1.5.2 Structure of hydroxyapatite | 38 |
| 1.5.3 Substitutions in hydroxyapatites..... | 41 |
| 1.5.3.1 Substitutions of Ca ²⁺ | 41 |
| 1.5.3.2 Substitutions of PO ₄ ³⁻ /OH ⁻ | 43 |

| | |
|---|-----------|
| 1.5.4 Non-stoichiometry in HAPs..... | 45 |
| 1.5.5 Applications of hydroxyapatites, specific application to the present study..... | 45 |
| 1.6 Objective of our work..... | 51 |
| Chapter 2 Catalyst preparation and experimental techniques | 66 |
| 2.1 Synthesis of hydroxyapatites | 66 |
| 2.1.1 Materials | 67 |
| 2.1.2 Preparation of carbonate-containing HAPs with different Ca/P ratios..... | 67 |
| 2.1.3 Preparation of strontium-substituted HAPs with various substitution extents..... | 68 |
| 2.2 Physicochemical characterization techniques..... | 69 |
| 2.2.1 X-ray powder diffraction & Rietveld refinement..... | 70 |
| 2.2.2 Fourier transforms infrared spectroscopy (FT-IR)..... | 73 |
| 2.2.3 FT-Raman spectroscopy..... | 73 |
| 2.2.4 Solid state nuclear magnetic resonance (NMR) spectroscopy..... | 73 |
| 2.2.5 X-Ray photoelectron spectroscopy (XPS) | 75 |
| 2.2.6 Low-Energy Ion Scattering (LEIS)..... | 76 |
| 2.2.7 Induced Coupled Plasma (ICP) | 76 |
| 2.2.8 Scanning electron microscopy (SEM) | 76 |
| 2.2.9 Porosity measurements by nitrogen adsorption (BET) | 76 |
| 2.2.10 Temperature-Programmed Desorption (TPD)..... | 77 |
| 2.2.10.1 Temperature-Programmed Desorption of Ammonia (TPD-NH ₃)..... | 77 |
| 2.2.10.2 Temperature-Programmed Desorption of Carbon dioxide (TPD-CO ₂) | 77 |
| 2.2.11 Thermo gravimetry & Differential Thermal Analysis (TGA/DTA) | 77 |
| 2.2.12 XPS after adsorption of 2-phenylethylamine (PEA-XPS) | 78 |
| 2.2.13 Reactor setup for isopropanol test | 79 |
| 2.3 Reaction analytical techniques | 80 |
| 2.3.1 Monoreactor setup employed for gas phase Guerbet reaction of ethanol | 80 |
| 2.3.2 Conditions employed for the catalytic test | 82 |
| 2.3.3 Treatment of the catalytic test data | 83 |

Chapter 3 Characterization & Reactivity of Hydroxyapatite-Based Catalysts with Various Carbonate Contents 89

3.1 Introduction 89

3.2 Results and discussion 90

| | |
|--|------------|
| 3.2.1 <i>Characterization of the solids</i> | 90 |
| 3.2.1.1 Bulk composition of the solids | 90 |
| 3.2.1.1 Specific surface areas | 91 |
| 3.2.1.3 Structure of the solids | 92 |
| 3.2.1.3.1 <i>Crystallographic structure</i> | 92 |
| 3.2.1.3.2 <i>Crystallites & grain shape</i> | 97 |
| 3.2.1.3.3 <i>Thermal stability and carbonate content in the prepared solids</i> | 98 |
| 3.2.1.3.4 <i>A & B-type CO₃²⁻ substitution</i> | 104 |
| 3.2.1.4 Surface composition of apatite solids | 106 |
| 3.2.1.4.1 <i>Surface Ca/P ratio and carbonate species</i> | 106 |
| 3.2.1.4.2 <i>Composition of the first atomic layer of the samples</i> | 109 |
| 3.2.1.5 Presence of HPO ₄ ²⁻ groups in the solids | 111 |
| 3.2.1.6 Acid-base properties of the solids..... | 113 |
| 3.2.1.6.1 <i>Total acid sites-nature and distribution</i> | 113 |
| 3.2.1.6.2 <i>Distribution of total basic sites</i> | 118 |
| 3.2.1.6.3 <i>Acid-base behaviour of HAP as catalysts</i> | 120 |
| 3.2.2 <i>Guerbet reaction of ethanol over HAP catalysts</i> | 123 |
| 3.2.2.1 Guerbet reaction products observed at iso-conversion | 123 |
| 3.2.2.1.1 <i>Correlation studies of isopropanol test and Guerbet reaction</i> | 127 |
| 3.2.2.1.2 <i>Direct correlation studies of Guerbet reaction and acid-base properties of the apatites</i> | 135 |
| 3.2.2.1.2.1 Selectivity to ethylene as a function of acid-base properties of HAP catalysts | 136 |
| 3.2.2.1.2.2 Selectivity to diethylether as a function of acid-base properties of HAP catalysts | 140 |
| 3.2.2.1.2.3 Selectivity to acetaldehyde as a function of acid-base properties of HAP catalysts | 142 |
| 3.2.2.1.2.4 Selectivity to 2-buten-1-ol as a function of acid-base properties of HAP catalysts | 143 |
| 3.2.2.1.2.5 Selectivity to Guerbet alcohols as a function of acid-base properties of HAP catalysts | 145 |
| 3.2.2.2 Guerbet reaction: Optimization of experimental conditions | 147 |
| 3.3 Conclusions..... | 155 |

Chapter 4 Guerbet reaction of ethanol over Strontium substituted hydroxyapatite catalysts..... 162

4.1 Introduction 162

4.2 Result and discussion..... 162

| | |
|--|-----|
| 4.2.1 <i>Catalyst Characterization</i> | 162 |
| 4.2.1.1 BET surface area | 162 |
| 4.2.1.2 X-ray diffraction and Rietveld refinement studies..... | 165 |
| 4.2.1.3 Scanning electron microscopy (SEM) | 170 |
| 4.2.1.4 ICP & XPS to determine elemental composition | 171 |
| 4.2.1.5 Low energy ion scattering (LEIS) | 174 |
| 4.2.1.6 Infrared spectra of the solids | 175 |
| 4.2.1.7 Raman spectra of solids..... | 177 |

| | |
|---|------------|
| 4.2.1.8 TPD-NH ₃ and TPD-CO ₂ | 179 |
| 4.3.1.9 Isopropanol test | 183 |
| 4.2.2 <i>Catalytic reaction</i> | 186 |
| 4.2.2.1 Guerbet reaction products observed at iso-conversion | 186 |
| 4.2.2.2 Guerbet reaction: Optimization of experimental conditions | 189 |
| 4.3 Conclusions..... | 195 |
| General Conclusions and Perspectives | 200 |
| Annexes..... | 204 |
| <i>Annexe 1 X-ray diffraction (XRD)</i> | 205 |
| <i>Annexe 2 Fourier Transform Infrared spectroscopy (FTIR)</i> | 206 |
| <i>Annexe 3 Raman Spectroscopy</i> | 208 |
| <i>Annexe 4 Nuclear Magnetic Resonance (NMR) spectroscopy</i> | 210 |
| <i>Annexe 5 X-ray photoelectron spectroscopy (XPS)</i> | 211 |
| <i>Annexe 6 Low-energy ion scattering (LEIS)</i> | 213 |
| <i>Annexe 7 Inductively coupled plasma (ICP)</i> | 215 |
| <i>Annexe 8 Scanning electron microscopy (SEM)</i> | 218 |
| <i>Annexe 9 Porosity measurements by nitrogen adsorption (BET)</i> | 220 |
| <i>Annexe 10 Temperature-Programmed Desorption (TPD)</i> | 223 |
| <i>Annexe 11 Thermogravimetry & Differential thermal analysis (TGA/DTA)</i> | 224 |

General Introduction

The rapid worldwide increase in the consumption of fossil fuels to meet the increasing energy demands suggests that time is not too far before depletion begins to adversely affect petroleum and natural gas resources. It is generally agreed that we will be running out of petroleum within 50 years, of natural gas within 65 years and of coal in about 200 years at the present pace of consumption [1,2]. This is expected to result in increased use of renewable energy sources, such as hydraulic energy, solar energy, wind energy, tidal energy, geothermal energy and also energy from renewable raw materials such as biomass, that will in principle never run out. However, biomass is very likely to be the only viable alternative to fossil resources for production of liquid biofuels and, especially, chemicals. So, it becomes necessary to develop and implement biorefinery processes that can transform biomass to a spectrum of marketable products and energy (including fuels and chemicals). This is one of the main concepts in EuroBioRef (EUROpean multilevel integrated BIOREFinery design for sustainable biomass processing), the project under which this work has been carried out.

Bioethanol and biobutanol are the most common primary alcohols that can be synthesized from biomass. In addition to their use as solvents and chemicals (or platform chemicals), they are used (ethanol) or being envisioned to be used (butanol) as liquid biofuels in Otto and diesel engines, making them important versatile molecules in the biorefineries. Biobutanol is used as a chemical, fuel and a fuel additive can also be produced directly from biomass, but its production through these routes (biotech and syngas conversion) is not economically feasible, at least for the moment. Better solution for these problems is to transform some amount of efficiently produced bioethanol to heavier alcohols like butanol through the Guerbet chemistry.

Both homogeneous and heterogeneous catalysts have been reported for the production of heavier alcohols through the Guerbet reaction. However considering the catalyst recovery/reusability and environmental feasibility, the heterogeneous catalysts are preferred over homogeneous catalysts. Several heterogeneous catalysts were investigated in the Guerbet reaction of ethanol and among all hydroxyapatites were found to be an active catalyst for heterogeneous gas phase Guerbet reaction of ethanol [3,4]. The drawback of using hydroxyapatite for the Guerbet reaction is that, at higher ethanol

conversions, the produced primary alcohols (for example *n*-butanol) undergo further condensation to produce heavier alcohols and other heavier products [5]. This could eventually reduce the selectivity to primary products like *n*-butanol. The heavier alcohols can however be used as solvents, fuel additives and plasticizers (*e.g.*, 1-butanol, 2-ethylhexanol, etc.) or can be further transformed to paraffins by dehydration/hydrogenolysis for use in aviation fuels, straightforwardly as blends. So, it would be better to find an application to use butanol and the entire heavier product mixtures formed during the Guerbet reaction. The overall aim of this thesis is to tailor the acid-base properties of hydroxyapatites and use them in the Guerbet reaction of ethanol to produce both butanol and heavier product mixtures, respecting the biorefinery concept of producing chemicals and fuels.

The thesis is divided into four chapters. In the first chapter, a literature review is presented mainly focusing on the need of utilization of biomass for the production of liquid energy fuels like ethanol, butanol etc... We also mentioned the advantages of Guerbet reaction for the conversion of bioethanol to butanol or heavier alcohols and different types of catalysts employed for this reaction including the heterogeneous hydroxyapatite catalysts. The structure, properties and application of the hydroxyapatite solids are also discussed in the first chapter.

The second chapter is concerning the procedures for the preparation of different hydroxyapatite solids and the experimental techniques used for their characterization. The analytical setup used for the Guerbet reaction of ethanol is also described at the end of this chapter.

Chapter 3 includes extended characterization of carbonate-containing apatite catalysts and the Guerbet reaction of ethanol over these catalysts. The first part of this chapter comprises of the structural, textural and acid-base properties of the hydroxyapatite solids. In the second part, we performed a correlation study between Guerbet reaction of ethanol and acid-base behaviour of the hydroxyapatite catalysts. Final part is the study dealing with the optimization of the Guerbet reaction conditions for the hydroxyapatite catalysts.

Chapter 4 comprised of characterization of Strontium-substituted apatites followed by ethanol reaction over the Sr-containing apatites. The first part consists of deep characterization of the solids to gain an insight regarding the structural, textural and acid-

base properties of the solids. Thereafter, the activity of these solids towards the Guerbet reaction of ethanol is examined.

Finally, the general conclusion highlighting the interesting results and the perspectives in this research is proposed.

[1] W. Soetaert, E. J. Vandamme, *Biofuels, Wiley series*, ISBN 978-0-470-02674-8 (2009) p. 1.

[2] C.J Campbell, The future of oil. *Energy Explor. Exploit*, vol 16 (1998) p .125–152.

[3] T. Tsuchida, S. Sakuma, T. Takeguchi, W. Ueda, Direct Synthesis of n-Butanol from Ethanol over Nonstoichiometric Hydroxyapatite, *Industrial & Engineering Chemistry Research*, vol 45 (2006) p. 8634-8642.

[4] T. Tsuchida, J. Kubo, T. Yoshioka, S. Sakuma, T. Takeguchi, W. Ueda, Reaction of ethanol over hydroxyapatite affected by Ca/P ratio of catalyst, *Journal of Catalysis*, vol 259 (2008) p. 183-189.

[5] T. Tsuchida, T. Yoshioka, S. Sakuma, T. Takeguchi, W. Ueda, Synthesis of Biogasoline from Ethanol over Hydroxyapatite Catalyst, *Industrial & Engineering Chemistry Research*, vol 47 (2008) p. 1443-1452.

Chapter 1 Bibliography

1.1 Need for Renewable energy resources

It is well known that developed and industrialized nations consume more energy per capita than the developing countries. There is a saying that the higher the living standards, the higher the energy per capita consumption [1]. Serious geopolitical implications arise from the fact that our society is heavily dependent on only a few – mainly fossil – energy resources such as petroleum, mainly produced in politically unstable oil-producing countries and regions. According to the World Energy Council, about 82 % of the world's energy needs are currently covered by fossil resources such as petroleum, natural gas and coal [2,3]. However, the rapid worldwide increase in the consumption of fossil fuels that occurred during the twentieth century to meet the energy demands suggests that time is not too far before depletion begins to adversely effects petroleum and natural gas resources. It is generally agreed that we will be running out of petroleum within 50 years, of natural gas within 65 years and of coal in about 200 years at the present pace of consumption [1,4]. Campbell and Laherrère (1998), well-known petroleum experts, have predicted that the world production of petroleum will reach its maximum production level (so-called 'peak-oil', which was expected around 2010), and, from then on, the world production rate of petroleum will inevitably start decreasing. As the demand for petroleum is soaring, especially to satisfy the needs of economically skyrocketing countries such as China and India, petroleum prices are expected to further sharply increase [5]. The effect is already visible today, with petroleum prices soaring to over 145 \$/barrel during July 2008, and with a present (2012) value above 100 \$/barrel, as shown in Figure 1-1 [6]. In this context, questions started arising worldwide concerning the energy supplies for our future demand.

Also, ecological disadvantages have come into prominence, as the use of fossil energy sources suffers from a number of ill consequences for the environment, including the greenhouse gas emissions, air pollution, acidic rains, etc. There is also considerable disagreement as to whether increased fossil fuel consumption is the primary cause of global climate change. The greater the consumption of fossil fuels, especially by motor vehicles and power plants, the larger the levels of air pollution in a given region.

Combustion of these fossil fuels is considered to be the largest contributing factor to the release of greenhouse gases into the atmosphere [1]

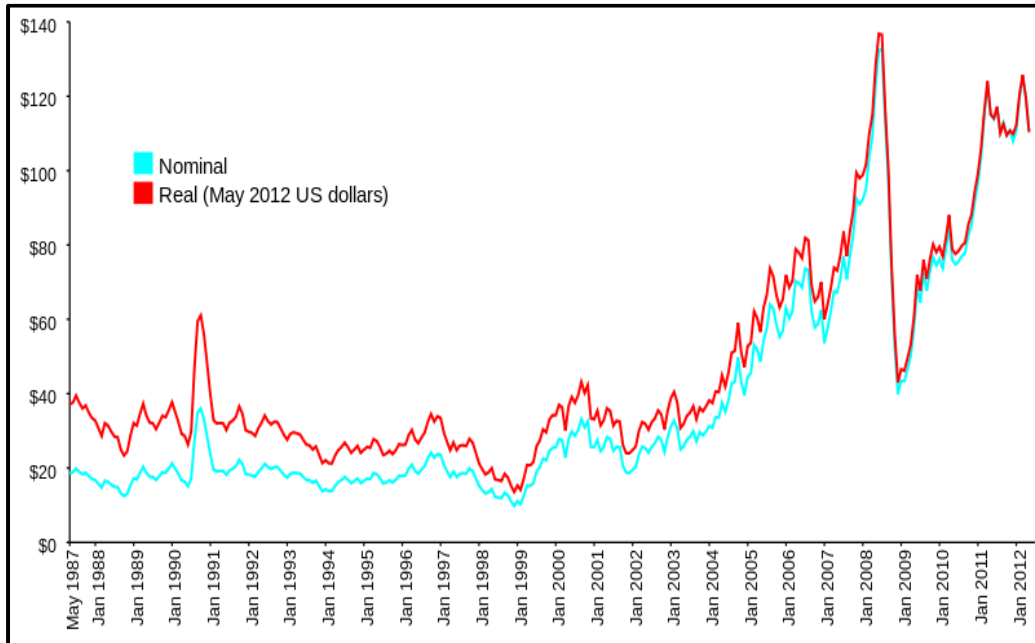


Figure 1-1 Brent barrel petroleum spot price since May 1987.

Carbon dioxide, for example, is one of the primary products of fossil fuel combustion, and is a greenhouse gas that is widely believed to be associated with global warming causing the average surface temperature of the Earth to rise in response, which is a point on which the largest majority of the climate scientists agree on, and that is believed to cause major adverse effects. The burning of fossil fuels produces around 21.3 billion tonnes of carbon dioxide (CO₂) per year, but it is estimated that natural processes can only absorb about half of that amount, so there is a net increase of *ca.* 10.65 billion tonnes of atmospheric carbon dioxide per year (one ton of atmospheric carbon is equivalent to 44/12 or 3.7 tonnes of carbon dioxide) [7]. Fossil fuels also contain some radioactive elements like Uranium and Thorium, so that they can also contribute to increased levels of radioactive pollution. Air pollution and the formation of smog are other problems arising from the use of fossil fuels. Moving away from fossil fuels would undoubtedly significantly decrease the environmental pollution, but some energy experts fear that renewable energy is still not ready to replace fossil fuels at a global level. This is expected to result in increased use of

renewable energy sources, such as hydraulic energy, solar energy, wind energy, tidal energy, geothermal energy and also energy from renewable raw materials such as biomass, that will in principle never run out [1]. Electricity and heat can be provided by several renewable alternatives (wind, sun, water, biomass, and so on), while biomass is very likely to be the only viable alternative to fossil resources for production of liquid biofuels and chemicals. Transformation of biomass to liquid fuels will be one of the best alternatives, not only because it is renewable, but also due to the reduction of the emissions of greenhouse gases like CO₂ (biomass-derived carbon is classified as carbon neutral and is not accounted as a source of CO₂ emissions by the Kyoto agreement).

1.2 Biomass and Biorefinery concept

1.2.1 Biomass

The directive adopted by the Industry, Research and Energy Committee of the European Parliament on the 11th of September 2008 gives the following definition of biomass: “Biomass” means the biodegradable fraction of products, waste and residues from agriculture (including vegetal and animal substances), aquaculture, forestry and related industries, the separated collected biodegradable fraction of industrial and municipal waste as well as wastewater sludge.

Generally speaking, biomass corresponds to any organic matter from living based on carbon, hydrogen and oxygen available on recurring basis. Especially, biomass chemicals/energy can be derived from five distinct energy sources: garbage, wood, waste, landfill gases, and alcohol fuels [8]. Depending upon the type of biomass used, the produced biofuels or chemicals are usually classified using two main categories: first generation and second generation fuels/chemicals. A first generation of fuels and chemicals is currently produced from sugars and vegetable oils derived from food crops. In that case, the raw materials include sunflower, jojoba, soya bean, safflower, ..., for biodiesel production, and corn, sugar cane, ..., for ethanol production. Those are, however, competing with food chains concerning the feedstock. For example, first generation

bioethanol is produced by fermenting plant-derived sugars to ethanol, using a process similar to that used for beer and wine production, which requires the use of food crops such as sugar cane, corn, wheat, or sugar beet as starting materials. These crops are required for food needs and, if too much biofuel is produced from them, food prices could rise and shortages might be experienced in some countries. Corn, wheat, and sugar beet also require high agricultural (entrants) under the form of, *e.g.*, fertilizers, which limits the extent of the neat greenhouse gas reductions that can be achieved using biomass. Further, many first generation biofuels depend on subsidies and are, in fact, not cost-competitive when compared to existing fossil resources-derived fuels, and some of them yield only very limited greenhouse gas emissions savings [9]. Furthermore, when demand outstrips the available volumes, first generation biofuels may no longer be a sustainable/suitable option.

Due to a strong demand in biofuels – mainly driven by regulations –, the price of corn and vegetable oil in the US and Europe has been increasing. So, it is now becoming widely recognised by governments and scientists that the lignocellulosic materials (*e.g.*, wood, straw, energy crops) offer much better opportunity, since they enable getting rid, to a certain extent, of the competition with the food sector, provided specific care is taken. Hence, a second generation of technologies are being developed to exploit the cheaper and heavily abundant lignocellulosic feedstock. The goal of the second generation biofuel processes is to extend the amount of biofuel that can be sustainably produced by using biomass consisting of the residual non-food parts of current crops, such as stems, leaves and husks, as well as other crops that are not used for food purposes (the so-called ‘non food crops’), such as switchgrass, for example. The first issue that second generation biofuel processes is facing is to extract useful feedstocks from this woody or fibrous biomass, where the useful sugars under a polymerized form (cellulose, hemicellulose) are locked in by lignin. Conversion of lignocellulosic biomass to biofuel indeed involves a pre-treatment followed by enzyme-catalyzed hydrolysis to generate fermentable sugars: The fractionation pre-treatment is used for the separation of biomass components (lignin, cellulose and hemicellulose). Pulping processes and hydrolytic processes are the commonly employed pre-treatment processes which include almost all the main fractionation technologies like acid & alkaline hydrolysis, enzymatic hydrolysis, organosolv.... During pre-treatment, the hemicellulose fraction ends up either with lignin or

with cellulose. Depending on the aforementioned process, the lignin fraction is either liquid or solid, while the other cellulose fraction is of the opposite nature. Then, cellulose (and/or hemicellulose in certain cases) is degraded by enzymes to fermentable sugars. The problem is that these sugars are not as pure as those that are directly extracted from sugar plants. They, *e.g.*, contain lignin fragments, which are hindering the action of the microorganisms subsequently used for fermentation to produce ethanol (or other compounds if desired). As a general matter, the main by-product of this process is lignin, which can be burned as a carbon neutral fuel to produce heat and power for the processing plant and possibly for surrounding homes [9], even if ‘smarter’ applications are considered to use this refractory natural polymer as a chemical or a chemicals’ precursor.

1.2.2 The Biorefinery concept

Early biorefinery-like concepts have been developed in the food and paper industries and are now extended for the production of energy, chemicals and materials from renewable feedstocks [10,11,12]. The idea underneath is to make the best use of the value derived from biomass by generating multiple products and energy *via* well integrated processes, valorizing co-products and by-products (zero waste concept), and optimizing the inputs and outputs [13]. Ultimately, biorefineries will produce different industrial products from biomass, like this is already achieved in fossil oil-based refineries, where many energy and chemical products are produced from crude oil. This will include low-value, high volume products such as transportation fuels (*e.g.*, bioethanol, biodiesel) and high value, low volume products or speciality chemicals such as cosmetics or nutraceuticals [14], thus yielding the required economical balance.

Biorefineries should then use various combinations of feedstock and conversion technologies to produce a variety of products. However, as a matter of fact, most of the existing biorefinery concepts use limited feedstocks and technologies, and solely produce ethanol or biodiesel. They thus generally focus on producing biofuels, with the consequence of substantially reducing the value-added of the biomass chain. Only a relatively small fraction of materials is used for chemistry and chemical products that have a higher value-added. Economical and production advantages increase with the overall

level of integration in the biorefinery. The benefits of an integrated biorefinery are mostly based in the diversification in feedstocks and marketable final products. As aforementioned, this is what is missing from the majority of the current biorefinery concepts that are limited in using one feedstock and producing one product. This means that new marketable products like high value-added chemical or biochemical products together with low value-added specific biofuels like high energy biofuels for aviation could enhance the viability and interest of biomass.

The 'EUROpean multilevel integrated BIOREFinery' (EuroBioRef) project, in the frame of which this PhD study has been carried out, is thus focused on developing and deploying a high integrated and diversified concept with feedstocks, technologies and processes that can be bundled to enable and define a new interweaved value chain with integrated flexible biorefinery facilities. The EuroBioRef concept was designed for sustainable biomass processing' (eurobioref.org), as a European project of the 'large-scale' type. It has been previously assessed after extensive analysis that EuroBioRef biorefineries should definitely be chemicals/materials-driven, meaning that the best part of the crops are being used to make high value chemicals and products, and that the residues are being used to produce energy, either consumed on-site or being exported under various forms. This is a rethinking of commonly admitted biorefineries concepts that are strongly biofuels-driven. This approach has recently been comforted due to a remarkable change in the environment outside of the EuroBioRef project, namely the announcement of plans for massive exploitation of cheap shale gas in the US, which might considerably change the deal. As a consequence, only biobased products with superior technical properties will be able to compete with fossile ressources-derived products. In this respect, the expected biorefineries are quite comparable to petrochemical refineries. Part of biomass is converted by successive operations involving hydrolysis, fermentation and chemo-catalytic routes into platform molecules that can be used as building blocks in the synthesis of chemicals, fuels and polymers, while the remaining part of biomass is converted to fuels through gasification (syngas), pyrolysis (bio oil), fermentation (biogas) [13].

According to some classifications, we can distinguish different types of biorefineries [14,15,16]: (1) Phase I biorefinery, which uses single feedstock, single process and single major product; (2) Phase II biorefinery with single feed stock, multiple processes and multiple major products; And (3) Phase III biorefinery, which is the most advanced type of

biorefinery that uses multiple feedstocks besides multiple processes and multiple products (e.g., EuroBioRef). Currently, four type of phase III biorefinery systems are being investigated in research and development: starch and sugar biorefinery, oilseed biorefinery, green biorefinery, lignocellulosic feedstock biorefinery, and aquatic biorefinery [17]. The starch and sugar biorefinery possess starch crops such as cereals (e.g., wheat, maize...) and potatoes or sugar crops such as sugarbeet or sugarcane to produce energy, chemicals and materials (Figure 1-2). Oilseed biorefineries mainly produce food and feed ingredients, biodiesel and oleochemicals from oilseeds such as rape, sunflower and soyabean (Figure 1-3). Green biorefineries use natural wet biomass such as green grass, clover, lucerne or alfalfa, and converts it into useful products including biogas, proteins, chemicals and materials (Figure 1-4). A lignocellulosic feedstock biorefinery will then use lignocellulosic biomass such as wood, straw etc.... (Figure 1-5). Finally, in aquatic biorefinery, aquatic biomass (micro-algae and sea weed) is used as a feedstock, characterised by high productivity and a high content of valuable components, including lipids, proteins, polysaccharides and other specific biomolecules (Figure 1-6). Of course, biorefinery concepts mixing the specificities of the aforementioned main types of biorefineries are also of high relevance [17].

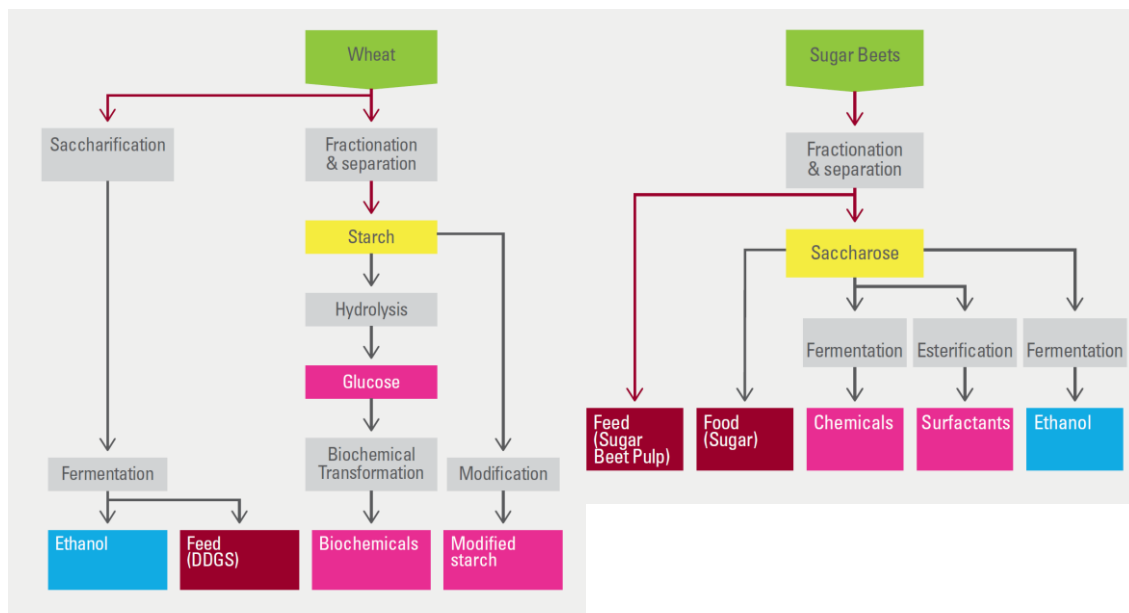


Figure 1-2 Schematic diagrams of starch and sugar biorefinery [17].

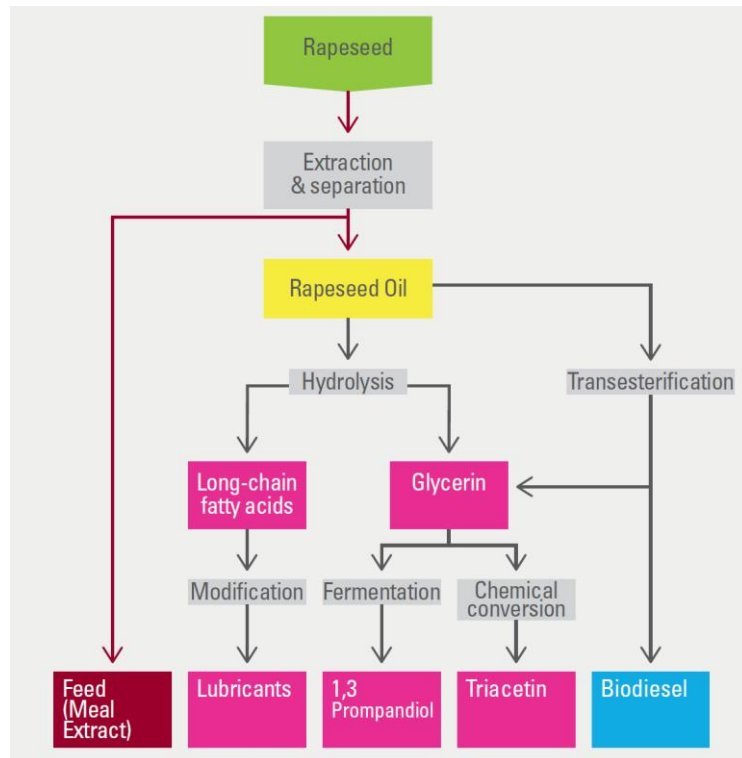


Figure 1-3 Schematic diagram of an example of oilseed biorefinery [17].

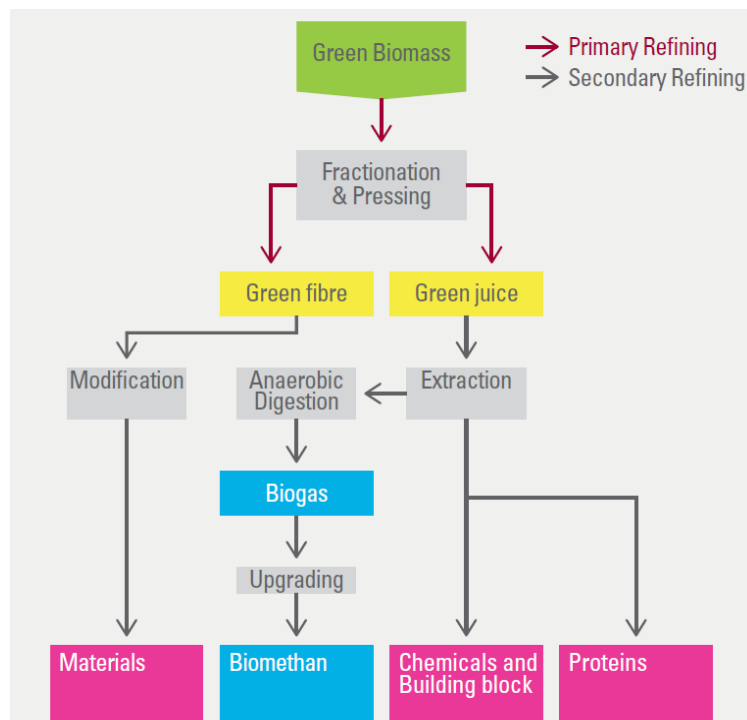


Figure 1-4 Schematic diagram of green biorefinery [17].

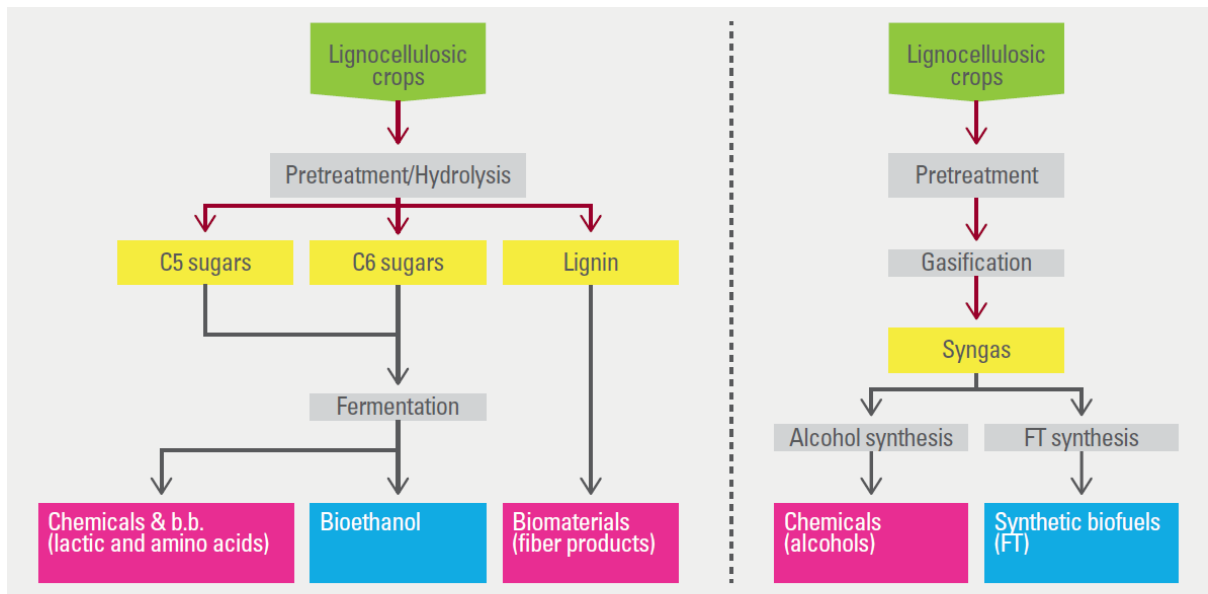


Figure 1-5 Schematic diagram of biochemical (left-hand side) and thermochemical (right hand side) approaches in lignocellulosic biorefinery [17].

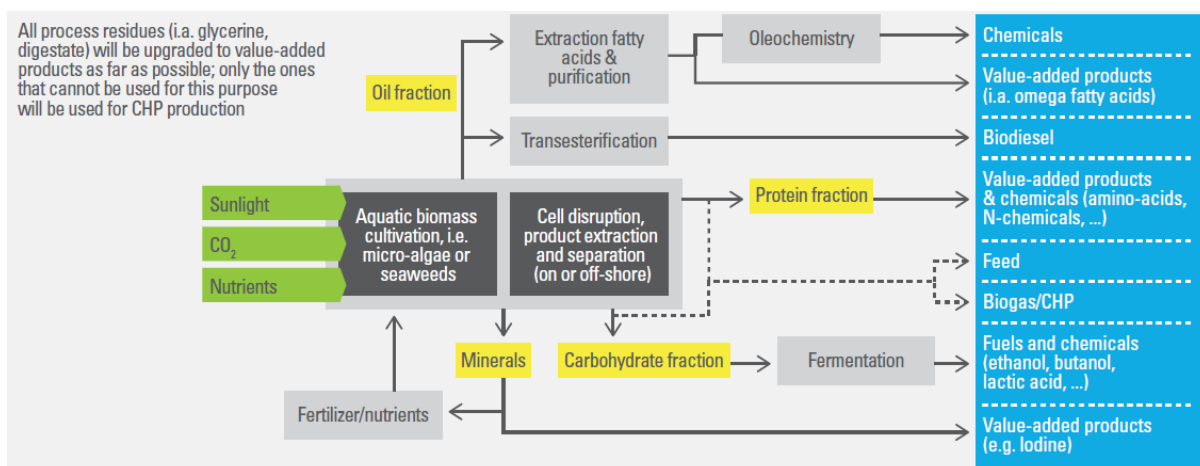


Figure 1-6 Schematic diagram of aquatic biorefinery [17].

1.3 Production of chemicals and fuel energy from Biomass

As aforementioned, simultaneous production of chemicals and energy is the main target in next generation biorefinery concepts, as this is the only way to yield economically viable units. However, during the past decades, bioenergy production from renewable biomass has considerably increased. The European Union then prompted its member states to

increase their use of biofuels to meet the target share of 5.75% of the total fuel market in 2010, without promoting biochemical development. In order to achieve this goal, it has then become essential to develop different biorefineries for yielding bioenergy products, depending on regional possibilities and resources availability. Energy sources are generally classified as solids (*e.g.*, wood, pellets), liquids (*e.g.*, ethanol, biodiesel) and gas (*e.g.*, biogas, H₂). They can be also divided into four groups depending on the kind of process used in production of energy products, that is, physical upgrading, microbiological, thermochemical and chemical processes. Chemical processes have been mainly employed for the conversion of renewable resources such as biomass to many energy products, which are being used as fuels in the transportation sector. The liquid energy sources that are envisioned to be used as biofuels (or that are actually currently used) for transportation purposes are dimethylether, biodiesel, ethyl-*tert*-butylether/methyl-*tert*-butylether, and primary alcohols such as ethanol and butanol [14].

1.3.1 Dimethyl ether

Dimethyl ether (DME), also known as methyl ether, methyl oxide, or wood ether is the simplest ether present with higher ethers proposed as diesel additives, and is generally proposed both under the form of a colourless liquid or a compressed gas. In addition to its fuel properties, DME is considered also as a chemical with various applications such as a laboratory reagent and solvent, an aerosol propellant, a refrigerant, etc... It can be produced from both fossil fuels, such as natural gas and coal, or renewable feedstocks, such as waste material and wood, thus offering a high energy security [18]. DME is produced generally in two steps. First, hydrocarbons obtained from biomass are converted to syngas. Then, syngas is converted to DME either through methanol intermediate production (conventional method), which is a two steps process, or directly from syngas in a one step more challenging process. The two steps process generally uses fixed bed catalytic dehydration of methanol using Cu-based catalysts, and also catalysts like silica-alumina, γ -alumina etc. The direct one step synthesis of DME requires a bifunctional catalyst system that acts at the same time as a methanol synthesis catalyst and a methanol dehydration catalyst in a single unit. For this purpose, the use of Cu/ZnO/ γ -Al₂O₃, water gas shift catalysts, has been reported [18,19].

Several bodies are actively studying the use of DME as a substitute fuel for diesel vehicles due to its low ignition temperature, high cetane number, high oxygen content, lower NO_x emissions etc... However, there are some disadvantages of using DME as a fuel. The viscosity of DME is lower than that of diesel, which causes leakage along the plungers and thus increases the wear of all the moving parts in the injection systems. Its high vapour pressure prevents stable fuel injection operation. Further, a DME volume of about 1.8 times that of diesel should be injected in order to supply the same amount of energy, also leading to longer injection periods. In addition to its limited production, total investment and operating costs are also required to set up necessary distribution infrastructure that seems to be critical concerning the DME's future as a transportation fuel. Nevertheless, at least for the moment, it can be used as a blend in small quantities in the transportation fuels [20].

1.3.2 Biodiesel (FAME)

Biodiesel is a well-known renewable fuel that is produced from a variety of vegetable oils such as rapeseed oil, soybean oil, sunflower oil and palm oil. The most widely used biodiesels are rape methyl esters (RMEs) in Europe and soybean methyl esters (SMEs) in the US. They are collectively known as fatty acid methyl esters (FAMEs) [20]. Transesterification is one of the most common methods to produce biodiesel. It consists on a reaction between a triester (triglyceride) and an alcohol to form monoesters (biodiesel), by separating them from their initial glycerol backbone, which is then released as a by-product. In this process, alcohols such as methanol and ethanol are the most widely used ones, and particularly methanol owing to its low price, availability and easier handling in the process. Transesterification reaction can be either carried out *via* catalytic or non-catalytic processes. Non-catalytic processes are slow and usually require high pressures and temperatures. Base catalysts (the most commonly used in the homogeneous phase), acid catalysts and enzymes are three categories of catalysts, which have been studied so far for biodiesel production by catalytic processes [21]. Especially, a significant amount of work has been carried out on homogeneous base and acid catalytic transesterification of vegetable oils. Sodium hydroxide and potassium hydroxide are usually used as homogeneous base catalysts and sulphuric acid and hydrochloric acid as homogeneous

acid catalysts. One of the major disadvantages of these homogeneous catalysts is that they cannot be reused or regenerated, because the catalyst is consumed in the reaction and separation of catalyst from products is difficult. Besides, the process is not environmentally friendly because of the large amount of wastewater produced in the separation step. In order to solve these problems, solid catalysts such as metal hydroxides, metal complexes, metal oxides such as calcium oxide, magnesium oxide, zirconium oxide and supported catalysts are being investigated [21].

Mixtures of FAME with diesel at concentrations upto 5% (vol) are currently used in France. FAME has a relatively high flash point and a high cetane number, which improves the safety in fuel handling and reduces the ignition delay and combustion noise. Nevertheless, there are some evidences that FAME attacks some plastics used for seal and coatings. Thus, the interaction of high percentage blends with the components of fuel injection system can limit their durability. Further, its lower volumetric energy density compared to that of conventional diesel requires large fuel volume to be transported for the same distance travelled. In addition, it causes emission of high amount of aldehydes and NO_x during combustion. Thus, neat FAME is not a viable option at present, but its addition to diesel at low concentrations can be considered to have an effect equivalent to that of oxygenated fuel additives [20]. Note that subsidies are making this sector profitable, but that the situation might change in a quite near future.

1.3.3 Methyl-tert-butyl-ether (MTBE) and Ethyl-tert-butylether (ETBE)

Efforts made for the synthesis of oxygenate fuel additives with high octane number and low Reid vapor pressure (RVP) also induced a research effort on tertiary ethers. Methyl-*tert*-butyl-ether (MTBE) is the most widely produced tertiary ether worldwide because of the availability of methanol. However, objections arising from environmental and health problems against the use of MTBE limited its application as a gasoline. MTBE was found to act as an underground water pollutant and was then banned in some countries [22]. In countries with large areas suitable for agriculture, ethanol-based oxygenates like ETBE are considered as a good alternative to MTBE, though the production cost of ETBE is higher than that of MTBE. ETBE can be considered as a partially biomass-derived oxygenate

gasoline additive (containing 33 % of renewable carbon as it is synthesised by a reaction between bioethanol and petro-sourced isobutene). According to European fuel regulations, 22 Vol.% of ETBE (which corresponds to 7 Vol.% of incorporated ethanol) can be used as a blend with gasoline. Note that there is a possibility to blend together 10 Vol.% of ethanol and 22 Vol.% of ETBE to gasoline (in other words, in conventional gasoline, it is possible to incorporate 17 Vol.% bioethanol equivalents). Recently, some research efforts concentrate on producing ETBE from *tert*-butyl alcohol and ethanol, catalyzed by β -zeolite in reactive distillation [23]. However, economical and sustainable sourcing of bio-*tert*-butyl alcohol is far from being a reality.

1.3.4 Primary alcohols

Ethanol and butanol are the most common primary alcohols that can be synthesized from biomass. In addition to their use as solvents and chemicals (or platform chemicals), they are used (ethanol) or being envisioned to be used (butanol) as liquid biofuels in Otto and diesel engines, making them important versatile molecules in the biorefineries. These alcohols can be prepared from biomass such as sugarcane, sugar beet, wheat, corn, switchgrass, agricultural residues, wood and many other industrial wastes. The most important characteristic of ethanol and butanol, which makes them suitable as fuel for Otto engines, is their high octane number. They are less toxic in nature and possess sufficient energy density to be directly used as fuels or blended with gasoline.

1.3.4.1 Bioethanol

As evocated above, ethanol can be produced from different raw materials using different processes. Three different feedstocks are widely used for the ethanol production: (i) sugar feedstock, which includes sugarcane and sugar beet, (ii) starch feedstock such as cereal grains, corn and potato and (iii) cellulosic feedstock comprising of wood, grass and other agricultural residues (this last option, known as ‘second generation bioethanol’ is however still at the demonstration pilot stage).

The production of ethanol from sugar and starch feedstock has normally a common pathway. At the beginning of the process, sugar and starch feedstocks are chopped and ground. The next step is acid/enzymatic hydrolysis and breaking down of the sugars or starch to monomer units such as glucose and fructose. For example, sugar cane containing disaccharide sucrose is hydrolyzed to glucose and fructose units using enzyme saccharomyces, and starch, a polysaccharide (in fact, two different polysaccharides), is converted to glucose by hydrolysis with dilute acid and then reacted with enzyme amylases [24]. The so-produced glucose and fructose units are then available for fermentation to ethanol (with, usually, a final concentration of 15 % in the fermentation broth), commonly using a yeast. After the fermentation process, it is necessary to separate the ethanol from the other materials (including huge amounts of water) by distillation, and the so-obtained ethanol has a concentration of about 95 %. Further dehydration of ethanol is normally done by addition of chemicals or drying agents to produce 99.9 % ethanol or absolute ethanol. The cheapest bioethanol is produced from sugarcane in Brazil, and the second cheapest production is in USA from corn. The first generation bioethanol, produced from sugarcane and corn grains is one of the easiest and most efficient processes among those currently under operation.

Devoting land to fuels production could reduce the land availability for food production, this is at present not a serious problem (only 3 % of the lands worldwide are used for industrial crops, this figure being as low as 2 % currently in the EC), but the industrial crops fraction could become progressively more important with the increasing demand in bioethanol. For this reason, it is important to shift production to second generation bioethanol utilizing fast growing plants like miscanthus or switchgrass that could be cultivated, *e.g.*, in unused land and especially starting to use cellulose-based feedstocks like wood and waste lignocellulosic materials as raw materials [25]. Two ways can be employed for the production of cellulosic ethanol, namely cellulolysis and gasification. Cellulolysis consists of several stages such as a pre-treatment step, cellulose hydrolysis, fermentation and distillation. Unlike production from sugar/starch feedstocks, an additional pre-treatment is then required for cellulosic feedstocks to liberate the cellulose from the rigid and crystalline lignin seal to make it accessible for subsequent hydrolysis step. The pre-treatment techniques generally used are acid hydrolysis, steam explosion, organosolve, sulfite pre-treatment to overcome recalcitrance of lignocellulose (SPORL), alkaline wet

oxidation and ozone pre-treatment [26,27]. Most of the pre-treatment processes are not effective for the feedstocks like forest biomass, which possesses high lignin content. Organosolve and SPORL are the only techniques that can reach 90 % of cellulose conversion from forest biomass. A new pre-treatment process called 'BALI' was recently developed in the EuroBioRef project by the Norwegian company Borregaard. It enables complete conversion of biomass to ethanol and other valuables out of various lignocellulosic sources, including forest products. In addition, it facilitates low cost hydrolysis of cellulose by low enzyme consumption and also by recirculation of the enzymes used for hydrolysis. Cellulose hydrolysis involves acidic or enzymatic breaking down of cellulose into glucose molecules. The hydrolysis is followed by fermentation and distillation like in the case sugar and starch feedstocks, except that the processes must be adjusted, as aforementioned, due to the presence of specific fermentation inhibitors derived from the first fractionation/hydrolysis step. In the gasification process, which is much less advanced and still largely at the research stage, the carbon-based complex cellulosic materials are converted to synthetic gas (syngas), which comprises CO, CO₂ and H₂. Then, syngas can be transformed to bioethanol using heterogeneous catalysts, or, as declared more recently, by fermentation using bacteria *Clostridium ljungdahlii* instead of yeast. However, the research concerning syngas conversion to the so-called 'higher alcohols' is still at the early stage with poor yields and also the gasification process seems to be more energy consuming, currently making it less applicable. Nevertheless, as aforementioned, it is expected that, in the future, the second generation lignocellulosic feedstocks will be the major sources for the production of bioethanol.

Ethanol is a colourless liquid soluble in water and can be used as a pure fuel or blended with gasoline or diesel. It is used in Otto engines and can be blended with gasoline up to 25% (gasohol) in adapted engines, but a blend of 10 % ethanol or less is used in most of the countries (conventional engines tolerance limit). Pure ethanol has been also used in heavy vehicles with diesel engines and as a mixture of up to 85 % with gasoline in flexible fuel vehicles (FFV) [14]. As aforementioned, bioethanol can also be considered as a biomass-derived platform molecule, which can be upgraded for the production of various chemicals, monomers, solvents, etc... Figure 1-7 shows some possible conversion pathways for bioethanol.

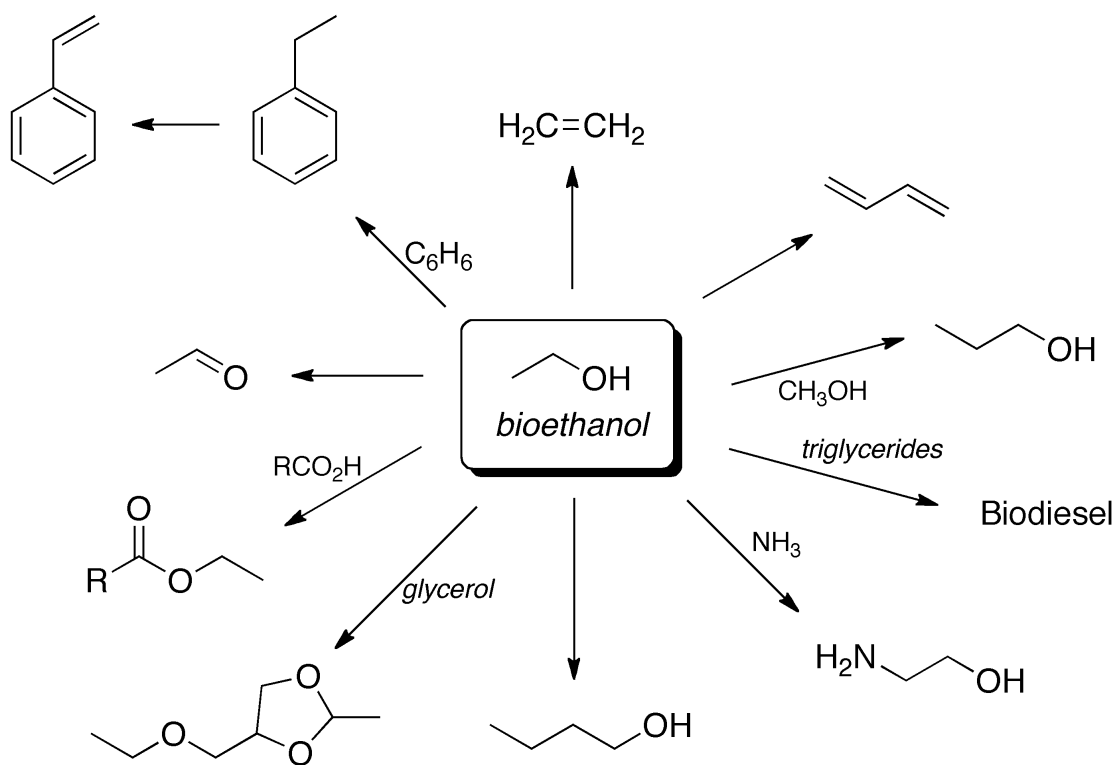


Figure 1-7 Potential conversion pathways of bioethanol.

While ethanol has many beneficial properties when substituting petroleum fractions in fuels, it has some shortcomings too. These shortcomings include a high vapour pressure, affinity for water and lower energy content, which thus involves significant logistical complexity to its blending, transport and use. Ethanol is blended at a late stage in the production chain, namely at the terminal instead of in the refinery, as it cannot be transported *via* pipelines in the United States. Further, the use of high blend ratios of ethanol with gasoline requires modified engines (Flex fuel vehicles), and, due to the lower energy content in ethanol, as the detrimental effect of reducing the vehicles mileage. Biobutanol can overcome many of these ethanol's shortcomings, which makes this compound very attractive and a significant production growth for this product is foreseen. Further, butanol production can be synergistic with existing and future ethanol production technologies [14], by, for example, essentially using the same production/distribution infrastructures.

1.3.4.2 Biobutanol

Biobutanol is considered as one of the major value added products in biorefinery because of its possible versatile use in both chemicals (as is or under the form of a platform C4 molecule) and biofuel sectors. It has a wide range of application and is used, *e.g.*, as an intermediate for butyl esters, as an ingredient in perfumes and pharmaceuticals, in the manufacture of solvents for paints, dyes, alkaloids etc..., as a swelling agent in textile industries, as a component of brake fluids and repellents. It is considered as a good substitute for the current fuels and can be advantageously blended with gasoline. Biobutanol with a higher molecular weight than ethanol has many similarities to bioethanol, but with some additional advantages [13,14]:

- Butanol has a higher energy content than ethanol and can be easily blended with gasoline at higher concentrations for use in standard vehicle engines;
- Butanol has a better tolerance to water contamination and is less corrosive than ethanol;
- Butanol is suitable for transport in pipelines, and has the potential to be easily incorporated into gasoline and without any additional supply infrastructure;
- Butanol/gasoline mixtures are less susceptible to demixtion in the presence of water compared to ethanol/gasoline blends, and demands no essential modifications to blending facilities, storage tanks or retail pumps.

Petroleum-derived butanol is produced by the Oxo process, more formally known as hydroformylation, a catalytic reaction of syngas with propylene to form butyraldehyde followed by hydrogenation. A variety of transition metal catalysts including phosphine complexes of cobalt and hydridocobalt clusters have been investigated. Platinum, ruthenium and cobalt catalysts have shown reasonable activity towards hydroformylation among which the Co ones are found to be more advantageous. Rhodium complexes demonstrated higher activities than cobalt at lower temperature and pressure, but are not favourable in terms of economy [28].

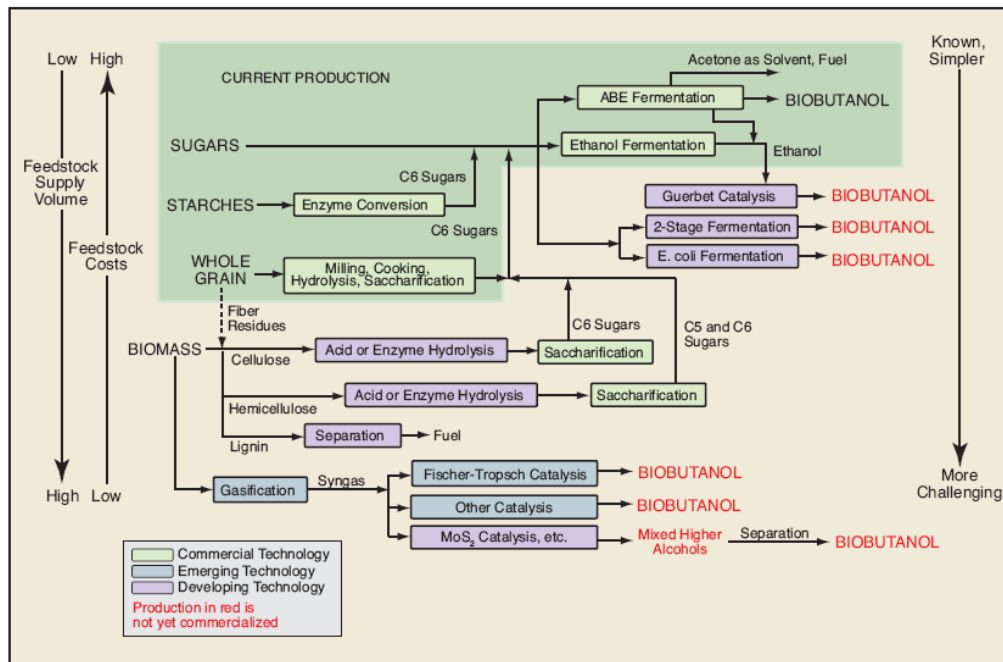


Figure 1-8. The various fermentation, chemical and thermochemical routes for yielding butanol from bio-resources. [29].

Bio-butanol can be obtained through several routes (Figure 1-8). It can be produced through a fermentation using the well-known ABE route (Acetone-Butanol-Ethanol fermentation) using *Clostridium Acetobutylicum*. This old process was developed during World War One to supply the British army with acetone for explosives production. In contrast to ethanol producing micro-organisms, the aforementioned strain can process the C5 sugars in the hemicelluloses, which is a great advantage of this route, being *de facto* not in competition with food. Unfortunately, both formed acetone and butanol are toxic for the micro-organisms so that the productivity remains low, as well as the concentration in the broth, with an increase in energy consumption as a consequence of the subsequently required separation/purification steps. Recently, a unique bacterial strain of *clostridia* named TU-103 has been discovered, which has the ability to produce butanol directly from cellulose. D. Mullin *et al.* have reported that, while *Clostridium* has been used for the production of butanol in the anaerobic conditions since a long time, TU-103 is the only bacteria, which can grow on cellulose and produce butanol in the presence of oxygen [30]. They reported that it is thus now possible to bypass the pre-treatment of cellulose with an acid or alkali before it goes through fermentation. In addition to *n*-butanol, the process also

yielded nominal amounts of acetone, butyric acid and acetic acid. However, this technology is not mature.

Recently, the press reported that some companies (*e.g.*, BP-Dupont, Metex) are developing genetically engineered micro-organisms to produce butanol through fermentation, which reflects the need for higher alcohols based on renewable resources. A second route to produce butanol is to perform gasification of the primary raw material (*e.g.*, biomass) to syngas (like aforementioned for ethanol), which is subsequently converted to butanol by catalytic processes such as the Fischer-Tropsch synthesis. This route can become economical only for large units, due to the syngas tough economy, which makes it particularly challenging and risky as many issues are still to be cleared.

Finally, the last possible route is the Guerbet alcohols synthesis. In this process, two ethanol molecules are reacted to produce *n*-butanol and water. As ethanol fermentation is now a well-established technology, this route can be more straightforward to produce this higher alcohol. Since *n*-butanol is a major chemical, we can find detailed studies comparing the economics of the various production routes. According to Figure 1-9, the Guerbet synthesis (case 4) is the most promising route, far better than the conventional petrochemistry-derived route (case 6). Nevertheless, this scenario assumes that a catalyst with a significant selectivity to *n*-butanol has been discovered, and the major drawback of the current catalysts is precisely their lack in selectivity to a specific Guerbet alcohol (or a limited conversion). As aforementioned, basic sites are necessary for this reaction, but the acid sites unavoidably present on the basic catalysts also catalyses dehydration reactions. Furthermore, the reaction over-proceeds to yield even higher alcohols such as C6 and C8, which requires downstream separation units and then additional costs.

The above analysis illustrates that the Guerbet chemistry has a real potential in industrial reactions to replace petrochemicals-based processes by bioalcohols-based processes, which would further be much more economical provided a selective catalytic system can be rationally tailored and optimized. Moreover a large investment has already been done on bioethanol R&D for producing it more efficiently from sugar and lignocellulosic biomass fermentation, gasification and catalytic process. So, biobutanol production and use can be made more efficient by adapting a part of investments used for bioethanol R&D and also

by converting the efficiently produced bioethanol to butanol by catalytic process through Guerbet reaction by using the already existing dedicated infrastructure.

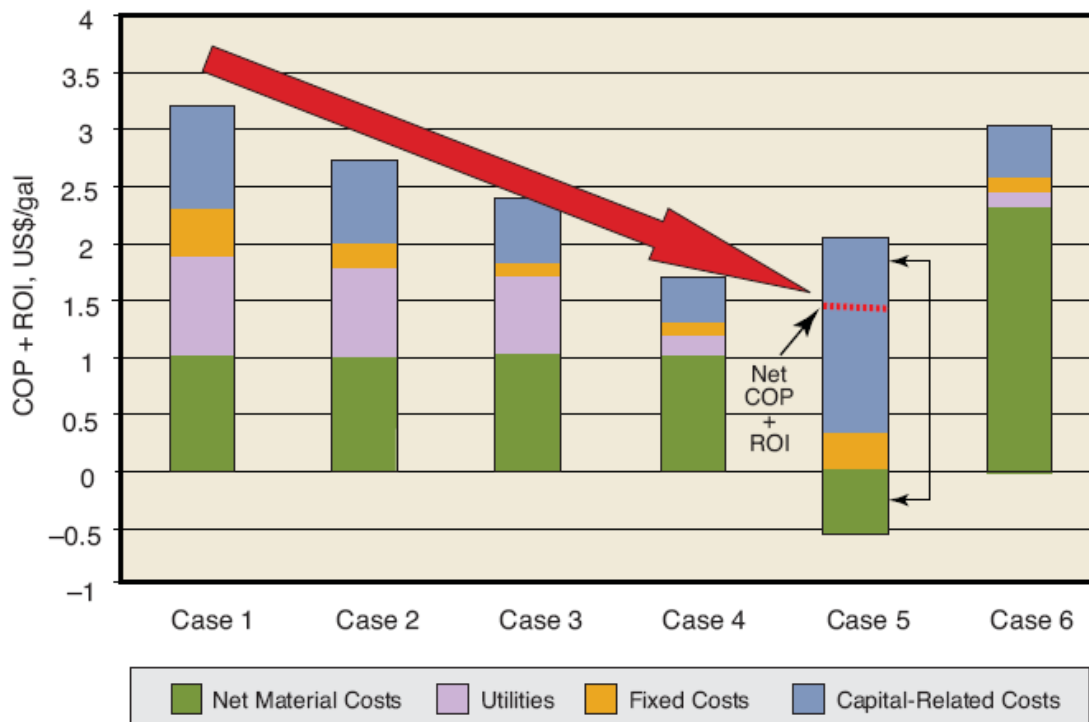


Figure 1-9. Improvement in the economics of current and emerging biobutanol technologies in terms of cost of production (COP) plus return on investment (ROI). Case 1: Classical ABE process based on *Clostridium Acetobutylicum* using wood chips as a raw material; Case 2: Improved variation using *Clostridium Beijerinckii* with corn as a starting material, which could be adapted to convert ethanol plants to butanol fermentation; Case 3: Process patented by David Ramey of Environmental Energy Inc., using a 2 steps dual immobilized reactors with continuous recovery (conversion to butyric acid and then to butanol). This process is also using corn. **Case 4: Guerbet process using ethanol source**; Case 5: Thermochemical route, through biomass gasification; Case 6: The well known oxoalcohols synthesis (petrochemistry based)

1.4 Guerbet reaction

The Guerbet reaction, named like this after Marcel Guerbet discovered it, is an organic reaction converting a primary aliphatic alcohol into its β -alkylated dimer alcohol with loss of one equivalent of water. Marcel Guerbet initially found out that the primary alcohol *1*-octanol, when heated at 200°C with its sodium derivative or with sodium derivative of other alcohols, gives rise to C16 and C24 alcohols [31]. Further, he reported that it is

applicable also to secondary alcohols by demonstrating the production of higher chain alcohols, namely 4-methylpentanol and 2,4-dimethylheptanol from *isopropanol*. At the same time, the reaction gave rise to by-products such as 3-methylbutyric acid, acetic acid and formic acid [32]. Weizmann *et.al* reported that the presence of a α -methylene group in the immediate vicinity of the hydroxyl group is a requisite for the aldol condensation step and hence for the Guerbet reaction. They have also confirmed that the Guerbet reaction between primary and secondary alcohol is predetermined by the fact that an aldehyde condenses with a ketone always to give an alkylidene-ketone even though there are some exceptions [33,34].

1.4.1 Mechanism of Guerbet reaction

The Guerbet reaction supposedly proceeds through a series of consecutive steps as shown in Figure 1-10 [35,36]:

- A dehydrogenation of the hydroxyl compounds to carbonyl compounds;
- An aldol condensation between the carbonyl compounds, followed by elimination of water;
- A hydrogenation of the α - β unsaturated aldehydes or ketones formed, the original hydroxyl compounds reacting as hydrogen donors, thus initiating a chain reaction.

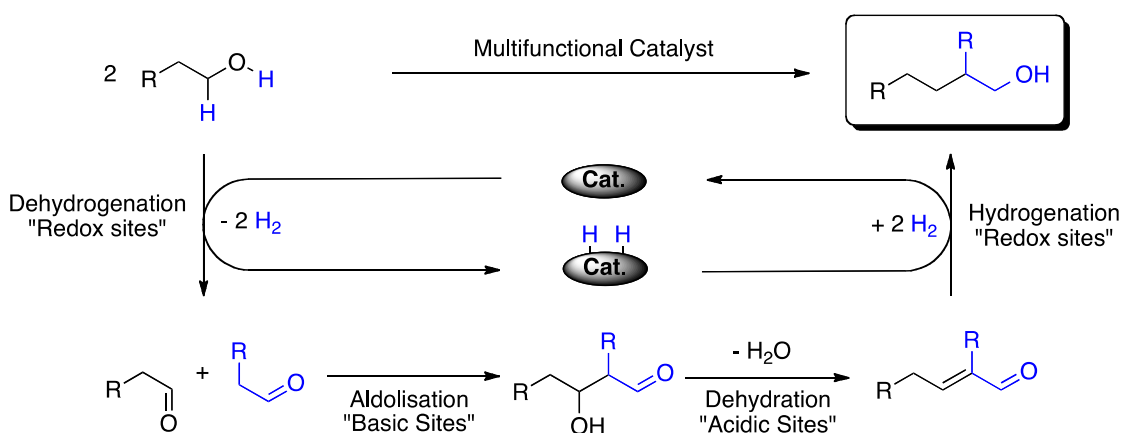


Figure 1-10 Proposed Guerbet reaction mechanism scheme.

Simultaneously to the formation of higher alcohols, acids are also often formed in equimolar amounts in the presence of alkali, which constituted a serious disadvantage to the use of the Guerbet reaction. The Guerbet reaction could be improved by decreasing the amount of formed undesirable acids and this was one of the challenges to be overcome [37,38]. Two solutions to overcome this problem are: removal of water formed during the time of reaction and replacing the alkoxides and alkali hydroxides by other condensing agents. The formation of undesirable acids could be minimized by the use of dean stark trap for the removal of water formed during the time of reaction. The activity can be enhanced by using a nickel catalyst but more gaseous products are also produced by Ni catalyst. Furthermore replacing sodium by potassium alkali resulted in more rapid alkoxide formation [37,38]. Weizmann *et.al* have shown that introduction of small amounts of copper-bronze helps suppressing the undesirable oxidation of the alcohol to the corresponding acid under the influence of alkali hydroxides or sodium alkoxides [33]. Alkyl borates or boric anhydride together with little amount of potassium hydroxide as a condensing agent leads to the almost complete suppression of acids corresponding to the starting alcohol and less alkali is required as compared with the usual Guerbet condensations [39,40,41].

1.4.2 Catalysts employed for the Guerbet reaction

The Guerbet reaction has been performed using both homogeneous and heterogeneous catalysts as well as mixed systems.

1.4.2.1 Homogeneous catalysts

The Guerbet reaction using homogeneous catalysts was first examined using transition metal complexes such as Rh, Ru, Pt, and Ir under very mild conditions of 110-140°C at atmospheric pressure [42,43,44,45]. Catalytic activity of Rh complex was found to be very high compared with that of Ru and Ir complexes. Pd and Au complexes are inactive in the Guerbet reaction because it is difficult to generate stable hydride metal complexes [42,43].

Burk *et al.* reported the Rh promoted Guerbet reaction of *1*-butanol and *1*-pentanol, and explained the roles of Rh and alkoxides in catalysing the reaction [44,45]. They found that Rh promotes alcohol dehydrogenation at the beginning of the reaction sequence and alkoxide assists in the saturation of an allyl alcohol intermediate. They also revealed the strong dependency of the reaction rate on the initial alkoxide concentration and indicated that the water formed during the reaction results in deactivation of the catalytic system. Y. Ishii and coworkers reported that an Ir complex catalyst in the presence of KOH/BuOK can convert the primary alcohols to dimer alcohols in higher yields (80%) under mild conditions of temperature (100-120°C), in the presence of a hydrogen acceptor, namely *1,7*-octadiene [43]. They found that, unlike Rh-catalyzed Guerbet reaction, the Ir-catalyzed reaction could be carried out even without removal of the water formed during the reaction. Carlini *et al* disclosed the Guerbet reaction using homogeneous Ni and Pd-based catalysts in the presence of basic alkoxides, but using a higher reaction temperature of 200°C [43,46,47,48]. They found that when Pd(0) and Pd(II) complexes were used in the presence of sodium methoxide base for Guerbet condensation of methanol and *n*-propanol to produce *isobutanol*, a remarkable activity was observed, irrespective of the Pd oxidation state. They also reported that the overall activity arises from both homogeneous and heterogeneous Pd species, which are in equilibrium. Carlini and co-workers also reported the Guerbet condensation of butanol to 2-ethylhexanol without any formation of byproducts using homogeneous Pd complex in the presence of sodium butoxide base [48]. The homogeneous catalysis of Guerbet reaction using the transition metal complexes is found to be highly active but not economically feasible since the metal complexes of Pd, Ru, Rh, Pt, etc., are highly expensive. The catalyst recovery from the reaction mixture and the catalyst reusability were not possible, thus making the process non feasible. Also, in order to promote the Guerbet reaction, bases such as alkali hydroxides or alkoxides are employed along with homogeneous catalysts, which are not environmental friendly. So, in order to make the Guerbet reaction economically feasible for industrial applications, there is a need for developing heterogeneous catalysts, which can also be environmental friendly in terms of catalyst separation and reusability.

1.4.2.2 Heterogeneous solid metal + liquid co-catalysts

Heterogeneous catalytic systems based on Cu, Ni, Rh, Ru and Pd metals in combination with soluble alkoxides as basic component were then employed in the synthesis of *isobutanol* from methanol and *n*-propanol [46,47,48,49,50]. Selectivity to *isobutanol* was almost 100% in all the experiments with significant *isobutanol* yield. The catalytic systems with metal components Cu, Ni, Pd when preactivated using hydrogen have shown lower or no activity compared to the non-preactivated catalysts. Deactivation of the catalytic system resulting from the formation of water, was prevented by the addition of excess alkoxide, for example, sodium methoxide, which reacts with water producing methanol and sodium hydroxide. The main disadvantage of using excess alkoxide is metal leaching, and also the production of alkali hydroxides like sodium hydroxide, which is not environmental friendly. The leached homogeneous metal species exhibit different properties depending on the metal. It has been shown that the copper chromite works well in the heterogeneous phase but Cu metal leaching occurred during the reaction. Further investigations showed that this leached homogeneous Cu species formed was inactive in catalyzing the Guerbet reaction. However, when Pd catalyst was used along with alkoxide, both heterogeneous Pd catalyst and the leached homogeneous Pd species were found to be active. This leaching also prevents any possible industrial application in the Guerbet reaction, which is another disadvantage of using solid heterogeneous catalysts in the presence of soluble basic alkoxides [45,46,47,48,49,50]. So, there was a further need for designing pure heterogeneous catalyst, where both redox transition metals and basic components coexist in the solid phase.

1.4.2.3 Monofunctional two component heterogeneous catalysts

A two-component heterogeneous catalytic system completely replacing the basic component alkali hydroxides by magnesium oxide, potassium carbonate, tripotassium phosphate, etc..., in conjugation with an active metal component like Cu, Ni, Cu-Ni, copper chromite was effective in promoting condensation to higher alcohols. In the absence of any metal component, and only by using alkali metal carbonate as condensing agents, ethanol and *n*-butanol have shown conversions less than 15% [41,51]. When

tripotassium phosphate is used along with Cu metal, the butanol conversion to 2-ethylhexanol was increased from 15% to 40% with high yields. So, the Guerbet condensation has been improved by conjugation of basic condensing agents with dehydrogenation metal catalysts. Further, catalytic activity was studied using different metallic dehydrogenation catalysts like Cu, Ni, Cu-Ni and CuCrO₄ in conjugation with the basic tripotassium phosphate. However, the addition of dehydrogenation catalysts produced gaseous by-products like CO, CO₂, CH₄ and H₂, Ni producing large amount of off gases and CuCrO₄ the least [41]. C. Carlini *et al.* reported the synthesis of *isobutanol* from methanol and propanol by using heterogeneous two component catalysts based on copper chromite and Mg/Al mixed oxides derived from hydrotalcite precursors. This system has shown almost complete selectivity towards *isobutanol* and was not affected by the co-produced water [52]. Now, it is necessary to simplify the two component catalytic system with one component heterogeneous catalytic system, where the dehydrogenating/hydrogenating and basic sites are present in the same matrix. The advantages of this kind of one component heterogeneous system is that the reactions can be performed in a gas phase flow reactor system thus opening various application perspectives.

1.4.2.4 Heterogeneous one component multifunctional catalysts

Various heterogeneous catalysts have been used to perform condensation reactions and hydrogenation reactions. However, for the Guerbet reaction to take place in one component system there is a need for multifunctional catalysts, which possess acid-base sites. Ueda *et al.* reported the condensation of various primary alcohols with methanol over solid basic catalysts such as MgO, CaO and ZnO [53,54,55,56]. The reaction took place only over MgO, as the other metal oxides were found to be inactive or non-selective. The multistep reaction to form higher alcohols over the mono functional basic MgO surface is facilitated by hydrogen transfer from methanol, which results in hydrogenating the C=C and C=O bonds to form saturated alcohols [53,54]. The alkali salt supported over zeolites as catalysts were found to be more active and selective in the Guerbet reaction of ethanol and methanol to higher alcohols compared to MgO catalysts [55]. N.J. Coville *et al.* reported that solid base catalyst MgO modified by acidic or basic ions have no added advantages

over pure MgO in the ethanol dimerisation reaction to butanol [56]. Some studies have proposed that the dimerisation of ethanol to butanol does not proceed through aldol condensation, but through a mechanism in which a C-H bond in the β -position in ethanol is activated by the basic zeolite or metal oxide and condenses with another molecule of ethanol by dehydration [56,57]. The Guerbet reaction of alcohols has also been studied using various Mg-Al mixed oxides derived from hydrotalcite type precursors [58,59,60,61,62]. It has been shown that the ethanol condensation does not only depend on the acid-base properties, but also on the composition and the surface arrangement of atoms in the Mg-Al mixed oxides. The rate of alcohol dehydration to ethers and olefins is higher for Al-rich Mg_yAlO_x solids but dehydrogenation and aldol condensation of ethanol, respectively to corresponding aldehyde and higher alcohols, is favoured over Mg-rich Mg_yAlO_x samples [58,62]. Introduction of copper into the hydrotalcite-derived Mg-Al mixed oxide enhanced the activity of catalyst towards Guerbet reaction [59,60].

Hydroxyapatite [$Ca_{10}(PO_4)_6(OH)_2$] is found to be an active and promising heterogeneous solid catalyst for the Guerbet reaction of ethanol to heavier products [63,64,65,66,67]. Ueda *et al.* reported that hydroxyapatite with $Ca/P < 1.67$ acts as an acidic catalyst producing more ethylene and ether by dehydration of ethanol. For $Ca/P \geq 1.67$, hydroxyapatite acts as a basic catalyst favouring dehydrogenation and condensation reactions of ethanol to form acetaldehyde and heavier alcohols [33,4]. Synthesis of biogasoline mixture using equimolar mixture of ethanol and higher alcohols has also been studied over hydroxyapatite catalyst [5]. It is shown that strontium hydroxyapatite catalyses the conversion of ethanol with higher *n*-butanol selectivity of 82% compared to 70% in normal calcium hydroxyapatite [66].

Since the thesis deals with HAPs as catalysts in the Guerbet reaction of ethanol, it is important to gain some insight regarding the structure and properties of HAPs which will then be discussed in the following section 1.5.

1.5 Hydroxyapatites (HAPs)

Hydroxyapatite (HAP), $\text{Ca}_{10}(\text{PO}_4)_6(\text{OH})_2$, the main inorganic constituent of biological hard tissues in animal organisms, is the most stable calcium phosphate salt at normal temperatures and pH between 4 and 12. Synthetic HAPs are widely used in fields such as bone regeneration, dental materials, and adsorbents for chromatography to separate proteins, fluorescence materials, fertilizers and food supplements as a source of calcium. The ion-exchange ability of HAP is used in the removal of toxic metal ions from liquid wastes. Exploiting their acid-base properties, HAPs are mainly used as supports and catalysts in reactions like dehydration, dehydrogenation, condensation and oxidation.

1.5.1 Synthesis of hydroxyapatites

Hydroxyapatites can be generally synthesized by using dry and wet chemical methods. The dry chemical methods include solid-state reaction and mechanical alloying. Precipitation, hydrothermal and sol-gel are the common wet chemical methods employed for hydroxyapatite preparation.

1.5.1.1 Dry chemical methods

Dry chemical methods of synthesis generally use solid-state reactions between calcium and phosphorus compounds, which are carried out at elevated temperatures. This method has the advantage of providing stoichiometric hydroxyapatite powders with $\text{Ca/P} = 1.67$. The phosphorus precursors used in the solid state reactions are $\text{CaHPO}_4 \cdot 2\text{H}_2\text{O}$, $\text{Ca}_3(\text{PO}_4)_2$ and $\text{Ca}_2\text{P}_2\text{O}_7$, which are reacted with CaCO_3 [68,69,70]. In addition to higher temperature, water is also supplied during the reaction as a source of hydroxyl groups in the hydroxyapatite solids. Silva *et al.* prepared nanocrystalline hydroxyapatite powder by using a mechanical alloying method in a dry environment. Mechanical alloying method does not require elevated temperatures as in the solid state reaction, instead, long milling

time of about 60 h are employed [71]. There is, however, a possibility of contamination of the solids during the time of milling in mechanical alloying method.

1.5.1.2 Wet chemical methods

The hydroxyapatites are mostly prepared by using wet chemical methods. HAPs obtained using this method possess higher surface area, low crystallinity, fine particle size and non-stoichiometry depending on various factors such as pH, aging time and temperature as well as the concentration of starting materials. The mainly employed wet methods are:

Hydrothermal synthesis

Hydrothermal synthesis is one of the oldest and well-known methods to synthesize hydroxyapatite solids using different precursors and various ranges of temperatures. Zhang and co-workers prepared rod-shaped HAPs by using dicalcium phosphate anhydrous (CaHPO_4) and CaCO_3 in a temperature range from 120 to 180°C [72]. Synthesis of hydroxyapatite *via* hydrothermal reaction was reported by Liu *et al* using $\text{Ca}(\text{OH})_2$ and $\text{CaHPO}_4 \cdot 2\text{H}_2\text{O}$. They studied the effect of temperature and pH on the morphology by synthesizing HAPs at different pH values ranging from 6 to 14, varying temperatures and found that variation in pH effect the changes in crystallite size and morphology [73]. Kothapalli and co-workers used calcium nitrate and ammonium dihydrogen phosphate as reagents for the hydrothermal synthesis of HAPs in the temperature range from 25 to 250°C and for reaction times between 2 to 10 h [74]. They have shown that the temperature at 170°C was critical in their synthesis; the length of the HAP crystals was maximal when the temperature was 170°C, and then started to decrease for temperatures beyond 170°C. Calcium nitrate and ammonium phosphate were employed by Chaudhry *et al.* for the synthesis of hydroxyapatite using a three pump continuous hydrothermal flow system [75]. Onda *et al.* have reported the hydrothermal synthesis of vanadium substituted M-HAPs (M = Ca, Sr, Pb) at 110°C using calcium nitrate and phosphorus/vanadium pentoxide as precursors [76]. The M-vanadate hydroxyapatite catalysts were column crystals with lengths of about 65–500 nm and widths of about 25–150 nm. Hence,

hydrothermal synthesis assists to prepare hydroxyapatites with different morphologies by varying temperature and pH.

Sol-gel method

The sol-gel method is also used to prepare HAPs, as it offers control over the formation of particular phases and enables processing at low temperature. The commonly employed reagents are $\text{Ca}(\text{NO}_3)_2 \cdot 4\text{H}_2\text{O}$ with $(\text{C}_2\text{H}_5\text{O})_3\text{PO}$ [77], $\text{Ca}(\text{OEt})_2$ with $\text{PO}(\text{OEt})_3$ [78], $\text{Ca}(\text{NO}_3)_2$ with $\text{HOOCCH}_2\text{PO}(\text{OH})_2$ [79], and $\text{Ca}(\text{NO}_3)_2 \cdot 4\text{H}_2\text{O}$ with P_2O_5 [80]. The main drawback of using this method is that the formed apatite solids can contain secondary phases such as CaO , which is reported to exhibit adverse effects on the biocompatibility of HAPs. As a solution to the above problem, CaO can be converted to CaCl_2 , by treating hydroxyapatites with HCl [77]. Other limitations of the sol-gel method were also reported including the high cost of the alkoxide-based starting materials, complex steps in order to complete the dissolution of starting materials [80], etc.

Precipitation

Precipitation is the most widely used method due to its simplicity and low processing temperature [81,82]. In this method, calcium is supplied as $\text{Ca}(\text{NO}_3)_2$, $\text{Ca}(\text{OH})_2$, CaCO_3 , CaCl_2 , CaF_2 or $\text{CaSO}_4 \cdot 2\text{H}_2\text{O}$ and phosphorus as $\text{NH}_4\text{H}_2\text{PO}_4$, $(\text{NH}_4)_2\text{HPO}_4$ or H_3PO_4 and sometimes under the form of Na^+ and K^+ salts [82,83,84]. However, ammonium salts are preferred to Na^+ or K^+ salts and nitrate salts to chloride or fluoride because ammonium and nitrate ions cannot be easily incorporated into HAP structure. During the synthesis, the pH is maintained above 10 by the addition of aqueous NH_3 to obtain stoichiometric HAP. Lowering of the pH value results in the formation of calcium deficient hydroxyapatite (CDHA) [4]. Orthophosphoric acid and calcium hydroxide are used as valuable precursors for the industrial production of HAPs, since the by-product is water and the method is known as a neutralization method [85]. Bigi and co-workers prepared HAPs by using $\text{Ca}(\text{NO}_3)_2 \cdot 4\text{H}_2\text{O}$ and $(\text{NH}_4)_2\text{HPO}_4$ respectively, as source of calcium and phosphate ions,

using precipitation method. During the synthesis, the pH of the solution was maintained at 10 by adding NH_4OH , and the reaction temperature was kept at 90°C for 5 h [86].

Even though wet synthesis methods are commonly used, there is a risk of contamination with impurities leading to the formation of non-stoichiometric apatites and resulting in changes in HAP structural characteristics and properties. It is important to control the pH, the temperature, and the concentration of reactants during the synthesis, as these parameters have a strong influence on crystallinity, morphology and particle size of HAPs.

1.5.2 Structure of hydroxyapatite

The basic apatite structure was nearly simultaneously published by Naray-Szabo [87] and Mehmel [88] in 1930. The structure is hexagonal with space group $\text{P6}_3/\text{m}$ and approximate lattice parameters $a = 9.37 \text{ \AA}$ and $c = 6.88 \text{ \AA}$. The unit cell, the smallest building unit, consists of Ca^{2+} , PO_4^{3-} and OH^- groups closely packed together in a hexagonal arrangement.

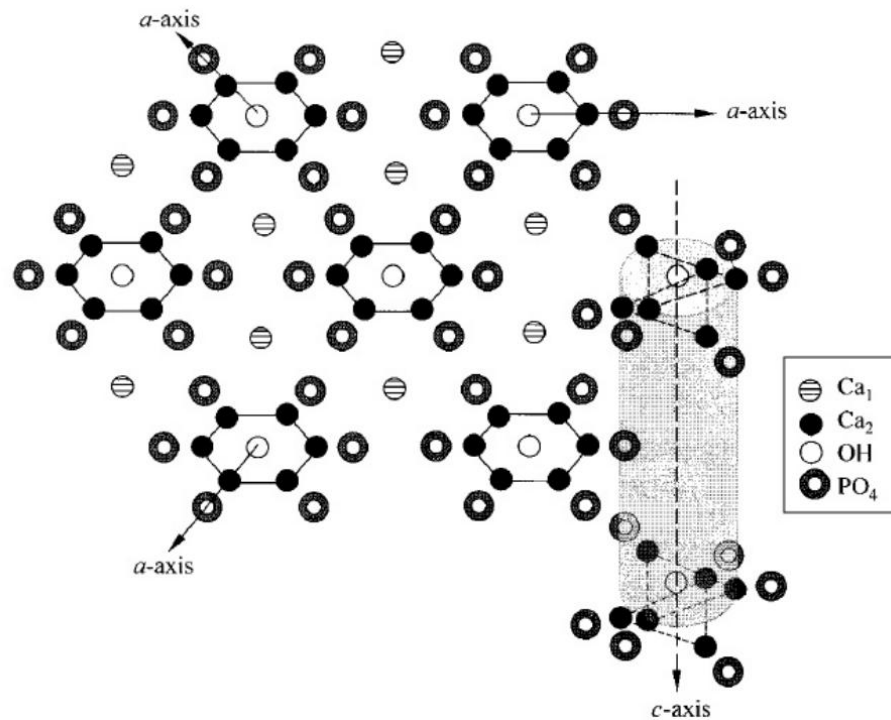


Figure 1-11 Primary structure of hydroxyapatite [89].

Considering the HAP chemical formula, $\text{Ca}_{10}(\text{PO}_4)_6(\text{OH})_2$, a single unit cell comprises 44 atoms, including 10 calcium atoms, 6 PO_4^{3-} tetrahedra, and 2 OH^- groups [89]. According to the position in the unit cell, ten calcium atoms can be classified into 4 Ca(I) and 6 Ca(II) and the O atoms correspond to 1 O_I , 1 O_{II} , and 2 O_{III} of each phosphate group. Regarding this, the chemical formula could be more precisely represented as $\text{Ca}(\text{I})_4\text{Ca}(\text{II})_6[\text{PO}_I\text{O}_{II}(\text{O}_{III})_2]_6(\text{O}_{\text{OH}}\text{H})_2$ [90,91,92]. The Ca(I) ions are aligned in columns, while Ca(II) are in equilateral triangles centred on the screw axes as shown in Figure 1-11.

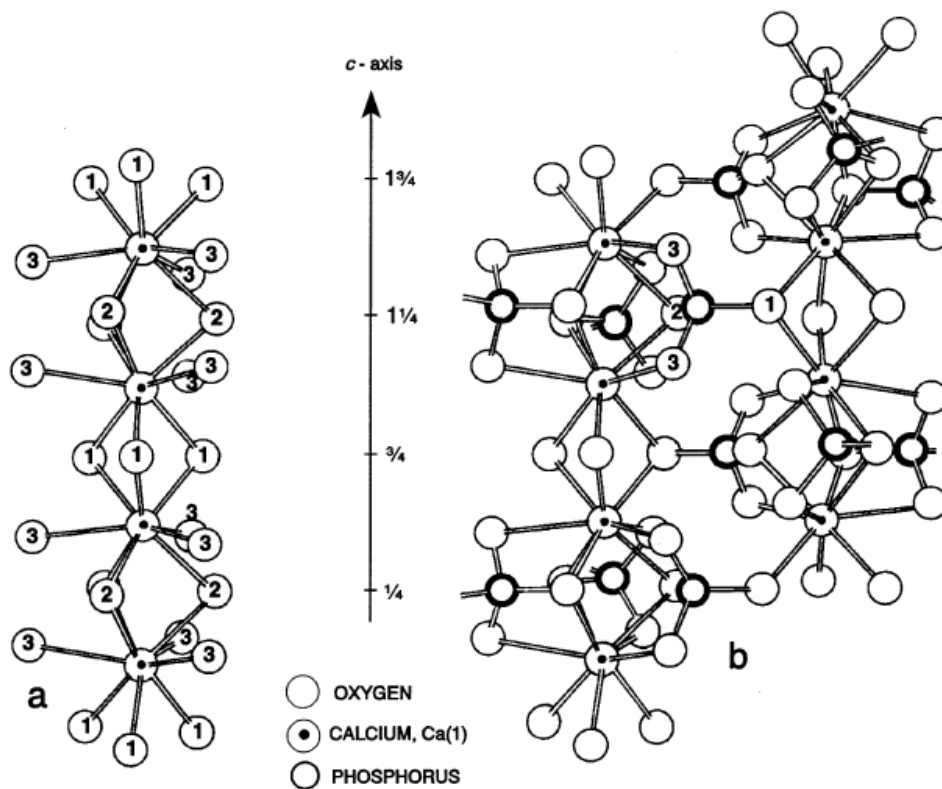


Figure 1-12 (a) Oxygen coordination of columnar Ca (I) ions (b) linking Ca (I) of columns *via* PO_4 tetrahedra [90,93].

Beevers and McIntyre have provided an excellent description of the HAP structure using ball and spoke model as that represented in Figure 1-12 [90, 93]. The central phosphorus atom is located in the $6h$ special position, which is coordinated to 4 oxygen atoms, under the form of a PO_4 tetrahedron, as reported by Hughes and Rakovan [94]. Three O atoms of each PO_4 tetrahedron are shared by one column, with the fourth O atom attached to a neighbouring column. The four columnar Ca(I) ions are situated in the $4f$ ($1/3, 2/3, Z$)

position and are nine-fold coordinated by O atoms, and these 9 O atoms are from 6 different PO₄ tetrahedra, as shown in Figure 1-12. These columns of Ca²⁺ ions and their coordinating O atoms are linked together by PO₄ tetrahedra in which three O atoms come from one column, and the fourth from the adjacent column. The result is a three-dimensional network of PO₄ tetrahedra with enmeshed columnar Ca(I) ions, and with channels passing through it. The Ca(II) and the OH ions are located in this channels.

The 6 Ca(II) ions are occupied in the *6h* special position [94] and are 7-fold coordinated by O atoms, 6 O atoms from 5 PO₄ tetrahedra and one from the OH group. Kay and co-workers suggested that 6 Ca(II) atoms are arranged into two Ca(II) triangles on the mirror planes at $z = 1/4$ and $z = 3/4$, and the successive Ca(II) triangles were rotated 60° around *c*-axis as shown in Figure 1-12 [68,95]. Similarly to the Ca(II) ions, 6 PO₄ tetrahedra are also arranged themselves into two PO₄ triangles on the mirror planes at $z = 1/4$ and $z = 3/4$, giving the stability to the HAP structure.

As in Figure 1-13, the OH⁻ groups are located in the centre of HAP column or channel parallel to *c*-axis and this specific position is closely related with the reactivity of HAP material [95,96]. The OH⁻ groups are too large to fit in the space created by the Ca(II) atoms on the mirror planes, and, hence, the OH⁻ groups has to be disordered randomly 0.36 Å above or below the mirror planes of the Ca-II triangles at $z = 1/4$ and $z = 3/4$. Kay and co-workers proposed two different models, the disordered model and the ordered model for the positioning of the OH⁻ groups within the column, based on their neutron diffraction data. In the disordered model, the orientation of the OH⁻ groups were proposed to be inverted at different positions, but in the ordered model the orientation of OH⁻ groups is the same, but the choice of the orientation was random [95].

The existence of alternative phase, *i.e.*, monoclinic HAP with the space group of P2₁/b has also been reported [97,98]. Contrary to F⁻ ions, OH⁻ and Cl⁻ ions are too large to fit inside the Ca(II) triangles and these ions are disordered above or below the Ca(II) triangles. It has been reported that, due to the incorporation of larger Cl⁻ ions, chlorapatites belong to the monoclinic system with space group P2₁/b [99]. The HAP exhibited monoclinic structure at room temperature, and the phase transition to hexagonal structure started as the temperature increased to 473 K, and, when the temperature reached 483 K, the hexagonal phase became the predominant one [68,97].

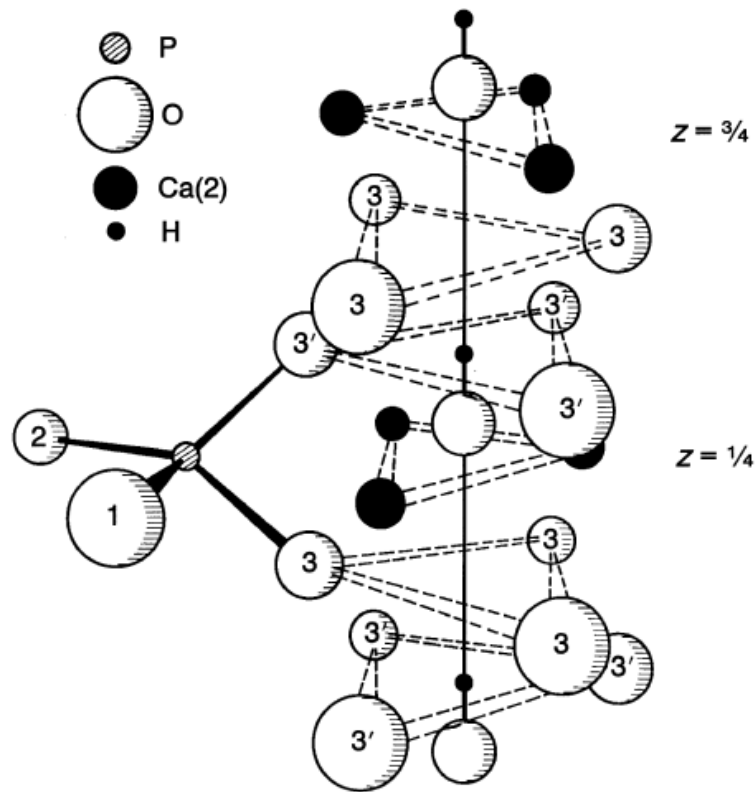


Figure 1-13 Arrangement of the Ca(II) triangles around c-axis [90].

1.5.3 Substitutions in hydroxyapatites

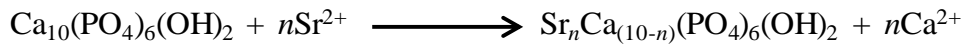
The biological apatite is usually non-stoichiometric and flexible to substitutions by different cations and anions. Similarly, synthetic apatite enables the incorporation of a wide range of different ionic substitutions and ion exchanges in its framework, leading to different degrees of modification in the original HAP structure. For example, Ca^{2+} can be substituted by cations like Na^+ , K^+ , Mg^{2+} , Sr^{2+} , Ba^{2+} , Zn^{2+} , Cu^{2+} , Co^{2+} , Ni^{2+} etc., whereas $\text{PO}_4^{3-}/\text{OH}^-$ can be substituted by CO_3^{2-} , HPO_4^{2-} , SO_4^{2-} , F^- , Cl^- , Br^- etc [89,90,100,101,102].

1.5.3.1 Substitutions of Ca^{2+}

The substitutions in the hydroxyapatite may cause changes in characteristics, such as lattice parameters, crystallinity, crystal symmetry, thermal stability, morphology, solubility, thus modifying their physical, chemical and biological properties [103,104]. As

a consequence, synthesis of substituted HAPs has attracted a lot of interest, as they can exhibit desirable properties and satisfy variety of needs in a wide range of applications. Large cations such as Sr^{2+} , Ba^{2+} , and Pb^{2+} are incorporated preferentially in the HAP structure by replacing Ca^{2+} ions on site (II). In contrast, small cations, such as Zn^{2+} and Mg^{2+} , first replace Ca^{2+} ions on site (I) [105].

It has been reported that the Sr-HAP samples can be prepared in the whole range of compositions, according to the equation given below [106,107]:



O'Donnell and co-workers prepared Sr-HAP solids with Sr substitution ranging from 0 to 100% by using two different precipitation routes: one is using the $\text{Ca}(\text{NO}_3)_2 \cdot 4\text{H}_2\text{O}$, $\text{Sr}(\text{NO}_3)_2$ and $(\text{NH}_4)_2\text{HPO}_4$ as precursors and the other route is using $\text{Ca}(\text{OH})_2$, $\text{Sr}(\text{OH})_2$ and H_3PO_4 precursors. They found that the crystallite size of the Sr-HA samples reached a minimum value when the Sr substitution increased to 50%. Crystallite size and morphology of the Sr apatites varied with the changes in Sr substitution [105,106].

Substitution by Zn exhibited inhibiting effect on the crystallization of HAP, and, hence, many researchers reported that it was not possible to synthesis of Zn-HAP over the entire compositional range. Bigi *et al* attempted to synthesize a group of apatite samples by varying the Zn concentration in the solution from 0 to 100 atom%, but the unique apatite phase was obtained with the Zn concentration up to approximately 25 atom% [108]. It has been found that the crystallite size and crystallinity was decreased with the increased Zn substitution [109]. Mg substitution exhibited a similar effect, with inhibition of the crystallization of HAP. The unique crystalline apatite phase was only achieved with Mg concentration in the range of 0 to 30 atom%, and a completely amorphous structure was observed while increasing the Mg concentration from 35 to 50 atom% [110].

If the substituting cation does not have a +2 charge as in Ca, the charge compensation mechanism may have a big influence on the apatite structure. Two main types of charge-compensating mechanisms have been advanced for the substitution of Ca^{2+} by trivalent cations (rare earth elements) in apatites: the replacement of 2 Ca^{2+} ions by a monovalent ion and a trivalent rare earth element ion, or the replacement of 3 Ca^{2+} ions by 2 rare earth element ions and a vacancy. From a catalytic point of view, the exchange of Ca^{2+} ions of

HAP with other cations in solution is more interesting, and this process is controlled by the relative size and charge of the substituting and host cations [105,111].

1.5.3.2 Substitutions of $\text{PO}_4^{3-}/\text{OH}^-$

The OH^- ions located in the HAP structure along the c -axis at the centre of Ca (II) triangles can be usually substituted by F^- , Cl^- , Br^- , CO_3^{2-} etc [111]. For example, when F^- ions are substituting OH^- ions in the apatite structure, F-apatite ($\text{Ca}_{10}(\text{PO}_4)_6\text{F}_2$) is formed, and when chloride (Cl^-) substitutes OH^- groups, Cl-apatite ($\text{Ca}_{10}(\text{PO}_4)_6\text{Cl}_2$) is the result. However, the positions of OH, Cl, or F in the OH-apatite, F-apatite and Cl-apatite, respectively, are different although OH, F, and Cl atoms lie along the c -axis at the center of the Ca(II) triangles. The substitution using F^- can greatly improve the physical, chemical and biological properties of HAPs, such as increment in the crystallinity and crystal size, decrement in the a -axis dimension without varying the c -axis, enhancement in the structural stability, improvement in corrosion resistance in biological environments etc. F-substituted apatites are less soluble than F-free apatites, which is the reason why fluorine is often used in toothpaste to prevent the decay of tooth by increasing the stability of apatites [89].

In the HAP lattice, the CO_3^{2-} ions are exchanged with either OH^- groups in the channel site, assigned to A-type substitution, or with PO_4^{3-} tetrahedra, known as B-type substitution [112,113,114]. The substitution of carbonate can cause a decrease in crystallinity and an increase in the extent of dissolution of apatites. A-type apatites could be obtained by treating pure hydroxyapatite in a dry CO_2 environment at 900°C for 3 days, while type-B apatites could be achieved by precipitation from aqueous solutions [115]. Gibson *et al.* found that the B-type CO_3^{2-} apatite synthesis was more complicated compared to the synthesis of A-type CO_3^{2-} apatite, due to the charge imbalance issue arisen by CO_3^{2-} content substituted PO_4^{3-} in the apatite lattice [116]. In order to compensate for the charge difference caused by the B-type CO_3^{2-} substitution, the sodium carbonate reagent was introduced as the source of CO_3^{2-} , and Na was used to co-substitute Ca [117,118]. The A and B types of carbonate substitutions have opposite effects on the lattice parameters like a and c . For type A substitution, a smaller OH^- is replaced by a larger CO_3^{2-} , resulting in an

expansion along the a -axis and contraction along the c -axis, whereas for B-type substitution, a larger PO_4^{3-} is replaced by a smaller CO_3^{2-} , leading to a contraction along the a -axis and an expansion along the c -axis [117,119]. Sometimes, the increased lattice parameter a was also found in B-type CO_3^{2-} -substituted HAPs, which is likely attributed to incorporation of lattice H_2O or some HPO_4^{2-} [120,121]. Legros *et al.* reported an interesting mechanism for the CO_3^{2-} incorporation into the biological apatite. They proposed the formation of a vacancy at O_{III} or $\text{O}_{\text{III}'}$ position when PO_4^{3-} was exchanged with CO_3^{2-} ions as shown in Figure 1-14 [122]. To maintain the charge balance in the whole HAP structure, the negative charge created by the O_{III} or the $\text{O}_{\text{III}'}$ vacancy was counterbalanced by releasing one Ca^{2+} and one OH^- ions. When the CO_3^{2-} substitution exceeds certain limits, the possible site for excess amount of CO_3^{2-} content were supposed to be either located in the hydrated layer of the crystals or present in the amorphous CaCO_3 [123,124].

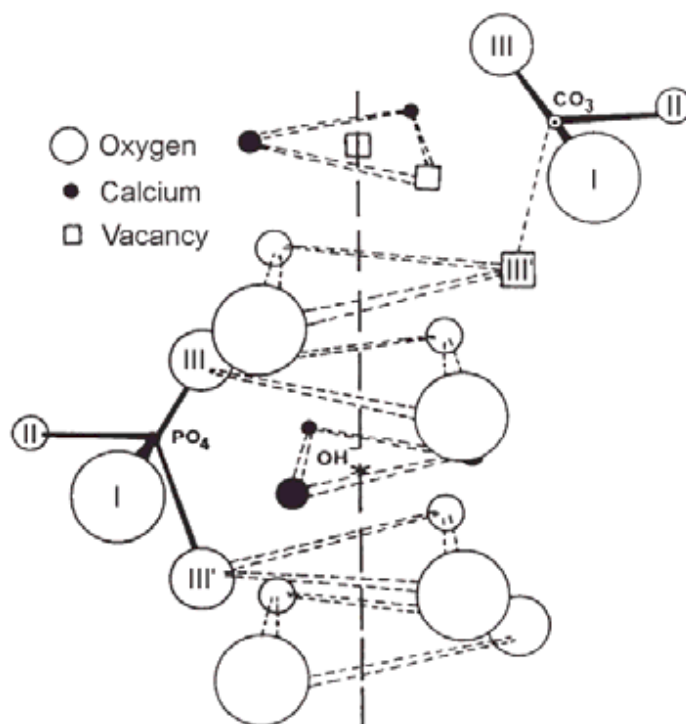


Figure 1-14 The diagram showing CO_3^{2-} substitution in HAP [92,125]

1.5.4 Non-stoichiometry in HAPs

The Ca/P ratio is used as a key indicator to measure the non-stoichiometry and acid-base properties of hydroxyapatite solids. The Ca/P ratio of stoichiometric hydroxyapatite $[\text{Ca}_{10}(\text{PO}_4)_6(\text{OH})_2]$ is considered as 1.67 but the wet-chemically synthesized hydroxyapatites are often non-stoichiometric with Ca/P ratio between 1.5 and 2. The $\text{Ca/P} > 1.67$ is mostly result of phosphate substitution by carbonate due to the incorporation of CO_2 under the form of CO_3^{2-} anions if the synthesis is carried out in open atmospheric conditions.

The non-stoichiometric hydroxyapatites with $\text{Ca/P} < 1.67$, generally known to be deficient apatites, are represented by formula $\text{Ca}_{10-x}(\text{PO}_4)_{6-x}(\text{HPO}_4)_x(\text{OH})_{2-x}$ with $0 < x < 1$. It is not possible to distinguish the stoichiometric and non-stoichiometric apatites by X-ray diffraction since no other crystalline phase $[\text{Ca}_3(\text{PO}_4)_2; \text{Ca/P} < 1.67]$ is observed [126]. It has been found that, as the Ca/P ratio decreased below 1.67, the IR bands of the HPO_4^{2-} ion at 870 cm^{-1} and 3670 cm^{-1} increased in intensity, and the OH vibrational band at 3572 cm^{-1} and 630 cm^{-1} decreased in intensity [127]. The stoichiometric HAP is stable to thermal decomposition up to 900°C , but non-stoichiometric HAP decomposes at 700°C due to dehydration according to the following equation [126,128]:



1.5.5 Applications of hydroxyapatites, specific application to the present study

As evocated above, since synthetic hydroxyapatites mimic the bioapatite present in bones and tooth, they have been widely used clinically for many years. They have good biocompatibility in bone contact as their chemical composition is similar to that of bone material. Porous HAP ceramics have found extensive use in biomedical applications including bone tissue regeneration, cell proliferation, and drug delivery. In bone tissue engineering, they have been applied as filling materials for bone defects and augmentation, artificial bone graft material, and prosthesis revision surgery. Their high surface areas lead

to excellent osteoconductivity and resorbability providing fast bone ingrowths [129]. HAPs are potential carrier for drugs and protein delivery systems [130,131]. Hydroxyapatites have been used as chromatographic materials for the separation and the purification of proteins. They have two different adsorption sites on their surface, phosphate and calcium, and these are responsible for the binding of basic and acidic side groups of proteins, respectively [132]. HAPs have a large capacity for elemental substitutions and this property enables their use for environmental applications like water purification, waste stabilization, contaminated soil remediation, and heavy metals adsorption [133].

Hydroxyapatites have been widely used as supports and catalysts in the field of catalysis research. As aforementioned, hydroxapatites have both acid and basic sites in a single crystal lattice and, hence, behave as good catalysts for the reactions like dehydration, dehydrogenation, condensation etc. The catalytic performances of hydroxyapatites in dehydration/dehydrogenation reactions of ethanol, propanol and butanol have been reported [134,135,136]. It has been found that the rate of alcohol dehydration increases with the decrease in the Ca/P molar ratio, and, hence, the acid properties of deficient hydroxyapatites for dehydration reaction can be mainly attributed to HPO_4^{2-} groups and OH^- vacancies in the lattice. S. Sebti *et al.* reported that HAPs are active catalysts for the Knoevenagel condensation, where basic sites like PO_4^{3-} and OH^- groups are involved [137]. Hydroxyapatites impregnated with NaNO_3 , KF , ZnCl_2 , etc., were synthesized and used as an efficient catalysts, respectively for reactions such as the Claisen-Schmidt condensation, the Knoevenagel condensation, and the Friedel-Crafts alkylation, which require acid and basic sites [138,139,140]. Fluorine-containing apatites have shown activity in the Michael addition reaction, where both acid and basic sites play an important role [141].

Because of its ion exchange or elemental substitution ability, hydroxyapatites were also used as a support for transition metals like Cu, Co, Pd, Ru, Au, etc., to catalyse organic reactions where redox sites are required. H. Tounsi *et al.* synthesized Cu-HAP by ion exchange in solution and used it as a catalyst for selective catalytic reduction of nitric oxide with ammonia. They found that highly dispersed CuO clusters on the HAP surface that could be easily reduced were responsible for the activity at temperatures below 250°C [142]. Hydroxyapatite-supported copper catalyst was found to be effective for three components coupling of aldehyde, alkyne and amine to prepare propargylamines. It has

been observed that Cu-HAP was more efficient than Ru-HAP and Fe-HAP in the coupling reaction [143]. Cu-containing hydroxyapatites were reported for the hydrolysis of chlorobenzene to phenol [144]. A chlorobenzene molecule enters the Ca-Cu-Ca triangles of the hydroxyapatite, and, from the interaction with the structural OH, a phenol molecule is formed, leaving a chloroapatite. The Cu-promoted HAP catalysts were more active than non-promoted HAP, but the selectivity to phenol decreased with the Cu content because benzene is also formed by side reaction. During the reaction, some of the Cu^{2+} ions got reduced to Cu^+ and Cu^0 , but, after reactivation under air, all the Cu^+ and Cu^0 species went back to Cu^{2+} .

K. Elkabouss *et al.* reported that cobalt-exchanged hydroxyapatites showed better catalytic performance than Co-free HAPs in the oxidative dehydrogenation reaction of 2-butanol and ethane respectively to butanone and ethylene [145]. The yield of ethylene increased from 2% to 20%, when Co content is increased respectively from 0 wt;% to 0.96 wt;% and the butanone yield was found to increase from 60% to 80% for an increase in Co content respectively from 0 wt.% to 0.38 wt.%. As the Co content increases, the butanone and ethylene yields pass through a maximum at certain Co concentration and then decreases with further increase in Co content. They proposed two reasons for the increase in catalytic activity due to Co addition: One is the compensation between the dehydrogenating activity of Co^{2+} species and thereby decrease in apatite basicity and the other one is the increase in lattice oxygen mobility induced by Co incorporation. Activity of Co-HAPs in the oxidation of volatile organic compounds like methanol depends on the mode in which Co is introduced into HAP [146]. It was found that in Co-HAPs prepared by coprecipitation, Co species is inserted in the apatite structure resulting in poor redox properties and hence lower methanol oxidation activity. Whereas for impregnated Co-HAPs, the easily reducible Co_3O_4 entities were formed over the hydroxyapatite supports thus making it active for methanol oxidation at lower temperature.

Kaneda and co-workers grafted monomeric PdCl_2 species on the stoichiometric HAP surface by chemisorption to produce PdHAP-0 (Figure 1-15). When PdHAP-0 was used as a catalyst for aerobic alcohol oxidation, the monomeric Pd^{2+} species were converted into Pd nanoparticles. They demonstrated that it is possible to control the size of Pd nanoparticles on hydroxyapatite surfaces by varying the kind of alcohol substrates in the oxidation reactions. Furthermore, when non-stoichiometric deficient apatite was used to

immobilize PdCl₂, ion-exchange between Pd²⁺ and Ca²⁺ occurred to form PdHAP-1 (Figure 1-15). This catalyst was not active like PdHAP-0 in the oxidation of alcohols, but it was an outstanding catalyst for C-C bond-forming reactions as the Mizoroki-Heck and Suzuki-Miyaura reactions [147,148]. Kaneda *et al.* also reported a hydroxyapatite bound palladium catalyst as an effective catalyst for the dehydrogenation of various types of indolines to give the corresponding indoles [149]. The chemisorbed PdCl₂ species were converted to Pd nanoclusters and promoted the dehalogenation and dehydrogenation reactions.

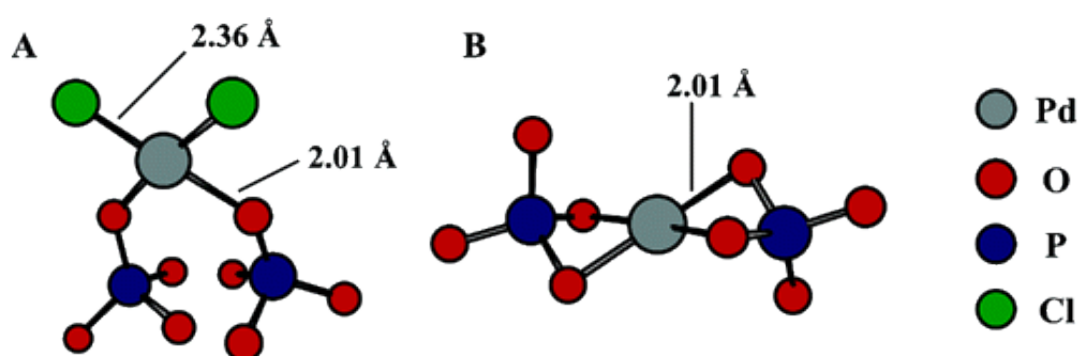


Figure 1-15 Proposed surface structures around Pd^{II} center of (A) PdHAP-0 and (B) PdHAP-1. [147]

M.S. Scurrall *et al.* prepared gold and ruthenium supported on HAP by deposition-precipitation method and examined them in the water gas shift (WGS) reaction [150]. They found that gold exists as metallic gold and is highly dispersed in the HAP. The amount of both acid and basic sites is more in Au/HAP compared with Ru/HAP. Au/HAP was more active than Ru/HAP for the water gas shift reaction by a factor of at least 15 for low temperatures of 110-120°C. The activities for the water gas shift reaction of Au/HAP and Ru/HAP become closer at higher reaction temperatures. H. Sun and co-workers used gold-supported hydroxyapatite as a multifunctional catalyst, for the direct synthesis of imines and oximes by the tandem oxidation of alcohols and amines [151]. They found that introduction of gold nanoparticles over the HAP surface significantly modifies the acid-base distribution, increasing the overall number of both acidic and basic sites. They also proposed that a delicate cooperation between metallic gold and the acid/base sites of the hydroxyapatite surface plays a key role in determining the efficiency and compatibility of

the Au/HAP catalysts for alcohol oxidation and subsequent condensation of the tandem reaction. Furthermore, the Au/HAP catalysts could be reused with almost the same catalytic performance.

Kaneda *et al.* found that monomeric Ru species on the surface of hydroxyapatite is an efficient heterogeneous catalyst for aerobic alcohol oxidation. They proposed that the Ru species on the surface of the Ru-HAPs exists as a monomeric Ru cation surrounded by oxygen and chlorine and attributed the catalytic behaviour to this monomeric Ru cation species (Figure 1-16). No Ru leaching was observed during oxidations and the Ru catalyst was recyclable [152]. They also presented a new type of hydroxyapatite-bound cationic Ru complex with potentially vacant coordination sites that are generated by simple modulation of the neutral Ru-HAP using silver salts. These cationic Ru-HAPs exhibited significant catalytic activities for Diels-Alder and aldol reactions under mild and neutral conditions by acting as Lewis acids toward carbonyl and cyano groups [153].

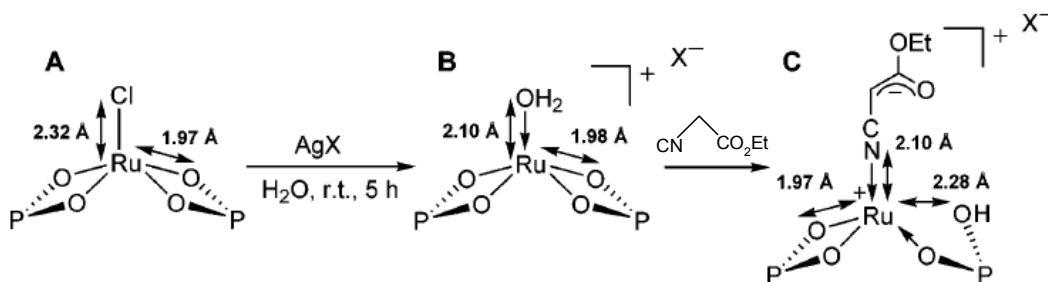


Figure 1-16 Proposed structures of (A) Ru-HAP, (B) cationic RuHAP and (C) Ru-enolate intermediate [153]

The Guerbet reaction of ethanol, which requires a multifunctional catalyst, has also been performed successfully over normal Ca and Sr hydroxyapatites [3,5,4,66,67]. The explanation of the role of acid-base sites of HAP and a reaction mechanism for Guerbet reaction of ethanol has been proposed by T. Tsuchida *et al.* as shown in Figure 1-17 [4]. They proposed that, at first, the O of the ethoxide intermediate is dissociatively adsorbed over a Lewis acid site like Ca and the proton-like hydrogen on covalently bound O in phosphate groups (soft basic sites) near the acid sites. Dissociative adsorption thereby results in the formation of stable hydrogen phosphate groups. The ethoxide is then dissociated into aldehyde and hydride-like hydrogen. Then, one of the two neighbouring

aldehyde intermediates is decomposed to an intermediate enolate ion, which reacts with the other aldehyde intermediate to form an aldol. Unsaturated aldehyde is then generated by dehydration of the aldol and, finally, *l*-butanol is obtained *via* hydrogenation of the unsaturated aldehyde (hydride reduction) taking up hydrogen generated by dissociative adsorption during the first steps [4].

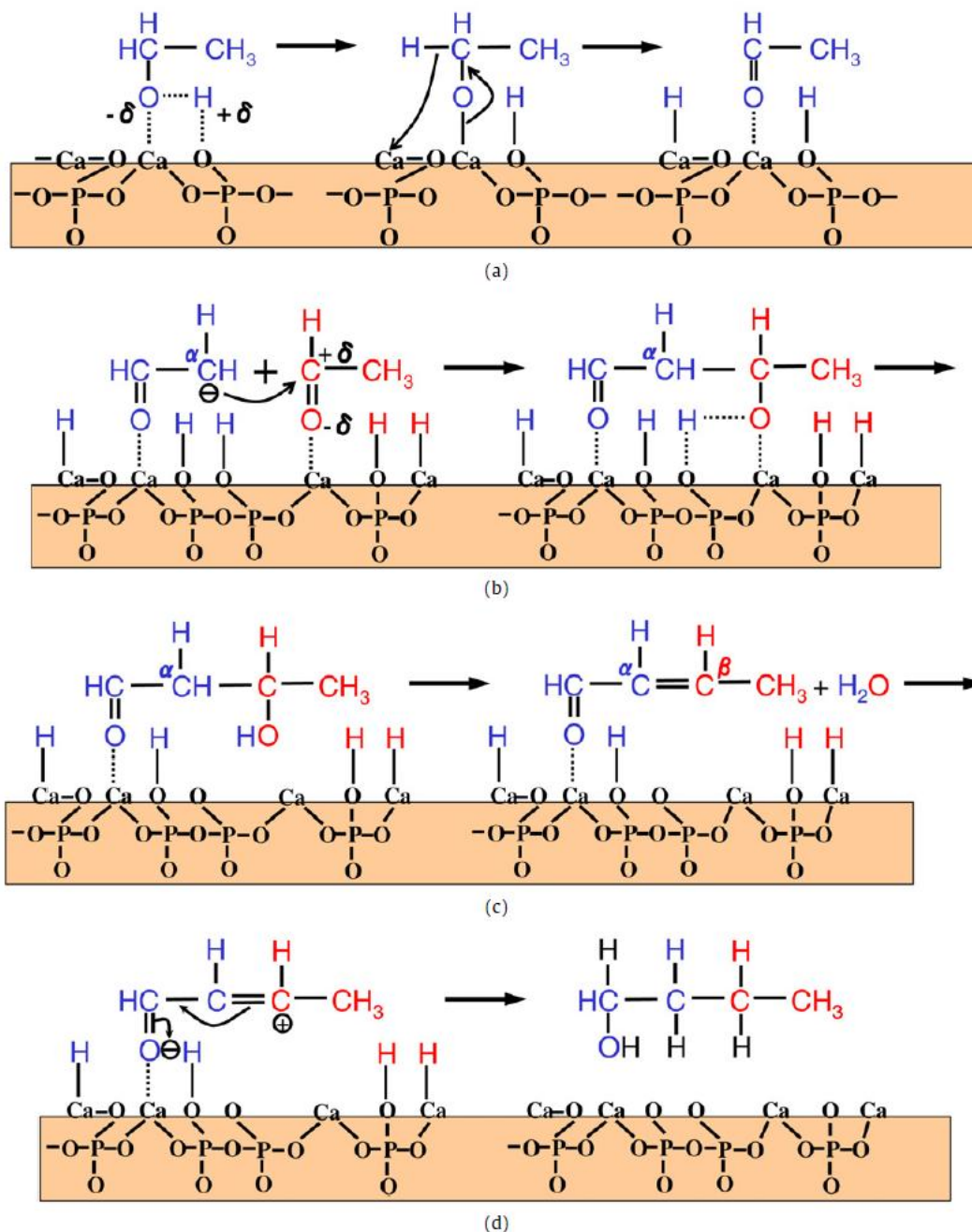


Figure 1-17 Scheme of ethanol reaction to butanol over HAP. [4]

1.6 Objective of our work

In the beginning of this chapter, we have mentioned the need for alternative renewable energy & carbon source and biomass is the only possible renewable raw material for the production of liquid biofuels and chemicals. Bioethanol is one of the major biofuels produced in large quantities from biomass but its high vapour pressure, affinity for water and lower energy content of ethanol avoid it to completely replace the existing fuels. Biobutanol, which is another primary alcohol used as a fuel and a fuel additive can also be produced directly from biomass, but its production through these routes (biotech and syngas conversion) is not economically feasible, at least for the moment [13,14]. Better solution for these problems is to transform some amount of bioethanol produced from biomass to heavier alcohols like butanol through the Guerbet reaction. Both homogeneous and heterogeneous catalysts have been reported for the production of heavier alcohols through the Guerbet reaction. Hydroxyapatite was found to be an active catalyst for heterogeneous gas phase reaction of ethanol [3,4]. The drawback of using hydroxyapatite for the Guerbet reaction is that at higher ethanol conversions, the produced primary alcohols (for example *n*-butanol) undergo further condensation to produce heavier alcohols and other heavier products [5]. This could eventually reduce the selectivity to primary products like *n*-butanol. The heavier alcohols can however be used as solvents, fuel additives and plastisizers (*e.g.*, 1-butanol, 2-ethylhexanol, etc.) or can be further transformed to paraffins by dehydration/hydrogenolysis for use in aviation fuels, straightforwardly as blends. So, it would be better to find an application to use butanol and the entire heavier product mixtures formed during the Guerbet reaction. The aviation fuels, which use the higher paraffins is one of the better solutions to make use of all the Guerbet products, since the most of the heavier products like alcohols, alkene, dienes etc. can be converted to paraffins. The overall aim of this thesis is to tailor the acid-base properties of hydroxyapatites and use them for Guerbet reaction of ethanol to produce both butanol and heavier product mixtures, respecting the biorefinery concept of producing chemicals and fuels. Moreover butanol can be used as a fuel, chemical or a next platform molecule which make it a molecule of interest in the biorefinery.

Tsuchida *et al.* reported the Guerbet reaction of ethanol over hydroxyapatites with different Ca/P ratios up to the stoichiometric value of 1.67. Tsuchida *et al.* obtained about 70%

selectivity to *n*-butanol but at the low ethanol conversion of 20% [4]. Our objective is to perform Guerbet reaction of ethanol using hydroxyapatites with different Ca/P ratio or carbonate content, especially with $\text{Ca/P} > 1.67$. Further we aim to study the Guerbet reaction at higher ethanol conversions to produce both butanol and heavier alcohol mixtures using hydroxyapatites with different Ca/P ratio. Since there are only few reports correlating the structure, textural and acid-base properties of hydroxyapatite with the Guerbet reaction of ethanol, we plan also to study the relation between catalytic performance and the catalyst properties of different hydroxyapatite catalysts.

The acid-base properties of hydroxyapatite may affect the product distribution in Guerbet reaction of ethanol. These properties can be tuned not only by varying the Ca/P ratio, but also by the substitution of the Ca by other metal ions. It has been reported that Sr HAPs are more selective to butanol than Ca-HAPs, in the Guerbet reaction of ethanol [66,67]. So, our second main objective was to synthesize Sr-substituted apatites with different Sr content varying from 0 mol.% to 100 mol.% and screen it in the gas phase Guerbet reaction of ethanol. Further, we will conduct a correlation study to connect the catalyst properties and the catalytic results obtained from the reaction of ethanol.

-
- [1] D. L. Klass, Biomass for Renewable Energy, Fuels, and Chemicals, *Elsevier*, ISBN: 978-0-12-410950-6 (1998) p. 1.
- [2] Anonymous (2004) Renewable Energy scenario to 2040: Half of the Global Energy Supply from renewables in 2040, *Report from the European Renewable Energy Council (EREC)*.
- [3] W. Soetaert, E. J. Vandamme, Biofuels, *Wiley series*, ISBN 978-0-470-02674-8 (2009) p. 1.
- [4] C.J Campbell, The future of oil. *Energy Explor. Exploit*, vol 16 (1998) p. 125–152.
- [5] C.J. Campbell, J.H. Laherrère, The end of cheap oil. *Scientific. American*, vol 278 (1998) p. 78–83.
- [6] http://en.wikipedia.org/wiki/2000s_energy_crisis.
- [7] http://en.wikipedia.org/wiki/Fossil_fuel.
- [8] <http://en.wikipedia.org/wiki/Biomass>
- [9] http://en.wikipedia.org/wiki/Second_generation_biofuels
- [10] <http://www.suschem.org/media.php?mld=4727>
- [11] www.eere.energy.gov/biomass/
- [12] J.J. Bozell, M.K. Patel, ACS symposium series 921, *American chemical society*, Washington (2006) p. 1.
- [13] G. Centi, R.A. Van Santen, Catalysis for renewable, *Wiley-VCH*, ISBN: 978-3-527-31788-2 (2008) p. 55.
- [14] J. Clark, F. Deswarte, Introduction to Chemicals from Biomass, *Wiley*, ISBN: 978-0-470-05805-3 (2008) p. 6.
- [15] D.L van Dyne, M.G. Blase, L.D. Clements, A strategy of returning agriculture and rural America to long-term full employment using biomass refineries, in perspectives on new crops and new uses, J. Janeck (Ed.), *ASHS press, Alexandria* (1999).
- [16] B. Kamm, M. Kamm; Principles of Biorefineries, *Applied Microbiology and Biotechnology*, vol 64 (2004) p. 137-145.
- [17] Joint European Biorefinery Vision for 2030, Star-COLIBRI project, Strategic Targets for 2020 – Collaboration Initiative on Biorefineries, (2011) p. 34-40.
- [18] http://www.chemsystems.com/reports/search/docs/abstracts/0708S3_abs.pdf

-
- [19] J.-W. Bae, H. S. Potdar, S.-H. Kang, K.-W. Jun, Coproduction of Methanol and Dimethyl Ether from Biomass-Derived Syngas on a Cu–ZnO–Al₂O₃/γ-Al₂O₃ Hybrid Catalyst, *Energy Fuels*, vol 22 (2008), p. 223–230
- [20] C. Arcoumanis, A technical study on fuels technology related to auto-oil II program, *Report for European Commission Directorate-General for Energy*, vol. II (2000).
- [21] M. Zabeti, W.M.A.W. Daud, M.K. Aroua, Activity of solid catalysts for biodiesel production: A review, *Fuel Processing Technology*, vol 90 (2009) p. 770-777.
- [22] L. Degirmenci, N. Oktar, G. Dogu, Product distributions in Ethyl tert-butyl ether synthesis over different solid acid catalysts, *Industrial & Engineering Chemistry Research*, vol 48 (2009) p. 2566-2576.
- [23] S. Assabumrungrat, D. Wongwattanasate, V. Pavarajarn, P. Praserttham, A. Arpornwichanop, S. Goto, Production of ethyl tert-butyl ether from tert-butyl alcohol and ethanol catalyzed by β-zeolite in reactive distillation, *Korean Journal of Chemical Engineering*, vol 21 (2004) p. 1139-1146.
- [24] <http://bioweb.sungrant.org/Technical/Biofuels/Technologies/Ethanol+Production/Ethanol+from+Sucrose/Default.html>.
- [25] http://en.wikipedia.org/wiki/Cellulosic_ethanol.
- [26] A.L. Macfarlane, M.M. Farid, J.J.J. Chen, Kinetics of delignification using a batch reactor with recycle, *Chemical Engineering and Processing: Process Intensification*, vol 48 (2009) p. 864-870.
- [27] J.Y. Zhu, X.J. Pan, G.S. Wang, R. Gleisner, Sulfite pretreatment (SPORL) for robust enzymatic saccharification of spruce and red pine, *Bioresource Technology*, vol 100 (2009) p. 2411-2418.
- [28] I. Ojima, C-Y. Tsai, M. Tzamarioudaki, D. Bonafoux, The Hydroformylation Reaction, *Organic Reactions* (2004) p. 1–354.
- [29] R. Cascone. "Biobutanol – A replacement for bioethanol?". *Chemical Engineering Progress, SBE Special Section, Biofuels*, S4 (2008).
- [30] <http://biomassmagazine.com/articles/7273/researchers-use-bacterium-to-convert-cellulose-into-n-butanol/?ref=brm>.
- [31] Guerbet, *Comptes rendus*, CXXXII (1901) p. 207.
- [32] Guerbet, *Comptes rendus*, vol 149 (1909) p. 129.
- [33] C.H. Weizmann, L. Haskelberg, E. Bergmann, Mechanism and applicability of the Guerbet reaction, *Journal of the Society of Chemical Industry*, vol 56 (1937) p. 587-591.

-
- [34] *Biokhimiya*, vol 6 (1941) p. 261.
- [35] C.H. Weizmann, Further observations of the Guerbet reaction (1949).
- [36] S. Veibel, J.I. Nielsen, On the mechanism of the Guerbet reaction, *Tetrahedron*, vol 23 (1967) p. 1723-1733.
- [37] C.A. Carter, Condensation of Alcohols, *U.S Patent* 2,457,866 (1949).
- [38] E.F. Pratt, D.G. Kubler, Disproportionative Condensations I. Modified Guerbet Reactions, *Journal of American Chemical Society*, vol 76 (1953).p. 52-56.
- [39] M. Sulzbacher, Improvements in and relating to the condensation of alcohols, *GB Patent* 655864 (1951).
- [40] M. Sulzbacher, The Guerbet reaction of Cetyl alcohol, *Journal of Applied Chemistry*, vol 5 (1955) p. 637-641.
- [41] R.E. Miller, G.E. Bennet, Producing 2-ethylhexanol by the Guerbet reaction, *Industrial & Engineering Chemistry*, vol 53 (1961) p. 33-36.
- [42] G. Gregorio, G. Pregalgia, R. Ugo, Condensation of alcohols catalysed by tertiary phosphine transition metal complexes, *Journal of Organometallic Chemistry*, vol 37 (1972) p. 385-387.
- [43] T. Matsu-ura, S. Sakaguchi, Y. Obora, Y. Ishii, Guerbet Reaction of Primary Alcohols Leading to β -Alkylated Dimer Alcohols Catalyzed by Iridium Complexes, *Journal of Organic Chemistry*, vol 71 (2006) p. 8306-8308.
- [44] P.L. Burk, R.L. Pruet, K.S. Campo, The rhodium-promoted guerbet reaction: Part I. Higher alcohols from lower alcohols, *Journal of Molecular Catalysis*, vol 33 (1985) p. 1-14.
- [45] P. L. Burk, R. L. Pruet, K. S. Campo, The rhodium-promoted guerbet reaction: Part II. Secondary alcohols and methanol as substrates, *Journal of Molecular Catalysis*, vol 33 (1985) p. 15-21.
- [46] C. Carlini, A. Macinai, M. Marchionna, M. Noviello, A.M.R. Galletti, G. Sbrana, Selective synthesis of isobutanol by means of the Guerbet reaction Part 3: Methanol/n-propanol condensation by using bifunctional catalytic systems based on nickel, rhodium and ruthenium species with basic components, *Journal of Molecular Catalysis A*, vol 206 (2003) p. 409-418.
- [47] C. Carlini, M.D. Girolamo, A. Macinai, M. Marchionna, M. Noviello, A.M.R. Galletti, G. Sbrana, Synthesis of isobutanol by the Guerbet condensation of methanol with n-propanol in the presence of heterogeneous and homogeneous palladium-based catalytic systems, *Journal of Molecular Catalysis A*, vol 204-205 (2003) p. 721-728.

-
- [48] C. Carlini, A. Macinai, A.M.R. Galletti, G. Sbrana, Selective synthesis of 2-ethyl-1-hexanol from n-butanol through the Guerbet reaction by using bifunctional catalysts based on copper or palladium precursors and sodium butoxide, *Journal of Molecular Catalysis A*, vol 212 (2004) 65-70.
- [49] C. Carlini, M.D. Girolamo, M. Marchionna, M. Noviello, A. M. R. Galletti, G. Sbrana, Selective synthesis of isobutanol by means of the Guerbet reaction: Part 1. Methanol/n-propanol condensation by using copper based catalytic systems, *Journal of Molecular Catalysis A*, vol 184 (2002) p. 273-280.
- [50] C. Carlini, M.D. Girolamo, A. Macinai, M. Marchionna, M. Noviello, A.M.R. Galletti, G. Sbrana, Selective synthesis of isobutanol by means of the Guerbet reaction: Part 2. Reaction of methanol/ethanol and methanol/ethanol/n-propanol mixtures over copper based/MeONa catalytic systems, *Journal of Molecular Catalysis A*, vol 200 (2003) p. 137-146.
- [51] M.N. Dvornikoff, M.W. Farrar, Condensation of Alcohols, *Journal of Organic Chemistry*, vol 22 (1957) p. 540-542.
- [52] C. Carlini, C. Flego, M. Marchionna, M. Noviello, A.M.R. Galletti, G. Sbrana, F. Basile, A. Vaccari, Guerbet condensation of methanol with n-propanol to isobutyl alcohol over heterogeneous copper chromite/Mg–Al mixed oxides catalysts, *Journal of Molecular Catalysis A*, vol 220 (2004) p. 215-220.
- [53] W. Ueda, T. Kuwabara, T. Ohshida, Y. Morikawa, A low-pressure guerbet reaction over magnesium oxide catalyst, *Journal of the Chemical Society, Chemical Communications*, (1990) p. 1558-1559.
- [54] W. Ueda, T. Ohshida, T. Kuwabara, Y. Morikawa, Condensation of alcohol over solid-base catalyst to form higher alcohols, *Catalysis letters*, vol 12 (1992) p. 97-104.
- [55] K. Gotoh, S. Nakamura, T. Mori, Y. Morikawa, Supported alkali salt catalysts active for the guerbet reaction between methanol and ethanol, *Studies in Surface Science and Catalysis*, vol.130 (2000) p. 2669–2674.
- [56] A.S. Ndou, N. Plint, N.J. Coville, Dimerisation of ethanol to butanol over solid-base catalysts, *Applied Catalysis A: General*, vol 251 (2003) p. 337-345.
- [57] C. Yang, Z.Y. Meng, Bimolecular Condensation of Ethanol to 1-Butanol Catalyzed by Alkali Cation Zeolites, *Journal of Catalysis*, vol 142, (1993) p. 37-44.
- [58] J.I. Di Cosimo, C.R. Apestegui, M.J.L. Ginés, E. Iglesia, Structural Requirements and Reaction Pathways in Condensation Reactions of Alcohols on Mg₂AlO₄ Catalysts, *Journal of Catalysis*, vol 190 (2000) p. 261-275.

-
- [59] C. Carlini, M. Marchionna, M. Noviello, A.M.R. Galletti, G. Sbrana, F. Basile, A. Vaccari, Guerbet condensation of methanol with n-propanol to isobutyl alcohol over heterogeneous bifunctional catalysts based on Mg–Al mixed oxides partially substituted by different metal components, *Journal of Molecular Catalysis A*, vol 232 (2005) p. 13-20.
- [60] I.C. Marcu, D. Tichit, F. Fajula, N. Tanchoux, Catalytic valorization of bioethanol over Cu-Mg-Al mixed oxide catalysts, *Catalysis Today*, vol 147, (2009) p. 231-238.
- [61] M. León, E. Díaz, S. Ordóñez, Ethanol catalytic condensation over Mg–Al mixed oxides derived from hydrotalcites, *Catalysis Today*, vol 164 (2011) p. 436–442.
- [62] D.L. Carvalho, R.R. de Avillez, M.T. Rodrigues, L.E.P. Borges, L.G. Appel, Mg and Al mixed oxides and the synthesis of n-butanol from ethanol, *Applied Catalysis A: General*, vol 415-416 (2012) p. 96-100.
- [63] T. Tsuchida, S. Sakuma, T. Takeguchi, W. Ueda, Direct Synthesis of n-Butanol from Ethanol over Nonstoichiometric Hydroxyapatite, *Industrial & Engineering Chemistry Research*, vol 45 (2006) p. 8634-8642.
- [64] T. Tsuchida, T. Yoshioka, S. Sakuma, T. Takeguchi, W. Ueda, Synthesis of Biogasoline from Ethanol over Hydroxyapatite Catalyst, *Industrial & Engineering Chemistry Research*, vol 47 (2008) p. 1443-1452.
- [65] T. Tsuchida, J. Kubo, T. Yoshioka, S. Sakuma, T. Takeguchi, W. Ueda, Reaction of ethanol over hydroxyapatite affected by Ca/P ratio of catalyst, *Journal of Catalysis*, vol 259 (2008) p. 183-189.
- [66] S. Ogo, A. Onda, K. Yanagisawa, Selective synthesis of 1-butanol from ethanol over strontium phosphate hydroxyapatite catalysts, *Applied Catalysis A: General*, vol 402 (2011) p. 188-195.
- [67] S. Ogo, A. Onda, Y. Iwasa, K. Hara, A. Fukuoka, K. Yanagisawa, 1-Butanol synthesis from ethanol over strontium phosphate hydroxyapatite catalysts with various Sr/P ratios, *Journal of Catalysis*, vol 296 (2012) p. 24-30.
- [68] H. Suda, M. Yashima, M. Kakihana, M. Yoshimura, Monoclinic ↔ hexagonal phase transition in hydroxyapatite studied by X-ray powder 128 diffraction and differential scanning calorimeter techniques, *Journal of Physical Chemistry*, vol 99 (2002) p. 6752-6754.
- [69] H. Monma, T. Kanazawa, *Journal of Chemical Society of Japan*, (1972) p. 339.
- [70] S-H. Rhee, Synthesis of hydroxyapatite via mechanochemical treatment, *Biomaterials*, vol 23 (2002) p. 1147-1152.

-
- [71] C.C. Silva, A.G. Pinheiro, M.A.R. Miranda, J.C. Góes, A.S.B. Sombra, Structural properties of hydroxyapatite obtained by mechanosynthesis, *Solid State Sciences*, vol 5 (2003) p. 553-558.
- [72] X. Zhang, K.S. Vecchio, Hydrothermal synthesis of hydroxyapatite rods, *Journal of Crystal Growth*, vol 308 (2007) p. 133-140.
- [73] J. Liu, X. Ye, H. Wang, M. Zhu, B. Wang, H. Yan, The influence of pH and temperature on the morphology of hydroxyapatite synthesized by hydrothermal method, *Ceramics International*, vol 29 (2003) p. 629-633.
- [74] C.R. Kothapalli, M. Wei, R.Z. Legeros, M.T. Shaw, Influence of temperature and aging time on HA synthesized by the hydrothermal method, *Journal of Materials Science: Materials in Medicine*, vol 16 (2005) p. 441-446.
- [75] A.A. Chaudhry, S. Haque, S. Kellici, P. Boldrin, I. Rehman, F.A. Khalid, J.A. Darr, Instant nano-hydroxyapatite: a continuous and rapid hydrothermal synthesis, *Chemical Communications*, vol 21 (2006) p. 2286-2288.
- [76] S. Ogo, A. Onda, K. Yanagisawa, Hydrothermal synthesis of vanadate-substituted hydroxyapatites and catalytic properties for conversion of 2-propanol, *Applied Catalysis A: General*, vol 348 (2008) p. 129-134.
- [77] M-F. Hsieh, L-H. Perng, T-S. Chin, H.-G. Perng, Phase purity of sol-gel-derived hydroxyapatite ceramic, *Biomaterials*, vol 22, (2001) p. 2601-2607.
- [78] Y. Masuda, K. Matubara, S. Sakka, Synthesis of hydroxyapatite from metal alkoxides through sol-gel technique, *Journal of the Ceramic Society of Japan*, vol 98 (1990) p. 1266-1277.
- [79] H. Takahashi, M. Yashima, M. Kakihana, M. Yoshimura, Synthesis of stoichiometric hydroxyapatite by a gel route from the aqueous solution of citric and phosphonoacetic acids, *European Journal of Solid State and Inorganic Chemistry*, vol 32 (1995) p. 829-835.
- [80] I-S. Kim, P.N. Kumta, Sol-gel synthesis and characterization of nanostructured hydroxyapatite powder, *Materials Science and Engineering B*, vol 111 (2004) p. 232-236.
- [81] A. Jilavenkatesa, R.A. Condrate SR, Sol-gel processing of hydroxyapatite, *Journal of Materials Science*, vol 33 (1998) p. 4111-4119.
- [82] D.L. Shi, X.J. Wen, Bioactive ceramics: structure, synthesis, and mechanical properties, in *Introduction to biomaterials*, Tsinghua University Press, (2006) p. 16-17.

-
- [83] N. Asaoka, S. Best, J.C. Knowles, W. Bonfield, Characterization of hydroxyapatite precipitated from different reactants, in *Proceedings of the eighth international symposium on ceramics in medicine*, Ponte Vedra, Florida, (1995) p. 331-337.
- [84] M. H. Santos, M.de Oliveira, L.P.de F. Souza, H.S. Mansur, W.L. Vasconcelos, Synthesis control and characterization of hydroxyapatite prepared by wet precipitation process, *Materials Research*, vol 7 (2004) p. 625-630.
- [85] L. Bernard, M. Freche, J.L Lacout, B. Biscans, Preparation of hydroxyapatite by neutralization at low temperature-influence of purity of the raw material, *Powder Technology*, vol 103 (1999) p. 19–25.
- [86] A. Bigi, E. Boanini, C. Capuccini, M. Gazzano, Strontium-substituted hydroxyapatite nanocrystals, *Inorganica Chimica Acta*, vol 360 (2007) p.1009-1016.
- [87] St. Naray-Szabo, *Zeitschrift für Kristallographie*, vol 75 (1930) p.387-398.
- [88] M. Mehmel, *Zeitschrift für Kristallographie*, vol 75 (1930) p. 323-331.
- [89] Donglu Shi, *Introduction to Biomaterials*, Tsinghua University Press, ISBN: 7-302-10807-2 (2005) p. 16.
- [90] J.C. Elliott, R.M. Wilson, S.E.P. Dowker, *JCPDS-international centre for diffraction data*, vol 45 (2002) p. 172-181.
- [91] X. Ma, D.E. Ellis, Initial stages of hydration and Zn substitution/occupation on hydroxyapatite (0001) surfaces, *Biomaterials*, vol 29 (2008) p. 257-265.
- [92] J. Li, Thesis in Structural Characterization of apatite like materials; University of Birmingham, UK (2009).
- [93] C.A. Beevers, D.B. McIntyre, *Mineralogical Magazine*, vol 27 (1946) p. 254-257.
- [94] J.M. Hughes, J. Rakovan, The crystal structure of apatite, $\text{Ca}_5(\text{PO}_4)_3(\text{F},\text{OH},\text{Cl})$, *Reviews in Mineralogy and Geochemistry*, vol 48 (2002) p. 1-12.
- [95] M.I. Kay, R.A. Young, A.S. Posner, Crystal structure of hydroxyapatite, *Nature*, vol 204 (1964) p. 1050-1052.
- [96] D. Arcos, J. Rodríguez-Carvajal, and M. Vallet-Regí, Neutron scattering for the study of improved bone implants, *Physica B: Condensed Matter*, vol 350 (2004) p. E607-E610.
- [97] H.B. Vanrees, M. Mengeot, E. Kostiner, Monoclinic-hexagonal transition in hydroxyapatite and deuterohydroxyapatite single crystals, *Materials Research Bulletin*, vol 8 (1973) p.1307-1309.

-
- [98] N. Hitmi, C. Lacabanne, R.A. Young, OH⁻ dipole reorientability in hydroxyapatites: Effect of tunnel size, *Journal of Physics and Chemistry of Solids*, vol 47 (1986) p. 533-546.
- [99] L. Calderin, M.J. Stott, A. Rubio, Electronic and crystallographic structure of apatites, *Physical Review B*, vol 67 (2003) p. 134106.
- [100] N.K. Tripathy, P.N. Patel, A. Panda, Preparation, IR, and lattice constant measurements of mixed (Ca + Cu + Zn) hydroxylapatites, *Journal of Solid State Chemistry*, vol 80 (1989) p. 1-5.
- [101] S.V. Chiranjeevirao, J. Hemmerle, J.C. Voegel, R.M. Frank, A method of preparation and characterization of magnesium-apatites, *Inorganica Chimica Acta*, vol 67 (1982) p. 183-187.
- [102] D.G. Nelson, J.D. Featherstone, Preparation, analysis, and characterization of carbonated apatites, *Calcified Tissue International*, vol 34 (1982) p. S69-81.
- [103] I.R. Gibson, S.M. Best, W. Bonfield, Chemical characterization of silicon-substituted hydroxyapatite, *Journal of Biomedical Materials Research*, vol 44 (1999) p. 422-428.
- [104] C.M. Serre, M. Papillard, P. Chavassieux, J.C. Voegel, G. Boivin, Influence of magnesium substitution on a collagen-apatite biomaterial on the production of a calcifying matrix by human osteoblasts, *Journal of Biomedical Materials Research*, vol 42 (1998) p. 626-633.
- [105] Z. Opre, Catalytic oxidation over transition metal containing hydroxyapatites, Swiss Federal Institute of Technology (ETH) Zurich, Diss. ETH No 17247 (2007).
- [106] M.D. O'Donnell, Y. Fredholm, A. de Rouffignac, R.G. Hill, Structural analysis of a series of strontium-substituted apatites, *Acta Biomaterialia*, vol 4 (2008) p. 1455-1464.
- [107] T.S.B. Narasaraju, D.E. Phebe, Some physico-chemical aspects of hydroxylapatite, *Journal of Materials Science*, vol 31 (1996) p. 1-21.
- [108] A. Bigi, E. Foresti, M. Gandolfi, M. Gazzano, N. Roveri, Inhibiting effect of zinc on hydroxylapatite crystallization, *Journal of Inorganic Biochemistry*, vol 58 (1995) p. 49-58.
- [109] F. Miyaji, Y. Kono, Y. Suyama, Formation and structure of zinc-substituted calcium hydroxyapatite, *Materials Research Bulletin*, vol 40 (2005) p. 209-220.
- [110] A. Bigi, G. Falini, E. Foresti, A. Ripamonti, M. Gazzano, N. Roveri, Magnesium influence on hydroxyapatite crystallization, *Journal of Inorganic Biochemistry*, vol 49 (1993) p. 69-78.

-
- [111] Y. Pan, M.E. Fleet, Compositions of the Apatite-Group Minerals: Substitution Mechanisms and Controlling Factors. In *Phosphates-Geochemical, Geobiological and Materials Importance, Reviews in Mineralogy and Geochemistry*. Edited by Kohn MJ, Rakovan J, Hughes JM. Mineralogical Society of America, Washington DC vol 48 (2002) p. 13-49.
- [112] R. Z. LeGeros, Calcium phosphates in oral biology and medicine, *S. Karger AG, Basel*, ISBN: 978-3-8055-5236-3, (1991).
- [113] A. Ślósarczyk, Z. Paszkiewicz, C. Paluszkiwicz, FTIR and XRD evaluation of carbonated hydroxyapatite powders synthesized by wet methods, *Journal of Molecular Structure*, vol 744-747 (2005) p. 657-661.
- [114] M. Mathew, S. Takagi, Structures of biological minerals in dental research, *Journal of Research of the National Institute of Standards and Technology*, vol 106 (2001) p. 1035-1044.
- [115] A.R. Stéphane, N. Michel, B.-A. Didier, R. Christian, D. Philippe, S. Laurent, and J.M. Pierre, Behavior of human osteoblastic cells on stoichiometric hydroxyapatite and type A carbonate apatite: Role of surface energy, *Journal of Biomedical Materials Research*, vol 50 (2000) p. 353-364.
- [116] I.R. Gibson, W. Bonfield, Novel synthesis and characterization of an AB-type carbonate-substituted hydroxyapatite, *Journal of Biomedical Materials Research*, vol 59 (2002) p. 697-708.
- [117] D.G. Nelson, J.D. Featherstone, Preparation, analysis, and characterization of carbonated apatites, *Calcified Tissue International*, vol 34 (1982) p. S69-81.
- [118] M. Vignoles, G. Bonel, R. Young, Occurrence of nitrogenous species in precipitated B-type carbonated hydroxyapatites, *Calcified Tissue International*, vol 40 (1987) p. 64-70.
- [119] R.Z. LeGeros, O.R. Trautz, E. Klein, J.P. LeGeros, Two types of carbonate substitution in the apatite structure, *Cellular and Molecular Life Sciences*, vol 25 (1969) p. 5-7.
- [120] O.V. Frank-Kamenetskaya, Structure, chemistry and synthesis of carbonate apatites-the main components of dental and bone tissues, *Minerals as Advanced Materials I*, (2008) p. 241-252.
- [121] R.T. Otto, X-ray diffraction of biological and synthetic apatites, *Annals of the New York Academy of Sciences*, vol 60 (1955) p. 696-712.
- [122] R. Legros, N. Balmain, G. Bonel, Structure and composition of the mineral phase of periosteal bone, *Journal of Chemical Research*, (1986) p. 8-9.

-
- [123] F.F.M. De Mul, M.H.J. Hottenhuis, P. Bouter, J. Greve, J. Arends, J.J. Ten Bosch, Micro-Raman line broadening in synthetic carbonated hydroxyapatite, *Journal of Dental Research*, vol 65 (1986) p. 437-440.
- [124] J.C. Elliott, Recent progress in the chemistry, crystal chemistry and structure of the apatites, *Calcified Tissue International*, vol 3 (1969) p. 293-307.
- [125] K. Beshah, C. Rey, M.J. Glimcher, M. Schimizu, R.G. Griffin, Solid state carbon-13 and proton NMR studies of carbonate-containing calcium phosphates and enamel, *Journal of Solid State Chemistry*, vol 84 (1990) p. 71-81.
- [126] S.Raynaud, E. Champion, D. Bernache-Assollant, P. Thomas, Calcium phosphate apatites with variable Ca/P atomic ratio I. Synthesis, characterization and thermal stability of powder, *Biomaterials*, vol 23 (2002) p. 1065-1072.
- [127] S.J. Joris, C.H. Amberg, Nature of deficiency in nonstoichiometric hydroxyapatites. I. Catalytic activity of calcium and strontium hydroxyapatites, *Journal of Physical Chemistry*, vol 75 (1971) p. 3167-3171.
- [128] H. Tanaka, M. Chikazawa, K. Kandori, T. Ishikawa, Influence of thermal treatment on the structure of calcium hydroxyapatite, *Physical Chemistry Chemical Physics*, vol 2 (2000) p. 2647-2650.
- [129] I. Sopyan, M. Mel, S. Ramesh, K.A. Khalid, Porous hydroxyapatite for artificial bone applications, *Science and Technology of Advanced Materials*, vol 8 (2007) p. 116-123.
- [130] C. Kojima, K. Watanabe, Adsorption and Desorption of Bioactive Proteins on Hydroxyapatite for Protein Delivery Systems, *Journal of Drug Delivery*, vol 2012 (2012).
- [131] S. Kano, A. Yamazaki, R. Otsuka, M. Ohgaki, M. Akao, M. Aoki, Application of hydroxyapatite-sol as drug carrier, *Bio-medical Materials and Engineering*, vol 4 (1994) p. 283-90.
- [132] G. Bernardi, M-G Giro, C. Gaillard; Chromatography of polypeptides and proteins on hydroxyapatite columns: Some new developments, *Biochimica et Biophysica Acta (BBA) - Protein Structure*, vol 278 (1972) p. 409.
- [133] C. Verwilghen, S. Rio, A. Nzihou, D. Gauthier, G. Flamant, P.J. Sharrock, Preparation of high specific surface area hydroxyapatite for environmental applications, *Journal of Materials Science*, vol 42 (2007) p. 6062-6066.
- [134] H. Monma, Catalytic behavior of calcium phosphates for decompositions of 2-propanol and ethanol, *Journal of Catalysis*, vol 75 (1982) p. 200-203.

-
- [135] J.A.S. Bett, L.G. Christner, W.K. Hall, Studies of the Hydrogen Held by Solids. XII. Hydroxyapatite Catalysts, *Journal of the American Chemical Society*, vol 89 (1967) p. 5535–5541.
- [136] C.L. Kibby, S.S. Lande, W.K. Hall, Tracer studies of acid-catalyzed reactions XI Stereoselectivity in alcohol dehydration over hydroxyapatite and alumina catalysts, *Journal of the American Chemical Society*, vol 94 (1972) p. 214–220.
- [137] S. Sebti, R. Tahir, R. Nazih, A. Saber, S. Boulaajaj, Hydroxyapatite as a new solid support for the Knoevenagel reaction in heterogeneous media without solvent, *Applied Catalysis A: General*, vol 228 (2002) p. 155–159.
- [138] S. Sebti, A. Solhy, R. Tahir, A. Smahi, Modified hydroxyapatite with sodium nitrate: an efficient new solid catalyst for the Claisen-Schmidt condensation, *Applied Catalysis A: General*, vol 235 (2002) p. 273–281.
- [139] A. Smahi, A. Solhy, H.E. Badaoui, A. Amoukal, A. Tikad, M. Maizi, S. Sebti, Potassium fluoride doped fluorapatite and hydroxyapatite as new catalysts in organic synthesis, *Applied Catalysis A: General*, vol 250 (2003) p. 151–159.
- [140] S. Sebti, R. Tahir, R. Nazih, S. Boulaajaj, Comparison of different Lewis acid supported on hydroxyapatite as new catalysts of Friedel-Crafts alkylation, *Applied Catalysis A: General*, vol 218 (2001) p. 25–30.
- [141] M. Zahouily, Y. Abrouki, A. Rayadh, S. Sebti, H. Dhimanec, M. David, Fluorapatite: efficient catalyst for the Michael addition, *Tetrahedron Letters*, vol 44 (2003) p. 2463–2465.
- [142] H. Tounsi, S. Djemal, C. Petitto, G. Delahay, Copper loaded hydroxyapatite catalyst for selective catalytic reduction of nitric oxide with ammonia, *Applied Catalysis B: Environmental*, vol 107 (2011) p. 158–163.
- [143] B.M. Choudary, C. Sridhar, M.L. Kantam, B. Sreedhar, Hydroxyapatite supported copper catalyst for effective three-component coupling, *Tetrahedron Letters*, vol 45 (2004) p. 7319–7321.
- [144] N.S. Fígoli, H.R. Keselman, P.C. L'Argentiere, C.L. Lazzaroni, Hydrolysis of chlorobenzene over Cu-promoted hydroxyapatites, *Journal of Catalysis*, vol 77 (1982) p. 64–73.
- [145] K. Elkabouss, M. Kacimi, M. Ziyad, S. Ammar, F.B-Verduraz, Cobalt-exchanged hydroxyapatite catalysts: Magnetic studies, spectroscopic investigations, performance in 2-butanol and ethane oxidative dehydrogenations, *Journal of Catalysis*, vol 226 (2004) p. 16–24.

-
- [146] B. Aellach, A. Ezzamarty, J. Leglise, C. Lamonier, J.-F Lamonier, Calcium-deficient and stoichiometric hydroxyapatites promoted by Cobalt for the catalytic removal of oxygenated Volatile Organic Compounds, *Catalysis Letters*, vol 135 (2010) p. 197–206.
- [147] K. Mori, T. Hara, T. Mizugaki, K. Ebitani, K. Kaneda, Hydroxyapatite-Supported Palladium Nanoclusters: A Highly Active Heterogeneous Catalyst for Selective Oxidation of Alcohols by Use of Molecular Oxygen, *Journal of the American Chemical Society*, vol 126 (2004) p. 10657-10666.
- [148] K. Mori, T. Hara, M. Oshiba, T. Mizugaki, K. Ebitani, K. Kaneda, Catalytic investigations of carbon–carbon bond-forming reactions by a hydroxyapatite-bound palladium complex, *New Journal of Chemistry*, vol 29 (2005) p. 1174-1181.
- [149] T. Hara, K. Mori, T. Mizugaki, K. Ebitani, K. Kaneda, Highly efficient dehydrogenation of indolines to indoles using hydroxyapatite-bound Pd catalyst, *Tetrahedron Letters*, vol 44 (2003) p. 6207–6210.
- [150] A. Venugopal, M.S. Scurrall, Hydroxyapatite as a novel support for gold and ruthenium catalysts: Behaviour in the water gas shift reaction, *Applied Catalysis A: General*, vol 245 (2003) p. 137–147.
- [151] H. Sun, F.-Z Su, J. Ni, Y. Cao, H.-Y He, K.-N Fan, Gold Supported on Hydroxyapatite as a Versatile Multifunctional Catalyst for the Direct Tandem Synthesis of Imines and Oximes, *Angewandte Chemie*, vol 121 (2009) p. 4454 –4457.
- [152] K. Yamaguchi, K. Mori, T. Mizugaki, K. Ebitani, K. Kaneda, Creation of a Monomeric Ru Species on the Surface of Hydroxyapatite as an Efficient Heterogeneous Catalyst for Aerobic Alcohol Oxidation, *Journal of the American Chemical Society*, vol 122 (2000) p. 7144-7145.
- [153] K. Mori, T. Hara, T. Mizugaki, K. Ebitani, K. Kaneda, Hydroxyapatite-Bound Cationic Ruthenium Complexes as Novel Heterogeneous Lewis Acid Catalysts for Diels–Alder and Aldol Reactions, *Journal of the American Chemical Society*, vol 125 (2003) p.11460-11461.

Chapter 2 Catalyst preparation and experimental techniques

In this chapter, we present the catalysts preparation procedures, the techniques that we used for characterizing the physicochemical features of the so-obtained solids, as well as the analytical techniques used the performances evaluation catalytic tests.

2.1 Synthesis of hydroxyapatites

The hydroxyapatite catalysts were synthesized by a precipitation method, using the lab device shown in Figure 2-1.

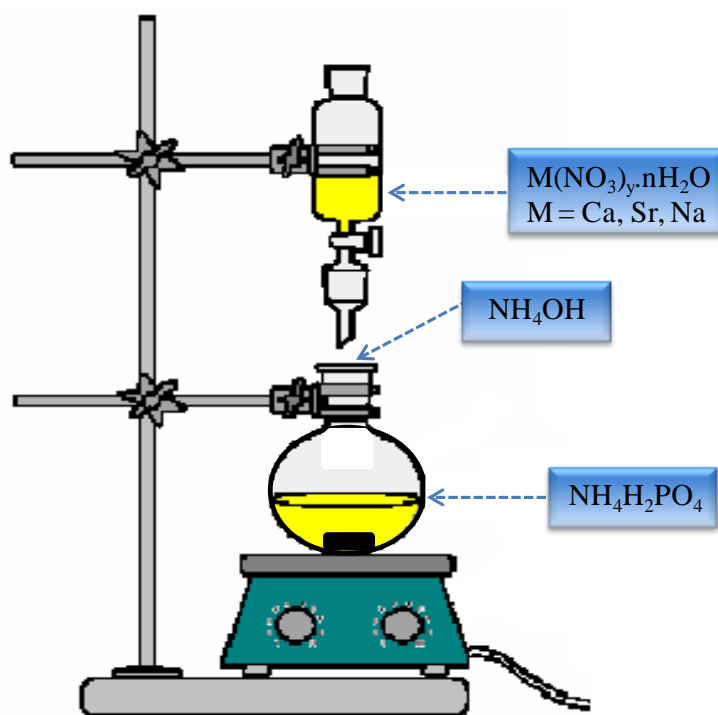


Figure 2-1 Schematic representation of the lab device used for the synthesis of the hydroxyapatites by precipitation.

2.1.1 Materials

Reagent grade chemicals such as calcium nitrate tetrahydrate $\text{Ca}(\text{NO}_3)_2 \cdot 4\text{H}_2\text{O}$, strontium nitrate $\text{Sr}(\text{NO}_3)_2$, ammonium dihydrogen phosphate $(\text{NH}_4)\text{H}_2\text{PO}_4$, sodium nitrate NaNO_3 , sodium carbonate Na_2CO_3 , (Sigma Aldrich), 25% NH_4OH were used as starting chemical precursors for the synthesis of HAPs.

2.1.2 Preparation of carbonate-containing HAPs with different Ca/P ratios

All the solids were synthesized by a precipitation method reported elsewhere [1]. Deficient and stoichiometric HAPs were prepared by fixing the Ca/P molar ratios of the solutions at 0.9 and 1.67, respectively. Two carbonated apatites, with and without sodium, were synthesized by moderately increasing the $(\text{Ca} + \text{Na})/\text{P}$ ratio of the solutions from the stoichiometric value of 1.67 to 2, with a Ca/Na molar ratio of 5.7 for the Na-containing solid. Finally, two carbonate-rich apatites with and without sodium were synthesized by increasing the $(\text{Ca} + \text{Na})/\text{P}$ ratio of the solutions from the stoichiometric value of 1.67 to 5.5 with a Ca/Na molar ratio of 5 for the Na-containing solid. The detailed preparation procedures of these samples are given below.

Stoichiometric hydroxyapatite (**Hap**) was synthesized by adding dropwise 300 mL of an aqueous solution containing 0.167 mol of $\text{Ca}(\text{NO}_3)_2 \cdot 4\text{H}_2\text{O}$ to 1000 mL of a solution containing 0.1 mol of $(\text{NH}_4)\text{H}_2\text{PO}_4$ placed under stirring at 80°C . The pH during the synthesis was maintained at 10 by properly adding a 25% NH_4OH solution. The formed precipitate was slowly filtered, washed with hot water, dried at 80°C before being calcined for 4 h under oxygen at 400°C ($2^\circ\text{C} \cdot \text{min}^{-1}$). Lowering the calcium quantity in the solution from 0.167 mol to 0.09 mol resulted in the formation of a calcium deficient hydroxyapatite (**HapD**).

For carbonated hydroxyapatite with $\text{Ca}/\text{P} > 1.67$, CO_2 was naturally introduced from the atmosphere as CO_3^{2-} anions, which were incorporated to compensate the charge due to excess calcium cations in the apatite solids. In this respect, the carbonated apatite (**Hap-CO₃**) was prepared by using a Ca/P molar ratio of 2 in the precursor solutions instead of the stoichiometric value of 1.67. The same procedure was used to synthesize a

sodium-containing carbonate apatite (**HapNa-CO₃**) prepared with a Ca/Na molar ratio of 5.7, keeping a (Ca + Na) /P molar ratio of 2.

Carbonate-rich hydroxyapatite was synthesized by adding dropwise an aqueous solution of (NH₄)H₂PO₄ (0.1 M) to a 300 mL solution containing 0.55 mol of calcium nitrate placed under stirring at 80°C. The higher Ca/P molar ratio of 5.5 compared to the stoichiometric value of 1.67 allowed us to introduce a higher quantity of carbonate ions in the synthesized hydroxyapatite. The corresponding solid was denoted as **HapE-CO₃**, which is a sodium-free carbonate-rich apatite. Even more carbonate ions and sodium ions were also introduced in a last sample, using sodium carbonate (5.83 g) dissolved in 1000 mL of an ammonium hydrogen phosphate solution (0.1 M). The Ca/Na molar ratio of the solution was fixed at 5. In that case, the resulting solid is a sodium-containing carbonate-rich apatite denoted as **HapE-Na-CO₃**.

2.1.3 Preparation of strontium-substituted HAPs with various substitution extents

All the stoichiometric Sr apatites were synthesized by a precipitation method, adding dropwise 300 mL of an aqueous solution containing 'x' moles of Ca(NO₃)₂.4H₂O or/and Sr(NO₃)₂ to 1000 mL of a 0.1 M (NH₄)H₂PO₄ solution placed under stirring and kept at a temperature of about 80°C. The values of x were fixed at 0.167, 0.1253, 0.0835 and 0.0418 mole, depending on the desired relative Ca and Sr contents in the apatite solids (presented in Table 2-1 below), and the (Ca+Sr)/P ratio of the solution during the synthesis of all these stoichiometric apatites was kept constant at the stoichiometric value of 1.67. The pH during the synthesis was maintained at 10 by addition of a 25 Vol.% NH₄OH solution. The formed precipitate was slowly filtered, washed with hot water and dried overnight at 80°C under static air before being calcined at 400°C, this temperature being reached at a rate of 2°C.min⁻¹, for 4 h under oxygen flow (2 L.h⁻¹).

In addition, deficient apatites were prepared using the same method but by maintaining the (Ca+Sr)/P ratio at 0.9 instead of 1.67 during the synthesis. Ca-deficient (**DAp**) and 100 mol.% Sr deficient apatites (**SrDAp-100**) were prepared by addition of 300 mL of 0.09 mol of Ca(NO₃)₂.4H₂O and Sr(NO₃)₂ respectively, to 1000 mL of a (NH₄)H₂PO₄

aqueous solution (0.1M). The 50 mol.% Sr-substituted apatite (**SrDap-50**) was obtained by adding a solution containing 0.045 mol of $\text{Ca}(\text{NO}_3)_2 \cdot 4\text{H}_2\text{O}$ and 0.045 mol of $\text{Sr}(\text{NO}_3)_2$ to 1000 mL of a $(\text{NH}_4)_2\text{H}_2\text{PO}_4$ aqueous solution (0.1M). The subsequent filtration/drying/calcination procedure was the same as above.

Table 2-1 Composition of the Ca and Sr in the solutions used for synthesis

| Sample name | x (mol) of strontium* | Sr substitution (%) ** | Comment |
|------------------|-----------------------|------------------------|---|
| HAp | 0 | 0 | Stoichiometric reference hydroxyapatite |
| SrAP-25 | 0.0418 | 25 | Stoichiometric 25 mol.% Sr substituted |
| SrAP-50 | 0.0835 | 50 | Stoichiometric 50 mol.% Sr substituted |
| SrAP-75 | 0.1253 | 75 | Stoichiometric 75 mol.% Sr substituted |
| SrAP-100 | 0 | 100 | Stoichiometric 100 mol.% Sr substituted |
| DAP | 0 | 0 | Deficient reference hydroxyapatite |
| SrDAP-50 | 0.045 | 50 | Deficient 50 mol.% Sr substituted |
| SrDAP-100 | 0.09 | 100 | Stoichiometric 100 mol.% Sr substituted |

*Total (Ca+Sr) is maintained at 0.167 mols for stoichiometric and at 0.09 mols for the deficient apatites.

** Ca and Sr together contribute to 100% in all the samples.

2.2 Physicochemical characterization techniques

Several techniques were used to determine the structural and textural properties of the catalysts, their elemental composition and their acid-base properties. Hereafter are detailed the experimental parameters used for each technique. If the reader needs complement of

information on the basics of each technique, they can be found at the annexes at the end of the document.

2.2.1 X-ray powder diffraction & Rietveld refinement

The XRD equipment used in our studies was a D8 Advance Bruker AXS powder diffractometer for studies at room temperature [Figure 2-2(a)], equipped with a copper tube ($K\alpha_{1,2}$, $K\alpha_1=1.54056 \text{ \AA}$) and a LynxEye Position Sensitive Detector. In our study, data were collected in the $10\text{-}90^\circ$ 2θ range with a step of 0.02° and a counting time of 1 s per step. High temperature XRD was also carried out on a D8 advanced Bruker AXS machine equipped with a HTK1200N high temperature chamber [Figure 2-2(b)] and connected to a VANTEC fast linear detector. Sample was deposited on a Pt sheet and experiment was performed by increasing temperature from 50°C to 1000°C acquiring a pattern every 25°C . For high temperature XRD, the data acquisition parameters were the following: an angular range of $10^\circ\text{-}70^\circ$ with a step of 0.015° and an acquisition time of 0.22 s per step. The phase identification was based on the comparison of the set of reflections of the sample with that of pure reference phases distributed by Joint Committee on Powder Diffraction Standards and International Center for Diffraction Data (JCPDS-ICDD). The unit cell parameters and crystallite size were determined using Rietveld refinement.

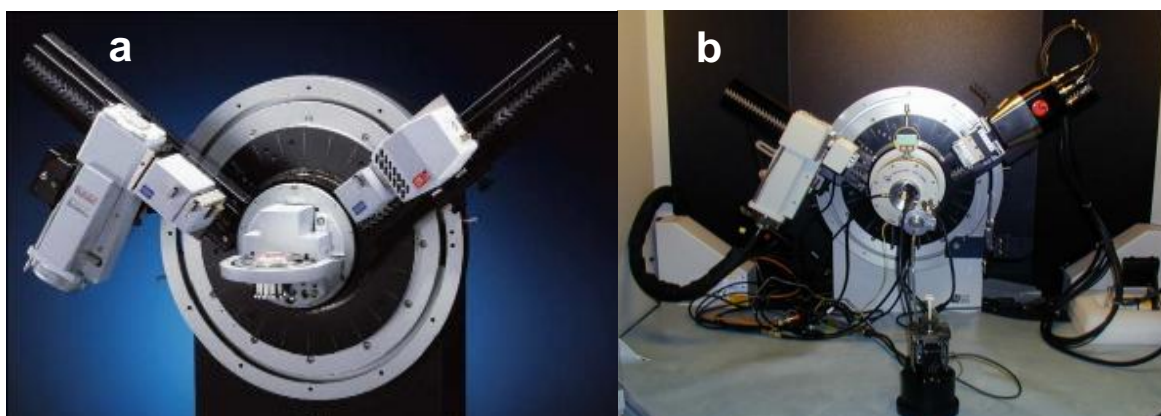


Figure 2-2 D8 Advance Bruker AXS diffractometers: (a) at room temperature and (b) equipped with high temperature chamber.

In 1969 Rietveld proposed a new technique for the analysis of powder diffraction data using the whole pattern fitting method [2,3]. The Rietveld method is really a powerful tool for the structural analysis of almost all types of polycrystalline materials. The method is based on the fact that the peak shapes of Bragg reflections and the changes in their peak width (FWHM) with the scattering angle 2θ , can be expressed analytically [4,5].

Peak-shape function, profile parameters and atomic and structural parameters are the three main parameters refined in the Rietveld method. The profile of the observed peak varies as a function of 2θ and is also a function of the sample and the instrument. The profile parameters comprise all the parameters including the lattice parameters and those parameters describing the shape and width of the diffraction peaks. The structural parameter explains the positions, types and occupancies of all the atoms in the structural model and also the isotropic or anisotropic thermal parameters. The change in the positional parameters can vary the magnitudes of structural factor and hence the relative peak intensities. Thermal parameters have the effect of emphasizing or de-emphasizing the high angle region. The scale, the occupancy parameters and the thermal parameters are connected to each other and they are more sensitive to the background correction compared to the positional parameters. Anisotropic refinement is sometimes possible using the thermal parameter refinement with neutron data. It is also difficult to refine occupancy parameters and chemical constraints should be applied if possible [4,6].

Once the structure is known and the right starting model is obtained, the Rietveld method allows the least-squares refinement (χ^2 minimization) of an atomic model together with an appropriate peak shape function. The Rietveld refinement of structural parameters can begin with good starting values of background contribution, the unit cell parameters and the profile parameters and with a complete structural model. The resultant profile fit and the values of the reliability factors (R-values) can provide an idea of the progress in a refinement. Profile and structural parameters must be refined simultaneously to acquire right estimated standard deviations and can be expressed numerically in terms of reliability factors or R-values [7]. Hence the R values are supposed to be useful indicators for the evaluation of refinement but they should not be over interpreted. There are two main criteria for predicting the quality of a Rietveld refinement; they are (1) the fitting of the calculated pattern to the observed data and (2) the chemical sense of structural model [4]. The software FullProf suite has been used in all our studies for the structural profile

refinement by Rietveld analysis [8]. The Thompson-Cox-Hastings pseudo-Voigt function was chosen for describing the peak profiles [9]. LaB₆ was used as standard to derive the instrument resolution i.e; the contribution of the instrument to the width of Bragg peaks. Expression of agreement factors are given below:

- the profile reliability factor : $R_p = \sum_i |y_i - y_{ci}| / \sum_i y_i$

where y_i is the intensity measured at $2\theta_i$ and y_{ci} is the calculated intensity.

- the weighted profile reliability factor

$$R_{wp} = \left[\frac{\sum_i w_i (y_i - y_{ci})^2}{\sum_i w_i y_i^2} \right]^{1/2} = \left[\frac{M}{\sum_i w_i y_i^2} \right]^{1/2}$$

where $w_i = 1/\text{var}(y_i)$, var_i , being the variance on the observed intensity (y_i) at step $2\theta_i$.

R_p and R_{wp} have to be compared to the expected reliability factor:

$$R_{\text{exp}} = \left[\frac{N - P + C}{\sum_i w_i y_i^2} \right]^{1/2}$$

where $N - P + C$ is the number of degrees of freedom, N is the number of points, P the number of refined parameters and C the number of strict constraint functions.

To attest the quality of the structural model, one must consider:

- The Bragg reliability factor :

$$R_{\text{Bragg}} = \sum_i \left| |I_{\text{obs}}| - |I_{\text{calc}}| \right| / \sum_i |I_{\text{obs}}|$$

- The Structure Factor reliability factor :

$$R_F = \sum_i \left| |F_{\text{obs}}| - |F_{\text{calc}}| \right| / \sum_i |F_{\text{obs}}|$$

The goodness of fit is given by:

$$\chi^2 = \left[\frac{R_{wp}}{R_{\text{exp}}} \right]^2 = \frac{\sum_i w_i (y_i - y_{ci})^2}{N - P + C} = \frac{M}{N - P + C}$$

2.2.2 Fourier transforms infrared spectroscopy (FT-IR)

For our studies, the FTIR sample preparation was done by grinding finely a quantity of the sample with a specially purified salt like potassium bromide to remove scattering effects from large crystals. This powder mixture is then pressed using a mechanical die to form a translucent pellet through which the IR radiation can pass. Spectra were recorded from 400 cm^{-1} to 4000 cm^{-1} at room temperature under vacuum in a Nicolet 460 Fourier transform infrared spectrometer. The samples were prepared by mixing properly 1 mg of powdered sample with 150 mg of dried KBr.

2.2.3 FT-Raman spectroscopy

The Raman spectra of the samples, were recorded at room temperature using a Labram infinity spectrometer (Horiba), equipped with a photodiode array detector cooled with liquid nitrogen. The exciting light source was the 532 nm line of an Nd:YAG laser and the wave number accuracy was $\pm 4\text{ cm}^{-1}$. Laser power was 12 mW and acquisition time was between 3 to 5 min. The Raman spectrometer was calibrated using the silicon line at 521 cm^{-1} . The spectra were collected between 200 and 1400 cm^{-1} .

2.2.4 Solid state nuclear magnetic resonance (NMR) spectroscopy

The most popular technique to get high-resolution NMR spectra is the magic angle spinning (MAS), where the solid sample is rotated very fast about an axis inclined at a "magic" angle $\theta = 54^{\circ}44'$ to the direction of B_0 [10]. This technique has been considered as the basis of solid state NMR. Cross polarization is routinely used for sensitivity improvement when measuring the solid state MAS NMR spectra of spin $I = 1/2$ nuclei (X). A fundamental RF pulse sequence and building-block in most of the solid-state NMR experiments starts with CP. It can be used to enhance the signal of less abundant nuclei (*e.g.* ^{13}C , ^{31}P , ^{15}N) by magnetization transfer from a high abundant nuclei (*e.g.* ^1H). To establish magnetization transfer, the RF pulses applied on the two frequency channels must

fulfill the Hartmann–Hahn condition. CP pulse sequence employ direct excitation of ^1H spin polarization followed by CP transfer to and signal detection of ^{13}C , ^{31}P , ^{15}N or similar nuclei as shown in Figure 2-3. By varying the contact time, it is possible to probe the less abundant nuclei located at different distances. [10].

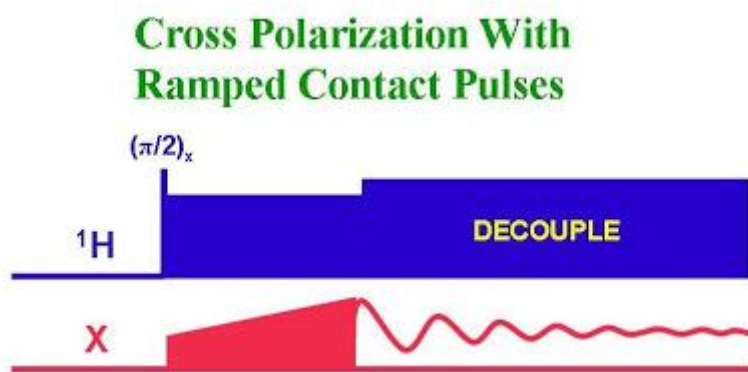


Figure 2-3 ^1H , X-CP MAS pulse sequence (X = ^{31}P , ^{13}C ,...).

With the development of more advanced spectroscopic methods as computational power has increased, it has become possible to obtain two dimensional spectra. Two dimensional nuclear magnetic resonance (2D NMR) is a set of NMR methods which provides data plotted in a space defined by two frequency axes rather than one and the spectra are plotted as a grid like a map. Two-dimensional NMR spectra provide more information about a molecule than one-dimensional NMR spectra and are especially useful in determining the structure of a molecule, particularly for molecules that are too complicated to work with using one-dimensional NMR. Cross Polarization Heteronuclear Correlation spectroscopy (CP HETCOR) gives signals based upon coupling between nuclei between two different types. Often one among the two nuclei is proton and other is heteronucleus like ^{31}P , ^{13}C etc. So the CP HETCOR spectra are usually plotted with proton NMR spectra on one axis and the ^{31}P or ^{13}C NMR spectra on the other.

All the 1D and CP HETCOR 2D NMR experiments were carried out using Bruker Advance spectrometer with ^1H Larmor frequency of 400 MHz (9.4 T). All the spectra were recorded at room temperature. The resonance frequencies of ^{31}P and ^{13}C were 161.9 and 100.6 MHz, respectively. A Bruker 4 mm CPMAS probe was used to perform all the

experiments and the spinning speed was 10 kHz. The chemical shifts were determined using TMS ($\delta = 0$ ppm) and H_3PO_4 ($\delta = 0$ ppm) as the reference compounds for ^1H and ^{31}P respectively. The contact time of 2ms was used for CPMAS and the contact times of 150 μs and 1ms were employed for CP HETCOR.

2.2.5 X-Ray photoelectron spectroscopy (XPS)

In this study, XPS analysis was performed by using XPS KRATOS, AXIS Ultra^{DLD} (Figure 2-4). Photoelectrons generated by a $\text{Al-K}\alpha$ X-ray source operating at 150 W (15 kV, 10 mA) having initial kinetic energies of up to 1486.69 eV, ensured an average depth for electron escape of $\sim 1\text{-}10$ nm. High resolution scans were acquired with 40 eV pass energy and 300 ms dwell times. All the resulting binding energy values were corrected using the C 1s peak (C-C) at 285 eV as a reference.



Figure 2-4 X-ray photoelectron spectrometer used for our studies.

2.2.6 Low-Energy Ion Scattering (LEIS)

In our studies, LEIS spectra were measured using a Qtac¹⁰⁰ spectrometer (ION TOF GmbH) [11]. Spectra were obtained using 3 keV and 6 keV ⁴He⁺ scattering. Assuming a sputter yield of 0.25 atoms per He-ion at a 4.3 nA target current at 3 keV, only $1.0 \times 10^{13} \text{ cm}^{-2}$ atoms are sputtered from the sample surface during the analysis (1% of a monolayer).

2.2.7 Induced Coupled Plasma (ICP)

ICP-MS was performed at the ‘Service Central d’Analyses du CNRS’ (Vernaison, France).

2.2.8 Scanning electron microscopy (SEM)

The Scanning Electron Microscope (SEM) images were taken on a Hitachi S 4700 equipped with micro-analysis (Energy-Dispersive X-ray Spectroscopy, EDS) and a field emission gun. The magnification of the microscope was kept at 20 K and 50 K for our studies.

2.2.9 Porosity measurements by nitrogen adsorption (BET)

For all our studies, N₂ adsorption-desorption was conducted using Micrometrics Tristar II apparatus at -196°C . Before analysis the samples were evacuated at 150°C for 4 h under vacuum and then the adsorption-desorption was conducted by passing nitrogen into the sample, which was kept under liquid nitrogen. BET model was used to calculate the specific surface area of the catalysts and the desorption isotherm of BJH model was used to determine the pore diameter and pore volume.

2.2.10 Temperature-Programmed Desorption (TPD)

There are different types of molecular probes for the characterization of a catalyst using TPD technique but two common probe molecules used to determine the chemical properties of the catalysts are NH_3 and CO_2 .

2.2.10.1 Temperature-Programmed Desorption of Ammonia (TPD- NH_3)

The density of acid sites in the samples was determined by temperature-programmed desorption (TPD) of NH_3 using a Micrometrics apparatus equipped with a mass spectrometer. 150 mg of sample were purged for 30 min in a He flow of $40 \text{ mL}\cdot\text{min}^{-1}$ at 400°C before being naturally cooled to room temperature. The sample was then contacted with a 10% NH_3/He atmosphere during 30 min in $30 \text{ mL}\cdot\text{min}^{-1}$ flow before being further purged for 2 h at room temperature under a $50 \text{ mL}\cdot\text{min}^{-1}$ He flow. After purging, the temperature was raised at a rate of $10^\circ\text{C}\cdot\text{min}^{-1}$ to 600°C in a $30 \text{ mL}\cdot\text{min}^{-1}$ He flow. The quantity of desorbed NH_3 was determined by mass spectrometry using the peak with $M/Z = 15$.

2.2.10.2 Temperature-Programmed Desorption of Carbon dioxide (TPD- CO_2)

The density of basic sites was similarly evaluated using TPD- CO_2 with 5% CO_2/He on the same micrometrics apparatus under the same conditions as those employed for TPD- NH_3 . The quantity of basic sites was determined by mass spectrometry using the peak located at $M/Z = 44$.

2.2.11 Thermo gravimetry & Differential Thermal Analysis (TGA/DTA)

Thermo gravimetric analysis (TGA) was performed using a Thermal Analysis instrument (TG92 Setaram) connected with a mass spectrometer (Omnistar), on 15 mg of sample. The

weight loss was recorded under synthetic air, at a heating rate of $10^{\circ}\text{C}\cdot\text{min}^{-1}$ from room temperature to 1000°C .

2.2.12 XPS after adsorption of 2-phenylethylamine (PEA-XPS)

PEA-XPS is a complementary technique to the TPD for determining the nature and distribution of acid sites over the catalyst surface by the adsorption of a probe molecule, namely 2-phenylethylamine (PEA) followed by XPS analysis [12,13]. PEA is a strong base that can be retained by weak, medium, and strong acid sites. However, the XPS measurements of PEA provide information only on the strong and medium acid sites and not on the weakest sites, which cannot hold the probe under the ultra-high vacuum conditions of the analyses. The PEA-XPS will give rise to a broad N 1s bands of BE in the range of ~ 396.5 to ~ 405.0 eV, which could be decomposed into two main peak indicating the presence of Brønsted sites and Lewis sites.

Prior to the adsorption, the calcined samples were outgassed at 250°C for 4 h under Ar flow. The cleaned powder was then transferred to a glass cell connected with vacuum/gas lines, and liquid PEA (purity $> 99\%$, purchased from Fluka) was introduced in the cell to cover up the powder during 2 h under an Ar flow. Then, the excess of non-adsorbed PEA was removed by filtration by primary vacuum using water pump in the presence of an Ar flow. The sample was then carefully transferred to the chamber of the spectrometer for analysis. PEA is a strong base that can be retained by weak, medium, and strong acid sites over solid surfaces. XPS analysis was then performed according to section 2.2.5 in this chapter. However, XPS measurements of PEA provide information only on the strong and medium acid sites and not on the weakest sites, which cannot hold this probe under the ultra-high vacuum conditions of the analyses, this latter being desorbed under such harsh conditions [12,13].

2.2.13 Reactor setup for isopropanol test

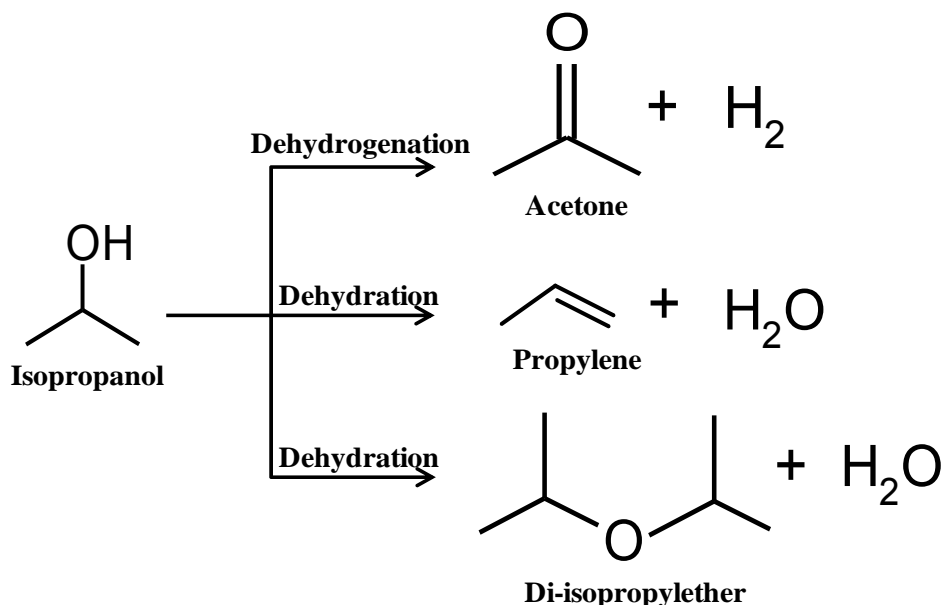


Figure 2-5 Scheme of isopropanol transformation reaction.

The acid-base properties of the hydroxyapatite catalysts have been determined by performing isopropanol decomposition test. As shown in Figure 2-5, isopropanol can be transformed to acetone by dehydrogenation on basic sites, and to propylene and di-isopropylether by, respectively, intra- and inter-dehydration on acid sites.

The isopropanol test has been performed using a setup consisting of mainly a saturator, a condenser; carrier gas supply, glass reactor and a gas chromatogram (GC) (Figure 2-6). Isopropanol was stored inside the saturator made of pyrex glass, which is connected to a condenser. He gas was bubbled at a rate of $25 \text{ mL}\cdot\text{min}^{-1}$ through the liquid isopropanol in the saturator and the formed vapours were sent to the reactor. The temperature of the condenser above the saturator was maintained at 10°C using a cryostat during the test. The isopropanol vapours were allowed to pass through the glass reactor resting inside a heating furnace, which controls the temperature of the reaction. As expected, the obtained products mainly consisted of acetone, propylene and di-isopropylether, which have been analysed using a GC (Alpha M.O.S-PR 2100).

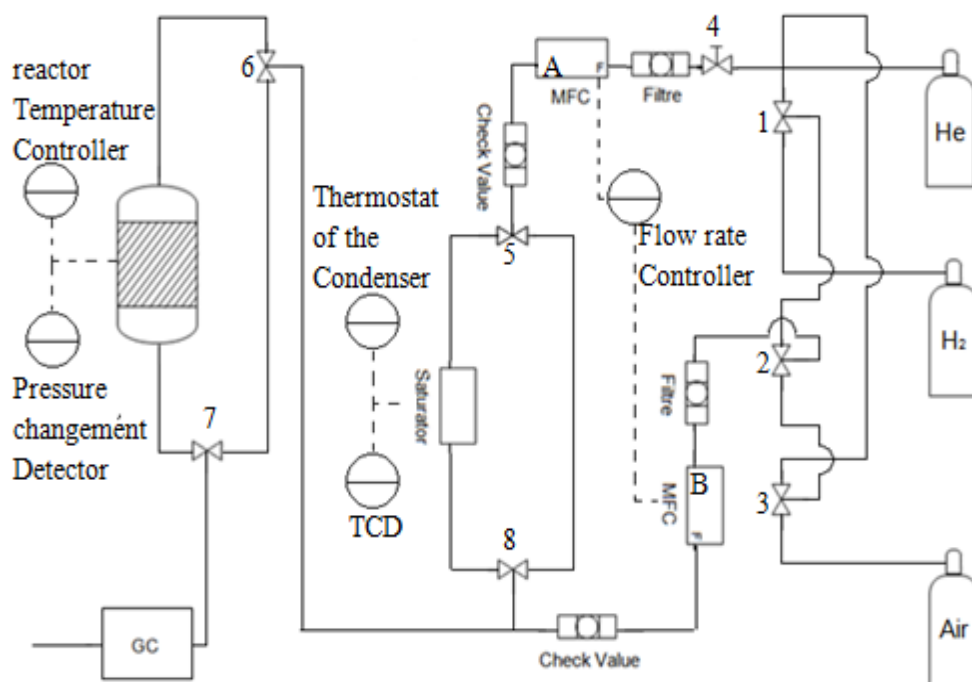


Figure 2-6 Reactor setup used for isopropanol test.

2.3 Reaction analytical techniques

2.3.1 Monoreactor setup employed for gas phase Guerbet reaction of ethanol

Figure 2-7 shows the monoreactor setup employed for the gas phase Guerbet reaction of ethanol. The entire setup is constituted of an ethanol feeding system, a reactor/furnace section and an analytical system. Ethanol (Merck, $\geq 99.8\%$) stored in a bottle lightly pressurized with Ar gas, was pumped using an HPLC pump (Gilson). The upflow rate of the pump has been maintained at $0.023 \text{ mL}\cdot\text{min}^{-1}$ to obtain 20 Vol.% of ethanol in a total flow of $50 \text{ mL}\cdot\text{min}^{-1}$. To reach a total flow rate of $50 \text{ mL}\cdot\text{min}^{-1}$, the ethanol was carried to an evaporating chamber heated at 120°C , where it got vaporized and mixed with the He carrier gas flowing at $40 \text{ mL}\cdot\text{min}^{-1}$. The ethanol vapours were then sent to the reactor system for the reaction.

The reactor system contained a fixed-bed glass reactor, which was placed inside a heating furnace. The glass reactor had an internal diameter of 12 mm and a sintered quartz present at its centre held the catalyst bed. In order to achieve a homogenous temperature distribution in the catalyst bed, a particular amount of catalyst was mixed with equal quantity of carborandum (Prolabo-120 μm). 500 mg of carborandum were further introduced above the catalyst bed to ensure homogeneity and to keep the catalyst bed in position. The entire glass reactor was placed inside the furnace, which was used to heat the catalyst bed during the reaction. Two thermocouples were used to measure the temperature during the reaction, the first one connected to the controller of heating furnace (regulation) and the other one near to the catalyst bed (reaction temperature).

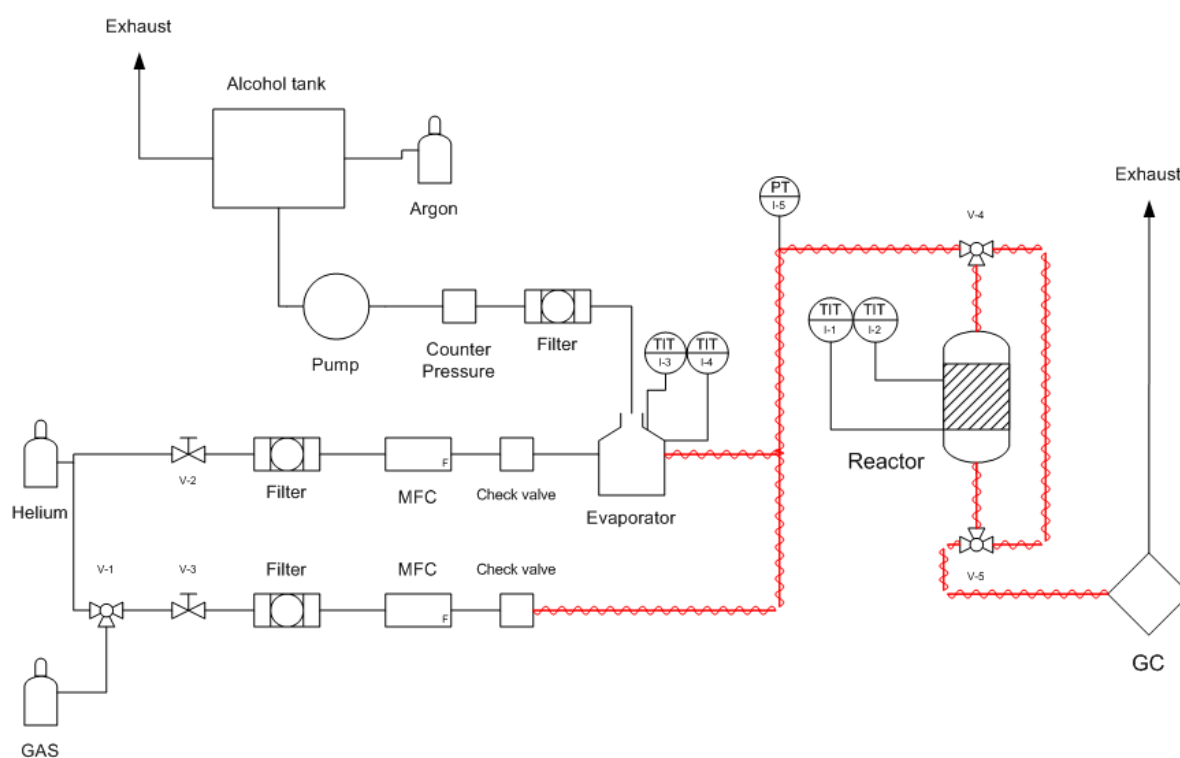


Figure 2-7 Monoreactor setup used for gas phase reaction of ethanol.

The temperature program was controlled using PC-controlled Eurotherm software. In short, during the reaction the ethanol was passed through the glass reactor filled with catalyst bed while controlling the temperature using the furnace. The outlet products were

then online carried to the Analytical system for online identification and quantification of the products.

The online analytical system consisted of a gas chromatogram (Agilent 7890A) followed by a mass spectrometer (Agilent 5975C). The products were separated using a Zebron ZB-Bioethanol column (length = 30 m, film thickness = 1 μm , internal diameter = 0.25 mm). The products thus separated were further split into two parts using a splitter, one part going to the Flame Ionization Detector (FID) and the other one to the MS. The signals obtained from the FID were used for the quantification of the products, whereas those obtained from the MS were used for the identification of the products.

2.3.2 Conditions employed for the catalytic test

As aforementioned, before each experiment, the hydroxyapatite catalyst was ground and sieved to a particle size in the 80-100 μm range. This powdered and sieved catalyst was then mixed with an equal quantity of carborandum (120 μm) and used as a catalyst bed followed by another layer of 500 mg carborandum to ensure thermal homogeneity and heat transfer inside the reactor. 20 Vol% ethanol in 40 $\text{mL}\cdot\text{min}^{-1}$ He (fixed total flow of 50 $\text{mL}\cdot\text{min}^{-1}$) were then used for the reaction. Krypton (5000 ppm in He) was used as an internal standard for the reaction analysis using MS. GHSV's of 15000 $\text{mL}\cdot\text{h}^{-1}\cdot\text{g}^{-1}$ and 5000 $\text{mL}\cdot\text{h}^{-1}\cdot\text{g}^{-1}$ have been obtained by using catalyst amounts of 200 mg and 600 mg, respectively.

Figure 2-8 shows the temperature programmed profile used for the reaction of ethanol. The inlet concentration of ethanol was measured by passing it through the reactor containing catalyst at 150°C. After reaching a stable ethanol feeding, the temperature was raised to 300°C at a rate of 5°C $\cdot\text{min}^{-1}$ and left for 5 h at this temperature. Temperature was then raised to 350°C and 400°C with a step each of 5 h duration.

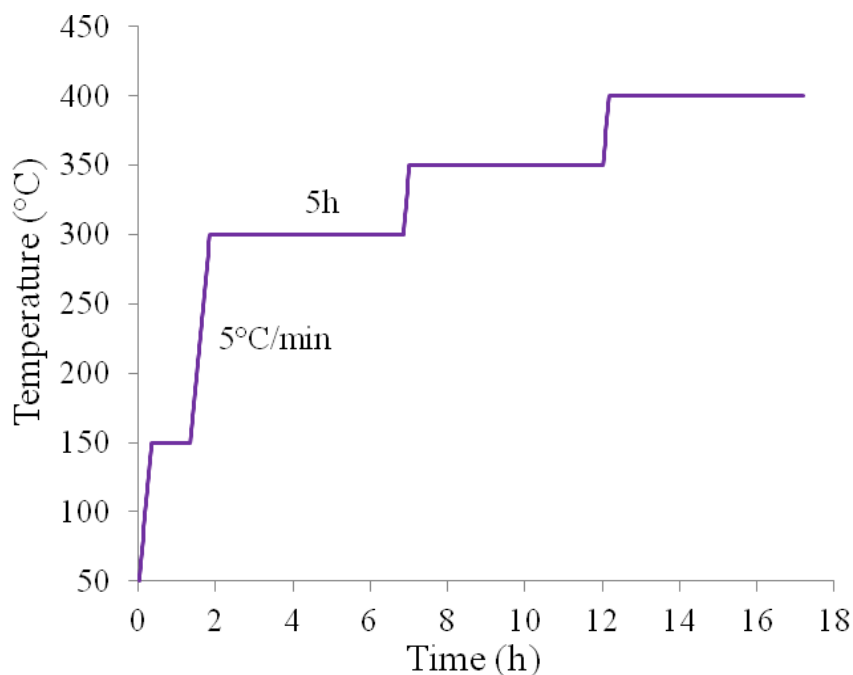


Figure 2-8 Temperature profile used for ethanol reaction.

2.3.3 Treatment of the catalytic test data

The products formed during the Guerbet reaction included liquid products such as aldehydes, alcohols, ethers, esters, etc., and gaseous products like light alkenes, butadiene, CO₂ etc. A chromatograph consisting of the main products for the ethanol reaction is shown in Figure 2-9. For performing the calibration of the so-formed liquid products, calibration solutions with three different concentrations (for each product) were prepared. A gas cylinder containing mixture of gaseous products with known concentration was used for the calibration of light gaseous products like CO, CO₂, CH₄, ethylene and butadiene. All the products were calibrated using the GC-MS and calibration curves were plotted after the integration of peaks resulting from the FID detector. Calibration curves for the light decomposition products like CO₂ and CO were plotted from the MS signals. The linear equation obtained from the calibration curves was used to quantify all the products and to calculate ethanol conversion, products selectivity and carbon balance.

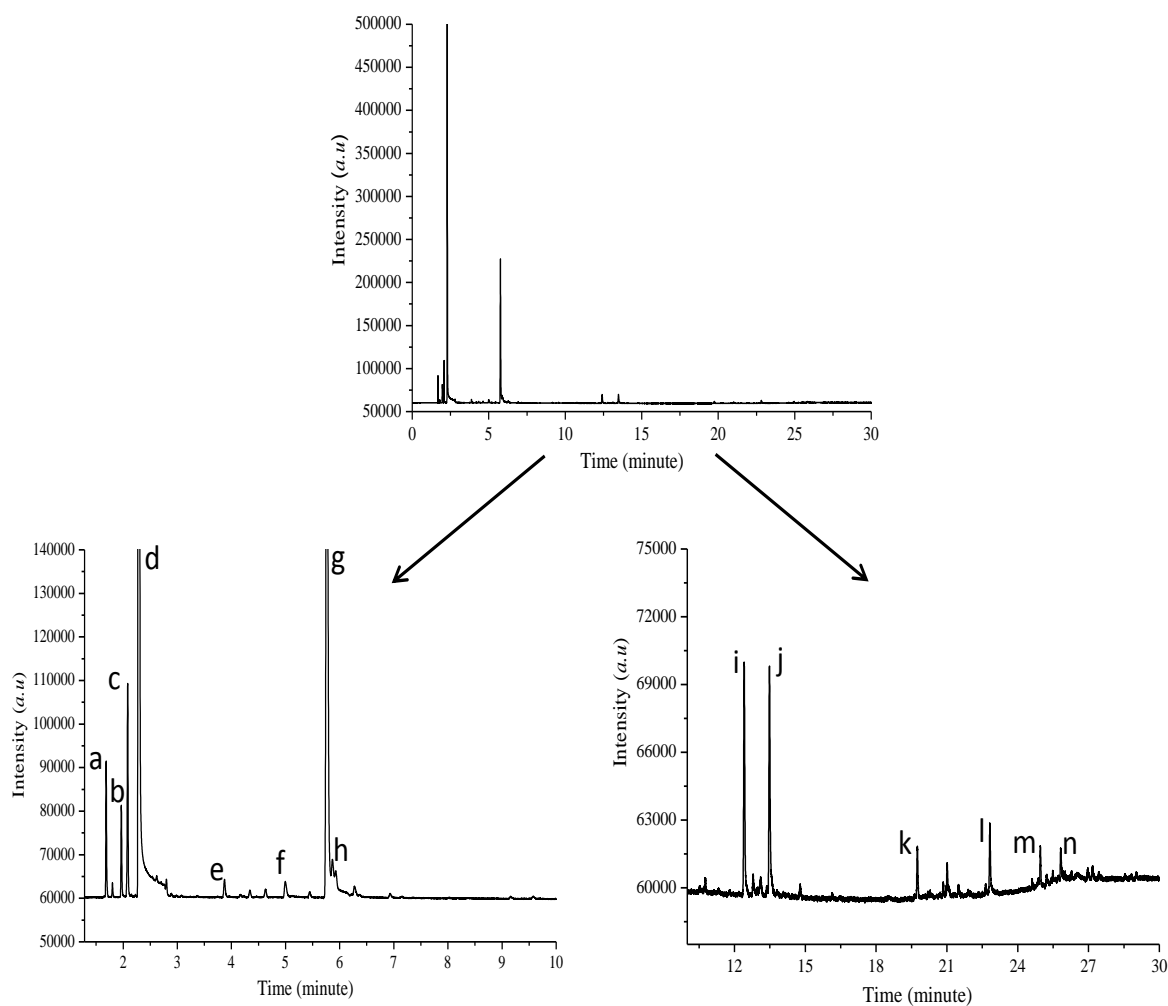


Figure 2-9 Chromatograph corresponding to FID signal for the Guerbet reaction of ethanol over Hap-CO₃ at 400°C and GHSV = 5000 mL.h⁻¹g⁻¹. (a= ethylene, b = acetaldehyde, c = 1,3-butadiene, d = ethanol, e = butyraldehyde, f = C6-diene, g = *n*-butanol, h = 2-buten-1-ol, i = 2-ethylbutanol, j = hexanol, k = 2-ethylhexanol, l = octanol, m = aromatic, n = decanol).

The conversion of ethanol was calculated by taking into account the initial number of moles of ethanol before reaction and the final number of moles of unreacted ethanol after reaction. The formula to calculate ethanol conversion is given below:

$$X = \frac{n_{Ei} - n_{Ef}}{n_{Ei}} \times 100$$

X = % Conversion;

n_{Ei} = Initial number of moles of ethanol (before reaction);

n_{Ef} = Final number of moles of ethanol (after reaction).

The selectivity of products formed during the reaction of ethanol was calculated using the following equation:

$$S_i = \frac{n_i * N_{ci}}{2 * (n_{Ei} - n_{Ef})} \times 100$$

S_i = Selectivity of product 'i' in %;

n_i = Number of moles of product 'i' formed;

N_{ci} = Number of carbon atoms in product 'i';

n_{Ei} = Initial number of moles of ethanol (before reaction);

n_{Ef} = Final number of moles of unreacted ethanol (after reaction).

The product yield calculated as follows:

$$Y_i = \frac{n_i * N_{ci}}{2 * n_{Ei}} \times 100$$

Y_i = Yield of product 'i';

n_i = Number of moles of product 'i' formed;

N_{ci} = Number of carbon atoms in product 'i';

n_{Ei} = Initial number of moles of ethanol (before reaction).

Finally, the carbon balance, which can be defined as the ratio of the sum of all the products including the unreacted ethanol of reaction outlet in terms of carbon number to the total number of moles of initial ethanol in terms of carbon number, was calculated according to the following formula:

$$CB = \frac{\sum_i (n_i * N_{ci}) + 2 * n_{Ef}}{2 * n_{Ei}} \times 100$$

CB = Carbon balance in %;

n_i = Number of moles of the outlet product 'i';

N_{ci} = Number of carbon atoms in the outlet product 'i';

n_{Ei} = Initial number of moles of ethanol (before reaction);

n_{Ef} = Final number of moles of unreacted ethanol (after reaction).

The value of the carbon balance helps to verify whether there are products which are not detected during the time of analysis and to confirm if there is any loss of products during the reaction. For example if there is any phenomenon like coking during the reaction, carbon balance will be lower than 100%.

-
- [1] C. Lamonier, J.-F. Lamonier, B. Aellach, A. Ezzamarty, J. Leglise, Specific tuning of acid/base sites in apatite materials to enhance their methanol thiolation catalytic performances, *Catalysis Today*, vol 164 (2011) p. 124-130.
- [2] H.M. Rietveld, A profile refinement method for nuclear and magnetic structures, *Journal of Applied Crystallography*, vol 2 (1969).p. 65-71.
- [3] H.M. Rietveld, Line profiles of neutron powder-diffraction peaks for structure refinement, *Acta Crystallographica*, vol 22 (1967) p. 151-152.
- [4] http://shodhganga.inflibnet.ac.in/bitstream/10603/710/8/08_chapter2.pdf.
- [5] J. Rodriguez-Carvajal, Recent advances in magnetic structure determination by neutron powder diffraction, *Physica B: Condensed Matter*, vol 192 (1993) p.55-69.
- [6] L.B. McCusker, R.B. Von Dreele, D.E. Cox, D. Louer, P. Scardi, Rietveld refinement guidelines, *Journal of Applied Crystallography*, vol 32 (1999) p. 36-50.
- [7] R.A. Young, *The Rietveld Method International Union of Crystallography*, Oxford University Press Inc (1993).
- [8] Rodríguez-Carvajal, J. Recent Developments of the Program FULLPROF, in Commission on Powder Diffraction International Union of Crystallography, Newsletter 26 (2001) 12-19.
- [9] P. Thomson, D.E. Cox, J.B. Hastings, Rietveld Refinement of Debye-Scherrer Synchrotron X-ray Data from Al₂O₃, *J. Appl. Cryst.* (1987). 20, 79-83.
- [10] G. Engelhardt, Handbook of Heterogeneous Catalysis, (G. Ertl, H. Knozinger, J. Weitkamp, eds) *Wiley-VCH, Weinheim*, vol 2 (1997) p. 525.
- [11] H.H. Brongersma, T. Grehl, P.A. van Hal, N.C.W. Kuijpers, S.G.J. Mathijssen, E.R. Schofield, R.A.P. Smith, H.R.J. ter Veen, High-sensitivity and high-resolution low-energy ion scattering, *Vacuum*, vol 84 (2010) p. 1005-1007.
- [12] A. Gervasini, A. Auroux, C. Guimon, Acidic Character of Metal-Loaded Amorphous and Crystalline Silica-Aluminas determined by XPS and Adsorption Calorimetry, *Journal of Physical Chemistry B*, vol 103 (1999) p. 7195-7205.
- [13] A. Gervasini, C. Messi, D. Flahaut, C. Guimon, Acid properties of iron oxide catalysts dispersed on silica-zirconia supports with different Zr content, *Applied Catalysis A: General*, vol 367 (2009) p. 113-121.



Chapter 3 Characterization & Reactivity of Hydroxyapatite-Based Catalysts with Various Carbonate Contents

3.1 Introduction

Natural hydroxyapatite (HAP), $\text{Ca}_{10}(\text{PO}_4)_6(\text{OH})_2$, the main inorganic constituent of biological hard tissues in animal organisms, is the most stable calcium phosphate salt. It can be synthesized at various temperatures and at a pH between 4 and 12. HAP contains both acid and basic sites in a single crystal lattice [1,2], and can thus be applied to reactions demanding bifunctional solid catalysts containing both antagonist functionalities, such as the Guerbet reaction [3], the Michael addition, the Knoevenagel condensation [4], the Claisen-Schmidt condensation or the Friedel-Crafts reaction [5]. The aforementioned native HAP authorizes large variations in compositions, and, as a general matter, the so-called 'HAPs' are highly non stoichiometric with the general formula ' $\text{Ca}_{10-x}(\text{PO}_4)_{6-x}(\text{HPO}_4)_x(\text{OH})_{2-x}$ ', with $0 < x \leq 1$. This yields a family of compounds with very different properties, with more acidic solids in the case of deficient HAPs ($x > 0$) to solids more and more basic when approaching the stoichiometry of the native HAP ($x = 0$), this latter being, therefore, predominantly basic [6,7,8]. The structure of HAP is flexible to both cationic and anionic substitutions, which yields the aforementioned possibility of modulating the number of acid-base sites in the HAP crystal. Cations can substitute either Ca (I) or Ca (II) ions or both ions simultaneously, and anions can replace either OH^- or PO_4^{3-} ions or both [9]. For example, the CO_3^{2-} anions can substitute for OH^- (A-type) or/and PO_4^{3-} (B-type) ions. The general formula for carbonate containing apatites, in which CO_3^{2-} ions can be located in two different positions, is $\text{Ca}_{10}[(\text{PO}_4)_{6-x-y}(\text{HPO}_4)_x(\text{CO}_3)_y][(\text{OH})_{2-(x+y)}(\text{CO}_3)_{x+y}]$, considering that the charge loss due to the PO_4^{3-} substitution is counterbalanced by addition of CO_3^{2-} in the A-site [10]. If some defects arise due to the formation of vacancies or related substitution of Ca by Na, charge will be compensated by less carbonates in A-sites. After introduction of both Na^+ and CO_3^{2-} ions to hydroxyapatites, the chemical formula can further be represented by $\text{Ca}_{10-v}\text{Na}_w[(\text{PO}_4)_{6-x-y}(\text{HPO}_4)_x(\text{CO}_3)_y][(\text{OH})_{2-(x+y)}(\text{CO}_3)_{x+y-v-w/2}]$.

Ueda *et al.* have studied the effect of Ca/P ratio of the hydroxyapatite on Guerbet reaction of ethanol [11]. They reported that the acid-base properties change by varying the Ca/P

ratio and the products distribution are strongly correlated to the acid-base properties of the hydroxyapatite. So a precise tuning of acid and basic sites in hydroxyapatite is required to yield a trade-off between the ethanol conversion and products selectivity. Even though there are few reports on ethanol condensation reaction over Ca (Sr)-HAP with different Ca (Sr)/P ratio [11,12], no studies have been reported to our knowledge for Guerbet reaction of ethanol over CO_3^{2-} modified HAP with Ca/P ratio higher than stoichiometric value 1.67.

In the present chapter, using XRD & Rietveld refinement as well as TGA, we precisely determined the crystallite nature and the global formula of HAPs prepared with varying the Ca/P ratio or the carbonate content. Further, LEIS was used to precisely determine the surface composition of the solids, to then check about a potential correlation with the crystallites growth/morphology. Total number of acid sites and basic sites in HAPs were determined by TPD- NH_3 and TPD- CO_2 , respectively. We also determined the distribution of the nature of the surface acid sites (Lewis & Brønsted) by XPS after adsorption of 2-phenylethylamine (PEA) used as a probe molecule [13,14]. The surface acid-base properties were further evaluated using isopropanol reactivity. A correlation study was done between the Guerbet reaction and acid-base properties of the obtained by the aforementioned characterizations, before optimizing the reaction conditions for producing a mixture of higher alcohols.

3.2 Results and discussion

3.2.1 Characterization of the solids

3.2.1.1 Bulk composition of the solids

It is known that the Ca/P atomic ratios obtained by chemical analysis of the final solids differ from those of the solutions used during the synthesis [15,16]. The Ca/P atomic ratios of all the prepared samples (see Table 3-1) were lower than their Ca/P molar ratios in the solutions, except for the deficient and the stoichiometric apatites, namely HapD and Hap. Indeed, for HapD and Hap, the Ca/P atomic ratios in the solid were 1.62 and 1.69, respectively, compared with 0.9 and 1.67 fixed during the synthesis. The chemical compositions of the solids further show that an increase in the Ca/P ratio was accompanied

with a linear increase in the carbon content (Figure 3-1). This can be due to the introduction of carbon under the form of carbonate ions in the apatite structure, which replace the phosphate ions.

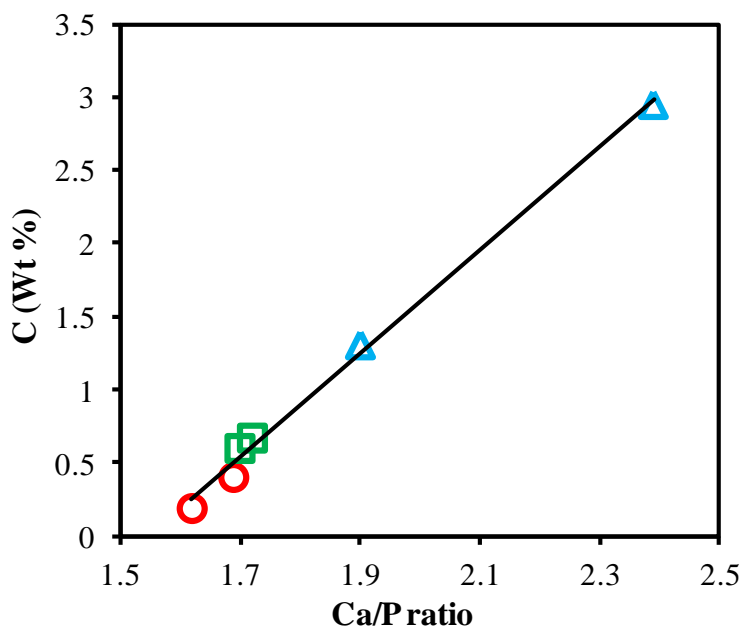


Figure 3-1 Carbon content as a function of the bulk Ca/P ratio of the solids (red circles representing HapD and Hap, green squares for carbonated apatites, namely Hap-CO₃ and HapNa-CO₃, and blue triangles for carbonate-rich apatites, namely HapE-CO₃ and HapE-Na-CO₃).

3.2.1.1 Specific surface areas

The specific surface areas of all the calcined solids were larger than 100 m².g⁻¹, except for the carbonates-rich apatites, namely HapE-CO₃ and HapE-Na-CO₃, with 76 and 72 m².g⁻¹, respectively (Table 3-1). Hence, this simple preparation method carried out in open atmosphere provided apatites with high surface areas, which decreased a little bit when introducing CO₃²⁻ ions in the case of carbonate-rich solids.

Table 3-1 Chemical composition and specific surface area of the prepared solids calcined at 400°C.

| Type of solid | Name | Ca/P molar ratio in solutions | Ca (wt.%) | P (wt.%) | Na (wt.%) | C (wt.%) | Ca/P atomic ratio | Specific surface area (m ² .g ⁻¹) |
|----------------|-------------------------|-------------------------------|-----------|----------|-----------|----------|-------------------|--|
| Deficient | HapD | 0.9 | 37.06 | 17.69 | - | 0.18 | 1.62 | 124 |
| Stoichiometric | Hap | 1.67 | 38.45 | 17.54 | - | 0.40 | 1.69 | 114 |
| Carbonated | Hap-CO ₃ | 2.0 | 38.10 | 17.29 | - | 0.59 | 1.70 | 107 |
| Carbonated | HapNa-CO ₃ | 2.0 | 38.17 | 17.14 | 0.64 | 0.67 | 1.72 | 109 |
| Carbonate-rich | HapE-CO ₃ | 5.5 | 37.03 | 15.04 | - | 1.30 | 1.90 | 76 |
| Carbonate-rich | HapE-Na-CO ₃ | 5.5 | 39.47 | 12.75 | <0.3 | 2.95 | 2.39 | 72 |

3.2.1.3 Structure of the solids

3.2.1.3.1 Crystallographic structure

All the X-ray diffraction patterns suggested only the presence of the crystalline hydroxyapatite phase (JCPDS 01-086-074) with small differences in Bragg peak positions (Figure 3-2). A small shift of the (3 0 0) Bragg peak towards higher 2θ values associated to a better crystallinity was observed when the carbonate content increased from HapD ($2\theta = 32.8^\circ$) to HapE-Na-CO₃ ($2\theta = 33.4^\circ$).

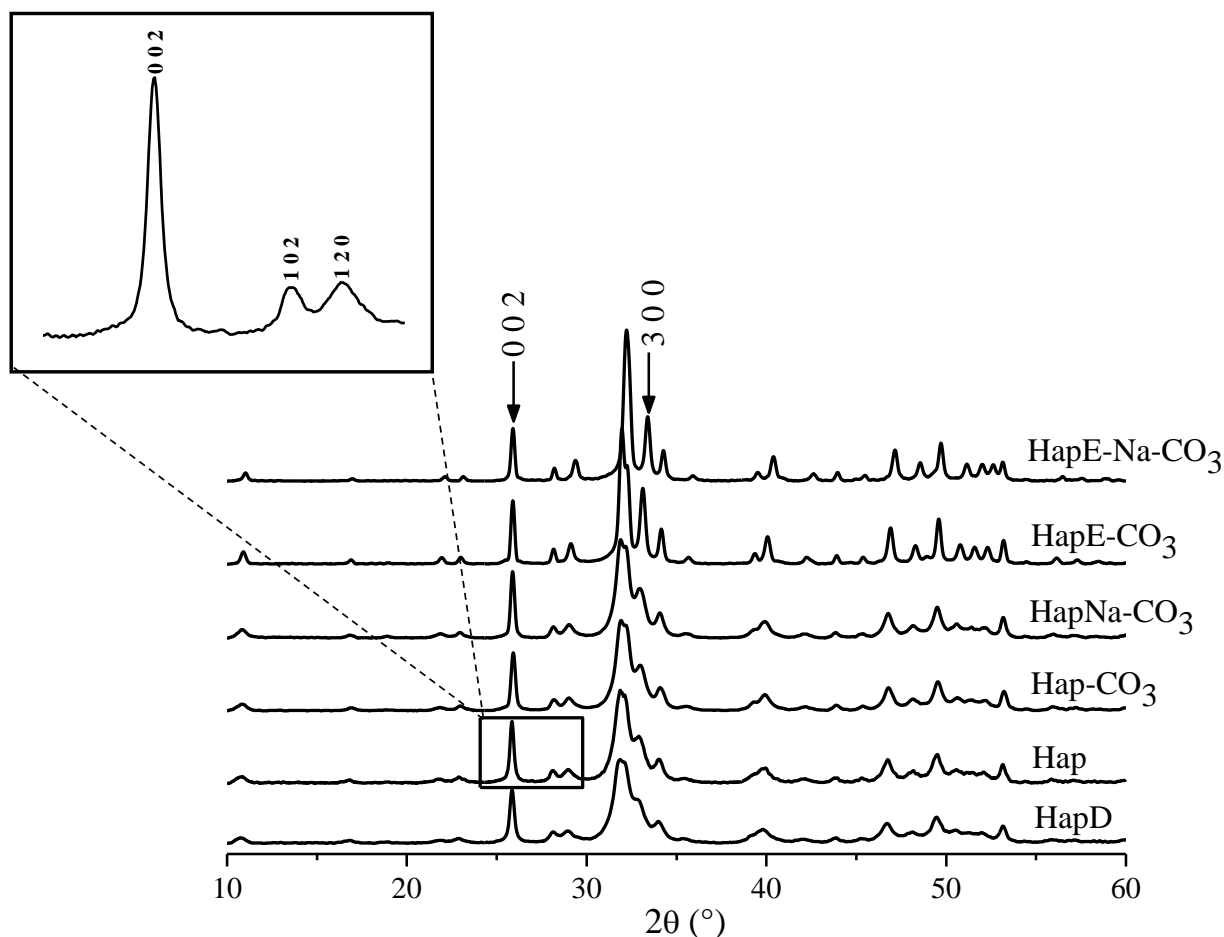


Figure 3-2 XRD patterns of calcined solids.

The apatite structure was refined in the $P6_3/m$ space group, using the structural model proposed by Hughes *et al.* [17]. The atomic positions of all the atoms were refined. To take into account the thermal vibrations, an overall parameter was used for all the crystallographic sites. For all the samples, the XRD pattern showed a thinner Full Width at Half Maximum (FWHM) for the (0 0 2) reflection compared to the FWHM of the other reflections (see inset in Figure 3-2), indicating the presence of anisotropic crystallites. Therefore, an anisotropic size-broadening model based on linear combination of spherical harmonics was used to simulate the size broadening [18], taking into account the instrument resolution from a LaB_6 pattern. From this model, the crystallites shape was deduced. As shown as an example in Figure 3-3 for Hap and HapE-Na- CO_3 , a good agreement was obtained between the calculated and the experimental data in all the solids.

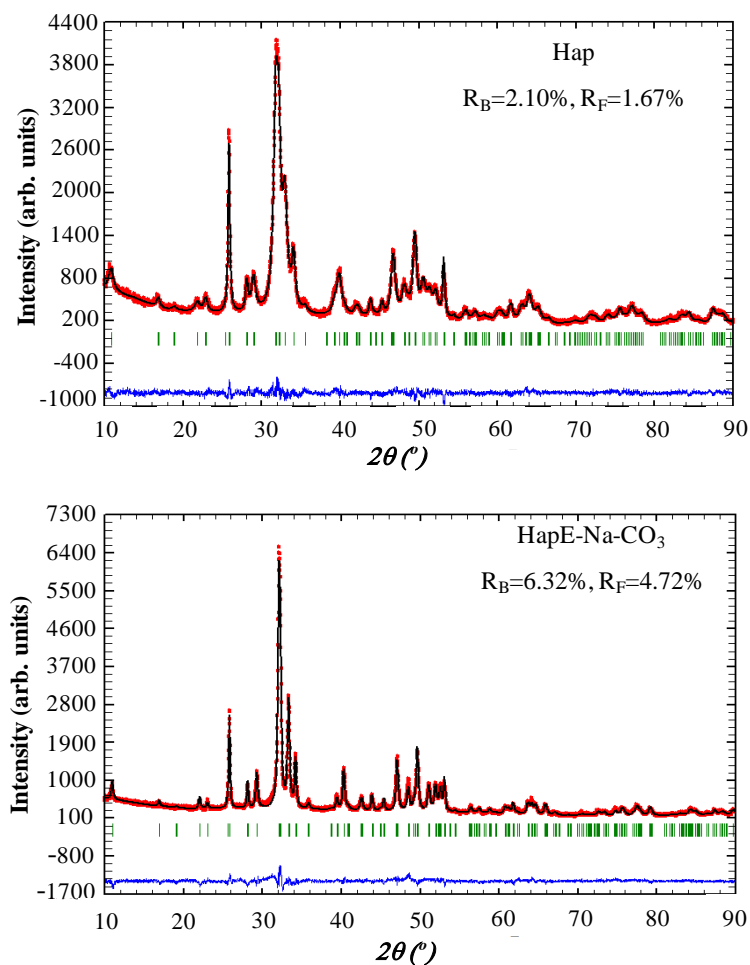


Figure 3-3 Calculated X-ray diffraction profiles of Hap and HapE-Na-CO₃ samples (black lines) compared to experimental data (red dots) showing a good agreement between calculated and experimental profiles as shown by the difference in blue. R_B and R_F , the reliability factors, are given to attest of the quality of the structural model.

Unit-cell parameters and crystallite size corresponding to (1 0 0) and (0 0 1) crystallographic planes thicknesses are given in Table 3-2. As expected, a decrease in the ‘ a ’ values with increasing carbonate content from 9.4210(4) Å in HapD to 9.3112(2) Å in HapE-Na-CO₃ was observed except for Hap, which showed a lower ‘ a ’ value compared to Hap-CO₃. This observation is in good agreement with the partial substitution of phosphate groups by carbonate ions, as previously reported [19,20,21]. In contrast, an increase in the carbonate content led almost to no evolution of the ‘ c ’ values, which correspond to the stacking direction of the apatite structure. Nevertheless, a slight increase in ‘ c ’ values was observed for the sodium-containing samples (HapNa-CO₃ & HapE-Na-CO₃), as already reported for sodium-substituted apatites compared to pure Hap [21,22].

Table 3-2 Cell Parameters, phosphorus occupancy and crystallite size determined using Rietveld refinement.

| Solids | Cell Parameters | | Phosphorus site occupancy (%) | (Ca + Na)/P [ICP] | Crystallite size (nm) corresponding to crystallographic plane | | |
|-------------------------|-----------------|--------------|-------------------------------|-------------------|---|---------|-----------------|
| | <i>a</i> (Å) | <i>c</i> (Å) | | | (1 0 0) | (0 0 1) | (0 0 1)/(1 0 0) |
| HapD | 9.4210(6) | 6.8853(4) | 97.0(4) % | 1.72(5) [1.62] | 7 | 22 | 3.2 |
| Hap | 9.4103(5) | 6.8871(4) | 94.6(4) % | 1.76(2) [1.69] | 8 | 26 | 3.2 |
| Hap-CO ₃ | 9.4142(5) | 6.8876(4) | 93.8(4) % | 1.77(2) [1.70] | 9 | 30 | 3.3 |
| HapNa-CO ₃ * | 9.4106(6) | 6.8909(4) | 93.8(4) % | 1.78(2) [1.77] | 10 | 36 | 3.6 |
| HapE-CO ₃ | 9.3742(5) | 6.8891(4) | 89.4(4) % | 1.87(2) [1.90] | 23 | 55 | 2.4 |
| HapE-Na-CO ₃ | 9.3111(8) | 6.8982(6) | 78.6(4) % | 2.12(2) [2.39] | 23 | 41 | 1.8 |

* Na occupancy was refined in the case of HapNa-CO₃ (see text)

N.B. Standard deviation for unit cell parameters, phosphorous occupancy and (Ca + Na)/P ratio are given in brackets by taking into account the Berar factor [23].

While structural models have been proposed for carbonate-containing apatites [20], because of the too low X-Ray scattering length of carbon atoms, it was not possible here to refine the carbonate positions. However, we could confirm the partial substitution of phosphate groups by refining the occupancy of phosphorous sites, thereby indirectly determining the occupancy of carbonates from the vacancies in the phosphorous sites. The phosphorous vacancies were then refined for all the compositions (see Table 3-2, P occupancy). As expected, the refinements led to the lowest phosphorous occupancies of 89.4(4)% and 78.6(4)%, respectively in the carbonate-rich HapE-CO₃ and HapE-Na-CO₃ samples, compared to the other apatites. This reveals the presence of higher amounts of carbonates in the phosphorous sites of carbonate-rich apatites, which is in good agreement with the introduction of carbonates in the P sites (B-type apatite sites). It was not possible to refine Na occupancy in the calcium site of HapE-Na-CO₃, in good agreement with the low sodium amount observed by ICP. In the case of HapNa-CO₃, introduction of sodium in the Ca (I) site led to a small occupancy corresponding to 0.18(9) Na for 9.82 calcium atoms in the apatite, in rather good agreement with the sodium amount measured by ICP

(0.28). Moreover, introduction of Na in Ca (II) site led to a negative occupancy indicating a preference of Na for the Ca (I) site and therefore, in the refinement, sodium was introduced only in the Ca (I) site. For the deficient apatite (HapD), refinement of calcium sites occupancies led to unrealistic values, which were higher than ‘1’. Therefore, the calcium occupancy was fixed to 1, and it was thus not possible to confirm the calcium deficiency only using X-ray diffraction. Moreover, for this composition, a phosphorous occupancy of 97.0(4)% was obtained, suggesting the presence of a small amount of carbonates in the B sites. As a general matter, the refined (Ca + Na)/P ratios were in rather good agreement with the ICP analysis. Figure 3-4 shows that the (Ca + Na)/P ratio refined from XRD data increased linearly with the same ratios determined by ICP. However, the XRD ratios exhibited slight deviation from the ideal ICP ratio especially for HapE-Na-CO₃ with higher (Ca + Na)/P ratio compared to the other apatites. This deviation is likely due to the limited accuracy on the phosphorus occupancy, since the overall parameter was used in refinement for all the crystallographic sites and thermal vibrations and occupancies in such refinement are strongly correlated.

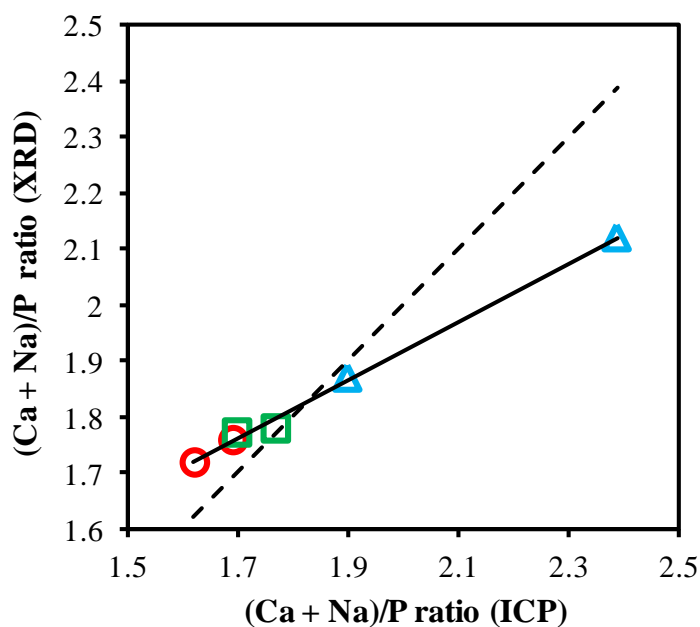


Figure 3-4 Variation in (Ca + Na)/P ratio from XRD as a function of (Ca + Na)/P ratio from ICP (red circles representing HapD and Hap, green squares for carbonated apatites, namely Hap-CO₃ and HapNa-CO₃, and blue triangles for carbonate-rich apatites, namely HapE-CO₃ and HapE-Na-CO₃). The dashed line represents the theoretical perfect correlation (1 to 1).

3.2.1.3.2 Crystallites & grain shape

As aforementioned, an anisotropic size-broadening was used to deduce the crystallites size. The crystallite size along the (1 0 0) and (0 0 1) planes, determined by Rietveld refinement, indicated that the crystal growth increased with an increase in the Ca/P ratio or carbonate content (Table 3-2). The crystallite size was much higher for carbonate-rich HapE-CO₃ (23 nm & 55 nm) and HapE-Na-CO₃ (23 nm & 41 nm) when compared to stoichiometric Hap (8 nm & 26 nm). The length/thickness ratio of Hap and HapD was identical (3.2), indicating similar crystallite shapes. Moreover, when the apatites richer in carbonate are considered, the length/thickness ratio was lower (2.4 & 1.8) compared to the stoichiometric apatite (3.2), indicating that the crystallites became more spherical for carbonate-rich apatites (Table 3-2). The length/thickness ratio was higher for carbonated apatites Hap-CO₃ (3.3) and HapNa-CO₃ (3.6), which is an indication of the presence of elongated crystallites in carbonated apatites compared to all the other apatites.

To verify whether the crystallite shapes obtained by Rietveld refinement have an influence on the grain shape, Scanning Electron Microscopy images were taken. The anisotropy observed by XRD was confirmed by SEM (Figure 3-5). Irregularly shaped agglomerates were observed for stoichiometric (Hap) and deficient apatites (HapD), while flat needle/rod-shaped clusters were observed for the carbonated apatites Hap-CO₃ and HapNa-CO₃. The pictures also revealed capsule and spherically shaped grains for HapE-CO₃ and HapE-Na-CO₃, respectively. In all the cases, the grain shapes were thus in good agreement with the crystallite shape determined by refinement from XRD diffractograms. However, using SEM, bigger particles with length in the order of 100 μm were observed, indicating polycrystalline grains.

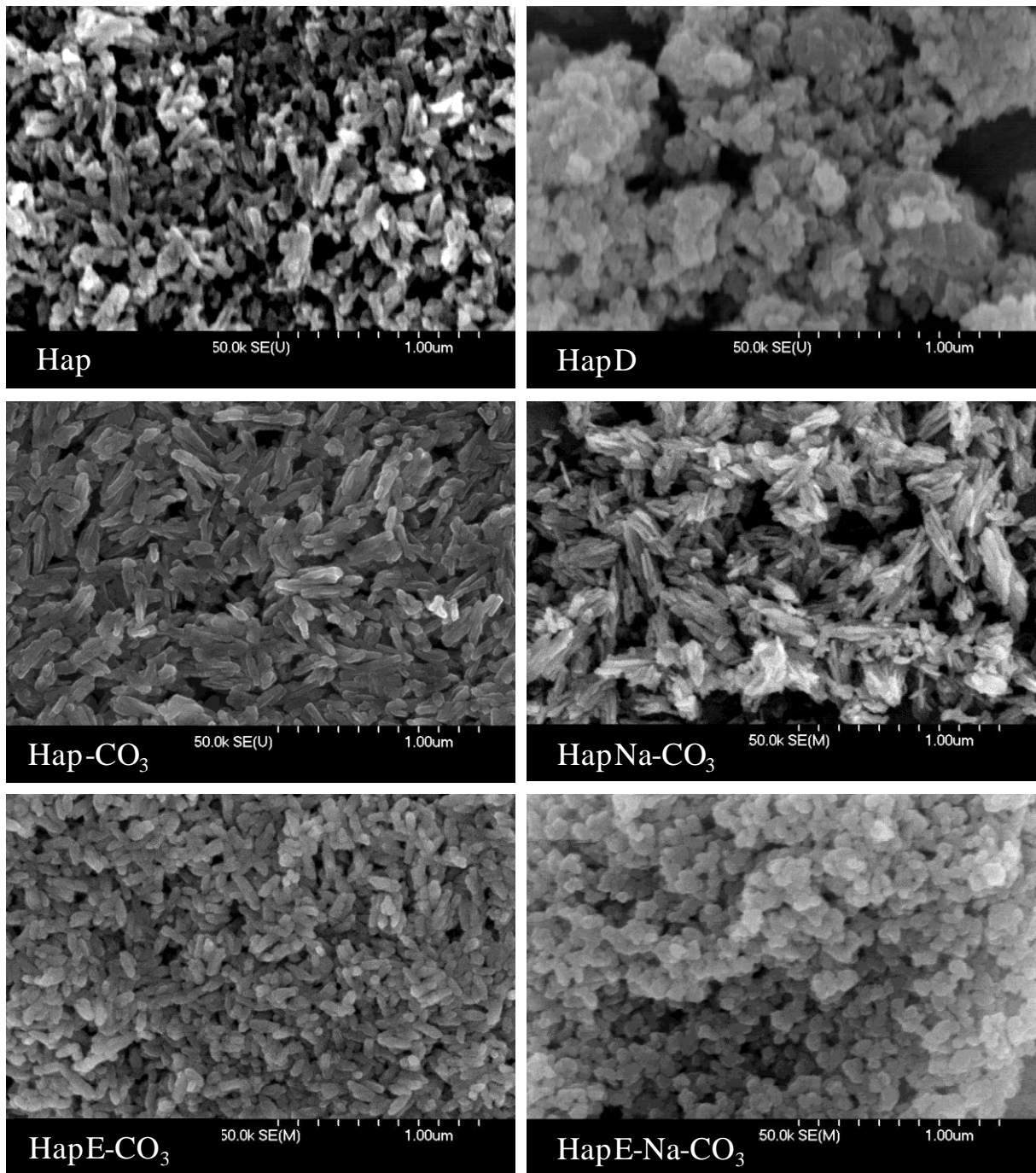
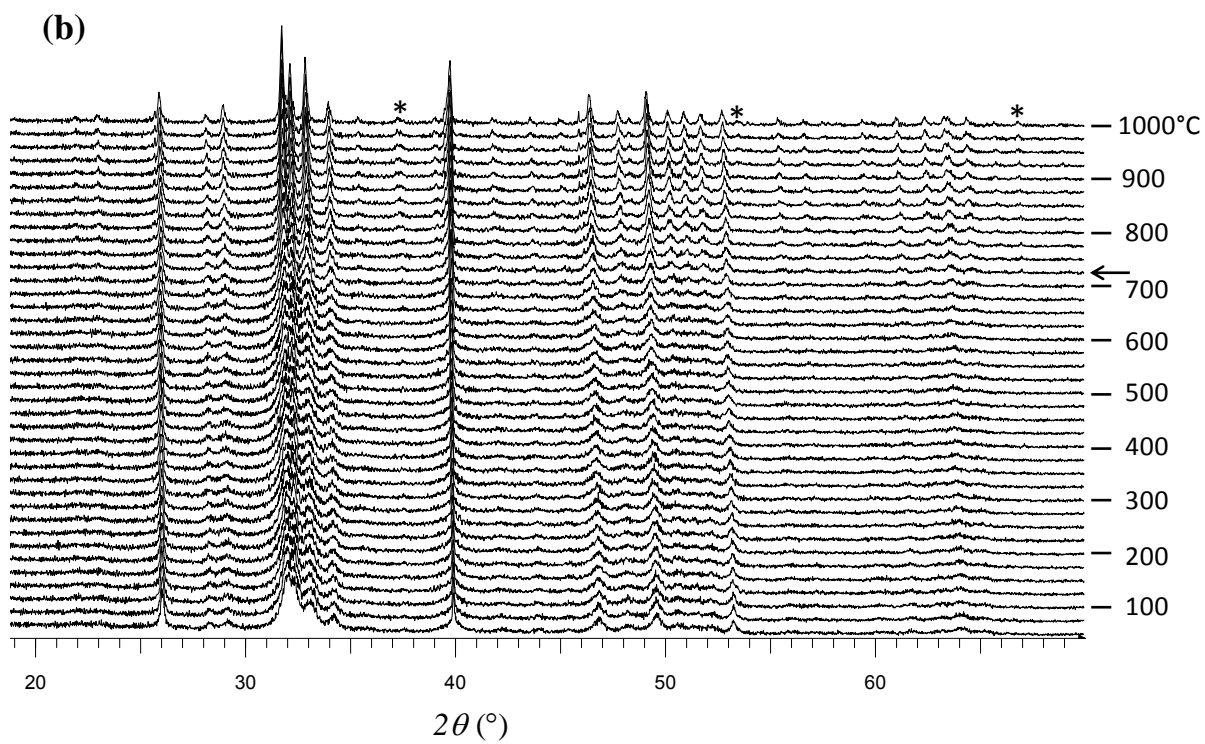
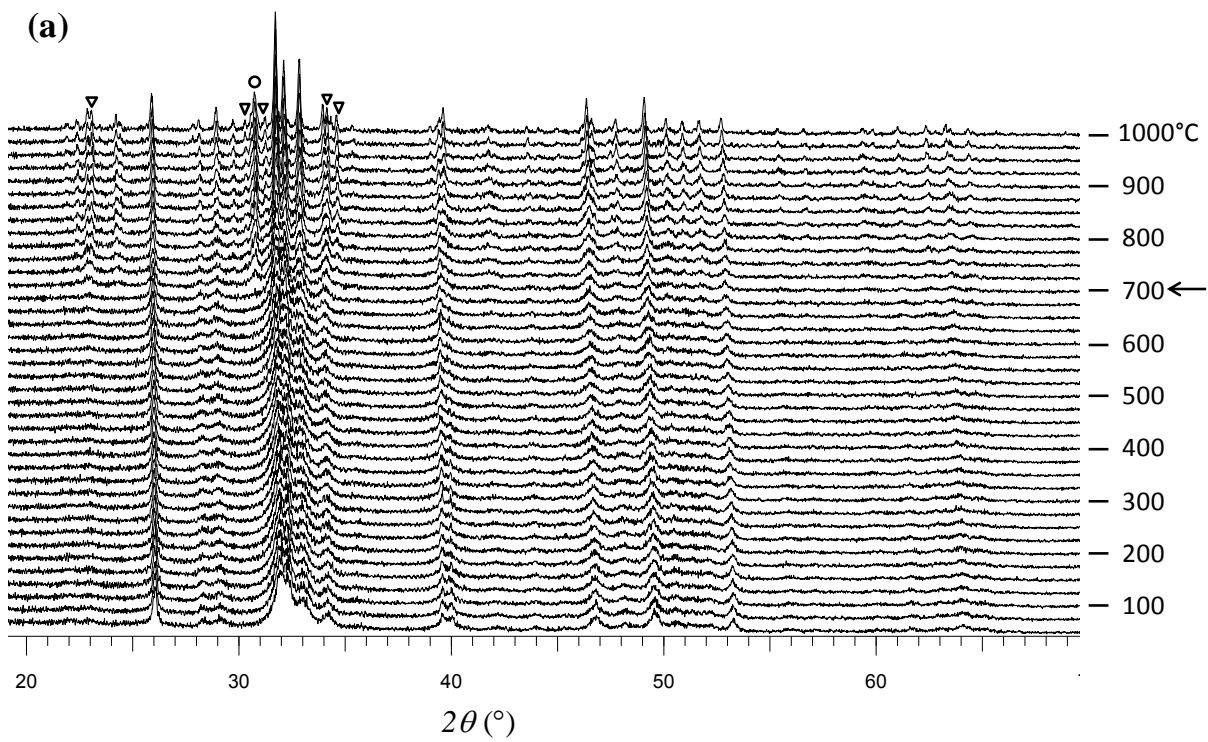


Figure 3-5 SEM images of calcined samples at 50.0 k magnification.

3.2.1.3.3 Thermal stability and carbonate content in the prepared solids

To check the thermal stability of the apatite solids, X-ray diffraction spectra were recorded upon temperature increase at variable temperature, carried out on 3 selected compositions, namely HapD (a deficient apatite), Hap-CO₃ (carbonated apatite very similar to Hap and

HapNa-CO₃), and HapE-Na-CO₃ (a carbonate-rich apatite, similar to HapE-CO₃). The deficient apatite HapD was chosen, since it is supposed to decompose to stoichiometric apatite (Hap-like) and Ca₃(PO₄)₂ [24,15], whereas all the other apatites with Ca/P ratio higher than 1.67 should decompose to stoichiometric apatite and CaO [15]. The so-obtained series of X-ray patterns are given in Figure 3-6. As expected, HapD decomposed to stoichiometric apatite and Ca₃(PO₄)₂ with the appearance of two forms of Ca₃(PO₄)₂, namely α -Ca₃(PO₄)₂ (JCPDS 01-070-0364) and *syn*-Ca₃(PO₄)₂ (JCPDS 00-009-0169), at 700°C [Figure 3-6(a)]. Compared to normal stoichiometric apatites (Ca/P = 1.67), Ca₃(PO₄)₂ formed from deficient HapD exhibits a smaller Ca/P ratio of 1.5 and the formation of Ca₃(PO₄)₂ is thus an indirect proof of calcium deficiency in HapD. In contrast, for temperatures higher than 725°C, the formation of calcium oxide was observed for Hap-CO₃, and the same transformation was noticed at 625°C for HapE-Na-CO₃ for which, in addition, a slight modification of the X-ray pattern was noticed at 550°C [Figure 3-6(c)]. It was characterised by a decrease in intensity and an increase in the FWHM of the (0 0 2) Bragg peak, and the appearance of an additional peak around $2\theta = 29.5^\circ$, which further disappeared at 650°C, maybe due to the reconstruction of the apatite structure. Since only one additional Bragg peak was observed, it was not possible to go further in the understanding of this modification.



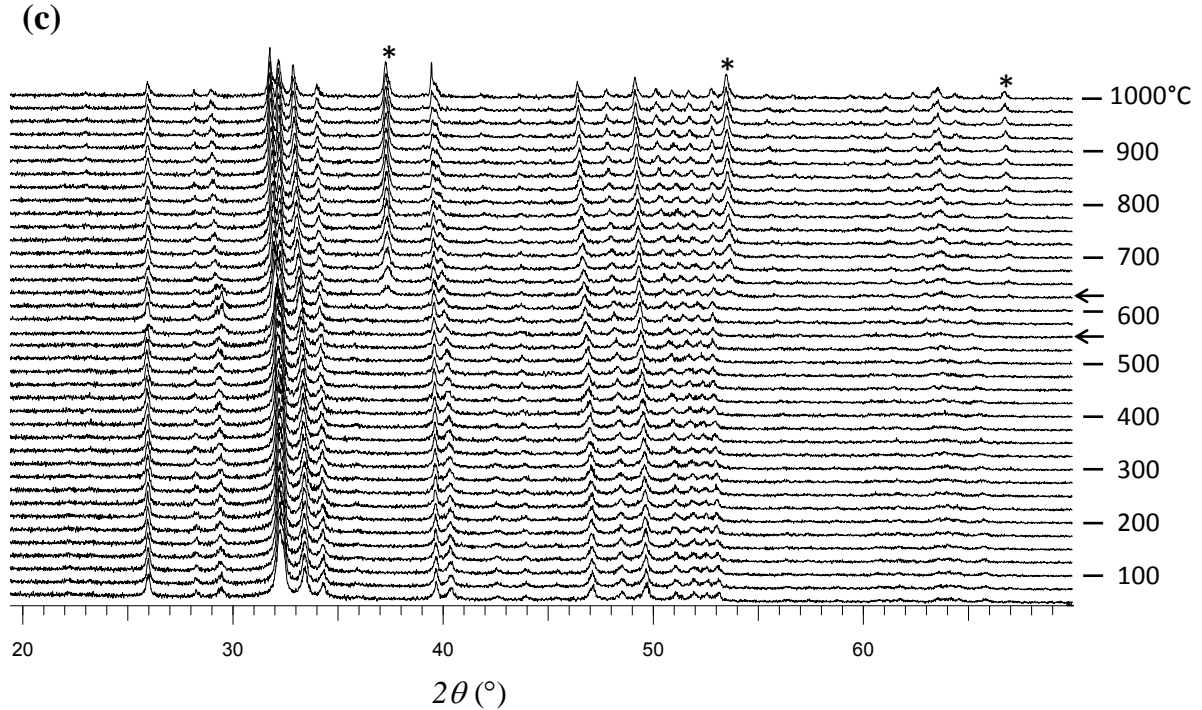


Figure 3-6 XRD patterns of (a) HapD, (b) Hap-CO₃ and (c) HapE-Na-CO₃ collected during temperature increase under air atmosphere. (α -Ca₃(PO₄)₂ is represented by \circ , *syn*-Ca₃(PO₄)₂ by Δ , CaO by *)

These transformations were further examined by means of thermogravimetric analysis combined with mass spectrometry (Figure 3-7), confirming the aforementioned XRD results. For all the compositions, a first mass loss was observed from room temperature to *ca.* 500°C, which can be assigned to the removal of physisorbed water and CO₂ and also of the constitutive water, as previously reported [25]. The thermograms can be divided into three groups, corresponding to the observed shapes of the recorded lines: (a) HapD and Hap-Na-CO₃, (b) Hap and Hap-CO₃ and (c) HapE-CO₃ and HapE-Na-CO₃. In group (a), a clear transition was observed at 700°C in good agreement with the decomposition of HapD observed by X-ray diffraction [Figure 3-6(a)]. For the second group (b), the transition occurred at around the same temperature of 700°C but was not sharp, and a plateau was not obtained at 1000°C. For carbonate-rich apatites HapE-CO₃ and HapE-Na-CO₃ [group (c)], the release of CO₂ started at a lower temperature, namely 550°C, and occurred in two steps with a change in the slope around 725°C in good agreement with the high temperature X-ray diffraction study. Assuming that the decomposition of all the apatites led to stoichiometric HAP and CaO (except for HapD, for which this is Ca₃(PO₄)₂ instead of CaO) at the end of the thermal study, it was possible to calculate the corresponding loss in CO₂ or otherwise CO₃²⁻ moles per apatite formula (Table 3-3). By comparison with the

CO_3^{2-} content in the B sites deduced from Rietveld refinement and the total CO_3^{2-} loss obtained from TGA, the first mass loss was easily attributed to the release of CO_3^{2-} from the A sites (channels) and the second mass loss to the release of CO_3^{2-} from the B sites. Interestingly, CO_3^{2-} was mainly located in the B sites for HapD, Hap, Hap- CO_3 and HapNa- CO_3 and in both A and B sites for the carbonate-rich apatites, namely, HapE- CO_3 and HapE-Na- CO_3 .

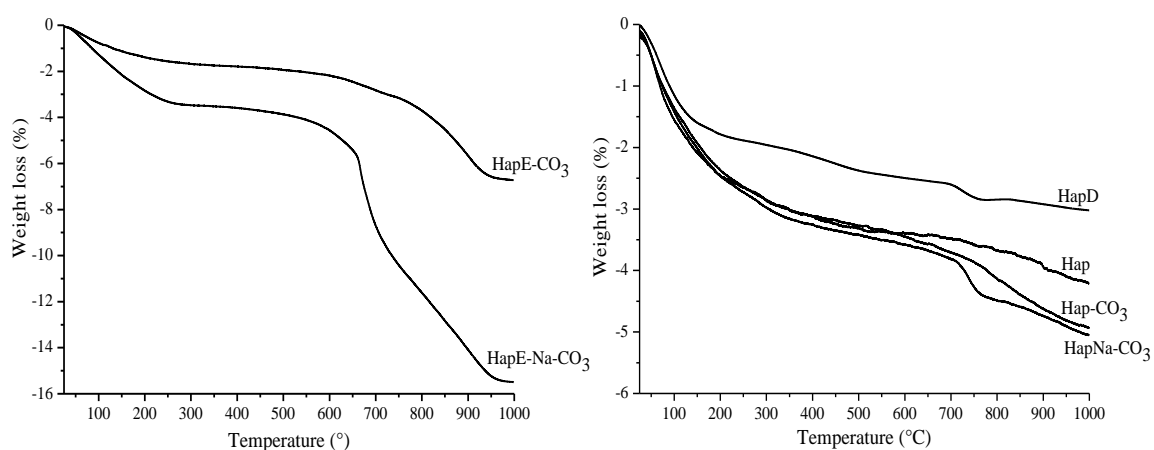


Figure 3-7 TG curves showing the weight loss of the samples calcined at 400°C.

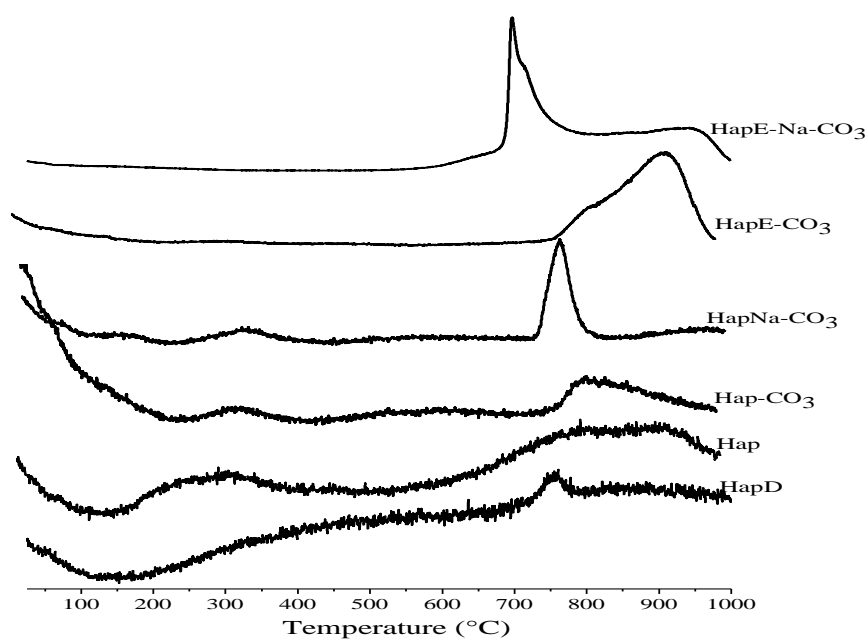


Figure 3-8 Derived curves of apatite solids obtained using MS with $m/z = 44$ showing the CO_2 loss.

The derived curve of CO₂ loss obtained by using mass spectrometer with m/z = 44 is shown in Figure 3-8. It is worth mentioning that the C/P ratio deduced from XRD and TGA were in good agreement with the ICP analysis, showing the good precision of the XRD refinement (Table 3-3). Moreover, a linear increase was observed in the case B-type CO₃²⁻ obtained both from TGA and XRD as shown in Figure 3-9, in excellent agreement with the theoretical line.

Table 3-3 Carbonate mole content in the apatite solids of general formula Ca_{10-d}[(PO₄)_{6-x}(CO₃)_x][(OH)_y(CO₃)_z]

| Solids | CO ₃ ²⁻ in the A sites from TGA (z)* | CO ₃ ²⁻ in the B sites from TGA (x)** | CO ₃ ²⁻ in the B sites from XRD (x) |
|-------------------------|--|---|---|
| HapD | - | 0.14 | 0.18(5) |
| Hap | - | 0.21*** | 0.32(5) |
| Hap-CO ₃ | - | 0.40 | 0.37(5) |
| HapNa-CO ₃ | - | 0.36*** | 0.37(6) |
| HapE-CO ₃ | 0.30 | 0.83 | 0.64(9) |
| HapE-Na-CO ₃ | 1.47 | 1.43 | 1.28(9) |

* Deduced from the weight loss starting from 500°C.

** Deduced from the weight loss starting from 700°C.

*** Underestimated since a plateau was not obtained.

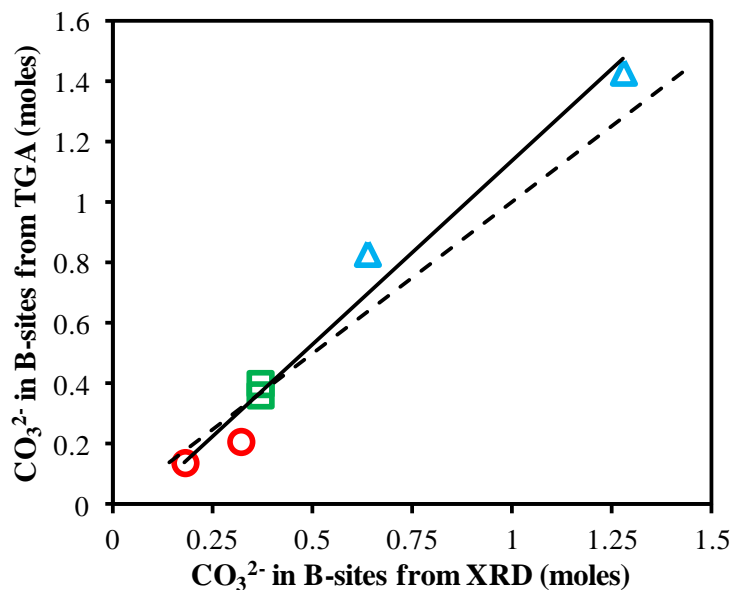


Figure 3-9 Plot of CO_3^{2-} in B-sites obtained from TGA as a function of CO_3^{2-} in B-sites obtained from XRD (red circles representing HapD and Hap, green squares for carbonated apatites, namely Hap- CO_3 and HapNa- CO_3 , and blue triangles for carbonate-rich apatites, namely HapE- CO_3 and HapE-Na- CO_3). The dashed line represents the theoretical perfect correlation (1 to 1 ratio).

3.2.1.3.4 A & B-type CO_3^{2-} substitution

Figure 3-10 and Figure 3-11 present two domains of the IR spectra of the apatite samples, focused on two different respective spectral regions, namely $700\text{--}1800\text{ cm}^{-1}$ and $3300\text{--}3700\text{ cm}^{-1}$. All the IR spectra confirmed the formation of carbonates-containing apatites with bands at 872 cm^{-1} , 1460 cm^{-1} and 1419 cm^{-1} [26,27,28].

The fundamental vibrational modes of PO_4 groups gave rise to bands at 565 cm^{-1} , 605 cm^{-1} , 963 cm^{-1} and $1030\text{--}1100\text{ cm}^{-1}$, as reported earlier [29,30]. Further, HPO_4^{2-} groups might also be present, with the characteristic band at 872 cm^{-1} , but which is known to overlap with a carbonate band, making straightforward conclusions impossible [26]. The broad vibrational band in the $3300\text{--}3700\text{ cm}^{-1}$ range is due to the presence of adsorbed and constitutive water molecules. The presence of carbonates in B-sites was confirmed by the increase in the intensity of the typical band at 872 cm^{-1} in carbonate-rich apatite [28,31], which could make the presence of HPO_4^{2-} species quite questionable, but these latter were detected using NMR spectroscopy (described later on). In addition, the peaks at 1460 cm^{-1}

and 1419 cm^{-1} can be attributed to CO_3^{2-} substituting PO_4^{3-} groups, which thus lead to the formation of B-type apatites [27]. The band at 3572 cm^{-1} is assigned to structural OH^- groups. It is worth noticing that the intensity of this band was higher for all the apatites except for carbonates-rich apatites (Figure 3-11). It was almost not detected in HapE-Na- CO_3 and was not so significant in the case of the HapE- CO_3 sample, confirming also the A-type substitution of OH^- by CO_3^{2-} ions in carbonate-rich apatites [28]. So, the A-type substitution was more evident when the carbonate content in the HAP was very high, which is good in agreement with the TGA results.

In brief, the IR spectra thus confirmed the A or/and B-type substitution by CO_3^{2-} groups in all the apatite solids, which is in agreement with the XRD and TGA observations.

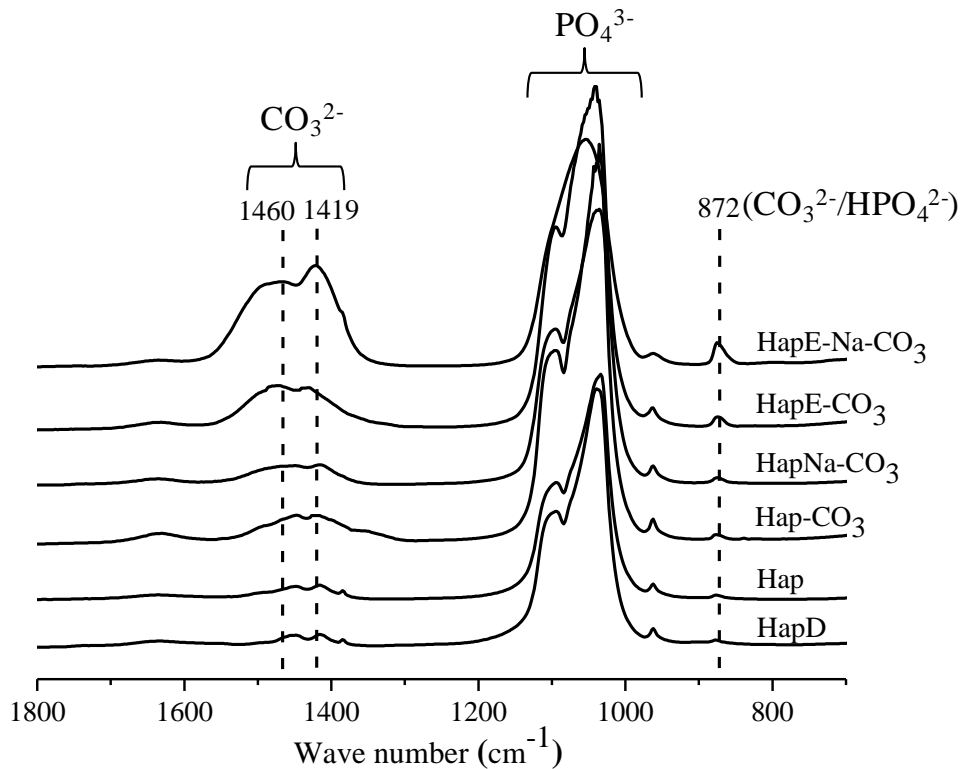


Figure 3-10 IR spectra of the carbonate apatites in the $700\text{-}1800\text{ cm}^{-1}$ region.

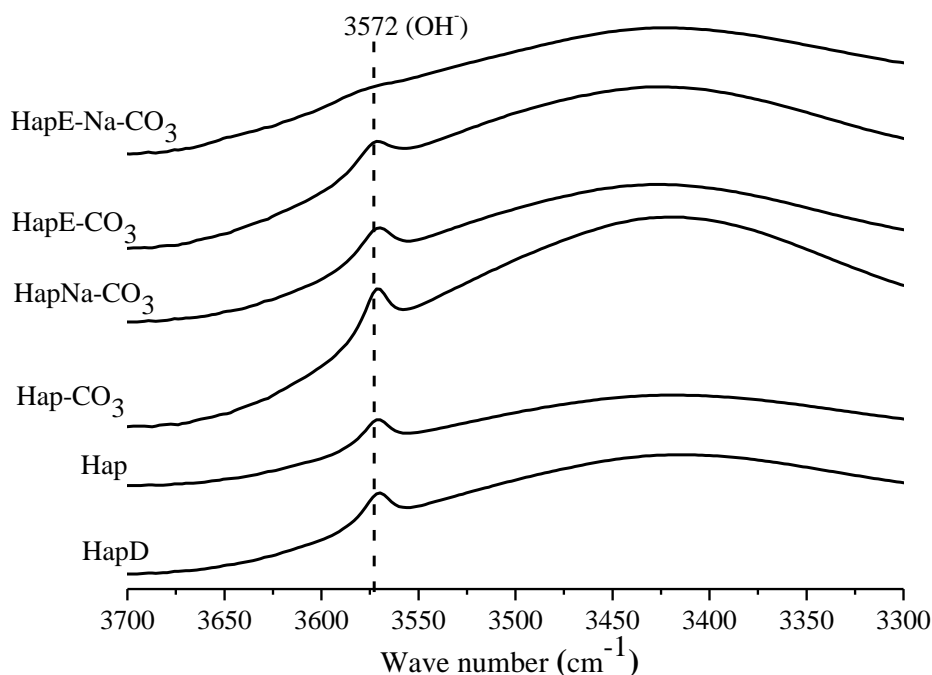


Figure 3-11 IR spectra of carbonated apatites of the carbonate apatites in the 3300-3700 cm^{-1} region.

3.2.1.4 Surface composition of apatite solids

3.2.1.4.1 Surface Ca/P ratio and carbonate species

XPS analysis was then carried out to get surface information. The comparison of the Ca/P ratios and of the $C_{\text{carbonates}}/P$ ratios determined by ICP, XRD/TGA and XPS are given in Table 3-4. Concerning the Ca/P ratios, the XPS surface analysis was in good agreement with the bulk analysis for almost all solids except HapD and Hap. The surface Ca/P ratio of 1.19 in HapD and 1.27 in Hap was much lower than the bulk ratios, which were 1.62 and 1.69, respectively. This is in good agreement with previous studies [11,32], and indicates that, for these two compositions, Ca is less exposed at the surface than phosphates, at least along the 10 nm analysis depth limit. For the other samples, the surface Ca/P ratios increased from 1.66 (Hap- CO_3) to 2.06 (HapE-Na- CO_3) with the increase in the content of carbonate ions and turned out to be almost similar to bulk ratios.

The surface carbon-based species have been examined using the characteristics of the C 1s photopeak. The decomposition of the C 1s peak allowed us to evidence four components, namely corresponding to C-C, C-O and C=O bonds, as well as a specific feature

corresponding to CO_3^{2-} , with respective binding energies of 285.0 (binding energies reference), 286.5, 288.5 and 290.0 eV (Figure 3-12).

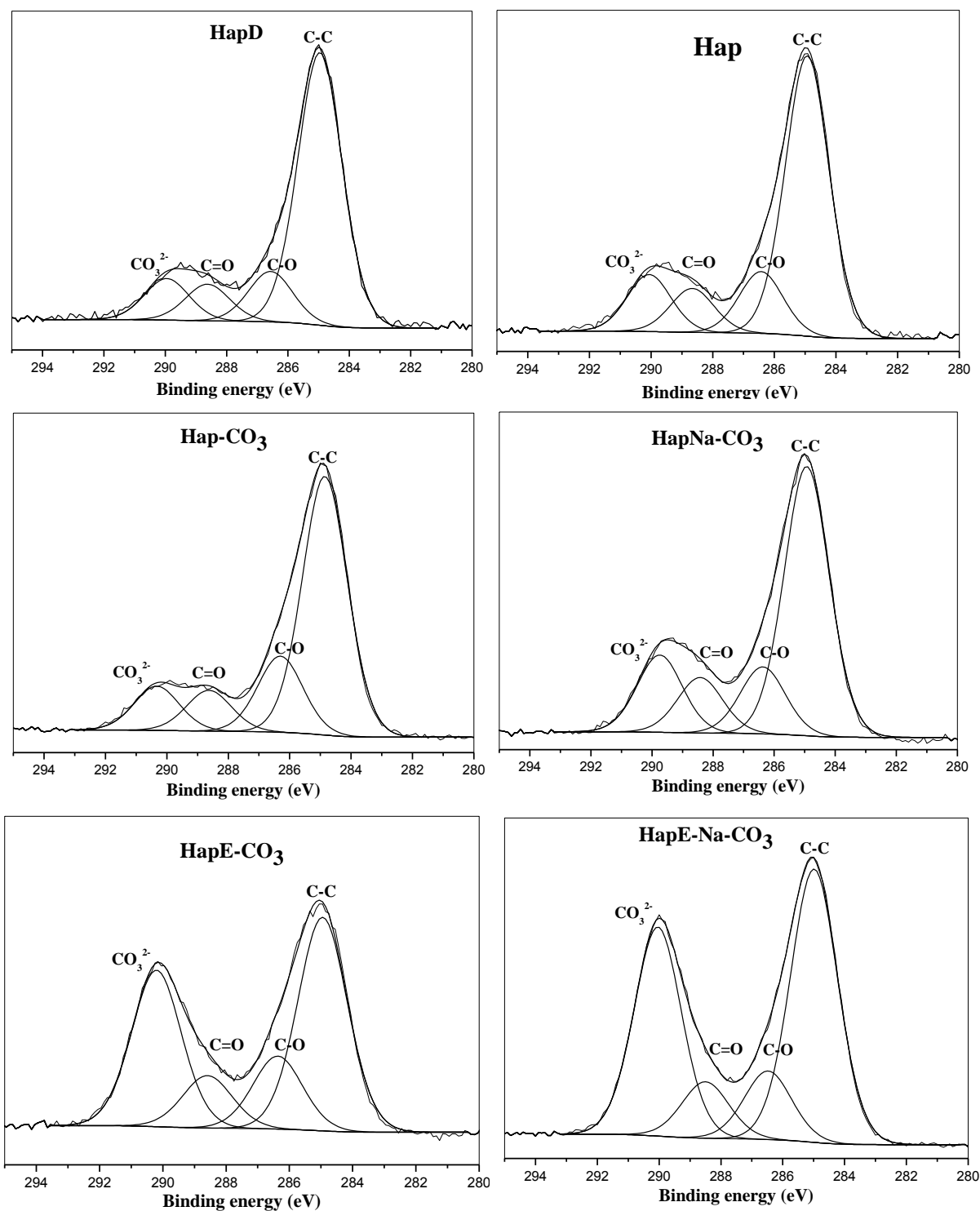


Figure 3-12 C1s photopeak of the samples.

The relative intensity of the peaks attributed to species containing C-O, C=O were similar, irrespective of the sample with C-O/C=O ratios between 1.2 and 1.8, whereas the intensity of the CO₃²⁻ species over the surface showed the global trend of increasing with the bulk CO₃²⁻ content along the series of prepared samples (Table 3-4).

Table 3-4 Comparison of Ca/P & C_{carbonate}/P atomic ratios in the apatites determined by ICP, XRD/TGA & XPS

| Solids | Ca/P atomic ratio (ICP) | Ca/P atomic ratio (XRD) (% difference relative to ICP) | Ca/P atomic ratio (XPS) (% difference relative to ICP) | C _{carbonates} /P atomic ratio (ICP) | C _{carbonates} /P atomic ratio (XRD-TGA) | C _{carbonates} /P atomic ratio (XPS) |
|-------------------------|-------------------------|---|---|---|---|---|
| HapD | 1.62 | 1.71 (+ 5.5%) | 1.19 (- 26.5%) | 0.03 | 0.02 | 0.07 |
| Hap | 1.69 | 1.76 (+ 4.1%) | 1.27 (- 24.9%) | 0.06 | 0.04* | 0.10 |
| Hap-CO ₃ | 1.70 | 1.77 (+ 4.1%) | 1.66 (- 2.4%) | 0.09 | 0.07 | 0.21 |
| HapNa-CO ₃ | 1.72 | 1.78 (+ 4.7%) | 1.67 (- 2.9%) | 0.10 | 0.06* | 0.14 |
| HapE-CO ₃ | 1.90 | 1.86 (- 2.1%) | 1.81 (-4.7%) | 0.22 | 0.21 | 0.14 |
| HapE-Na-CO ₃ | 2.39 | 2.12 (- 11.3%) | 2.06 (-13.8%) | 0.59 | 0.61 | 0.23 |

* underestimated since a plateau was not obtained.

Previous studies have shown that a variation in the Ca/P ratios in HAPs drastically changes their chemical properties [11]. Likewise, the carbonate apatites with different Ca/P surface ratios, and, further, different C_{carbonates}/P ratios should exhibit different surface properties, depending in part on the amount of carbonates present on their surface – or, at least,

absorbable at their surface. This will be checked later on in the paper when examining the acid-base properties of the solids.

As a partial conclusion for this part, while for all the samples, the $C_{\text{carbonates}}/P$ ratios obtained from XRD/TGA were comparable and in rather good agreement with the $C_{\text{carbonates}}/P$ ratios obtained from ICP (Table 3-4), the $C_{\text{carbonates}}/P$ ratio determined by XPS was not consistent, showing the surface complexity in hydroxyapatite solids.

3.2.1.4.2 Composition of the first atomic layer of the samples

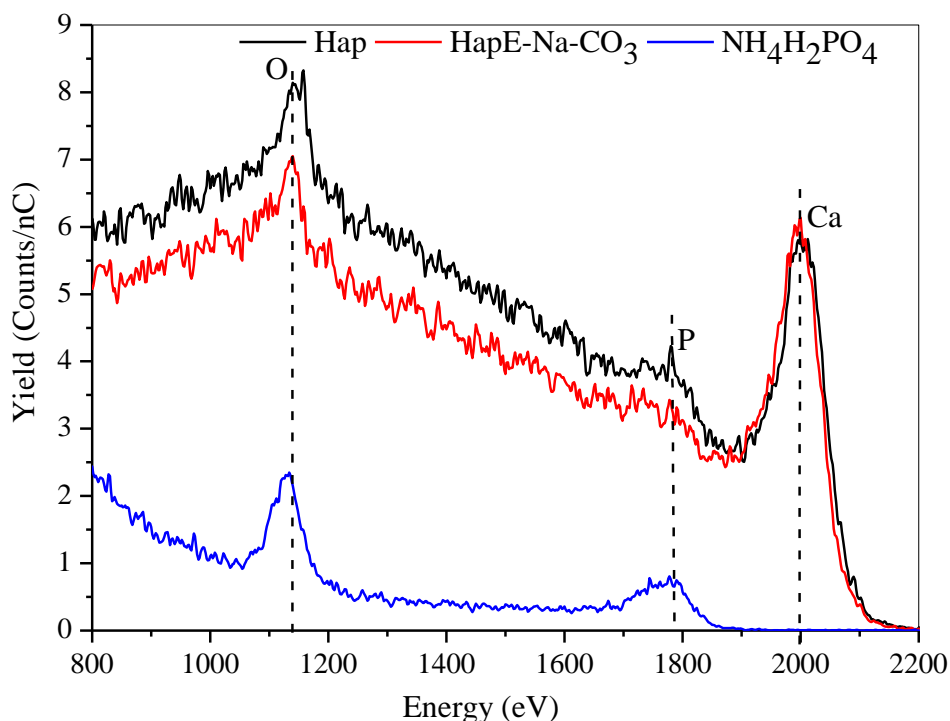


Figure 3-13 LEIS spectra of the calcined hydroxyapatites

To gain insights on the composition in the first atomic layer of a solid, LEIS is a powerful technique. To verify whether the Ca/P ratio or the carbonate content affects the topmost surface atomic distribution, stoichiometric Hap (low Ca/P ratio and carbonate content) and HapE-Na-CO₃ (high Ca/P ratio and carbonate content) were chosen for analysis (Figure 3-13). For Hap and HapE-Na-CO₃ two peaks due to Ca and O are clearly observed at 2000 eV and 1135 eV, respectively. A small peak due to P is observed at 1790 eV, but seems to be overlapped by the background signal resulting from the contribution of a

uniform distribution of lighter atoms (H, C & O). To confirm the presence of this peak and to clearly assess the expected position of a peak due to P, LEIS was performed using $\text{NH}_4\text{H}_2\text{PO}_4$ as a standard, which is a precursor used in the hydroxyapatites synthesis. A signal is clearly observed at 1790 eV, thus confirming the presence of P on the apatites surfaces. Despite the poor resolution around the phosphorous peak, it is worth noting that it is less intense for HapE-Na- CO_3 than for Hap.

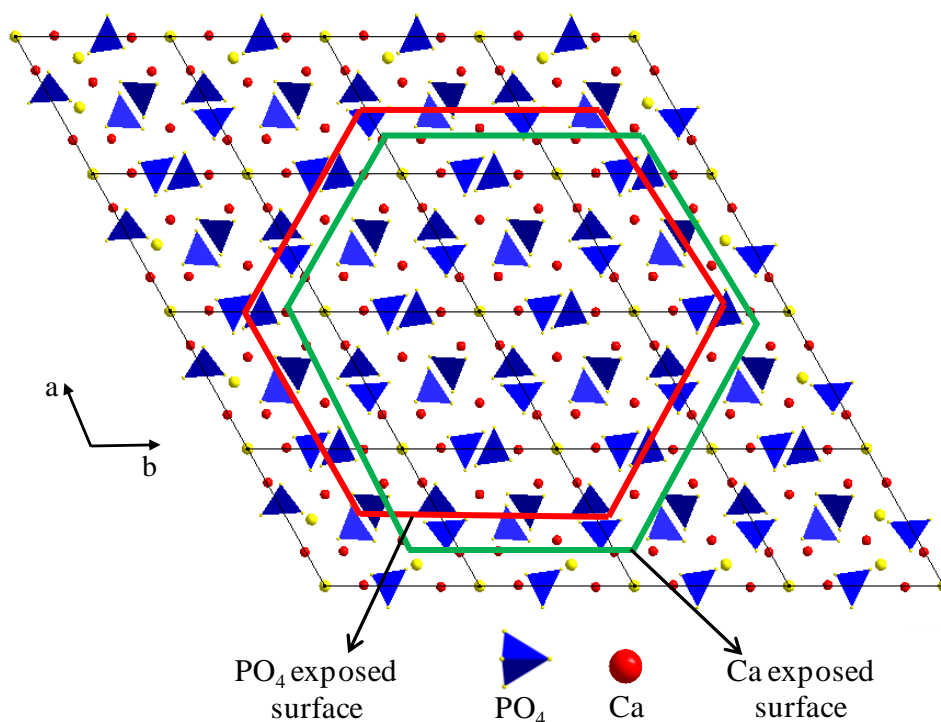


Figure 3-14 Schematic representation of the hydroxyapatite lattice: The green line shows the crystallite surface cleavage through Ca atoms, which is actually occurring according to our study, and the red line shows the theoretical crystallite cleavage through P atoms that could also have possibly occurred.

These results suggest that Ca ions and O ions are more exposed on the first atomic layer of hydroxyapatites, irrespective of the Ca/P ratio (1.69 & 2.39) and of the carbonate content (0.40 & 2.95 wt.%) in Hap and HapE-Na- CO_3 , respectively. This may contradict the results obtained by XPS, which showed a lower Ca/P ratio for Hap. However, we have to remind that the LEIS technique only probes the topmost atomic layer of the samples, while XPS gives information on the composition along a depth of a few nanometers. The O ions in the first atomic layer are supposed to arise from the PO_4^{3-} , CO_3^{2-} and $\text{CaO}/\text{Ca-O}^-$ species over the surface of the apatites. So, we could also propose that the surface of the

hydroxyapatite crystallites mainly consists of Ca ions compared with P atoms. Since the results obtained from Rietveld refinements have shown that the crystallite growth is more along [0 0 1] or in the *c*-axis direction, the Ca ions should be more exposed along the *c*-axis, that is, on *ac* and *bc* planes. A schematic representation of the two possible crystallite surface cleavages is shown in Figure 3-14. We then suppose that, in our study, the apatite crystallites are mainly cleaved in such a way that Ca atoms are more exposed to the surface, represented by the green line in Figure 3-14.

3.2.1.5 Presence of HPO_4^{2-} groups in the solids

Since, it was not possible to clearly determine if HPO_4^{2-} groups are present or not in the solids by using FTIR-spectroscopy, ^1H - ^{31}P CP NMR was performed. This technique enables detecting the presence of P belonging to acidic HPO_4^{2-} groups and of P belonging to PO_4 (orthophosphate) species.

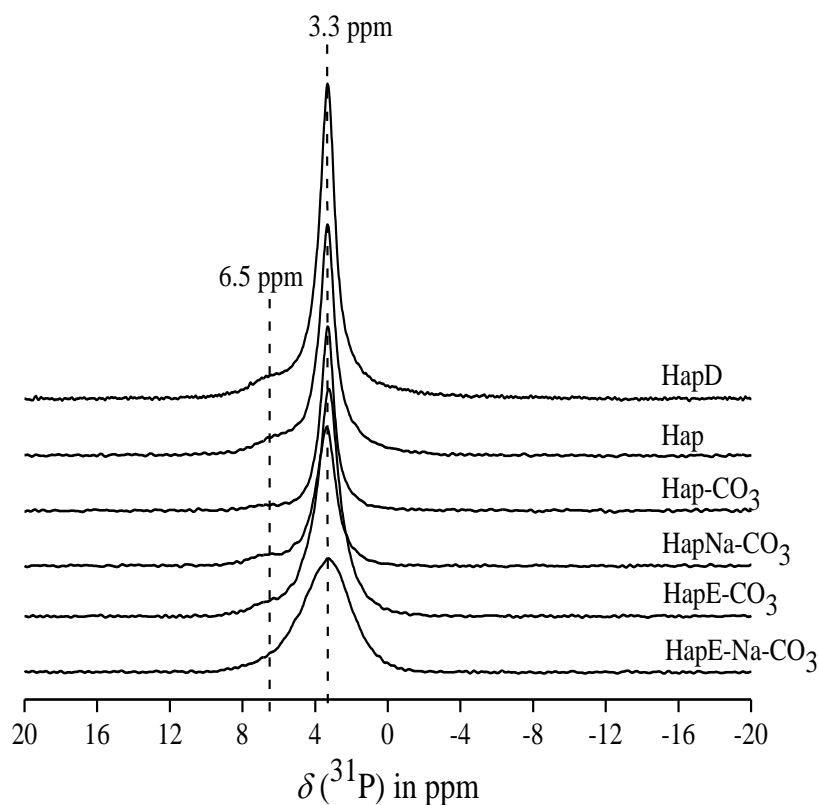


Figure 3-15 ^{31}P CP MAS-NMR spectra of hydroxyapatite solids.

All the samples exhibited a common signal resonating at 3.3 ppm due to PO_4^{3-} species [33] (Figure 3-15). Moreover, the line shape of the peaks tended to vary with the carbonate content, carbonate-rich apatites giving rise to broader peaks. This phenomenon is due to the distortions or defects in the P environment, resulting from the statistical carbonate substitution/removal of the ions in the apatite structure [33]. In addition to this signal, a broad peak centered at 6.5 ppm was clearly observed for HapD and Hap, which both contain a lower carbonate content compared to the other samples. For the other apatites, it is difficult to differentiate this signal due to its low intensity, and also because of the broadening of signal of the orthophosphate species at 3.3 ppm. Previous reports have shown that this peak can be attributed to phosphorus in the HPO_4^{2-} species or to phosphorus in the close vicinity of interstitial H_2O [34].

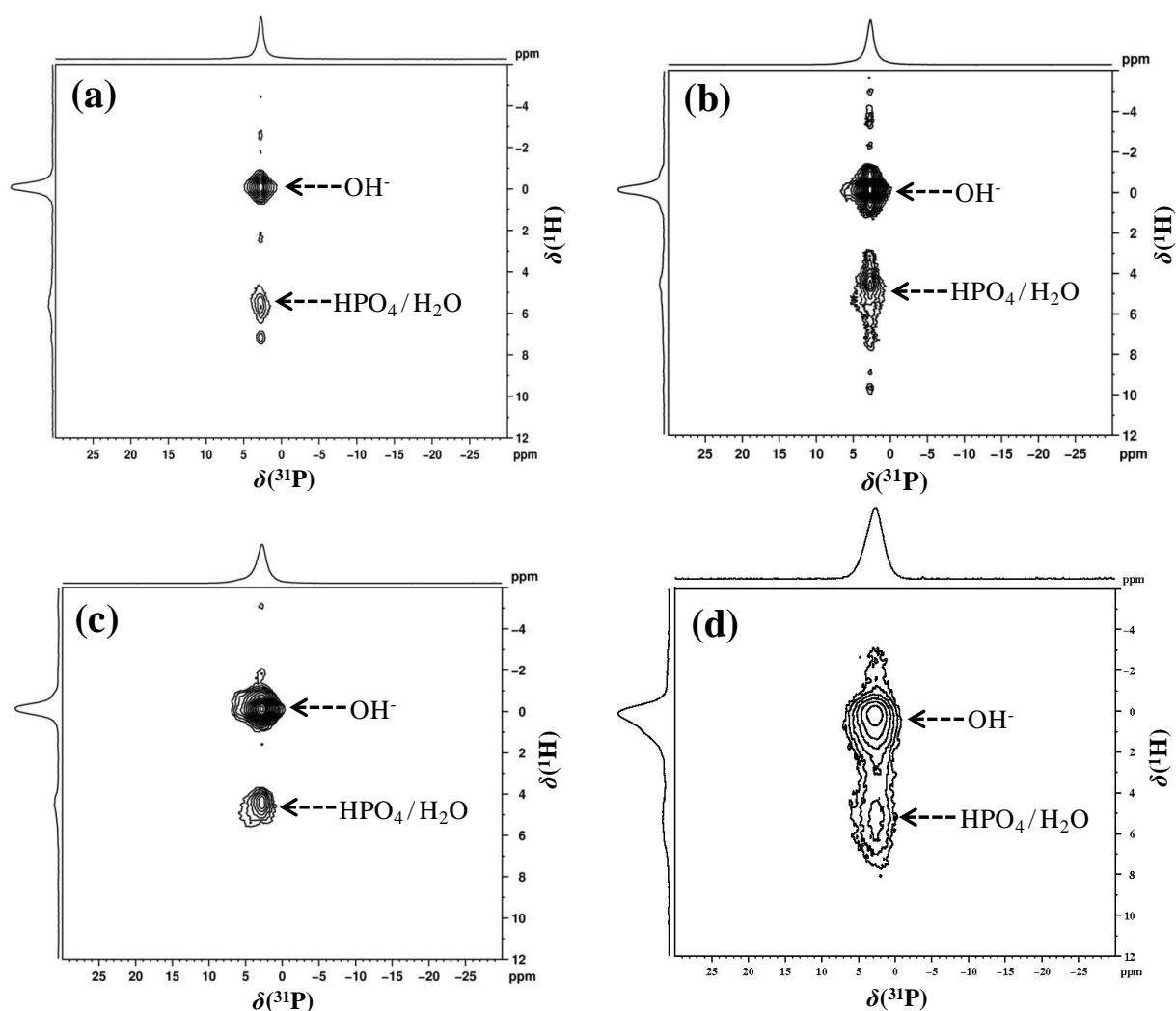


Figure 3-16 2D HETCOR spectra of (a) HapD, (b) Hap, (c) HapNa- CO_3 , and (d) HapE-Na- CO_3 .

In order to confirm the presence of HPO_4^{2-} groups, 2D ^1H - ^{31}P heteronuclear correlation (HETCOR) spectrum were then recorded. Figure 3-16 shows the 2D spectra of the solids at the short contact time of 1 ms at which the intensity of the signal due to HPO_4^{2-} groups is known to be more pronounced than the H_2O signal in the close vicinity of phosphorus [34]. The 2D spectrum of all the apatite solids clearly shows a signal resonating at 0 ppm along the ^1H axis due presence of the proton of OH^- that cross polarize with P of phosphate groups and a second signal resonating between 3 to 8 ppm along the ^1H axis mainly due to protons from HPO_4^{2-} groups. So the acidic HPO_4^{2-} groups were present in all the hydroxyapatite solids irrespective of the Ca/P ratio. However, quantification is not possible with this technique, which thus remains qualitative.

3.2.1.6 Acid-base properties of the solids

3.2.1.6.1 Total acid sites-nature and distribution

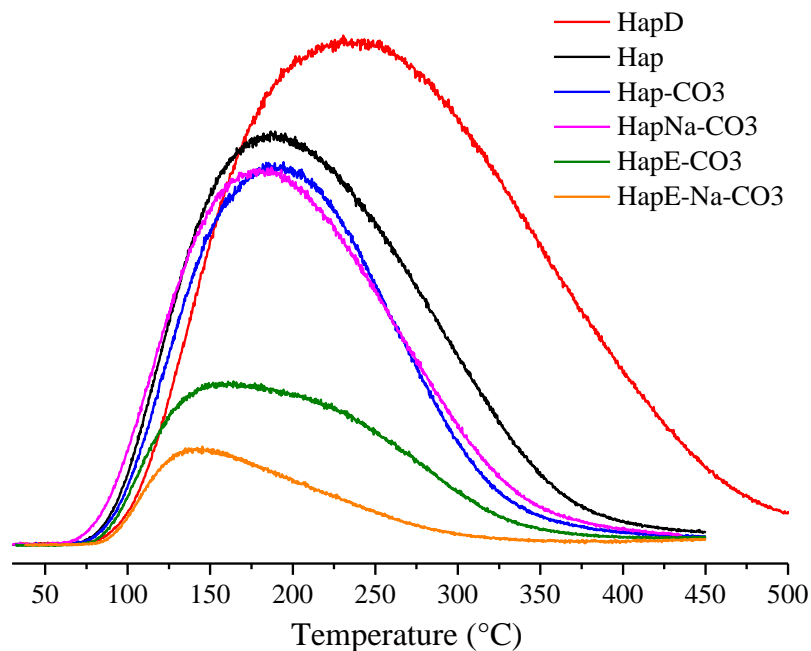


Figure 3-17 NH_3 -TPD curves of the apatite solids.

Figure 3-17 shows the NH_3 -TPD curves for all the apatite solids. It clearly appears that the peak corresponding to the deficient apatite HapD is much broader having a higher

Full Width at Half Maximum (FWHM) value of 224, thus much larger than that of the other apatites. This reflects the presence of stronger acid sites in a very broad temperature range extending upto 500°C. In addition, the maximum of the peak of HapD was shifted to high desorption temperature of 240°C compared to other apatites. The FWHM decreased further to 162 for Hap, whose peak is broadened up to a desorption temperature of 425°C. The FWHM was lowered for carbonated apatites Hap-CO₃ (137) and HapNa-CO₃ (139) compared to more acidic apatites HapD and Hap, but these samples still possessed acid sites of a relatively high strength, of which the desorption temperature extends up to 350°C. The intensity of the signals obtained for carbonate-rich apatites was clearly lower compared that of the other apatites, though the desorption temperature extended up to 350°C similarly to carbonated apatites. Hence, Hap and especially HapD show their predominant acidic character with stronger acid sites compared to other apatites.

The total number of acid sites in the samples was determined by integrating the NH₃-TPD profiles and is reported in Table 3-5. The specific acidity of the apatites decreased rather linearly from 1.16 to 0.28 μmol.m⁻² with the increase in the Ca/P ratio and the carbonate content as shown in Figure 3-18. The variation in the specific acidity can be due many parameters, such as the crystallites morphology, the surface Ca/P ratio, and the quantity of surface HPO₄²⁻, CO₃²⁻, CaO species, resulting from the replacement of PO₄³⁻/OH groups [11,35]. It has been observed from LEIS that Ca²⁺ (Lewis acid sites) present in *ac* and *bc* unit cell faces of apatites become more exposed to the surface if crystallite grows along [001] direction, which is good in agreement with previous reports [35,36]. The crystallite growth along the *c*-axis (0 0 1 direction) is increasing with the carbonate content, which means that the carbonate-rich apatites, which have a larger crystallite size along the *c*-axis, should possess more acid sites due to the exposure of a larger amount of Ca²⁺ species. Instead, carbonate-rich apatites presented a lower density in acid sites, maybe because most of the Ca exists under the form of CaO or Ca-O⁻ species present over the surface due to excess Ca/P ratio in carbonate-rich apatite solids. The Ca 2p_{3/2} XPS peak of carbonate-rich apatites was broadened with higher FWHM compared with the peak of stoichiometric Hap (data not shown) supposedly due to the presence of CaO. Moreover the high temperature XRD showed peaks due to CaO species, which are more predominant in carbonate-rich apatites. So we suppose that the CaO phase might also be present in all the apatite solids at room temperature, but in a highly dispersed state, similarly to recent findings on Sr apatites, which reported the presence of highly dispersed SrO species [37].

HapD has a higher number of acid sites due to the contribution from HPO_4^{2-} groups or OH^- vacancies, which are more numerous in deficient apatites and good in agreement with previous reports [11].

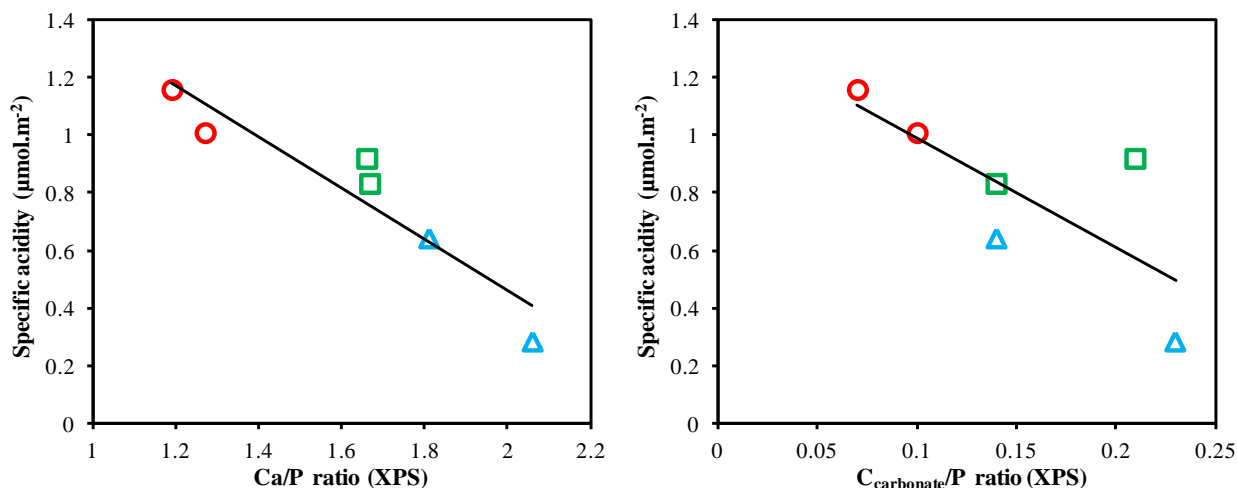


Figure 3-18 Variation of specific acidity in apatites with Ca/P ratio and $\text{C}_{\text{carbonate}}/\text{P}$ ratio (red circles representing HapD and Hap, green squares for carbonated apatites, namely Hap- CO_3 and HapNa- CO_3 , and blue triangles for carbonate-rich apatites, namely HapE- CO_3 and HapE-Na- CO_3).

PEA-XPS investigation of the apatite surfaces was used as a complementary way to the TPD approach to determine the Brønsted or Lewis nature of the surface acid sites, as previously reported [13,14]. The PEA-XPS spectra of all the samples presented a broad N 1s peak centered at binding energies in the 396.5–405.0 eV range, which could be decomposed into two peaks, at BEs of 398.0–405.0 eV and 396.5–403.5 eV, thus revealing the presence of Brønsted and Lewis acid sites, respectively (Figure 3-19). Also, it has been reported that the basic probe can be retained on Brønsted sites by the formation of an ammonium cation and on Lewis sites by the formation of a complex [13,14]. Taking into account the hydroxyapatite surface, we could propose that the ammonium cation can be formed with PEA mainly on acidic HPO_4^{2-} groups present on the HAP surface and the complex formation can take place over Ca^{2+} or OH^- vacancies (δ^+) (Figure 3-20).

Hence, in all the apatite solids, HPO_4^{2-} groups act as Brønsted acid sites and Ca^{2+} /vacancies as Lewis acid sites. The obtained relative distribution of Lewis and Brønsted acid sites is reported in Table 3-5 together with the specific amount of each site.

Table 3-5 Nature and distribution of acid sites determined by NH₃-TPD and PEA-XPS.

| Solids | Number of acid sites ($\mu\text{mol.g}^{-1}$) | Specific acidity ($\mu\text{mol.m}^{-2}$) | Nature & distribution of acid sites | |
|-------------------------|--|--|-------------------------------------|----------------------------|
| | | | Lewis | Brønsted |
| | | | ($\mu\text{mol.m}^{-2}$) | ($\mu\text{mol.m}^{-2}$) |
| HapD | 143.4 | 1.16 | 0.77 (66.7%) | 0.39 (33.3%) |
| Hap | 114.5 | 1.01 | 0.82 (80.7%) | 0.19 (19.3%) |
| Hap-CO ₃ | 98.7 | 0.92 | 0.84 (91.1%) | 0.08 (8.9%) |
| HapNa-CO ₃ | 90.6 | 0.83 | 0.78 (93.5%) | 0.05(6.5%) |
| HapE-CO ₃ | 48.6 | 0.64 | 0.60 (94%) | 0.04 (6%) |
| HapE-Na-CO ₃ | 21.2 | 0.28 | 0.28 (95.3%) | 0.01 (4.7%) |

Irrespective of the sample, the contribution of the Lewis acid sites was dominant and varied between 66.7% and 95.3%. PEA-XPS showed that all the solids possess Brønsted HPO₄²⁻ groups irrespective of the Ca/P ratio, which is in good agreement with the results of 2D NMR. More HPO₄²⁻ groups present in HapD resulted in the presence of more Brønsted sites, when compared to the other samples. Contribution from Brønsted HPO₄²⁻ groups was lower in carbonate-rich HAPs compared with the other solids, which supposedly results from the substitution of OH/PO₄³⁻ by CO₃²⁻ group, required to counterbalance the charge [35]. For carbonate-rich apatites, there is also an observable decrease in the number of Lewis acid sites (Ca²⁺) compared to the other apatites, though they possess higher Ca/P ratios compared to the other apatites. This decrease in the number of Lewis acid sites can be due to the formation of CaO species over the carbonate-rich apatites, which is no more a Lewis acid site but leaves a basic site on the surface. Hence, the HapD and Hap have much more contribution of 33.3% and 19.3% respectively from the Brønsted acid sites compared to all other apatites, whose Brønsted acid sites contribution varies between 4.7% (HapE-Na-CO₃) and 8.9% (Hap-CO₃). For HapD and Hap, this larger contribution of Brønsted

acid sites is linked with the observation of higher FWHMs of 224 and 162, respectively, of their NH_3 -TPD profiles, so that we can deduce that on these samples, strong Brønsted acid sites are created.

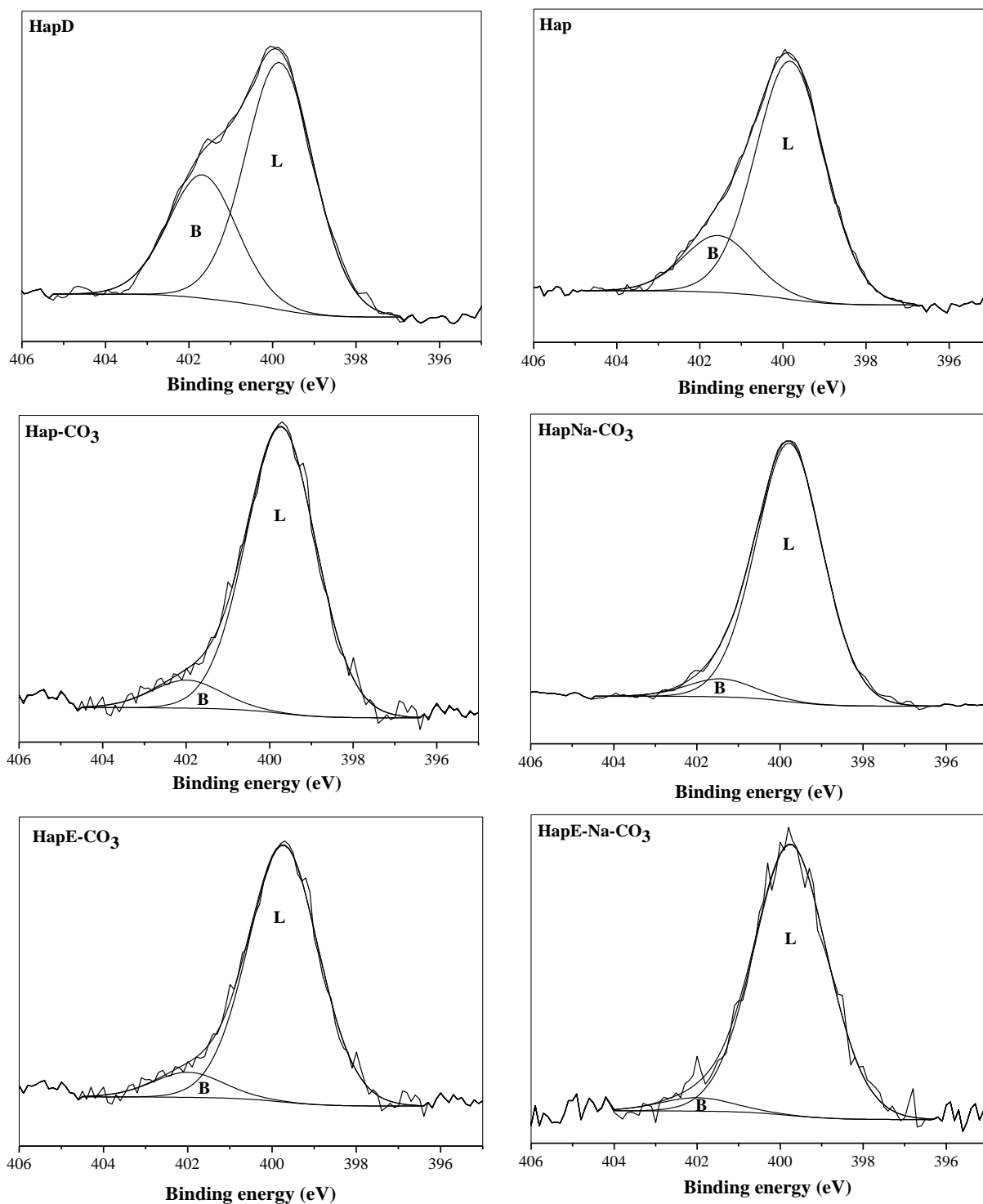


Figure 3-19 Decomposition of the N 1s PEA photopic after adsorption on the solids surface.

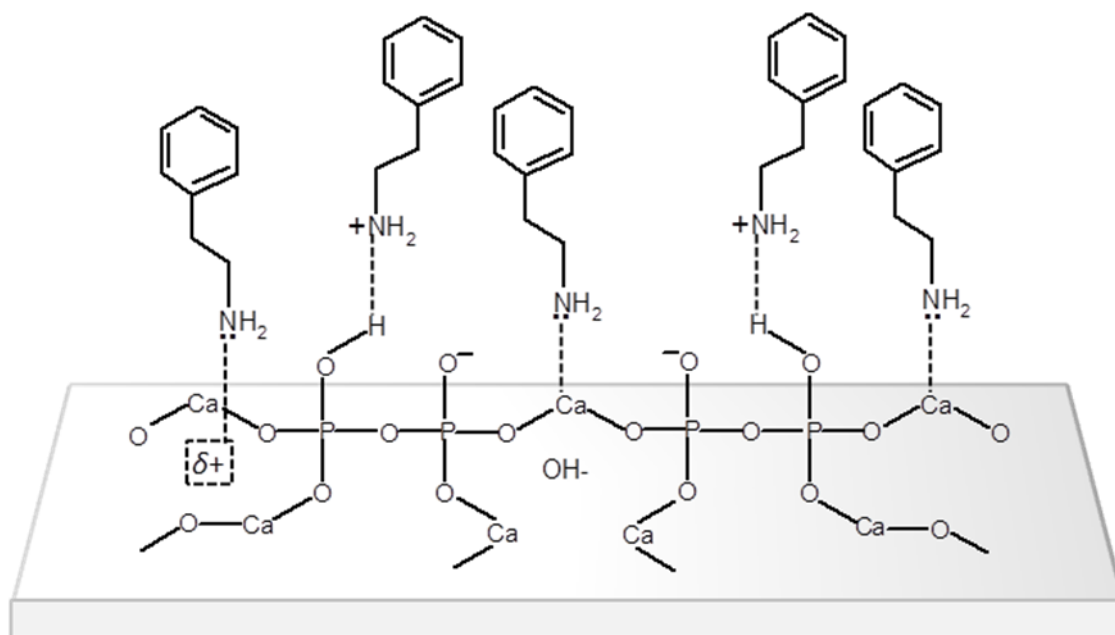


Figure 3-20 Model of PEA adsorption over Lewis and Brønsted acid sites on the surface of apatites. [($\delta+$) = OH⁻ vacancies].

3.2.1.6.2 Distribution of total basic sites

Basic sites with at least three different strengths can be distinguished from the CO₂-TPD profiles (Figure 3-21). The main contribution to the CO₂ desorption peak seems to be due to weak basic sites, and the resulting maximum is observed at $125 \pm 10^\circ\text{C}$ over all the apatites. A second peak at around 220°C due the presence of basic sites with medium strength is also observed, more clearly for HapNa-CO₃ and Hap-CO₃ with more intense signal. A last peak is observed at around 340°C due to the presence of strong basic sites for Hap, Hap-CO₃ and HapNa-CO₃. This peak was not observed in the deficient apatite HapD and in the carbonate-rich apatites (HapE-CO₃ and HapE-Na-CO₃). Since the carbonate-rich apatites are the solids that have shown the A-type substitution of CO₃²⁻ replacing the OH⁻ groups, we suppose that the absence of the peak due to stronger basic sites arising from the lack in basic OH⁻ species. It is known that in the case of deficient apatite (HapD), deficiency of Ca²⁺ ions is compensated by the addition of H⁺ and removal of OH⁻ ions and this may be the reason for the absence of OH⁻ peaks in HapD. But, further investigations are needed to confirm this assumption of OH⁻ as stronger basic sites.

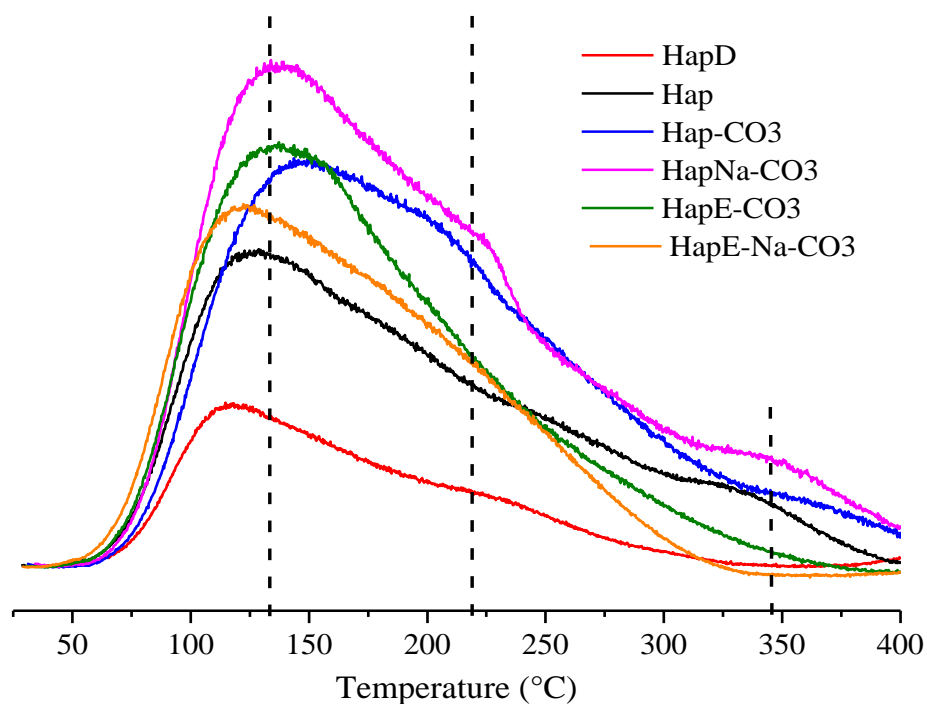


Figure 3-21 CO₂-TPD curves of the apatite solids.

Table 3-6 Amount of basic sites determined by TPD-CO₂.

| Solids | TPD-CO ₂ | |
|-------------------------|---|---|
| | Number of basic sites ($\mu\text{mol.g}^{-1}$) | Specific basicity ($\mu\text{mol.m}^{-2}$) |
| HapD | 6.2 | 0.05 |
| Hap | 15.1 | 0.13 |
| Hap-CO ₃ | 20.4 | 0.19 |
| HapNa-CO ₃ | 23.3 | 0.21 |
| HapE-CO ₃ | 16.9 | 0.22 |
| HapE-Na-CO ₃ | 15.6 | 0.22 |

The amount of basic sites was determined by integrating the TPD profile of CO₂. The number of basic sites tended to increase from 6.2 μmol.g⁻¹ to 23.3 μmol.g⁻¹ when the Ca/P ratio or the carbonate content increased from HapD to HapNa-CO₃, and then decreased with further increase in the Ca/P ratio or carbonate content in carbonate rich apatites (Table 3-6). In contrast, the specific basicity increased from 0.05 μmol.m⁻² to 0.21 μmol.m⁻² when the Ca/P ratio or the carbonate content increased from HapD to HapNa-CO₃ and remained almost unchanged with further increase in Ca/P ratio, namely in carbonate-rich apatites, HapE-CO₃ and HaE-Na-CO₃.

3.2.1.6.3 Acid-base behaviour of HAP as catalysts

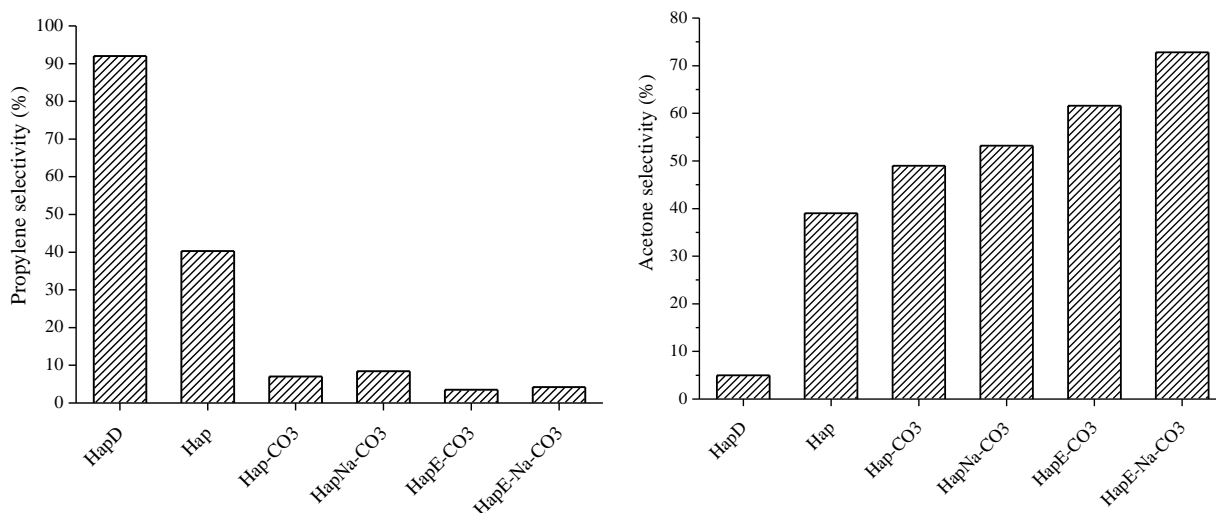


Figure 3-22 Selectivity to propylene and acetone at 20% conversion of isopropanol

Isopropanol test was performed at an *isopropanol* conversion of 20% and the variation in propylene and acetone distribution over hydroxyapatites with different composition is shown in Figure 3-22. The catalytic conversion of *isopropanol* over all the apatites yielded propylene, acetone, *di-isopropyl* ether and negligible amount of dienes. Acetone can be formed on basic sites and propylene and *di-isopropyl* ether over acid sites, as previously reported [25]. The propylene formation was much higher over deficient apatite HapD and Hap compared to all the other apatites underlining the acidic behavior of these catalysts, which is good in agreement with TPD-NH₃ and PEA-XPS. The high amount of acid sites and the presence of more Brønsted acid sites (HPO₄²⁻ groups) with higher strength in HapD

and Hap can explain this predominant formation of propylene. The propylene selectivity was lowered from 92% to 40.3% with increase in Ca/P ratio from 1.62 in HapD to 1.69 in Hap, but Hap still possessed a relatively high acidic character compared to the other catalysts. For carbonated apatites, Hap-CO₃ (Ca/P = 1.70) and HapNa-CO₃ (Ca/P = 1.72), the propylene formation was found to reduce drastically to 7% and 8.4% respectively. This shows decrease in the acidic behavior of HAPs with increase in Ca/P ratio or carbonate amount above certain limit. Selectivity to propylene was lowered to 3.5% and 4.2%, respectively, for carbonate-rich apatites HapE-CO₃ (Ca/P = .90) and HapE-Na-CO₃ (Ca/P = 2.39), showing the lack in acidic nature in apatites with very high Ca/P ratios or carbonate contents.

Selectivity to acetone tended to increase readily with the increase in the Ca/P ratio from HapD to HapE-Na-CO₃. HapD with lower Ca/P ratio of 1.62 was less selective to acetone (5%) than all the other apatites, which is good in agreement with the lower number of basic sites (6.2 $\mu\text{mol.g}^{-1}$) over this sample. Selectivity to acetone increased considerably to 39% in Hap (Ca/P = 1.69). Further increase in the Ca/P ratio for carbonated apatites, namely Hap-CO₃ and HapNa-CO₃, led to an increase in the acetone selectivity to 49%, and 53.2%, respectively. Though the carbonate-rich solids, HapE-CO₃ (Ca/P = 1.90) and HapE-Na-CO₃ (Ca/P = 2.39) possess a lower number of basic sites compared to carbonated apatites, they have shown higher selectivity to acetone compared to all the other apatites. This can be due to the presence of more basic CaO species over carbonate-rich apatites, which enhance the dehydrogenation of *isopropanol* to acetone. Comparing the carbonate-rich apatites HapE-CO₃ and HapE-Na-CO₃, the latter was found to be more selective to acetone, though it possesses a lower amount of basic sites compared to HapE-CO₃. This can be thus due to formation of more CaO species over HapE-Na-CO₃ compared to HapE-CO₃. It is also worth noting that, though catalysts Hap, Hap-CO₃ and HapNa-CO₃ possess stronger basic sites, they have shown lower selectivity to acetone compared to carbonate-rich apatites, which lack in stronger basic sites. This might indicate that dehydrogenation of *isopropanol* to acetone probably took mainly place over weak or medium basic sites.

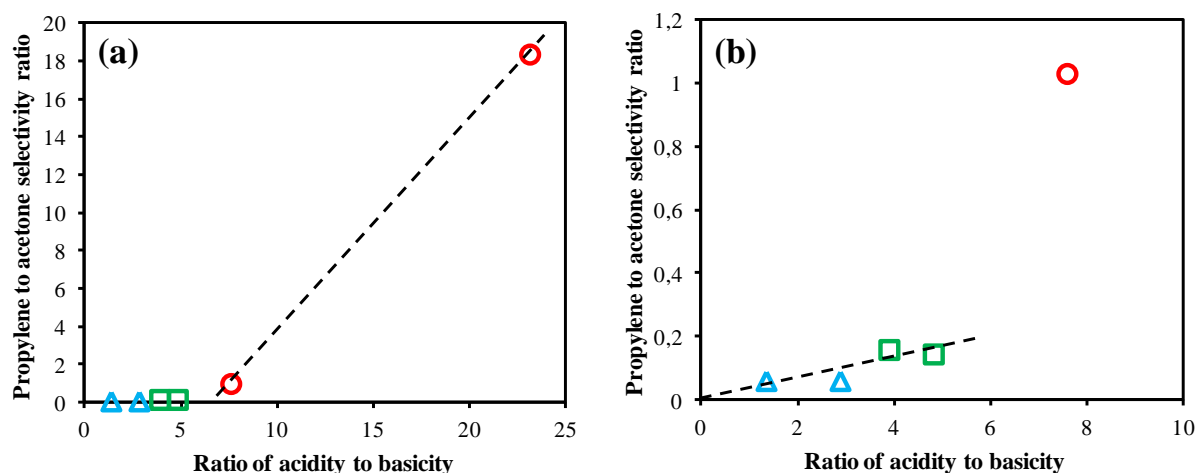


Figure 3-23 (a) Ratio of propylene to acetone selectivity as a function of the ratio between the number of acid sites to the number of basic sites and (b) Same figure focused on a narrower range of acidity/basicity ratio (red circles representing HapD and Hap, green squares for carbonated apatites, namely Hap-CO₃ and HapNa-CO₃, and blue triangles for carbonate-rich apatites, namely HapE-CO₃ and HapE-Na-CO₃).

The plot of the propylene/acetone selectivity ratio (indirectly representing the acid/base behavior) as a function of the number of acid sites to the number of basic sites (direct acid-base behavior) is shown in the Figure 3-23. Hap and HapD clearly shows a deviation (represented by dashed line) from the other apatites, which can be related to their higher acidic behavior [Figure 3-23(a)]. In addition, a rather linear increase in the propylene/acetone selectivity ratio with the acidity/basicity ratio [dashed line in Figure 3-23(b)] was observed for carbonated and carbonate-rich apatites. Then, a remarkable correlation is observed between the *isopropanol* reactivity and acid-base properties for these samples.

Formation of *di-isopropyl* ether was observed in small amounts, 2% in HapD and 0.9 % in Hap and trace amounts (below the quantification limit of *ca.* 0.5%, with a slightly visible GC peak quite mixed with the background and thus not exploitable) over the other apatites. The *di-isopropyl* ether is generally formed by an intermolecular dehydration mechanism over the acid sites. The distribution of acid sites is different on HapD and Hap samples compared to all the other samples. While all the samples possess Lewis sites vary in the range between 20.2 $\mu\text{mol.g}^{-1}$ to 95.6 $\mu\text{mol.g}^{-1}$ the situation is different concerning Brønsted sites. The carbonate and carbonate-rich apatites possess only $4.4 \pm 4 \mu\text{mol.g}^{-1}$ of Brønsted sites compared to 47.8 $\mu\text{mol.g}^{-1}$ over HapD and 22.1 $\mu\text{mol.g}^{-1}$ over Hap.

As a conclusion to this part, HapD and Hap have shown their predominant acidic behaviour compared to all other apatites, which have shown much lower propylene selectivity. This predominant acidic behaviour is mainly due to the presence of stronger acid sites, especially of the Brønsted type. Presence of highly dispersed basic CaO species created from excess Ca/P ratio than stoichiometric value (1.67) could be the reason for the higher acetone selectivity over carbonate-rich apatites. Also, it was found that it is mainly the weak and medium basic sites and not the stronger basic sites, which seem to be responsible for the dehydrogenation of *isopropanol* to acetone

3.2.2 Guerbet reaction of ethanol over HAP catalysts

3.2.2.1 Guerbet reaction products observed at iso-conversion

Table 3-7 Selectivity to Guerbet reaction products at 14% of ethanol conversion.

| Catalyst | Group <i>i</i> | | Group <i>ii</i> | | Group <i>iii</i> | |
|------------------------------|----------------|------|---------------------|-----------------------|----------------------|-------------------------|
| | HapD | Hap | Hap-CO ₃ | HapNa-CO ₃ | HapE-CO ₃ | HapE-Na-CO ₃ |
| Ethylene | 3.1 | 2 | 1.3 | 1.6 | 1.2 | 1.5 |
| Acetaldehyde | 5.8 | 9 | 7.2 | 13.1 | 15.5 | 19 |
| 2-buten- <i>l</i> -ol | 2 | 1 | 3.2 | 5.1 | 8 | 10.2 |
| Butanol | 49 | 50 | 71 | 59 | 46 | 41 |
| C6-C10 alcohols ^a | 18 | 19.4 | 8.8 | 2.9 | 7 | 1.1 |
| Total alcohols ^b | 69 | 70.4 | 83 | 67 | 61 | 52.3 |
| Diethyl ether | 5 | 4.5 | 1.1 | 0.8 | 0.6 | 2 |
| Dienes ^c | 3.1 | 1.2 | 2 | 2.2 | 1.5 | 1.2 |
| Ethyl butyrate | - | - | - | 1.5 | 3.5 | 10.3 |
| Others ^d | 14 | 12.9 | 5.4 | 13.8 | 16.7 | 13.7 |

^a Hexanol, 2-ethylbutanol, octanol, 2-ethylhexanol and decanol;

^b 2-buten-*l*-ol, butanol and C6-C10 alcohols;

^c 1,3-butadiene and small amounts of C6-dienes;

^d Higher aldehydes, higher alkenes, aromatics.

Table 3-7 shows the selectivity to the main products for the Guerbet reaction of ethanol, taken at the iso-conversion of 14%. This iso-conversion of ethanol was achieved by properly adjusting the temperature between 300°C and 400°C at GHSV's between 5000 mL.h⁻¹.g⁻¹ and 15000 mL.h⁻¹.g⁻¹. Butanol is the major product observed in the Guerbet reaction of ethanol over all the catalysts, its selectivity being higher over the carbonated apatites, namely Hap-CO₃ (71%) and HapNa-CO₃ (59%). Formation of ethylene, which is issued from intramolecular dehydration of ethanol, was observed in rather small quantities over all the apatites, and especially over HapD (3.2%) and Hap (2%), its selectivity being less than 1.6% over the other solids. Acetaldehyde, a dehydrogenation product of ethanol was produced over all the catalysts, and especially over the carbonate-rich apatites, namely HapE-CO₃ (15.5%) and HapE-Na-CO₃ (19%). The formation of 2-buten-1-ol, which is produced by dehydrogenation of ethanol followed by aldol condensation and hydrogenation of the C=O bond while leaving the C=C bond non-hydrogenated, was also observed, in quantities increasing when increasing the carbonates content. In contrast, trace amount of butyraldehyde which is formed similarly as 2-buten-1-ol but by hydrogenation of the C=C bond leaving the C=C bond non-hydrogenated. Small amounts of diethylether, resulting from intermolecular dehydration of ethanol over acid sites, as well as dienes were also observed over all the catalysts. Further, 'other' compounds were also detected, namely higher aldehydes, higher alkenes and trace amount of aromatics, which are formed by multiple consecutive steps, by uncontrolled reaction over the various sites present at the surface of the solids.

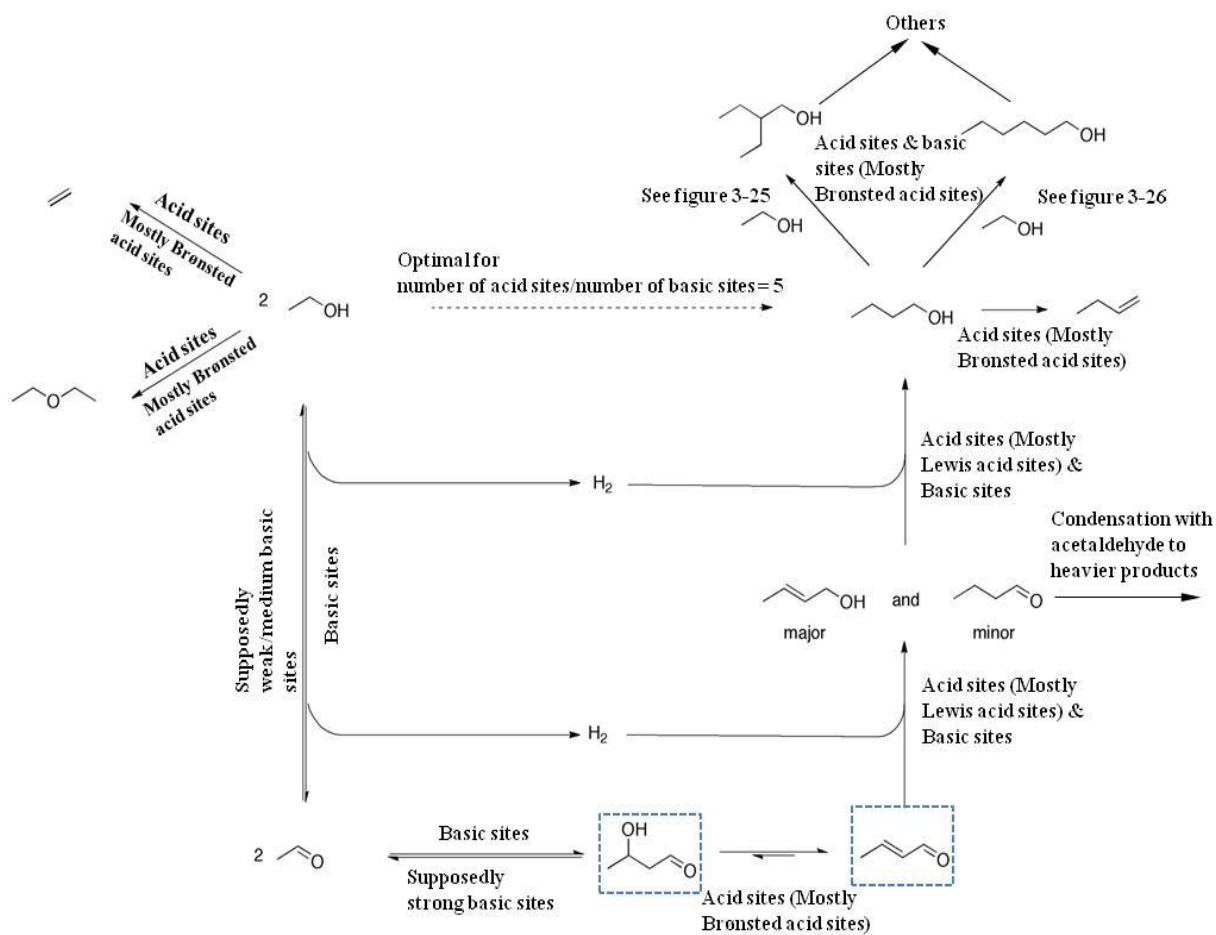


Figure 3-24 Scheme of the role of acid and basic sites in the apatite catalysts towards different pathways. The dashed box represents the intermediates which are not observed in the reaction.

[Basic sites: PO_4^{3-} , OH^- & CaO , Brønsted acid sites: HPO_4^{2-} , Lewis acid sites: Ca^{2+} & OH^- vacancies (δ^+)

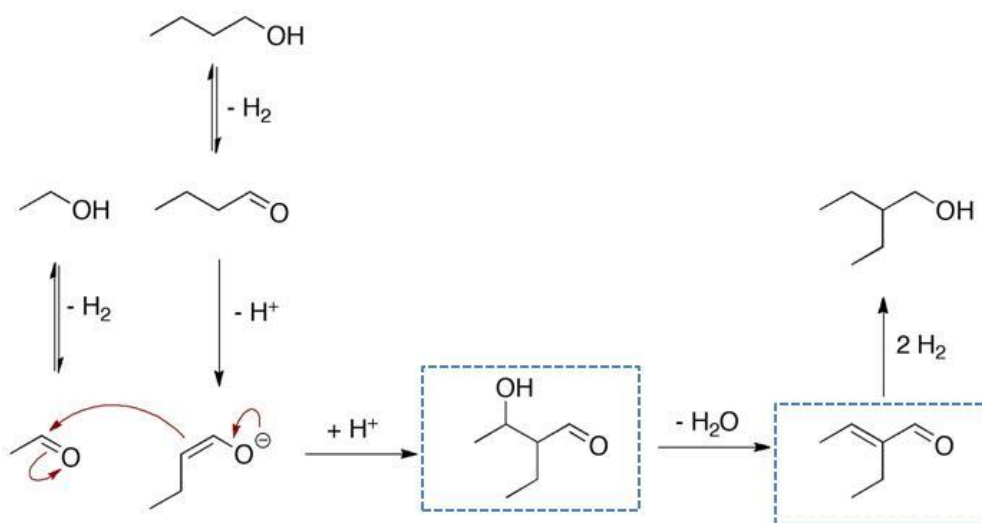


Figure 3-25 Mechanism for the condensation of ethanol and butanol to form 2-ethylbutanol. The dashed box represents the intermediates which are not observed in the reaction

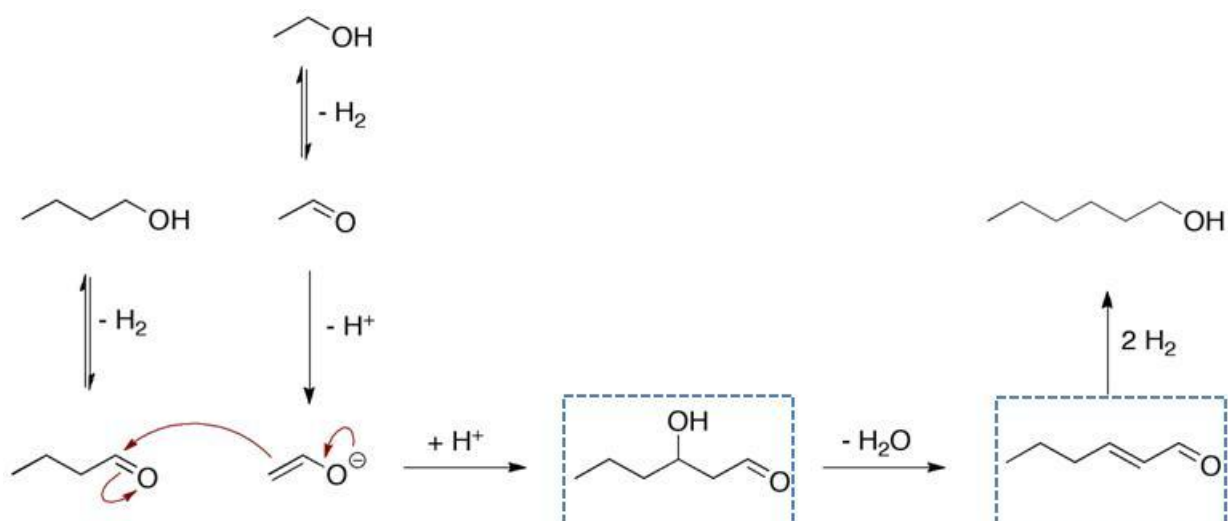


Figure 3-26 Mechanism for the condensation of ethanol and butanol to form hexanol. The dashed box represents the intermediates which are not observed in the reaction

Figure 3-24 shows the Guerbet reaction scheme taking place over different types of acid and basic sites in the apatite catalysts, considering the products observed in our reaction. In this figure are compiled all the conclusions deduced from the results precisely documented in the two next parts (see sections 3.2.2.1.1 & 3.2.2.1.2), which are quite all-inclusive for the reader who will need further details. In order for the Guerbet reaction of ethanol to effectively proceed to heavier alcohols, both acid and basic sites are necessary, but the strength, the nature and the relative balance of these sites have a great influence on each step of the Guerbet cycle, and are also involved in the occurrence of undesirable side-reactions, thereby conditioning the products distribution. Hereafter are the conclusions of the next study compiled in Figure 3-24. The first step of the Guerbet cycle is the dehydrogenation of ethanol over the basic sites to produce acetaldehyde. This dehydrogenation takes place mainly on the weak or medium basic sites and is especially promoted by CaO species, as explained earlier in the manuscript in the part dealing with acid-base properties of apatite catalysts (Section 3.2.1.6.3). The as-formed acetaldehyde further undergoes aldol condensation over basic sites (probably over stronger basic sites) to form an intermediate aldol (never observed in our conditions). Further dehydration of aldol takes place over acid sites (mostly Brønsted acid sites) to produce crotonaldehyde, which was also not observed (or in trace amounts). The crotonaldehyde then undergoes partial hydrogenation by proton exchange mechanism over HAP catalysts to form 2-buten-1-ol and butyraldehyde over both types of acid (mostly Lewis acid sites) and over basic sites. These compounds can further undergo hydrogenation over the same acid-base sites in the

apatite catalysts to form butanol. Butanol can further react with ethanol and go through an additional Guerbet cycle of mechanism over acid sites (mostly Brønsted acid sites) and basic sites to form 2-ethylbutanol (Figure 3-25) or hexanol (Figure 3-26), depending on the type of attack,. The formation of these heavier alcohols was promoted more over catalysts having more number of acid sites, mainly Brønsted acid sites. Also, there are some competing reactions, especially dehydration reactions that can form olefins (ethylene, butene etc...) or diethylether, which occur in parallel with the Guerbet cycle (mostly over Brønsted acid sites). So, there should be a compromise between the acid and the basic sites number and also concerning their strength and nature over the HAP catalysts to give a global formulation that is selective towards higher alcohols. We especially identified the best ratio between the number of acid sites to basic sites of 5 to attain maximum selectivity to higher alcohols over HAP catalysts. If the amount or the strength or the nature of acid sites becomes too high, the dehydration reactions (producing olefins) become more prominent and if the amount or the strength of basic sites exceeds this may preferably lead to the formation of products like aldehydes. In contrast, if there is any deficiency in the acid or basic sites, the reaction cannot proceed further towards the butanol or heavier alcohols, thus resulting in increased selectivity to some intermediates of the Guerbet cycle.

All these observations are derived from / supported by the conclusions of the following study, which is divided into two main parts, namely, correlation studies of isopropanol test and Guerbet reaction and direct correlation studies of Guerbet reaction and acid-base properties of apatites.

3.2.2.1.1 Correlation studies of isopropanol test and Guerbet reaction

A correlation study was performed between the selectivity to products observed when targeting the Guerbet reaction starting from ethanol (ethylene, diethylether, acetaldehyde, alcohols...) and the selectivity to *isopropanol* reaction products (both taken at iso-conversion) to get an indirect insight on the acid-base behavior of all the apatite catalysts. Indeed, the *isopropanol* test on apatite catalysts produced mainly propylene (and also small quantities of *di-isopropylether*) and acetone, which is an indirect representation of the acidic behavior and the basic character, respectively, of the probed solids. In the following figures, the catalysts are divided into three groups: (*i*) HapD and Hap represented by red

colored circles, (ii) carbonated apatite catalysts, namely Hap-CO₃ and HapNa-CO₃, represented by green squares, and (iii) carbonate-rich apatites, namely HapE-CO₃ and HapE-Na-CO₃, represented by blue triangles.

Since ethylene, diethylether (Guerbet reaction products) and propylene, *di-isopropylether* (isopropanol reaction products) are supposed to be formed by by inter- and intramolecular, dehydration reactions over acid sites, a correlation study were performed between these products. As *di-isopropylether* was hardly detected over group *ii* and group *iii* catalysts due to the GC analysis detection limit of *ca.* 0.5%, its quantity was accounted as $0.25\% \pm 0.25\%$ over these samples.

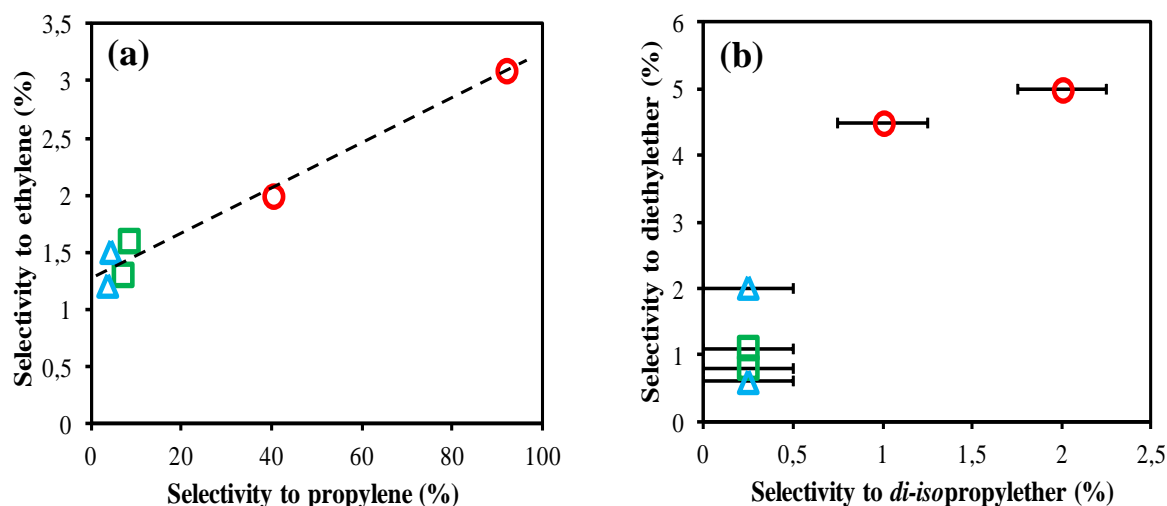


Figure 3-27 (a) Selectivity to ethylene as a function of the selectivity to propylene; (b) Selectivity to diethylether as a function of the selectivity to *di-isopropylether* (red circles representing HapD and Hap, green squares for carbonated apatites, namely Hap-CO₃ and HapNa-CO₃, and blue triangles for carbonate-rich apatites, namely HapE-CO₃ and HapE-Na-CO₃).

Figure 3-27(a) shows a good correlation between ethylene and propylene selectivities. The selectivity to ethylene did not vary much for group *ii* & *iii* catalysts, with a value of $1.4 \pm 0.2\%$, but increased for group *i* catalysts, namely Hap (2%) and HapD (3.1%). Then, HapD and Hap exhibited higher selectivity to both ethylene and propylene, thus showing their predominant acidic nature compared to the other apatite catalysts. A consistent correlation was obtained for the plot of *diethylether* selectivity as a function of *di-isopropylether* selectivity [Figure 3-27(b)], with the presence of low amounts of both compounds over group *ii* & group *iii* catalysts, and of more significant amounts over

group *i* catalysts. Then, the predominant acidic nature of group *i* catalysts was responsible for both inter- and intra-molecular dehydration of the respective substrates.

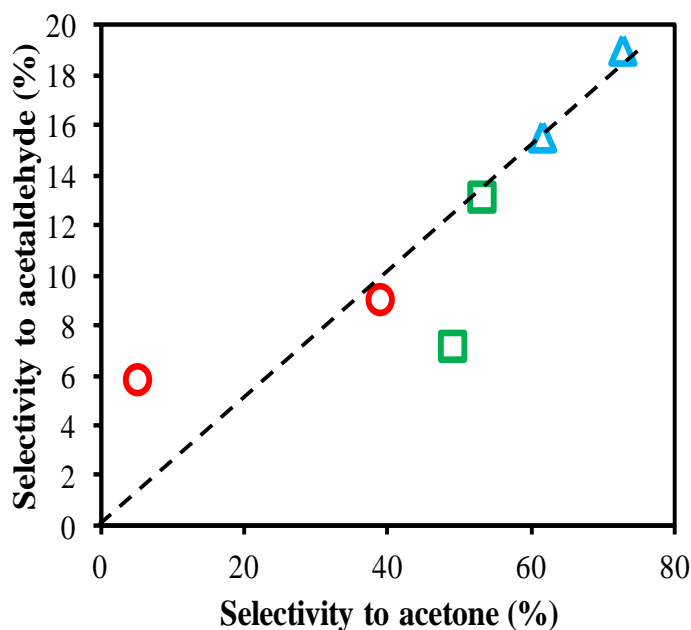


Figure 3-28 Selectivity to acetaldehyde as a function of the selectivity to acetone (red circles representing HapD and Hap, green squares for carbonated apatites, namely Hap-CO₃ and HapNa-CO₃, and blue triangles for carbonate-rich apatites, namely HapE-CO₃ and HapE-Na-CO₃).

Figure 3-28 shows the variation in the acetaldehyde selectivity (dehydrogenation product from ethanol in the Guerbet reaction) with the acetone selectivity (dehydrogenation product of *isopropanol*), both originating from a reaction over basic sites. A rather good correlation is obtained. Selectivity to acetaldehyde increased from 5.8% in HapD (group *iii*) to 19% in HapE-Na-CO₃ (group *iii*) along with an increase in acetone selectivity, respectively from 5% to 72.8%. Higher selectivity to both acetone and acetaldehyde over the carbonate-rich apatites (group *iii*) indicated their predominant basic character compared to the other apatites. In addition, a linear increase (represented by the dashed line in Figure 3-28) was observed especially for the apatites that are highly selective to acetone and acetaldehyde. However, a direct correlation considering acetaldehyde selectivity is difficult because acetaldehyde is an intermediate in the Guerbet reaction of ethanol and can further undergo condensation reaction to heavier products through the whole sequence of Guerbet reaction steps. This is not the case for acetone formation, as this product is a ‘dead-end’

product in the reaction of *isopropanol* that is not further consumed to form other compounds. So, there is a large chance to underestimate the basic nature of a catalyst in the ethanol conversion reaction by only looking at its acetaldehyde selectivity, because acetaldehyde can further undergo condensation to heavier products through the Guerbet chemistry. This may be the reason why some catalysts (*e.g.*, Hap-CO₃, represented by the lower green square) show deviation from the linearity to lower acetaldehyde selectivity, while supposedly behaving significant dehydrogenation properties.

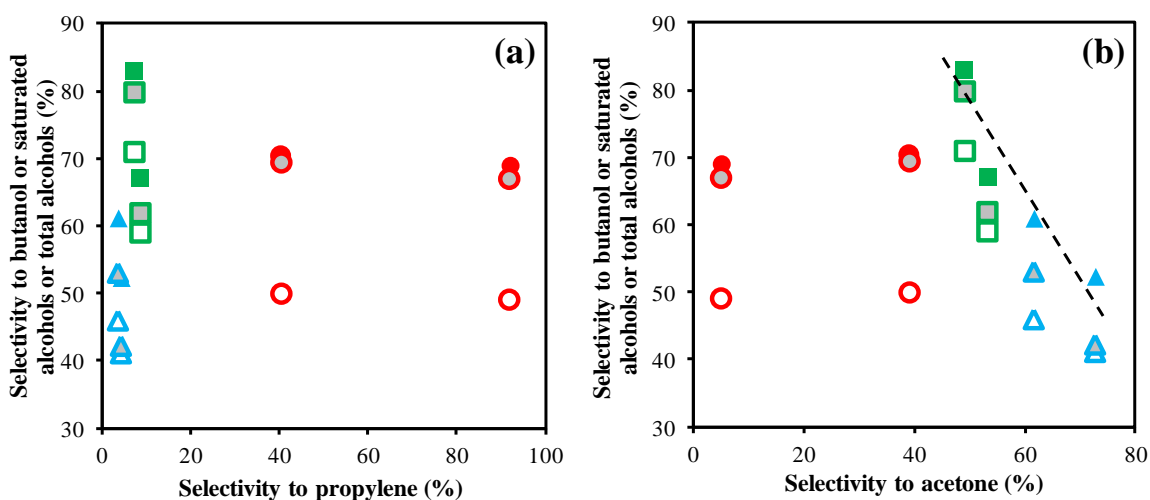


Figure 3-29 (a) Selectivity to butanol or saturated alcohols or total alcohols as a function of the selectivity to propylene, (b) Selectivity to butanol or saturated alcohols or total alcohols as a function of the selectivity to acetone. Selectivity to butanol is represented by open symbols, while selectivity to saturated alcohols (excluding 2-buten-1-ol) is represented by grey-filled symbols and selectivity to total alcohols (thus including 2-buten-1-ol) is represented by color-filled symbols (red circles representing HapD and Hap, green squares for carbonated apatites, namely Hap-CO₃ and HapNa-CO₃, and blue triangles for carbonate-rich apatites, namely HapE-CO₃ and HapE-Na-CO₃).

No straightforward linear correlation was observed between propylene selectivity (acid character) and any class of Guerbet alcohols (butanol or saturated alcohol or total alcohol) selectivity, as shown in Figure 3-29(a). However, a sharp increase in Guerbet alcohols selectivity from carbonate-rich apatites to carbonated apatites was observed for small increase in propylene selectivity. The behavior of Hap and HapD is deviating from that of the other catalysts due to their higher propylene selectivity, and, hence, to an especially predominant acidic behavior compared to the other catalysts (see also Figure 3-27). The

selectivity to Guerbet alcohols (butanol or saturated alcohols or total alcohols) remained almost similar in HapD and Hap, while the selectivity to propylene over these samples gave a *ca.* 2-fold increase with values of 40.3% and 92%, respectively. This reveals that a too large increase in the acidic character of the solids has definitely no significant effect in the selectivity to Guerbet alcohols. However, it is worth mentioning that the difference between saturated alcohols selectivity (grey filled symbols) and butanol selectivity (open symbols) is higher in HapD and Hap compared to the other catalysts, which shows the ability of these apatites, with predominant acidic behavior, to further condense butanol & ethanol to C6-C10 alcohols. Moreover, the difference between total alcohols selectivity (filled symbols) and saturated alcohols selectivity (grey filled symbols), which is due to the selectivity of 2-buten-1-ol, was more pronounced in carbonate-rich apatites.

A relationship between the selectivities to all the types of Guerbet alcohols (butanol or saturated alcohols or total alcohols) and the selectivity to acetone (dehydrogenation character) is further shown in Figure 3-29(b). In any case, the Guerbet alcohols selectivity was at least 40%, even for the samples with rather low acetone selectivity (*e.g.*, even for HapD that exhibited an acetone selectivity of 5.8%, and thus a dehydrogenation property which is not predominant). Further, the selectivity to butanol, to saturated alcohols and to total alcohols remained similar in HapD and Hap (group *i*), though acetone selectivity increased from 5% (HapD) to 39% (Hap), thus suggesting that only a ‘slight’ dehydrogenation property might be needed to initiate and smoothly run Guerbet cycles. This dehydrogenation property is supposedly due to the weak or/and medium basic sites since HapD lacks stronger basic sites (as shown in sections 3.2.1.6.2 & 3.2.1.6.3). All the types of Guerbet alcohols selectivities then reached a maximum when a slight increase in acetone selectivity to 49% in Hap-CO₃ was observed, but this increase is most likely linked with a difference of acid properties. A linear decrease in total alcohols selectivity (represented by a dashed line) was observed with further increase in acetone selectivity for group *ii* and group *iii* catalysts. A similar trend was also observed for butanol and saturated alcohols selectivities. Since high acetone selectivity represents a highly basic behavior of the catalysts, the above observation of a linear decrease in alcohol selectivity strongly suggests that too much basic behavior had a detrimental effect on the alcohols selectivity. A large difference between the saturated alcohols selectivity (grey filled symbols) and butanol selectivity (open symbols) in HapD and Hap catalysts compared to the other catalysts is clearly observed in Figure 3-29 (b) as in Figure 3-29(a). The deviation in

butanol or saturated or total alcohols and the acetone selectivities away from the line of linear correlation was again confirmed in the case of HapD and Hap.

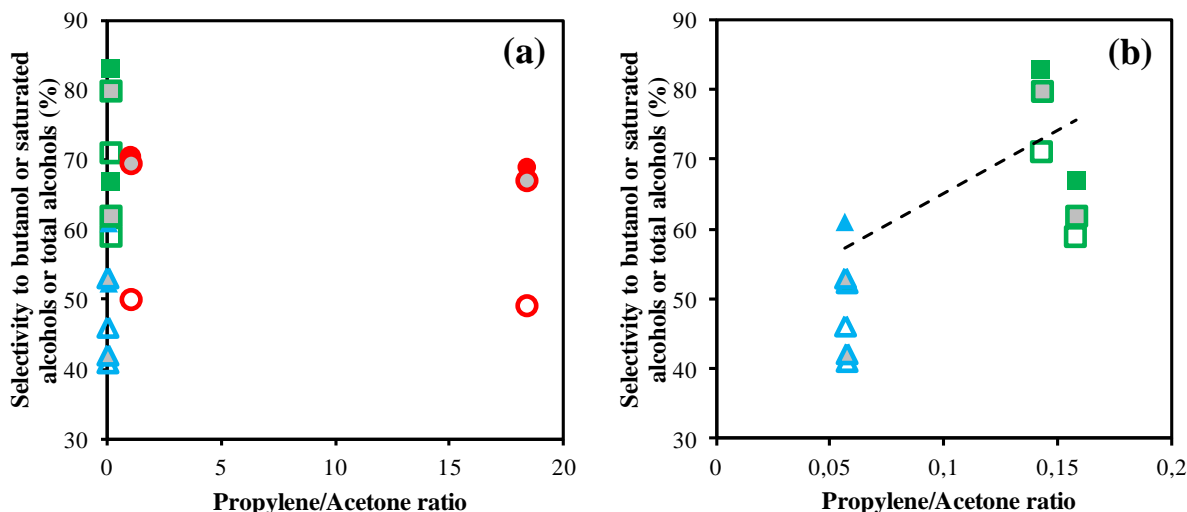


Figure 3-30 (a) Selectivity to butanol or saturated alcohols or to total alcohols as a function of the propylene/acetone ratio (b) Same figure focused on a narrower range of propylene/acetone ratio (from 0 to 0.2). Selectivity to butanol is represented by open symbols, while selectivity to saturated alcohols (excluding 2-buten-1-ol) is represented by grey-filled symbols and total alcohols is represented by color-filled symbols (red circles representing HapD and Hap, green squares for carbonated apatites, namely Hap-CO₃ and HapNa-CO₃, and blue triangles for carbonate-rich apatites, namely HapE-CO₃ and HapE-Na-CO₃).

Since the Guerbet reaction of ethanol to all kinds of heavier alcohols depends both on the acidic and the basic behavior of the catalysts, we further investigated the variation in butanol and total alcohols selectivities as a function of the propylene to acetone ratio. Figure 3-30 (a) shows an increase in the butanol, saturated and total alcohols selectivities from carbonate-rich apatites to carbonated apatites, when an increase in the propylene/acetone ratio is observed, from, respectively, 0.05 to 0.15. The selectivity to all the types of Guerbet alcohols (butanol, saturated and total alcohols) then decreased with further increase in the propylene/acetone ratio from 0.15 in carbonated apatites to 1.0 in Hap. Furthermore increasing the propylene/acetone ratio from 1.0 to 18.4 did not yield any effect in butanol or saturated or heavier alcohols selectivities. Figure 3-30 (b) clearly shows that there is a particular narrow range for the propylene/acetone ratio that represents the acid-base behavior in apatites to obtain maximum selectivity to all Guerbet alcohols. The large difference between the saturated alcohols selectivity (grey filled symbols) and

butanol selectivity (open symbols) once again underlined that condensation of butanol and ethanol to C6-C10 alcohols is more pronounced over Hap and HapD, over which the acid character is much more predominant than the basic one. Hence this observation really points out the fact that very fine-tuning between the quantities of both antagonist sites is required to promote the Guerbet reaction.

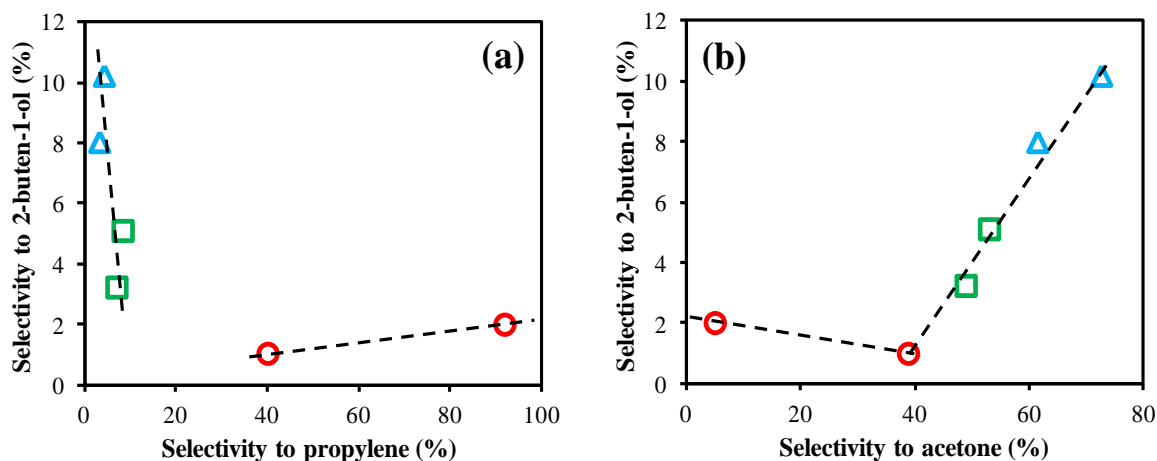


Figure 3-31 Selectivity to 2-buten-1-ol as a function of (a) the selectivity to propylene and (b) the selectivity to acetone (red circles representing HapD and Hap, green squares for carbonated apatites, namely Hap-CO₃ and HapNa-CO₃, and blue triangles for carbonate-rich apatites, namely HapE-CO₃ and HapE-Na-CO₃).

Since 2-buten-1-ol is an intermediate in the Guerbet reaction of ethanol to butanol, a direct correlation with catalysts acid-base behavior becomes difficult, as in the case of acetaldehyde. However, to verify the presence of any indirect correlation, the variation in the 2-buten-1-ol selectivity as a function of the propylene and the acetone selectivities was studied, as shown in Figure 3-31. A linear decrease (represented by a dashed line) in the selectivity to 2-buten-1-ol from 10.2% to 3.2% was observed when the propylene selectivity increased from carbonate rich apatite (4.2%) to carbonated apatite (7%) [Figure 3-31(a)]. Selectivity to 2-buten-1-ol reached a minimum of 1% with further increase in propylene selectivity to 40.3% in Hap. Further increase in propylene selectivity to 92% did not yield any significant variation of the 2-buten-1-ol selectivity. Since propylene formation is related to the acidic behavior, the above observation reveals that 2-buten-1-ol selectivity was decreased even with a slight increase in the acidic behavior for catalysts that are less acidic in nature (*i.e.*, with a higher relative proportion of basic sites). Further increasing too much the acidic behavior had no effect on 2-buten-1-ol selectivity. Figure 3-

31(a) clearly shows a deviation of two acidic catalysts from the linear behavior of all other catalysts, which is good in agreement with previous observations. Figure 3-31(b) shows that an increase in acetone selectivity from 5% to 39% could not yield much variation in the 2-buten-1-ol selectivity. However, a linear increase (represented by the dashed line) in 2-buten-1-ol selectivity from 3.2% to 10.2% was clearly observed with further increase in acetone selectivity from 39 % to 72.8%. Hence, the 2-buten-1-ol selectivity over apatite catalysts remains unchanged with increase in the basic behavior up to a certain limit and then starts increasing linearly with the basic character.

As a conclusion to this part, interesting correlations were obtained between the Guerbet ethanol reaction and the *isopropanol* test. The selectivities to propylene and *diisopropylether* were both found to be correlated with the ethylene and the diethylether selectivities, respectively, and their formation confirms the higher acidic behavior of Hap and HapD (group *i*) compared to the other catalysts. The deviation observed for the highly efficient Guerbet catalyst Hap-CO₃ further confirmed the difficulty in the direct correlation of acetaldehyde selectivity, which is an intermediate in the Guerbet reaction. Selectivity to C6-C10 alcohols were larger over group *i* catalysts, which are more acidic in nature, thus revealing the fact that the presence of acid sites facilitates butanol and ethanol condensation. Almost all the observations clearly indicated that very fine tuning of the apatite catalysts is necessary to avoid the competitive side reactions like dehydration and to have a maximum selectivity to Guerbet alcohols.

3.2.2.1.2 Direct correlation studies of Guerbet reaction and acid-base properties of the apatites

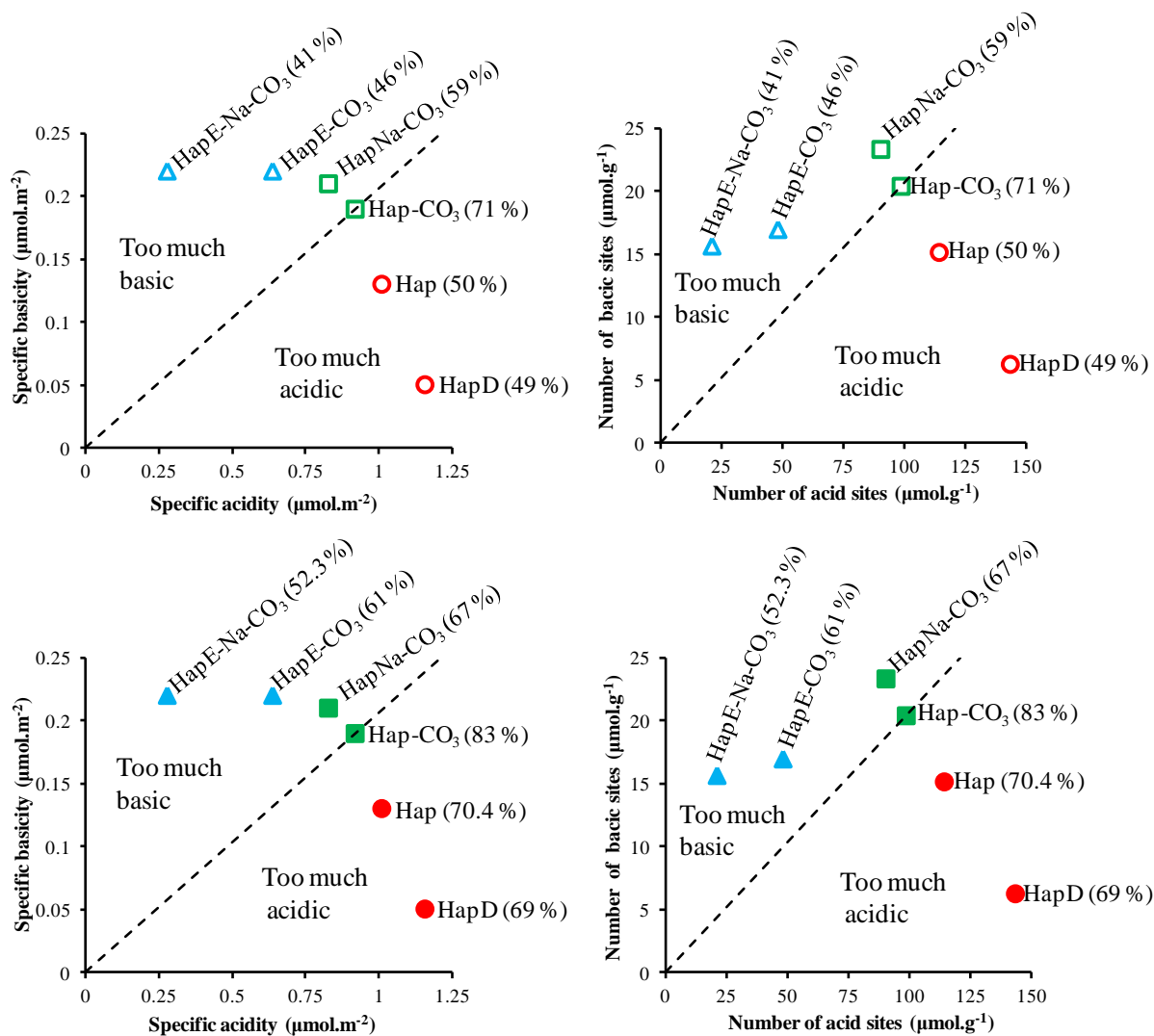


Figure 3-32 Basicity of apatite catalysts as a function of acidity of the catalysts (both expressed per gram and per m^2 – specific acidity). (red circles representing HapD and Hap, green squares for carbonated apatites, namely Hap-CO₃ and HapNa-CO₃, and blue triangles for carbonate-rich apatites, namely HapE-CO₃ and HapE-Na-CO₃). Selectivity to butanol is given in brackets next to open symbols while the value of selectivity to total alcohols is given in brackets next to filled symbols.

After indirect correlation with the results of the *isopropanol* test, direct correlation of the Guerbet reactivity with the measured acid-base properties was studied.

Plots of the number of basic sites as a function of the number or density of acid sites (Figure 3-32) for the apatite catalysts have shown an interesting relation between acid-base properties and the Guerbet reaction, though direct linear relation was not observed. A

similar trend was observed for the plots of specific acid-base properties (per square meters) and of the total number of acid-base sites (per gram, representative of the number of sites present in the reactor for a given catalytic test – use of iso-mass of catalysts each test). From the results, we assumed that Hap-CO₃ is not so far from being an ideal catalyst that possesses well-balanced acid-base properties, enabling a maximum selectivity to butanol or to total alcohols. Then, we plotted a dashed line from the origin to the point representing Hap-CO₃. On this line, the relative density of base to acid sites is 0.2 (slope). Then, we can suppose that any apatite catalyst (or if we may generalize this assumption, that any solid) which lies in this line shows a good compromise between acid and basic sites and can give a maximum selectivity to butanol or to total alcohols. Then, the ideal catalyst should have 5 times more acid sites than basic ones (furthermore, well distributed on the surface to enable the Guerbet reaction sequence, thus using antagonist sites that are supposedly close one to another). Catalysts that are in the region above this line possess too much basic sites. This is the reason why HapNa-CO₃ shows a lower selectivity to butanol or to total alcohols though it possesses a higher amount of basic sites compared to the so-called ‘ideal’ Hap-CO₃ catalyst. This is the same for carbonate-rich apatites, namely HapE-CO₃ and HapE-Na-CO₃, with basicity/acidity ratios (slopes) of 0.4 and 0.7, respectively, compared to the ‘ideal’ 0.2. Moreover, the catalysts that lie below the dashed line possess a too large proportion of acid sites compared to the ideal Hap-CO₃ catalyst. This is the reason why Hap and HapD with basicity/acidity ratios of 0.04 and 0.13, respectively, show lower butanol or total alcohols selectivities compared to Hap-CO₃, though they possess higher amount or density of acid sites than Hap-CO₃.

In the followings, we systematically looked for potential correlations between the number/nature of sites with the selectivity to the main products. This enabled revealing global trends, corroborating the above observations of Figure 6.

3.2.2.1.2.1 Selectivity to ethylene as a function of acid-base properties of HAP catalysts

Selectivity to ethylene remains almost unchanged, though the number of acid sites increased from 21.2 $\mu\text{mol.g}^{-1}$ (HapE-Na-CO₃) to 98.7 $\mu\text{mol.g}^{-1}$ (Hap-CO₃), as shown by dashed line parallel to the x -axis in Figure 3-33(a). In contrast, further increase in the amount of acid sites to 114.5 $\mu\text{mol.g}^{-1}$ (Hap) and 143.4 $\mu\text{mol.g}^{-1}$ (HapD) yielded, as a

consequence, a linear increase of the ethylene selectivity to 2% and 3.1%, respectively. This, again, as shown using the comparison with the *isopropanol* reactivity test, clearly indicates the predominant acidic behavior of Hap, and especially of HapD, compared to the other samples.

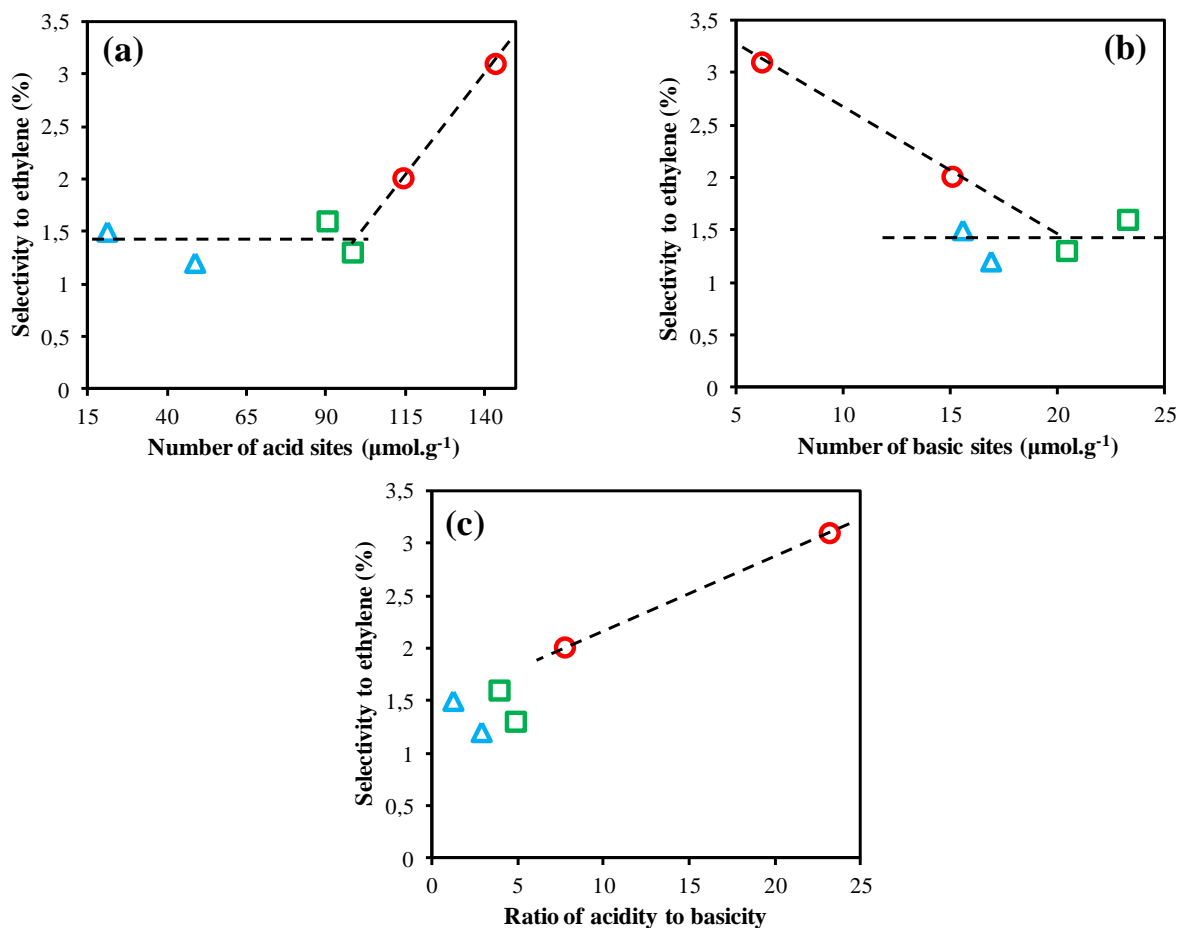


Figure 3-33 Selectivity of ethylene as a function of (a) the number of acid sites, (b) the number of basic sites, and (c) the ratio of acidity to basicity in HAPs (red circles representing HapD and Hap, green squares for carbonated apatites, namely Hap-CO₃ and HapNa-CO₃, and blue triangles for carbonate-rich apatites, namely HapE-CO₃ and HapE-Na-CO₃).

It is well known that ethylene is formed by ethanol dehydration over acid sites. Thus, while it is obvious that a direct relation between ethylene selectivity and the number basic sites should not exist, a graph was plotted to present the selectivity to ethylene as a function of the number of basic sites [Figure 3-33 (b)], in order to check about potential indirect correlations. A linear decrease in ethylene selectivity from 3.1% to 2% was observed with an increase in the number of basic sites from 6.2% in HapD to 15.1% in Hap. Further increase in the number of basic sites yielded a slight decrease in the ethylene selectivity,

which then remained essentially unchanged above all the other apatites, with a value close to 1.5%. We obviously suppose the initial linear decrease in ethylene selectivity is not related to the increase in the amount of basic sites, but with the higher amount of acid sites above the concerned samples, as explained above. However, this again clearly shows that the behavior of HapD and Hap deviates from that of the other catalysts, underlining the predominant influence of their acidic nature on their chemical properties (reactivity) compared to the other apatites.

Since both acid and basic sites have important roles in Guerbet chemistry, the variation in ethylene selectivity as a function of the ratio of acidity to basicity was studied [Figure 3-33(c)]. The ethylene selectivity remained almost unchanged with the increase in the ratio of acidity to basicity from 1.3 (HapE-Na-CO₃) to 4.8 (Hap-CO₃). Further increase in this ratio to 7.8 (Hap) and 20.2 (HapD) yielded a linear increase in ethylene selectivity to 2% and 3.1%, respectively. Hence, the trend observed in the variation in ethylene selectivity with acidity to basicity ratio was found to be similar with the variation in ethylene selectivity with number of acid sites alone [Figure 3-33(a)], which reflects the predominance of acid sites over basic sites in the apatite catalysts (they possess more acid sites than basic sites). We then wanted to deepen the interpretation of the results and checked about the influence of the nature of the acid sites.

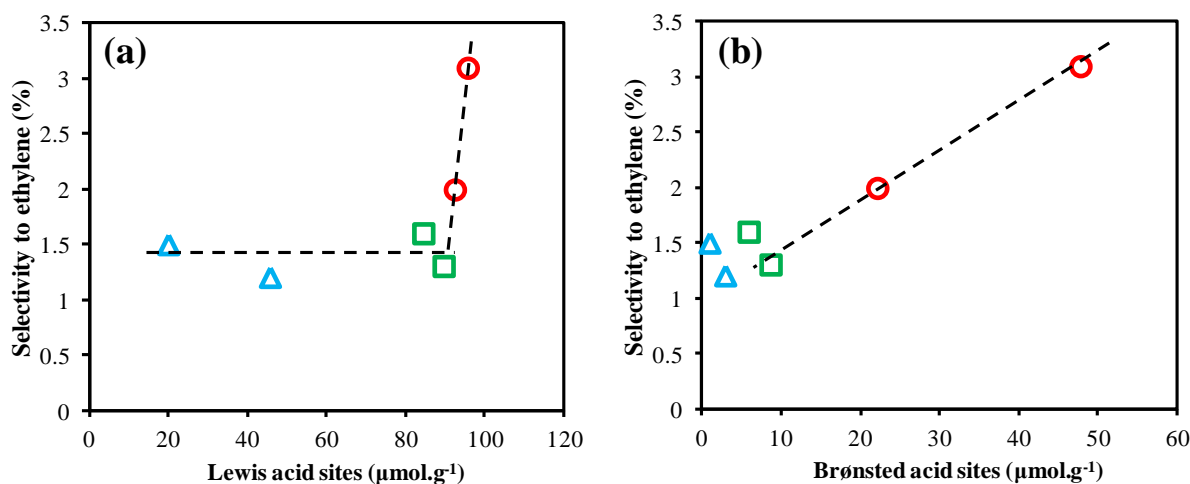


Figure 3-34 Selectivity of ethylene as a function of (a) the number of Lewis acid sites, and (b) the number of Brønsted sites (red circles representing HapD and Hap, green squares for carbonated apatites, namely Hap-CO₃ and HapNa-CO₃, and blue triangles for carbonate-rich apatites, namely HapE-CO₃ and HapE-Na-CO₃).

The selectivity to ethylene as a function of the number of the Lewis and of the Brønsted acid sites is shown in Figure 3-34. Figure 3-34(a) shows that ethylene selectivity remained almost unchanged though the amount of Lewis acid sites increased from $20.2 \mu\text{mol.g}^{-1}$ (HapE-Na-CO₃) to $89.9 \mu\text{mol.g}^{-1}$ (Hap-CO₃). Further slight increase in the number of Lewis acid sites to $92.4 \mu\text{mol.g}^{-1}$ (Hap) and $95.6 \mu\text{mol.g}^{-1}$ (HapD) was observed related to a sudden increase in the ethanol selectivity to 2% and 3.1%, respectively. Increase in the number of Brønsted acid sites from $1 \mu\text{mol.g}^{-1}$ (HapE-Na-CO₃) to $8.8 \mu\text{mol.g}^{-1}$ (Hap-CO₃) did not yield any significant variation in the ethylene selectivity. In contrast to a sudden increase in ethylene selectivity with Lewis acid sites, a linear increase in ethylene selectivity to 2% (Hap) and 3.1% (HapD) was observed with further increase in the number of Brønsted acid sites, respectively to $22.1 \mu\text{mol.g}^{-1}$ and $47.8 \mu\text{mol.g}^{-1}$.

Since the number of both Lewis and Brønsted acid sites contribute to total number of acid sites, variation in these sites should be equally reflected in total acid sites. Hence, a comparison in ethylene selectivity for both Lewis and Brønsted acid sites (Figure 3-34) together with total acid sites [Figure 3-33 (a)] can provide the information regarding the nature of sites that contributes mainly towards the ethylene selectivity. Figure 3-33(a) shows that ethylene selectivity linearly increased from 2% in Hap to 3.1% in HapD with increase in total number of acid sites from $114.5 \mu\text{mol.g}^{-1}$ to $143.4 \mu\text{mol.g}^{-1}$ (an increase of $28.9 \mu\text{mol.g}^{-1}$). For the same increase in ethylene selectivity from 2 % to 3.1 %, the number of Lewis sites increased from $92.4 \mu\text{mol.g}^{-1}$ to $95.6 \mu\text{mol.g}^{-1}$ (an increase of only $3.2 \mu\text{mol.g}^{-1}$) and the number of Brønsted sites increased from $22.1 \mu\text{mol.g}^{-1}$ to $47.8 \mu\text{mol.g}^{-1}$ (an increase of $25.7 \mu\text{mol.g}^{-1}$). This is a clear indication that it is the Brønsted acid sites that mainly contribute to the ethylene selectivity. If this were not the case, ethylene selectivity would have increased with slight increase in total number of acid sites as observed in the case of Lewis acid sites. Then, we can deduce that ethanol dehydration mainly proceeds over Brønsted acid sites. To this respect, it is also worth mentioning that the Guerbet reaction releases water. Then, at least some Lewis sites observed during *ex situ* measurements might undergo hydration and be converted to Brønsted sites during the reaction, which can either be used for catalysis or be dehydrated to recover the initial Lewis sites under the reaction conditions. Equilibrium should be reached, but it is very difficult to predict the proportion between species.

3.2.2.1.2.2 Selectivity to diethylether as a function of acid-base properties of HAP catalysts

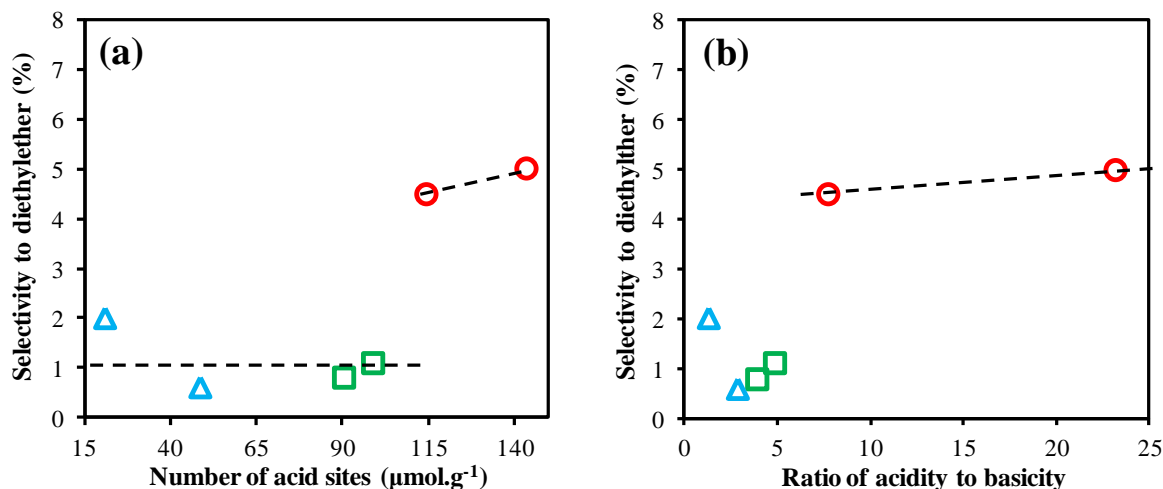


Figure 3-35 Selectivity to diethylether as a function of (a) the number of acid sites and (b) the ratio of acidity to basicity in HAPs (red circles representing HapD and Hap, green squares for carbonated apatites, namely Hap-CO₃ and HapNa-CO₃, and blue triangles for carbonate-rich apatites, namely HapE-CO₃ and HapE-Na-CO₃).

Diethylether is formed by intermolecular dehydration of ethanol over the acid sites. Figure 3-35(a) shows the variation in selectivity to diethylether as a function of the number of acid sites. The selectivity to diethylether remained almost unchanged (at *ca.* 1%) even with a significant increase in the number of acid sites from 21.2 $\mu\text{mol.g}^{-1}$ to 98.7 $\mu\text{mol.g}^{-1}$ (note that HapE-Na-CO₃ shows slight deviation). The diethylether selectivity then increased to 4.5% with increase in the number of acid sites to 114.5 $\mu\text{mol.g}^{-1}$ and remained similar for further increase in the number of acid sites to 143.4 $\mu\text{mol.g}^{-1}$. This observation indicates that increase in the number of acid sites has no effect on selectivity to diethylether up to a certain limit and, then, a sudden increase in the diethylether selectivity is observed for a further rather small increase in the amount of acid sites. A deviation for catalysts with higher number of acid sites compared to the other catalysts is then clearly observed. Almost similar trend was obtained for the plot of diethylether selectivity as a function of the ratio of acidity to basicity as shown in Figure 3-35(b). All the above observations are good in agreement with the previous results showing the variation of diethylether selectivity as a function of the *di-isopropylether* selectivity [Figure 3-27(b)].

To further study the effect of the nature of acid sites on selectivity to diethylether, the variation in diethylether selectivity was plotted as a function of the number of Lewis and of

Brønsted acid sites, as shown in Figure 3-36. The selectivity of diethylether remains almost unchanged with increase in the number of Lewis acid sites from $20.2 \mu\text{mol.g}^{-1}$ to $89.9 \mu\text{mol.g}^{-1}$, as shown in Figure 3-36 (a). Diethylether selectivity increased from 1.1% to 4.5% and 5%, though the number of Lewis acid sites did not vary much. Figure 3-36(b) shows that the diethylether selectivity remains almost same for an increase in number of Brønsted acid sites from $1 \mu\text{mol.g}^{-1}$ to $8.8 \mu\text{mol.g}^{-1}$. Selectivity to diethylether then increased to 4.5% with an increase in the number of Brønsted acid sites from $8.8 \mu\text{mol.g}^{-1}$ to $22.1 \mu\text{mol.g}^{-1}$. As aforementioned, variation with respect to the number of Lewis and Brønsted sites will be equally reflected, as in the total number of acid sites. For the increase in diethylether selectivity from 1.1% to 4.5%, the total number of acid sites increased from $98.7 \mu\text{mol.g}^{-1}$ to $114.5 \mu\text{mol.g}^{-1}$ (*i.e.*, an increase of $15.8 \mu\text{mol.g}^{-1}$). Comparing this increase in total acid sites number with the increase in the number of Lewis acid sites (of only $2.5 \mu\text{mol.g}^{-1}$), and increase in the number of Brønsted sites (of $13.3 \mu\text{mol.g}^{-1}$), we could conclude that the Brønsted acid sites are mainly responsible for the formation of diethylether by intermolecular dehydration of ethanol.

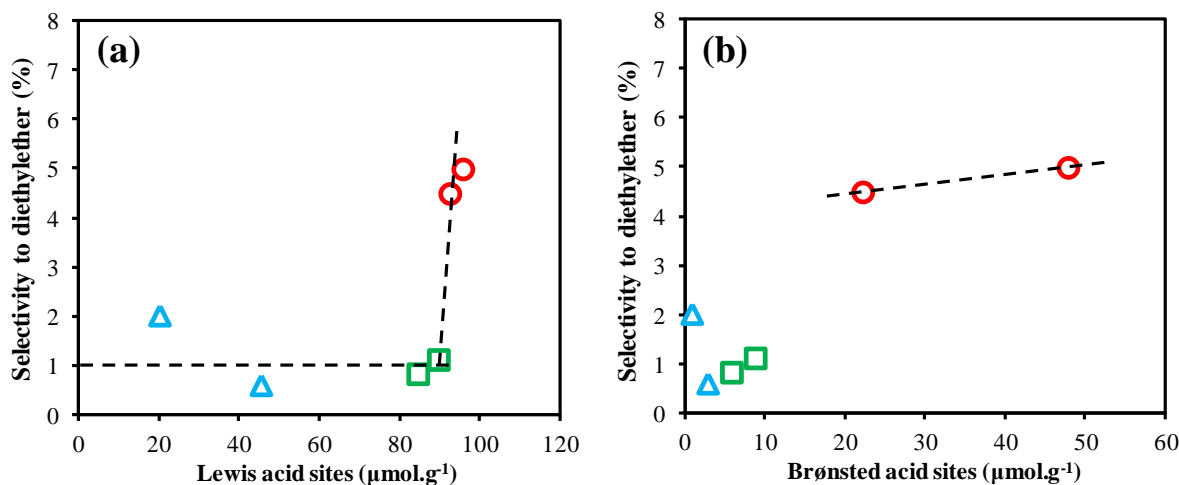


Figure 3-36 Selectivity to diethylether as a function of (a) the number of Lewis acid sites and (b) the number of Brønsted acid sites in HAPs (red circles representing HapD and Hap, green squares for carbonated apatites, namely Hap-CO₃ and HapNa-CO₃, and blue triangles for carbonate-rich apatites, namely HapE-CO₃ and HapE-Na-CO₃).

3.2.2.1.2.3 Selectivity to acetaldehyde as a function of acid-base properties of HAP catalysts

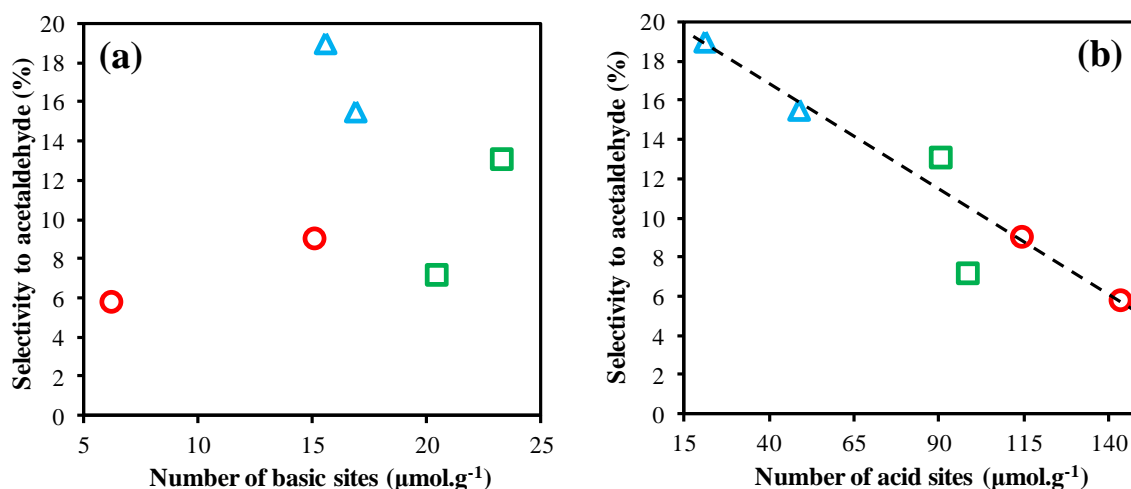


Figure 3-37 Selectivity of acetaldehyde as a function of (a) the number of acid sites and (b) the number of basic sites in HAPs (red circles representing HapD and Hap, green squares for carbonated apatites, namely Hap-CO₃ and HapNa-CO₃, and blue triangles for carbonate-rich apatites, namely HapE-CO₃ and HapE-Na-CO₃).

Figure 3-37 shows the variation in acetaldehyde selectivity with the number of acid and basic sites. As aforementioned, it is difficult to have the correlation of acetaldehyde with acid and, especially, basic properties, this latter being supposedly more relevant in that case (dehydrogenation), since acetaldehyde is an intermediate in Guerbet reaction of ethanol, is further consumed during the reaction over efficient catalysts. Hence, a linear relation was not observed between acetaldehyde selectivity and the number of basic sites, especially in carbonate rich apatites which have shown higher acetaldehyde selectivity compared to other apatites [Figure 3-37(a)]. As aforementioned, the lack of stronger basic sites (suppose to further condense acetaldehyde) and the presence of more CaO species (supposedly promote dehydrogenation) in carbonate-rich apatites can also be the cause of this higher acetaldehyde selectivity. However, to verify the possibility of indirect correlation, the variation in the selectivity of acetaldehyde with the number of acid sites was examined as in Figure 3-37(b). A very interesting linear correlation between acetaldehyde selectivity and number of acid sites was obtained. The acetaldehyde selectivity was higher over carbonate-rich apatites HapE-Na-CO₃ (19%) and HapE-CO₃ (15.5%) with lower numbers of acid sites (21.2 $\mu\text{mol.g}^{-1}$ and 48.6 $\mu\text{mol.g}^{-1}$, respectively) compared to other apatites. We suppose that the carbonate-rich apatites lack in a sufficient

number of acid sites, which assists in the condensation of acetaldehyde further to heavier Guerbet products (see Figure 3-32). The acetaldehyde selectivity decreased to 13.1% (HapNa-CO₃) and 7.2% (Hap-CO₃) with increase in number of acid sites to 90.6 μmol.g⁻¹ and 98.7 μmol.g⁻¹, respectively. This decrease in acetaldehyde selectivity is due to the presence of a sufficient number of acid sites in HapNa-CO₃ and Hap-CO₃ catalysts, which assists in condensation of acetaldehyde to heavier products. This confirms that the main reason why Hap-CO₃ shows very low selectivity to acetaldehyde and is highly selective to butanol or heavier alcohols. The lower acetaldehyde selectivity over Hap and HapD with higher number of acid sites compared to the other apatites is not only due to condensation of acetaldehyde, but also to an increased ethylene and diethylether formation over acid sites, in competition with the intermediate formation of acetaldehyde over basic sites, which are two reactions primary consuming ethanol. Hence, the amount of acid sites can indirectly influence the formation of acetaldehyde selectivity.

3.2.2.1.2.4 Selectivity to 2-buten-1-ol as a function of acid-base properties of HAP catalysts

Since 2-buten-1-ol is an intermediate in the Guerbet reaction of ethanol to butanol, finding a direct correlation of its selectivity with the acid-base properties of the solids is rather difficult as in the case of acetaldehyde. However, to identify if potential indirect correlations can arise, the 2-buten-1-ol selectivity was plotted as a function of the acid-base properties of the samples (Figure 3-38).

Figure 3-38(a) shows that the selectivity to 2-buten-1-ol decreased linearly from 10.2 % (HapE-Na-CO₃) to 3.2 % (Hap-CO₃) with an increase in the number of acid sites from 21.2 μmol.g⁻¹ to 98.7 μmol.g⁻¹, respectively. HapD and Hap, which possess higher number of acid sites, showed slight deviation from the linearity like in the previous observations. The variation in 2-buten-1-ol selectivity was not consistent with the number of basic sites, and it was difficult to extract some relation in that case, as shown in Figure 3-38(b). The plot of selectivity to 2-buten-1-ol as a function of the ratio of the number of acid sites to the number of basic sites [Figure 3-38(c)] has shown a trend similar to that presented in Figure 3-38(a), but emphasizing the deviation of HapD and Hap. These results are in good agreement with the results deduced from the plot of 2-buten-1-ol selectivity vs. propylene selectivity [Figure 3-31(a)].

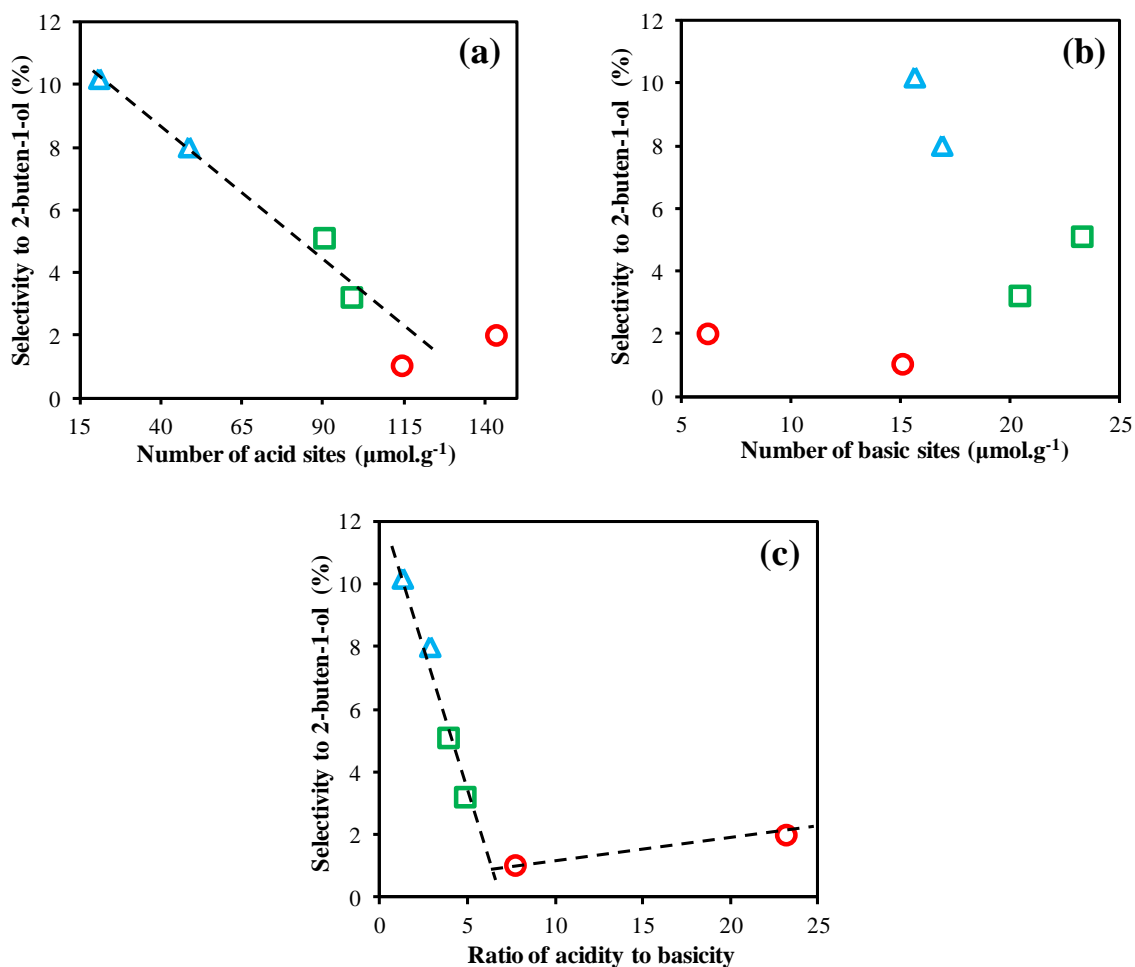


Figure 3-38 Selectivity to 2-buten-1-ol as a function of (a) the number of acid sites, (b) the number of basic sites, and (c) the ratio of acidity to basicity in HAPs (red circles representing HapD and Hap, green squares for carbonated apatites, namely Hap-CO₃ and HapNa-CO₃, and blue triangles for carbonate-rich apatites, namely HapE-CO₃ and HapE-Na-CO₃).

Though indirectly, this above observation clearly indicates that the carbonate-rich catalysts HapE-CO₃ and HapE-Na-CO₃ showing higher selectivity to 2-buten-1-ol due to the lack of a sufficient number of acid sites further transform the intermediate 2-buten-1-ol to butanol during the Guerbet reaction of ethanol. The 2-buten-1-ol selectivity was decreased to 5.1% and 3.2% in carbonated apatites with increase in the number of acid sites, thus confirming the assistance of acid sites in transformation of 2-buten-1-ol to butanol. The catalysts HapD and Hap with higher number of acid sites have also shown lower selectivity to 2-buten-1-ol though they deviate from the linearity of other apatites.

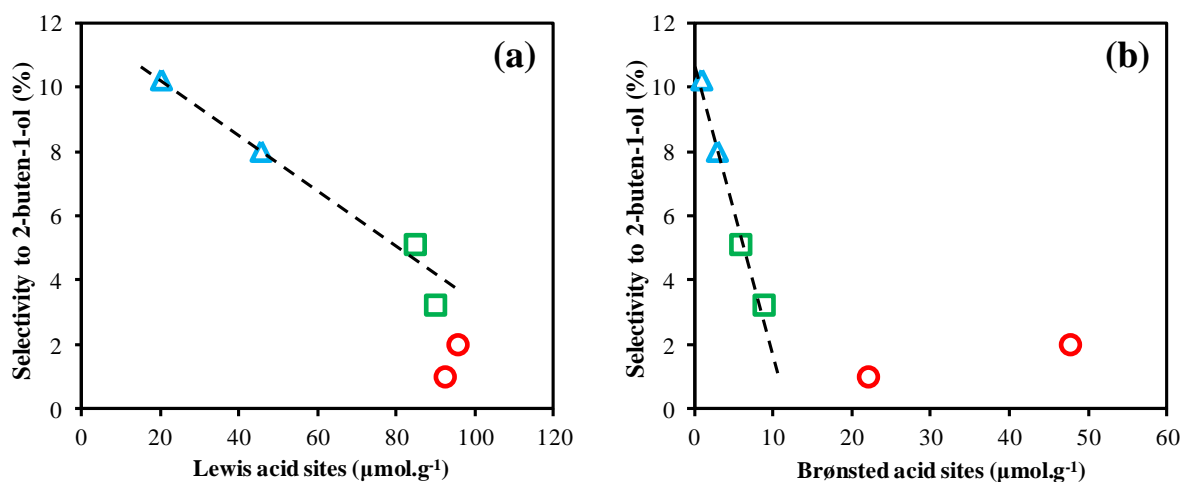


Figure 3-39 Selectivity of 2-buten-1-ol as a function of (a) the number of Lewis acid sites, and (b) the number of Brønsted acid sites in HAPs (red circles representing HapD and Hap, green squares for carbonated apatites, namely Hap-CO₃ and HapNa-CO₃, and blue triangles for carbonate-rich apatites, namely HapE-CO₃ and HapE-Na-CO₃).

To gain an insight on the nature of the acid sites, which mainly assist in the 2-buten-1-ol transformation to butanol, the selectivity of 2-buten-1-ol as a function of the number of Lewis and Brønsted acid sites was plotted (Figure 3-39). 2-buten-1-ol selectivity decreased linearly from 10.2% to 3.2% with increase in the number of Lewis acid sites from 20.2 μmol.g⁻¹ to 89.9 μmol.g⁻¹, respectively. A similar but sharp decrease in 2-buten-1-ol selectivity was observed with a small increase in the number of Brønsted acid sites from 1 μmol.g⁻¹ to 8.8 μmol.g⁻¹. As aforementioned, by comparing the increase in the number of total acid sites (of 77.5 μmol.g⁻¹), the increase in the number of Lewis acid sites (of only 69.7 μmol.g⁻¹) and increase in the number of Brønsted sites (of 7.8 μmol.g⁻¹) with the decrease in 2-buten-1-ol selectivity from 10.2% to 3.2%, we could conclude that it is mainly the Lewis acid sites that contribute to the 2-buten-1-ol transformation to butanol.

3.2.2.1.2.5 Selectivity to Guerbet alcohols as a function of acid-base properties of HAP catalysts

It is difficult to find a direct correlation between the Guerbet alcohols selectivities (butanol, saturated alcohols or total alcohols) and number of acid sites. However, a rather linear increase (represented by the dashed line for total alcohols) in all the Guerbet alcohols selectivities was observed with an increase in number of acid sites from 21.2 μmol.g⁻¹ (HapE-Na-CO₃) to 98.7 μmol.g⁻¹ (Hap-CO₃), as shown in Figure 3-40(a).

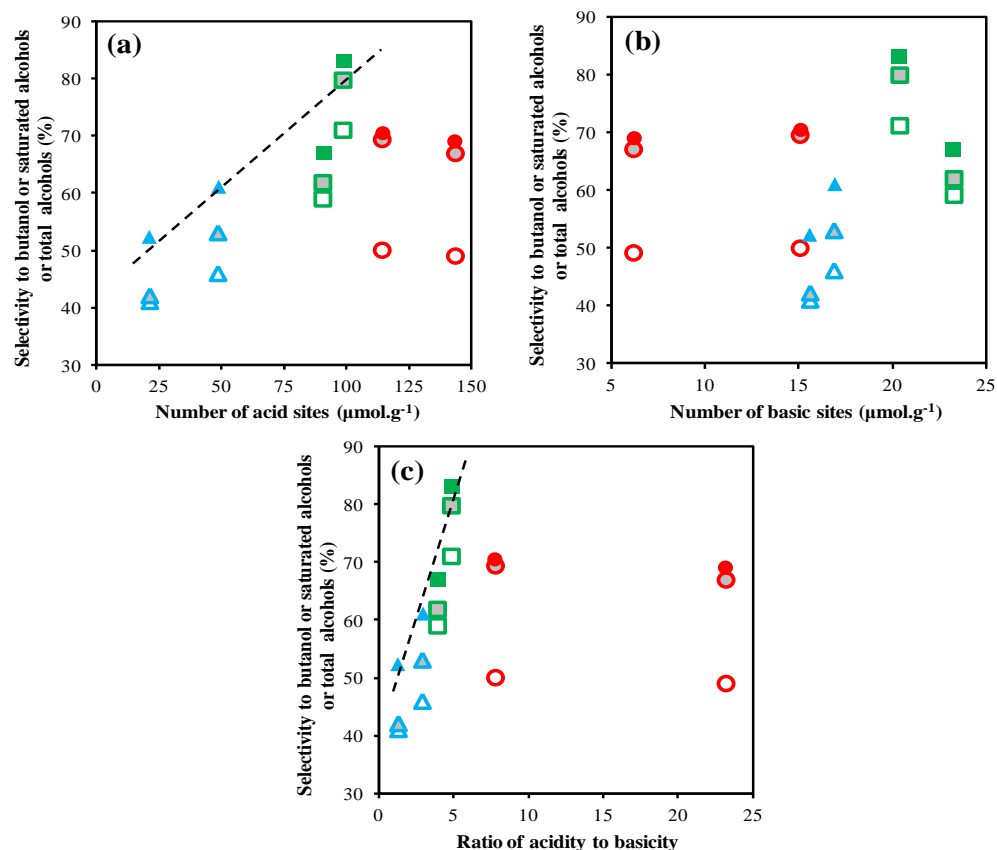


Figure 3-40(a) Selectivity to butanol or saturated alcohols or total alcohols as a function of the number of acid sites, (b) Selectivity to butanol or saturated alcohols or total alcohols as a function of the number of basic sites, (c) Selectivity to butanol or saturated alcohols or total alcohols as a function of the ratio of the number of acid sites to the number of basic sites.. Selectivity to butanol is represented by open symbols, while selectivity to saturated alcohols (excluding 2-buten-1-ol) is represented by grey-filled symbols and heavier alcohols is represented by color-filled symbols (red circles representing HapD and Hap, green squares for carbonated apatites, namely Hap-CO₃ and HapNa-CO₃, and blue triangles for carbonate-rich apatites, namely HapE-CO₃ and HapE-Na-CO₃).

Hap and HapD again showed deviation from linearity due to their higher number of acid sites (114.5 $\mu\text{mol.g}^{-1}$ and 143.4 $\mu\text{mol.g}^{-1}$, respectively). Selectivity to butanol, saturated alcohols or total alcohols remains unchanged even when the number of acid sites increased from 114.5 $\mu\text{mol.g}^{-1}$ (Hap) to 143.4 $\mu\text{mol.g}^{-1}$ (HapD), which shows that too much increase in the number of acid sites has not much influence on the Guerbet alcohols selectivity. The difference between the grey-filled symbols (saturated alcohols selectivity) and open symbols (butanol selectivity) is the C6-C10 alcohols, and this difference is higher over Hap and HapD compared to other catalysts. It is an indirect representation showing the ability of these apatites with predominant acidic behavior to further condense butanol & ethanol

to C6-C10 alcohols. All these observations are in good agreement with Figure 3-29(a) showing the relation between Guerbet alcohols selectivity with propylene selectivity. In contrast, a consistent correlation was not obtained between the butanol, saturated alcohols or total alcohols with the number of basic sites, as shown in Figure 3-40(b). However, a difference between the grey-filled symbols and the open symbols, which represents the formation of C6-C10 alcohols, is clearly observed, though no consistent trend could be revealed.

Since the production of Guerbet alcohols is subjected to the contribution from both acid and basic sites, the Guerbet alcohols (butanol, saturated alcohols or total alcohols) selectivity as a function of the ratio of the number of acid sites to basic sites was plotted [Figure 3-40(c)]. The trend was similar to that observed when plotting selectivity as a function of the number of acid sites as in Figure 3-40(a). The selectivity to all the Guerbet alcohols sharply increased from carbonate rich apatite HapE-Na-CO₃ to carbonated apatite Hap-CO₃ with an increase in the acidity to basicity ratio from 1.3 to 4.8. Further increase in the acidity to basicity ratio from 4.8 (Hap-CO₃) to 7.8 (Hap) led to a decrease in the Guerbet alcohols selectivity. The selectivity to butanol, saturated alcohols or total alcohols remains unchanged for an increase in the acidity to basicity ratio to a maximum of 23.2. The above observations are good in agreement with the variation in the Guerbet alcohols selectivity with the propylene/acetone ratio, which is an indirect representation of the acid/base ratio (Figure 3-30).

3.2.2.2 Guerbet reaction: Optimization of experimental conditions

In the literature, we can find studies related to the Guerbet reaction of ethanol over hydroxyapatites, but they mostly focus on maximizing the selectivity to butanol and, hence, the authors had to use ethanol conversions less than 30% [11,12]. The aim of the present work was to push the ethanol conversion so as to increase the yield in heavier alcohols, instead of aiming at only synthesizing butanol. Thus, in contrast to the above-described iso-conversion studies, the ethanol reaction was performed at different temperatures and GHSVs in order to obtain optimal conditions for the production of heavier alcohols.

Table 3-8 Conversion and products distribution over hydroxyapatite catalysts at GHSV = 5000 mL.h⁻¹.g⁻¹.

| GHSV = 5000 mL.h ⁻¹ .g ⁻¹ | | | | | | |
|---|------|------|---------------------|-----------------------|----------------------|-------------------------|
| | HapD | Hap | Hap-CO ₃ | HapNa-CO ₃ | HapE-CO ₃ | HapE-Na-CO ₃ |
| Conversion at | | | | | | |
| 300°C | 14.2 | 13 | 5.8 | 5.4 | 4.8 | 4.5 |
| 350°C | 27 | 32.2 | 15.2 | 9.5 | 9 | 6.8 |
| 400°C | 62.1 | 65.1 | 40 | 26 | 17 | 12 |
| Yield at 300°C | | | | | | |
| Alkenes | | | | | | |
| ethylene | 0.4 | 0.1 | 0.1 | 0.02 | 0.1 | 0.2 |
| Aldehydes | | | | | | |
| acetaldehyde | 0.8 | 1.8 | 0.3 | 0.5 | 1.0 | 1.8 |
| butanal | - | - | - | - | 0.01 | - |
| Dienes | | | | | | |
| butadiene | 0.2 | 0.2 | 0.04 | 0.02 | - | - |
| C6-dienes | 0.3 | - | - | - | - | - |
| Alcohols | | | | | | |
| butanol | 7.1 | 6.5 | 4.2 | 3.7 | 2.2 | 1.1 |
| C6-C10 alcohols | 3.2 | 2.6 | 0.5 | 0.4 | 0.4 | - |
| 2-buten-1-ol | 0.1 | 0.1 | 0.2 | 0.4 | 0.4 | 0.5 |
| Diethylether | 0.7 | 0.6 | 0.04 | 0.03 | - | - |
| Ethylbutyrate | - | - | - | - | 0.1 | 0.5 |
| Yield at 350°C | | | | | | |
| Alkenes | | | | | | |
| ethylene | 2.6 | 1.4 | 0.2 | 0.1 | 0.1 | 0.2 |
| butene | 0.3 | 0.5 | - | - | - | - |
| hexene | 0.1 | 0.2 | - | - | - | - |
| Aldehydes | | | | | | |
| acetaldehyde | 0.8 | 2.6 | 0.7 | 1.1 | 1.5 | 2.0 |
| butanal | - | 0.3 | 0.1 | - | 0.1 | - |
| Dienes | | | | | | |
| butadiene | 1.4 | 1.2 | 0.3 | 0.1 | 0.05 | 0.03 |
| C6-dienes | 0.7 | 0.6 | 0.1 | - | - | - |
| Alcohols | | | | | | |
| butanol | 15.1 | 18.2 | 10.6 | 6.2 | 4.4 | 2.9 |
| C6-C10 alcohols | 3.5 | 5.4 | 1.4 | 0.3 | 0.7 | 0.1 |
| 2-buten-1-ol | 0.2 | 0.1 | 0.5 | 0.5 | 0.7 | 0.5 |
| Diethylether | 1.6 | 1.2 | 0.2 | 0.1 | 0.1 | 0.3 |
| Ethylbutyrate | - | - | - | 0.1 | 0.3 | 0.7 |
| Aromatics | - | - | 0.1 | 0.3 | 0.3 | 0.04 |
| Yield at 400°C | | | | | | |
| Alkenes | | | | | | |
| ethylene | 36.7 | 11.4 | 0.6 | 0.4 | 0.2 | 0.3 |
| butene | 3.0 | 2.8 | 0.1 | - | - | - |
| hexene | 0.3 | 2.7 | 0.04 | - | - | - |
| Aldehydes | | | | | | |
| acetaldehyde | 1.9 | 3.1 | 1.4 | 1.6 | 2.6 | 2.3 |
| butanal | - | 0.8 | 0.5 | 0.2 | 0.4 | 0.2 |
| Dienes | | | | | | |
| butadiene | 2.4 | 3.3 | 1.1 | 0.7 | 0.2 | 0.1 |
| C6-dienes | 0.7 | 5.3 | 0.3 | 0.1 | 0.1 | - |
| Alcohols | | | | | | |
| butanol | 6.4 | 21.5 | 22.4 | 15.2 | 7.7 | 4.9 |
| C6-C10 alcohols | 0.2 | 3.1 | 6.8 | 2.6 | 1.4 | 0.3 |
| 2-buten-1-ol | 0.1 | 0.2 | 0.8 | 1.2 | 1.2 | 1.1 |
| Diethylether | 5.0 | 2.0 | 0.2 | 0.2 | 0.1 | 0.2 |
| Ethylbutyrate | - | - | 0.1 | 0.3 | 0.6 | 1.2 |
| Aromatics | - | - | 0.9 | 1.0 | 1.1 | 0.8 |

Table 3-9 Conversion and products distribution over hydroxyapatite catalysts at GHSV = 15000 mL.h⁻¹.g⁻¹.

| GHSV = 15000 mL.h⁻¹.g⁻¹ | | | | | | |
|--|-------------|------------|---------------------------|-----------------------------|----------------------------|-------------------------------|
| | HapD | Hap | Hap-CO₃ | HapNa-CO₃ | HapE-CO₃ | HapE-Na-CO₃ |
| Conversion at | | | | | | |
| 300°C | 4.2 | 4.5 | 4.0 | 3.0 | 1.0 | 0.5 |
| 350°C | 10.4 | 11 | 8.6 | 6.7 | 3.3 | 2.2 |
| 400°C | 32 | 33 | 21 | 12 | 6 | 5.8 |
| Yield at 400°C | | | | | | |
| Alkenes | | | | | | |
| ethylene | 12.8 | 5.6 | 0.44 | 0.19 | 0.09 | 0.06 |
| butene | 0.8 | 1.1 | - | - | - | - |
| hexene | 0.10 | 0.30 | 0.04 | - | - | - |
| Aldehydes | | | | | | |
| acetaldehyde | 2.5 | 2.1 | 1.2 | 1.6 | 1.3 | 1.4 |
| butanal | 0.10 | 0.26 | 0.15 | 0.14 | 0.13 | - |
| Dienes | | | | | | |
| butadiene | 3.3 | 2.7 | 0.5 | 0.3 | 0.1 | - |
| C6-dienes | 0.48 | 1.2 | 0.11 | - | - | - |
| Alcohols | | | | | | |
| butanol | 7.8 | 14.9 | 12.6 | 7.0 | 3.6 | 3.0 |
| C6-C10 alcohols | 0.7 | 2.5 | 2.2 | 1.0 | 0.2 | - |
| Ethylbutyrate | - | - | 0.08 | 0.18 | 0.39 | 0.81 |
| Aromatics | - | - | 0.19 | 0.14 | 0.12 | 0.09 |

Table 3-8 and Table 3-9 show the ethanol conversion and the product distribution over the prepared samples at different temperatures and GHSVs. As a general matter, the reactivity trend followed that observed at iso-conversion, and the already obtained conclusions roughly apply.

The reaction products consisted of alkenes, dienes, aldehydes, alcohols, diethylether, ethylbutyrate and aromatics, the major products being ethylene, acetaldehyde, and C4-C10 alcohols including significant amounts of butanol. Condensation products with only even number of carbon atoms like C4, C6, C8, *etc...*, were observed, indicating that the products formed during the reaction are not subjected to any cleavage-involving mechanism. Further, the nature of the obtained products undoubtedly suggests that the ethanol reaction over hydroxyapatites under these conditions indeed takes place through the aldol condensation mechanism shown before in Figure 3-24. Only trace amount of light gaseous products such as CO₂ were observed, confirming that the ethanol or the reaction products were not further decomposed over hydroxyapatite catalysts, which is in agreement with previous reports [3].

As a visual example, the ethanol conversion observed at 400°C and at the two different GHSVs we used (namely, 5000 mL.h⁻¹g⁻¹ and 15000 mL.h⁻¹g⁻¹, obtained using 0.2 g and 0.6 g of catalyst, respectively) are shown in Figure 3-41 hereafter. The ethanol conversion increased with decreasing GHSV from 15000 mL.h⁻¹g⁻¹ to 5000 mL.h⁻¹g⁻¹. A similar trend was observed for the temperatures of 300°C and 350°C (Table 3-8 & 3-9). This is obviously related with considerations of contact time variations.

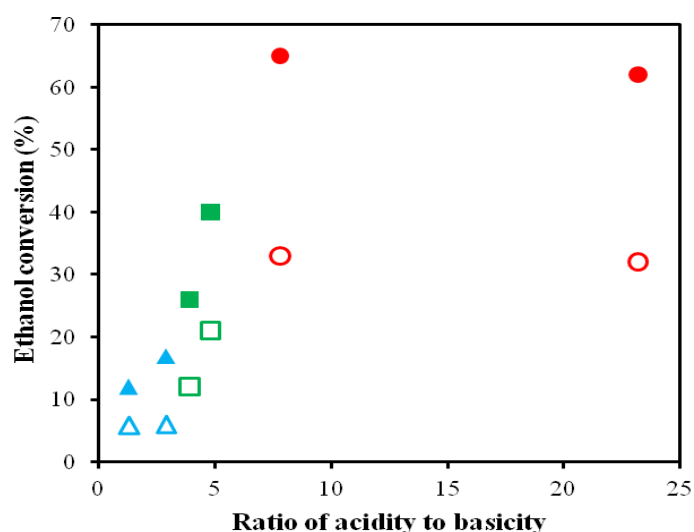


Figure 3-41 Ethanol conversion as a function of the ratio of acidity to basicity at 400°C; GHSV = 5000 mL.h⁻¹g⁻¹ (color-filled symbols); GHSV = 15000 mL.h⁻¹g⁻¹ (open symbols) (red circles representing HapD and Hap, green squares for carbonated apatites, namely Hap-CO₃ and HapNa-CO₃, and blue triangles for carbonate-rich apatites, namely HapE-CO₃ and HapE-Na-CO₃).

As a general matter, the ethanol conversion increased with the increase in the ratio of the number of acid sites to basic sites from 1.3 (HapE-Na-CO₃) to 7.8 (Hap), and then remained unchanged with further increase to 23.2 (HapD). This is consistent with the results observed at iso-conversion, revealing that a too large increase in the amount of acid sites in the HAP catalysts had no positive effect on the ethanol conversion.

Yield to minor products such as diethyl ether, ethyl butyrate and aromatics increased with a decrease in GHSV, indicating that dehydration and some dehydrogenation / polymerization reactions were promoted at lower GHSV. Selectivity to acetaldehyde decreased with decrease in GHSV, suggesting that the aldol condensation of

acetaldehyde to heavier products became more prominent due to the increase in the resulting acetaldehyde contact time (Tables 3-8 & 3-9). C4-C10 alcohols selectivity increased with decrease in GHSV for all the catalysts except for HapD and Hap, over which dehydration products like ethylene, diethylether and dienes, resulting from competing side reactions on acid sites, were detected. Since our aim here was to maximize ethanol conversion while yielding a maximal amount of total alcohols, further studies were performed at $GHSV = 5000 \text{ mL}\cdot\text{h}^{-1}\cdot\text{g}^{-1}$.

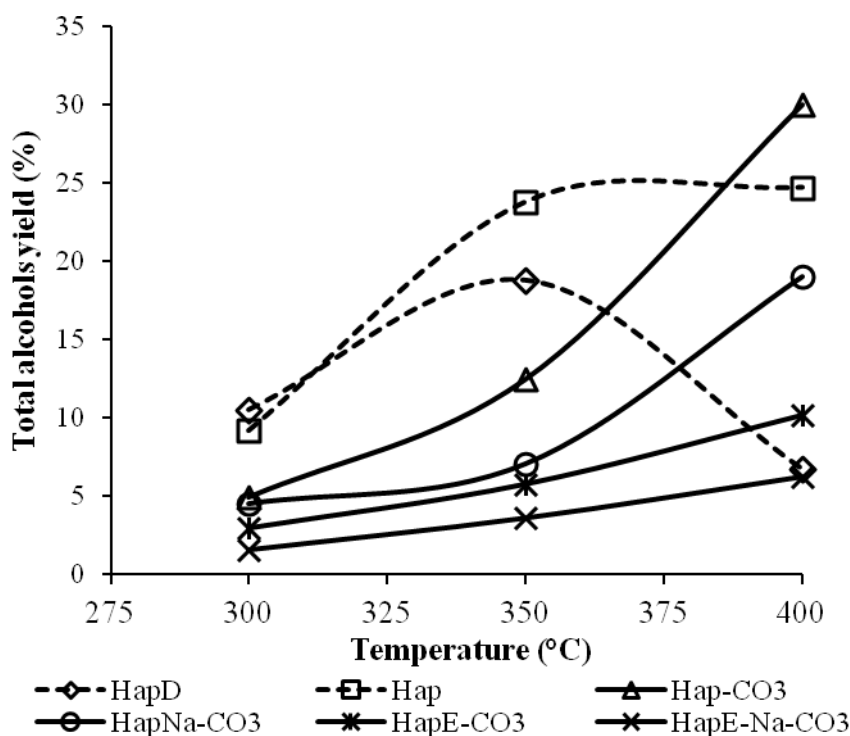


Figure 3-42 Influence of temperature towards heavier alcohols yield ($GHSV = 5000 \text{ mL}\cdot\text{h}^{-1}\cdot\text{g}^{-1}$).

Except for Hap and HapD (represented by the dashed lines), C4-C10 total alcohols yield increased while increasing the temperature up to 400°C (Figure 3-42). Above this temperature the yield towards aromatics and olefins severely increased, which subsequently decreased the alcohols yield (data not shown). In Hap, the total alcohols yield remained constant at 350°C and 400°C , whereas in HapD an optimum temperature for the production of heavier alcohols was observed at 350°C . The volcano curve obtained for HapD and the plateau for Hap clearly reflects the highly acidic behavior of HapD compared with Hap. HapD and Hap have shown almost similar selectivity to Guerbet

alcohols and the difference in their behaviors was not much evident during iso-conversion studies, where ethanol conversion of HapD and Hap were maintained at 14% at lower temperature (~300°C). It is clearly observed from the dashed lines in Figure 3-42 that the deviation between the HapD and Hap concerning the total alcohols yield tended to increase with increase in temperature. This observation clearly underlines the enhancement in acidic behavior of HapD, which possess higher number of acid sites, especially Brønsted acid sites, thus leading to higher ethylene yield compared to that in Hap (Table 3-8).

Further, as aforementioned, the behavior of HapD and Hap (represented by dashed lines) was different from that of the other catalysts. This discrepancy could also be related to the increase in ethylene (and diethylether) yield for Hap and HapD, which is not observed for the other hydroxyapatites (Table 3-8). This increase is much more pronounced for the HapD catalyst in comparison with Hap. In HapD, the ethylene yield increased from 2.6% to 36.7% and for Hap from 1.4% to 11.4% when the temperature increased from 350°C to 400°C, respectively. This is good in agreement with previous results at iso-conversion, where HapD and Hap showed deviations from other catalyst due to their high acidic behavior. As aforementioned, dehydration of ethanol to ethylene (and to diethylether) is the main competing reaction, which is responsible for the decrease in heavier alcohol yields. The temperature of 400°C was found to be the most favorable temperature for the production of Guerbet alcohols over all the catalysts except for HapD and following study will be focused at this temperature.

Figure 3-43 shows the variation in the ethanol conversion and in the yield in the major products as a function of the ratio of the number of acid sites to the number of basic sites of the hydroxyapatites, at 400°C and a GHSV of 5000 mL.h⁻¹g⁻¹. As aforementioned, the ethanol conversion increased with increasing the acidity/basicity ratio up to a certain limit and then remained unchanged with further increase in this ratio. The yield to total alcohols increased rather linearly from 6.3% to 30% with increasing the acidity/basicity ratio from 1.3 (HapE-Na-CO₃) to 4.8 (Hap-CO₃), respectively, and then decreased with further increase in the acidity/basicity ratio. Hence, the Hap and HapD with higher acidity/basicity ratios of 7.8 and 23.2 showed total alcohols yields of 24.8% and 6.7%, respectively. The Hap-CO₃ with an acidity/basicity ratio of 4.8 exhibited superior performances in terms of maximum total alcohol yield, which is in good agreement with the results of the iso-conversion study.

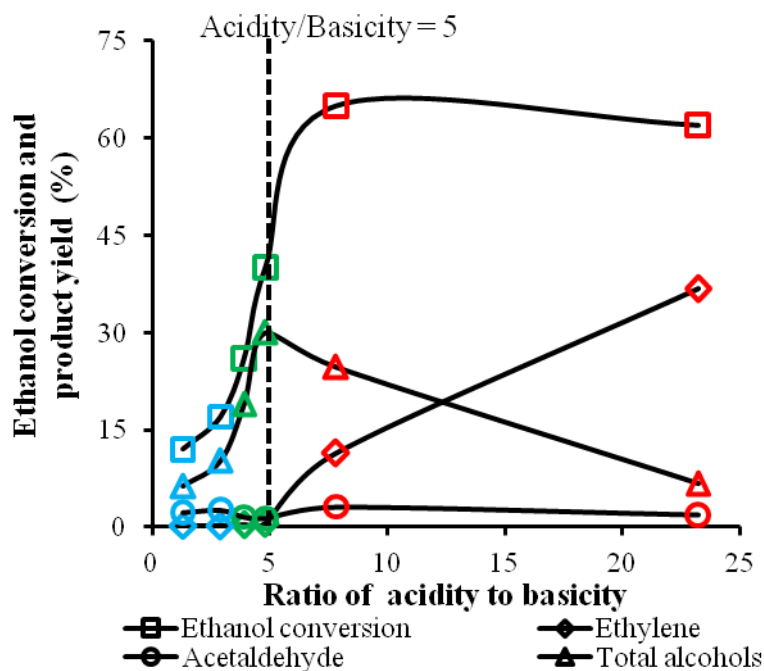


Figure 3-43 Ethanol conversion and major product yields at 400°C and GHSV = 5000 mL.h⁻¹.g⁻¹ as a function of the ratio of number of acid sites to the number of basic sites (red color symbols representing HapD and Hap, green color for carbonated apatites, namely Hap-CO₃ and HapNa-CO₃, and blue color for carbonate-rich apatites, namely HapE-CO₃ and HapE-Na-CO₃).

The catalysts Hap and HapD deviate from the linearity due to their high acidity/basicity ratio (highly acidic behavior), which is represented by the higher ethylene yields of 11.4% and 36.7%, respectively. The ethylene yield was almost similar for all the other catalysts with acidity/basicity ratios ≤ 5 . All the above observations are in good agreement with the iso-conversion studies, where Hap-CO₃ behaved as an ideal catalyst and Hap and HapD as highly acidic catalysts. It is worth mentioning that the yield to total alcohols over HapD drastically decreased compared to iso-conversion studies, which is explained by the dehydration of ethanol to ethylene over acid sites, which became more pronounced at higher temperature of 400°C. Since ethylene is a product directly formed from the ethanol in the presence of acidic catalysts (primary reaction product), we suppose it can be formed much easier at higher temperatures, when pushing catalytic reactivity, compared to higher alcohols, which are formed by a multiple steps reaction from ethanol. Further, the energy of activation of dehydration might be favorable compared to the other steps, even if we cannot give any evidence at the moment. The yield to acetaldehyde remained almost unchanged with the increase in the acidity/basicity ratio. However, the selectivity to acetaldehyde remained higher over carbonate-rich apatites HapE-CO₃ (15.5%) and

HapE-Na-CO₃ (19%) compared to other catalysts, as observed in iso-conversion studies, showing the lack in a sufficient amount of acid sites to condense acetaldehyde further to aldol.

The observed yield in acetaldehyde was low on the left side of the ‘ideal’ dashed line in Figure 3-43, because it was consumed through the Guerbet reaction after formation, while its yield is low on the right side of this same line, in part due to Guerbet reaction also, but mainly due to preferential consumption of ethanol by dehydration to give ethylene (and diethylether).

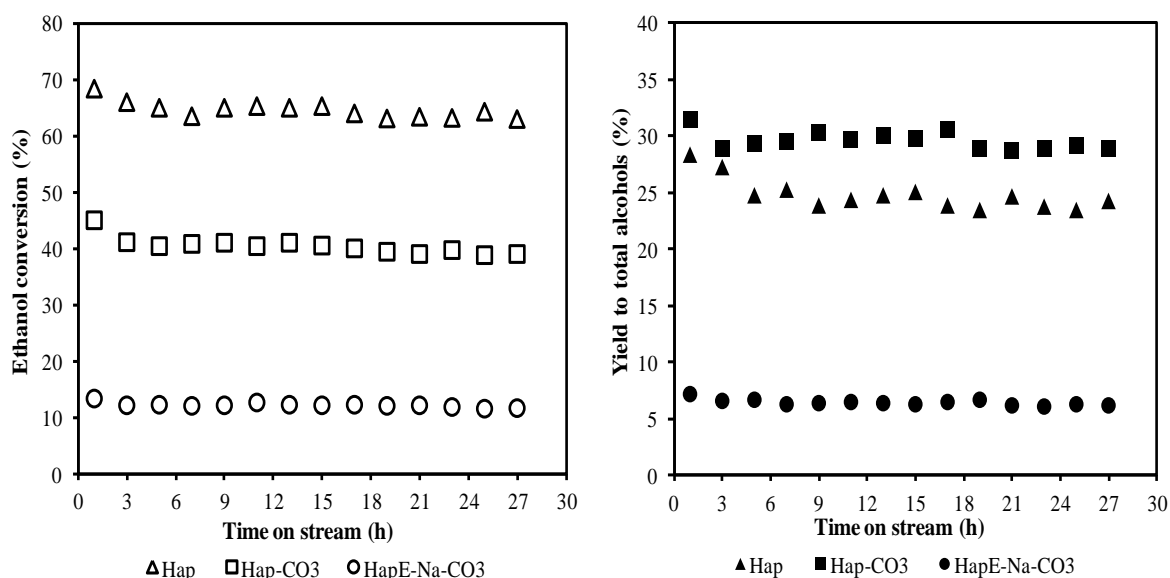


Figure 3-44 Ethanol conversion and total alcohols yield over stoichiometric (Hap), carbonated (Hap-CO₃) and carbonate rich (HapE-Na-CO₃) hydroxyapatites at 400°C and GHSV = 5000 mL.h⁻¹.g⁻¹ as a function of time on stream.

In order to get and insight on the effect of carbonate substitution on the catalytic performances stability, ethanol conversion was recorded for more than 24 h over the catalysts (Figure 3-44). We found that all the catalysts were quite stable, without deactivation, which suggests the potential industrial relevance of such systems.

As a partial conclusion, the ethanol conversion was higher over HapD and Hap due to their acidic behaviors compared to the other catalysts. It was found that the acidic behavior of HapD becomes predominant at higher temperatures and resulted in higher ethylene yield. The ethanol conversion and total alcohols yield were found to be optimum over Hap-CO₃ catalyst with acidity/basicity ratio of nearly 5, which is in good agreement with iso-

conversion studies. For the catalysts that possess acidity/basicity ratio < 5 , ethanol conversion was lower, which resulted in lower yield to total alcohols. In contrast, catalysts with acidity/basicity ratio > 5 (Hap & HapD) have shown higher ethanol conversion, but were found to be less selective to total alcohols because of increase in ethylene selectivity, thereby decreasing the total alcohols selectivity. Hence, it confirms that a fine-tuning of acid-base sites in HAP is necessary to have higher ethanol conversion without losing the Guerbet alcohols selectivity.

3.3 Conclusions

Hydroxyapatites with different Ca/P ratios were successfully synthesized using a precipitation method. Their carbonate content increased linearly with increasing the Ca/P ratio. The occupancy of atoms was calculated using Rietveld refinement, and the so-obtained (Ca + Na)/P ratios were good in agreement with those obtained from ICP. A good correlation was observed between the anisotropic crystallite shape obtained from XRD and the grain shape observed in SEM. Global tentative formulae for the apatites were deduced from the amount of CO_3^{2-} substituted in the OH^- sites (A-type) and the PO_4^{3-} sites (B-type) ($\text{Ca}_{10-\delta}[(\text{PO}_4)_{6-x}(\text{CO}_3)_x][(\text{OH})_y(\text{CO}_3)_z]$). LEIS have shown that Ca^{2+} is more exposed at the topmost surface of the apatite solids, irrespective of the Ca/P ratio. Combining the results of XRD refinement and LEIS, we proposed that Ca^{2+} are more exposed along the 0 0 1 direction on the *ac* and *bc* planes. The presence of HPO_4^{2-} suggested by IR spectra was confirmed in all the apatites using 2D NMR (HETCOR sequence). Further, PEA-XPS proved that HPO_4^{2-} species act as Brønsted acid sites, and Ca^{2+} or OH^- vacancies (δ^+) as Lewis acid sites. The acid-base behavior of solids was determined using *isopropanol* reactivity, which is good in agreement with the acid-base properties directly obtained using NH_3 -TPD, PEA-XPS and CO_2 -TPD. As a remarkable feature, HapD (deficient apatite) and Hap (stoichiometric apatite) showed a much more pronounced acidic behavior than that of the other apatites.

Further correlation study combining the Guerbet reaction results with the aforementioned results showed that the amount, the strength and the nature of the acid-base properties accordingly affect each step in the Guerbet reaction cycle. The first step of the Guerbet

cycle is the dehydrogenation of ethanol over the basic sites to produce acetaldehyde, which takes place mainly on weak or medium basic sites, and which seemed especially promoted by CaO species. The acetaldehyde further undergoes aldol condensation over basic sites (supposedly of a strong type) to form an intermediate aldol (never observed in our conditions), which further undergoes dehydration over acid sites (mostly Brønsted acid sites). The so-formed crotonaldehyde then undergoes partial hydrogenation by a proton exchange mechanism to form 2-buten-1-ol and butyraldehyde over both types of acid (mostly Lewis acid sites) and over basic sites. These compounds can further undergo hydrogenation over the same acid-base sites to form butanol. Butanol can then further react with ethanol and be subjected to an additional Guerbet cycle. Also, there are some competing reactions, especially dehydration reactions that can form olefins (ethylene, butene etc...) or diethylether, which occur in parallel to the Guerbet cycle (mostly over Brønsted acid sites). So, there should be a compromise between the acid and the basic sites number and also concerning their strength and nature over the HAP catalysts to yield a global formulation that is selective towards higher alcohols. We especially identified that the best ratio between the number of acid sites to the number of basic sites was 5 (observed in the Hap-CO₃ sample) to enable reaching a maximum selectivity to higher alcohols over HAP catalysts.

-
- [1] L.C. Kibby, K.W. Hall, Studies of acid catalyzed reactions: XII. Alcohol decomposition over hydroxyapatite catalysts, *Journal of Catalysis*, vol 29 (1973) p. 144-159.
- [2] S.J. Joris, C.H. Amberg, Nature of deficiency in nonstoichiometric hydroxyapatites I. Catalytic activity of calcium and strontium hydroxyapatites, *Journal of Physical Chemistry*, vol 75 (1971) p. 3167–3171.
- [3] T. Tsuchida, S. Sakuma, T. Takeguchi, W. Ueda, Direct Synthesis of n-Butanol from Ethanol over Nonstoichiometric Hydroxyapatite, *Industrial & Engineering Chemistry Research*, vol 45 (2006) p. 8634-8642.
- [4] A. Sohly, R. Tahir, S. Sebti, R. Skouta, M. Bousmina, M. Zahouily, M. Larzek, Efficient synthesis of chalcone derivatives catalyzed by re-usable hydroxyapatite, *Applied Catalysis A: General*, vol 374 (2010) p. 189-193.
- [5] S. Sebti, R. Tahir, R. Nazih, S. Boulaajaj, Comparison of different Lewis acid supported on hydroxyapatite as new catalysts of Friedel-Crafts alkylation, *Applied Catalysis A: General*, vol 218 (2001) p. 25–30.
- [6] S. Koutsopoulos, Synthesis and characterization of hydroxyapatite crystals: A review study on the analytical methods, *Journal of Biomedical Materials Research*, vol 62 (2002) p. 600-612.
- [7] C.L. Kibby, K.W. Hall, Dehydrogenation of alcohols and hydrogen transfer from alcohols to ketones over hydroxyapatite catalysts, *Journal of Catalysis*, vol 31 (1973) p. 65-73.
- [8] N. Cheikhi, M. Kacimi, M. Rouimi, M. Ziyad, L.F. Liotta, G. Pantaleo, G. Deganello, Direct synthesis of methyl isobutyl ketone in gas-phase reaction over palladium-loaded hydroxyapatite, *Journal of Catalysis*, vol 232 (2005) p. 257-267.
- [9] T.J. Webster, E.A. Massa-Schlueter, J.L. Smith, B.E. Slamovich, Osteoblast response to hydroxyapatite doped with divalent and trivalent cations, *Biomaterials*, vol 25 (2004) p. 2111-2121.
- [10] N.S. Resende, M. Nele, V.M.M. Salim, Effect of anion substitution on the acid properties of hydroxyapatite, *Thermochimica Acta*, vol 451 (2006) p. 16-21.
- [11] T. Tsuchida, J.Kubo, T. Yoshioka, S. Sakuma, T. Takeguchi, W. Ueda Reaction of ethanol over hydroxyapatite affected by Ca/P ratio of catalyst, *Journal of Catalysis*, vol 259 (2008) p. 183-189.
- [12] S. Ogo, A. Onda, K. Yanagisawa, Selective synthesis of 1-butanol from ethanol over strontium phosphate hydroxyapatite catalysts, *Applied Catalysis A: General*, 402 (2011) 188– 195.

-
- [13] A. Gervasini, A. Auroux, C. Guimon, Acidic Character of Metal-Loaded Amorphous and Crystalline Silica-Aluminas determined by XPS and Adsorption Calorimetry, *Journal of Physical Chemistry B*, vol 103 (1999) p. 7195-7205.
- [14] A. Gervasini, C. Messi, D. Flahaut, C. Guimon, Acid properties of iron oxide catalysts dispersed on silica-zirconia supports with different Zr content, *Applied Catalysis A: General*, 367 (2009) 113–121.
- [15] S. Raynaud, E. Champion, D. Bernache-Assollant, P. Thomas, Calcium phosphate apatites with variable Ca/P atomic ratio I. Synthesis, characterization and thermal stability of powder, *Biomaterials*, vol 23 (2002) p. 1065-1072.
- [16] B. Aellach, A. Ezzamarty, J. Leglise, C. Lamonier, J.-F Lamonier, Calcium-deficient and stoichiometric hydroxyapatites promoted by Cobalt for the catalytic removal of oxygenated Volatile Organic Compounds, *Catalysis Letters*, vol 135 (2010) p. 197–206.
- [17] J.M. Hughes, M. Cameron, K.D. Crowley, Structural variations in natural F, OH and Cl apatites, *American Mineralogist*, 74 (1989), 870-876.
- [18] M. Jarvinen, Application of symmetrized harmonics expansion to correction of the preferred orientation effect, *Journal of Applied Crystallography*, vol 26 (1993) p. 525-531.
- [19] A. Krajewski, M. Mazzochi, P.L. Buldini, A. Ravaglioli, A. Tinti, P. Taddei and C. Fagnano, Synthesis of carbonated hydroxyapatites: efficiency of the substitution and critical evaluation of analytical methods, *Journal of Molecular Structure*, vol 744 (2005) p. 221-228.
- [20] R.M. Wilson, J.C. Elliott, S.E.P. Dowker, R.I. Smith, Rietveld structure refinement of precipitated carbonate apatite using neutron diffraction data, *Biomaterials*, vol 25 (2004) p. 2205-2213.
- [21] R.Z. Legeros, O.R. Trautz, J.P. Legeros, E. Klein, W.P. Shirra, Apatite Crystallites: Effects of Carbonate on Morphology, *Science*, vol 155 (1967) p. 1409-1411.
- [22] S. Kannan, J.M.G. Ventura, A.F. Lemos, A. Barba and J.M.F. Ferreira, Effect of sodium addition on the preparation of hydroxyapatites and biphasic ceramics, *Ceramics International*, vol 34 (2008) p. 7-13.
- [23] J.F. Berar and P. Lelann, E.s.d.'s and estimated probable error obtained in Rietveld refinements with local correlations, *Journal of Applied Crystallography* vol 24, (1991) p. 1-5.
- [24] I.R. Gibson, I. Rehman, S.M. Best, W. Bonfield, Characterization of the transformation from calcium-deficient apatite to β -tricalcium phosphate, *Journal of Material Science : Materials in medicine*, vol 12 (2000) p. 799-804.

-
- [25] C. Lamonier, J.-F. Lamonier, B. Aellach, A. Ezzamarty, J. Leglise, Specific tuning of acid/base sites in apatite materials to enhance their methanol thiolation catalytic performances, *Catalysis Today*, vol 164 (2011) p. 124-130.
- [26] N. Elazarifi, A. Ezzamarty, J. Leglise, L.C. de Ménorval, C. Moreau, Kinetic study of the condensation of benzaldehyde with ethylcyanoacetate in the presence of Al-enriched fluoroapatites and hydroxyapatites as catalysts, *Applied Catalysis A: General*, vol 267 (2004) p. 235.
- [27] S. Kannan, I.A.F. Lemos, J.H.G. Rocha and J.M.F. Ferreira, Synthesis and characterization of magnesium substituted biphasic mixtures of controlled hydroxyapatite/ β -tricalcium phosphate ratios, *Journal of Solid State Chemistry*, vol 178 (2005) p. 3190.
- [28] M.E. Fleet and X. Liu, Coupled substitution of type A and B carbonate in sodium-bearing apatite, *Biomaterials*, vol 28 (2007) p. 916.
- [29] G. Bonel, Contribution a l'étude de la carbonatation des apatites. I. Synthèse et étude des propriétés physico-chimiques des apatites carbonatées du type A, *Annali di Chimica*, vol 7 (1972) p. 65-88.
- [30] J.C. Elliott, Space group and lattice constants of $\text{Ca}_{10}(\text{PO}_4)_6\text{CO}_3$, *Journal of Applied Crystallography*, vol 13 (1980) p. 618-621.
- [31] A. Krajewski, M. Mazzochi, P.L. Buldini, A. Ravaglioli, A. Tinti, P. Taddei and C. Fagnano, *Journal of Molecular Structure*, vol 744 (2005) p. 221.
- [32] S. Sugiyama, T. Miyamoto, H. Hayashi, J. B. Moffat, Effects of non-stoichiometry of calcium and strontium hydroxyapatites on the oxidation of ethane in the presence of tetrachloromethane, *Journal of Molecular Catalysis A Chemical*, vol 135 (1998) p. 199.
- [33] Z.R. Hinedi, S. Goldberg, A.C. Chang, J.P. Yesinowski, A ^{31}P and ^1H MAS NMR study of phosphate sorption onto Calcium carbonate, *Journal of Colloid and Interface Science*, vol 152 (1992) p. 141-160.
- [34] C. Jager, T. Welzel, W. Meyer-Zaika, M. Epple, A solid-state NMR investigation of the structure of nanocrystalline hydroxyapatite, *Magnetic resonance in chemistry*, vol 44 (2006) p. 573-580.
- [35] N.S. Resende, M. Nele, V.M.M. Salim, Effect of anion substitution on the acid properties of hydroxyapatite, *Thermochimica Acta*, vol 451 (2006) p. 16-21.
- [36] T. Kawasaki, S. Takahashi, K. Ikeda, Hydroxyapatite high-performance liquid chromatography: column performance for proteins, *European Journal of Biochemistry*, vol 152 (1985) p. 361-371.

[37] S. Ogo, A. Onda, Y. Iwasa, K. Hara, A. Fukuoka, K. Yanagisawa, 1-Butanol synthesis from ethanol over strontium phosphate hydroxyapatite catalysts with various Sr/P ratios, *Journal of Catalysis*, vol 296 (2012) p. 24-30.

Chapter 4 Guerbet reaction of ethanol over Strontium substituted hydroxyapatite catalysts

4.1 Introduction

Guerbet reaction is of great relevance due to the increasing interest in heavier alcohols, which can be used as fine chemicals or fuel additives. Both homogeneous and heterogeneous catalysts have been used for the production of heavier alcohols from ethanol and even butanol. Concerning heterogeneous catalysis, hydroxyapatite has been proven as a promising catalytic system for the gas phase Guerbet reaction of ethanol. Recently, it has been reported that strontium apatites have shown more selectivity for the production of butanol from ethanol [1].

In this chapter, we discuss the physicochemical characterizations of hydroxyapatites prepared with various calcium-strontium substitution extents, and about their catalytic performances in the Guerbet reaction of ethanol.

4.2 Result and discussion

4.2.1 Catalyst Characterization

4.2.1.1 BET surface area

The BET specific surface areas of all the solids, of which the preparation method is described in the section 2.1.3 (Chapter 2), are given in Table 4-1. The variation in specific surface area with strontium substitution is shown in Figure 4-1. The specific surface area drastically decreased with Sr introduction, even with relatively small amount of Sr substitution. Deficient and stoichiometric solids showed similar trends in the variation of specific surface area with Sr substitution. The specific surface area of the stoichiometric apatites decreased from $114 \text{ m}^2 \cdot \text{g}^{-1}$ to $33 \text{ m}^2 \cdot \text{g}^{-1}$ with increase in Sr substitution, respectively from HAp to SrAp-50, and then remains unchanged for further increase in Sr

substitution to 75 mol.% in SrAp-75. Further increase in Sr substitution from SrAp-75 to SrAp-100 increased the surface area from $33 \text{ m}^2 \cdot \text{g}^{-1}$ to $44 \text{ m}^2 \cdot \text{g}^{-1}$, respectively.

Table 4-1 Specific surface area and BJH pore size distribution of the prepared solids calcined at 400°C .

| Catalysts | BET specific surface area ($\text{m}^2 \cdot \text{g}^{-1}$) | Pore volume-BJH ($\text{cm}^3 \cdot \text{g}^{-1}$) | Average pore diameter (nm) |
|-----------|--|---|----------------------------|
| HAp | 114 | 0.76 | 24.9 |
| SrAp-25 | 43 | 0.16 | 14.7 |
| SrAp-50 | 33 | 0.14 | 17.6 |
| SrAp-75 | 33 | 0.16 | 18.2 |
| SrAp-100 | 44 | 0.32 | 27.5 |
| DAp | 124 | 0.75 | 21.2 |
| SrDAp-50 | 50 | 0.26 | 19.9 |
| SrDAp-100 | 59 | 0.43 | 26.6 |

The specific surface area of the deficient apatites decreased from $124 \text{ m}^2 \cdot \text{g}^{-1}$ in DAp to $50 \text{ m}^2 \cdot \text{g}^{-1}$ in SrDAp-50 and further increased to $59 \text{ m}^2 \cdot \text{g}^{-1}$ in SrDAp-100 (Figure 4-1).

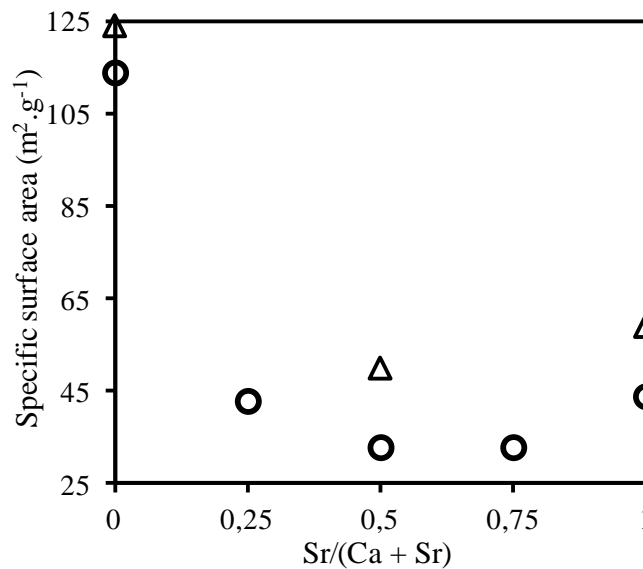


Figure 4-1 Specific surface area as a function of Sr substitution in apatite solids (open circles represents the stoichiometric apatites and triangles the deficient apatites).

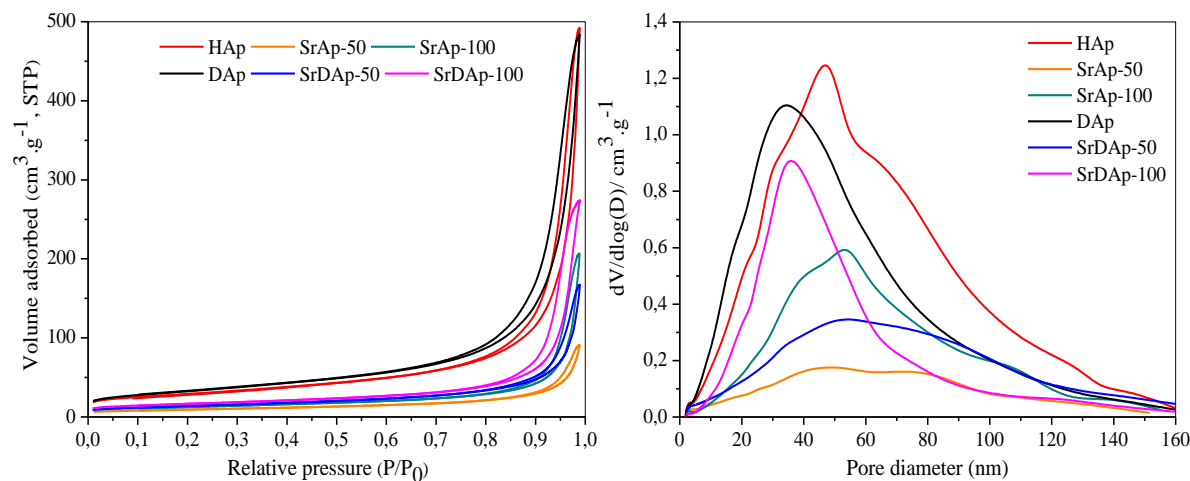


Figure 4-2 Nitrogen adsorption isotherms and BJH pore size distribution curves of apatites

Figure 4-2 shows the N_2 adsorption–desorption isotherms of the stoichiometric and the deficient apatites. They exhibit a type IV curve with a hysteresis loop largely characteristic of mesoporous solids. All the apatites exhibited hysteresis loops at $P/P_0 > 0.8$. The pore diameter of all the stoichiometric and deficient apatite solids is non uniform and exhibited a broad distribution ranging from 10 nm to 150 nm, with the maximum distribution of pores in between 30 nm and 60 nm.

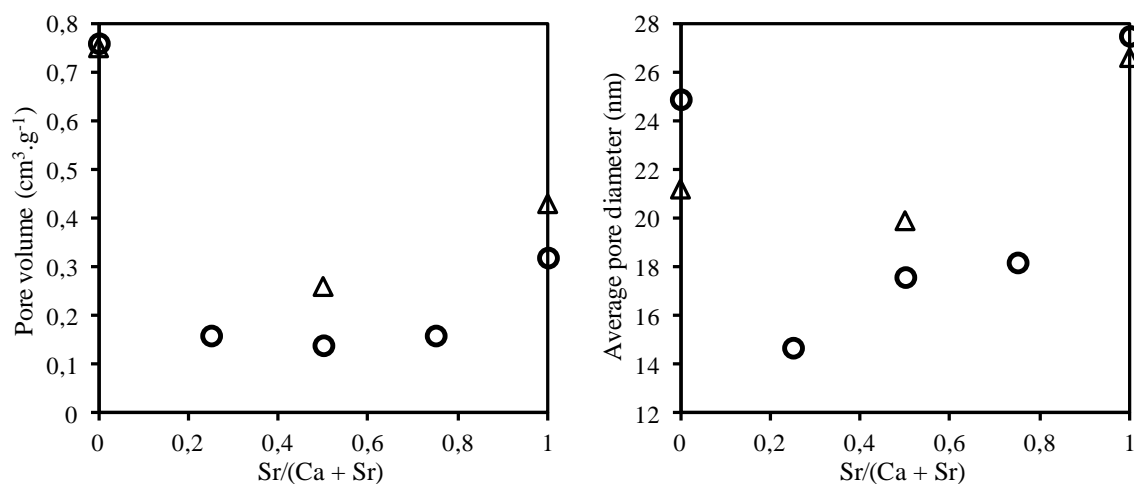


Figure 4-3 Variation in pore volume and average pore diameter with Sr substitution apatites (open circles represents the stoichiometric apatites and triangles the deficient apatites).

The pore volume and average pore diameter have shown similar trends, *i.e.*, both show the tendency to decrease with increase in Sr content up to 50 mol.% and then increased with further increase in the Sr content except for SrAp-25, which slightly deviates from this trend (Figure 4-3).

To verify whether the crystallinity has some influence on the surface area of apatite, XRD and Rietveld refinement were subsequently performed, and the results are given in the next section.

4.2.1.2 X-ray diffraction and Rietveld refinement studies

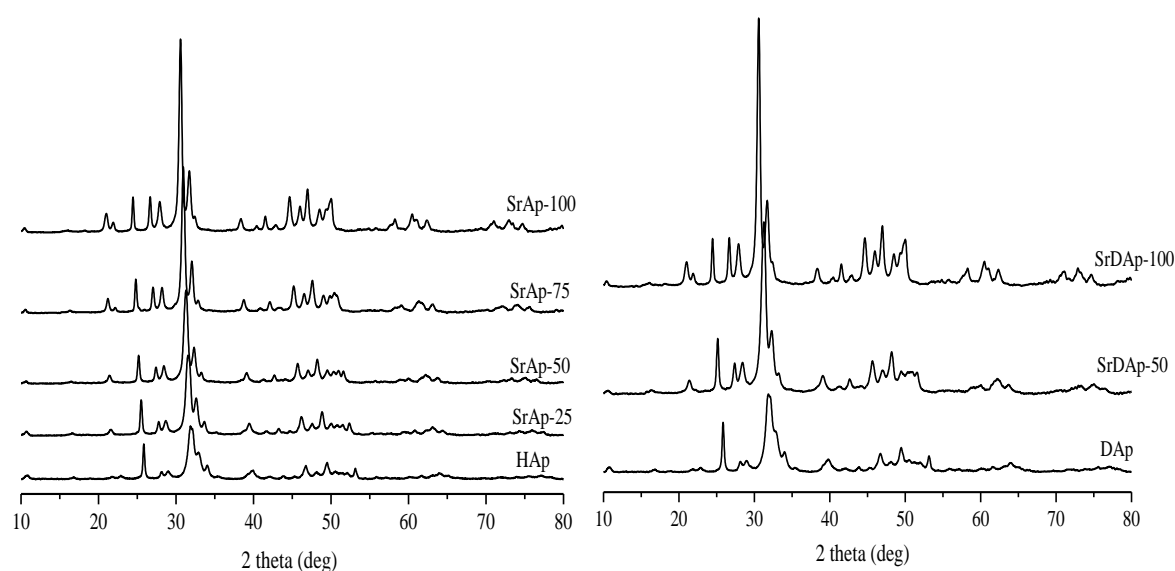


Figure 4-4 Diffraction patterns of stoichiometric and deficient solids calcined at 400°C.

Figure 4-4 shows the powder diffractograms of the stoichiometric and deficient strontium apatites prepared with varying the Sr substitution. Irrespective of the Sr content, all the solids showed diffraction patterns which are characteristic of a pure hydroxyapatite phase. All the solids exhibited the hexagonal structure, which crystallises in the $P6_3/m$ space group. When the strontium content was increased from 0 to 100 mol.%, the XRD pattern shifted towards lower values of 2 theta, which was accompanied with an increase in the intensity of the peaks. These observations are good in agreement with previous reports that

showed that when a smaller Ca ion is substituted with a larger Sr ion, there is an expansion of original apatite lattice [2].

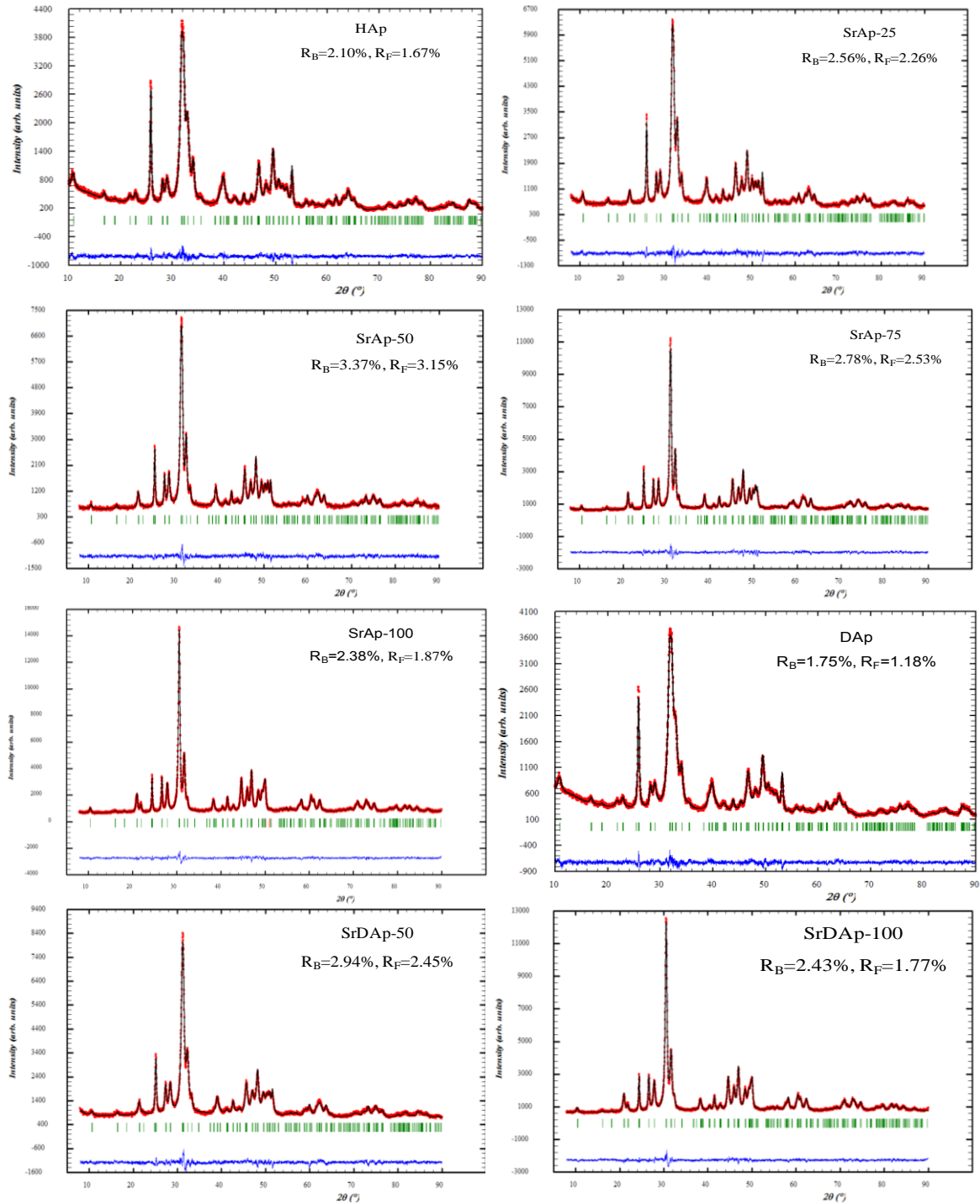


Figure 4-5 Calculated X-ray diffraction profile (in black) compared to experimental data (in red) showing a good agreement as shown by the difference in blue.

To confirm the above XRD observation, Rietveld refinement was performed to calculate the lattice parameters and crystallite size of the apatite solids (Figure 4-5). For all the samples, the peak due to diffraction on the (0 0 2) plane showed a thinner Full Width at Half Maximum, which reflects the presence of anisotropic crystallites. Therefore, Rietveld refinement based on an anisotropic size-broadening model was performed taking into account the instrument resolution from a LaB₆ pattern. The obtained results are given in Table 4-2.

Table 4-2 Unit cell parameters and crystallite size of the solids determined by Rietveld refinement.

| Solids | Cell Parameters | | Crystallite size (nm) corresponding to crystallographic plane | | |
|-----------|-----------------|--------------|---|---------|-------------------|
| | | | (1 0 0) | (0 0 1) | (0 0 1) / (1 0 0) |
| | <i>a</i> (Å) | <i>c</i> (Å) | | | |
| HAp | 9.4103(5) | 6.8871(4) | 8 | 26 | 3,2 |
| SrAp-25 | 9.5070(5) | 6.9821(4) | 12 | 26 | 2,2 |
| SrAp-50 | 9.5951(6) | 7.0817(5) | 13 | 25 | 1,9 |
| SrAp-75 | 9.6833(6) | 7.1848(5) | 17 | 26 | 1,5 |
| SrAp-100 | 9.7742(4) | 7.2828 (4) | 14 | 31 | 2,2 |
| DAP | 9.4210(6) | 6.8853(4) | 7 | 22 | 3,2 |
| SrDAP-50 | 9.5966(9) | 7.0843(7) | 10 | 19 | 1,9 |
| SrDAP-100 | 9.7799(5) | 7.2832(4) | 13 | 27 | 2,1 |

The lattice parameters increased with the increase in the amount of strontium. Figure 4-6 show an evidence of a linear increase in both *a* and *c* unit cell parameters with the increase in the Sr/(Ca+Sr) ratio. This increase in unit cell parameters with the Sr content reflects the aforementioned expansion of the apatite unit cell, in good agreement with previous reports [2,3]. All the apatites have larger crystallite size along the (0 0 1) plane compared

to the (1 0 0) plane, irrespective of the Sr content. The crystallite size along the (1 0 0) plane for stoichiometric apatite solids increased from 8 nm to 14 nm with the increase in the strontium content, respectively, from HAp to SrAp-100, except for SrAp-75, which exhibited a larger crystallite size of 17 nm. The crystallite size of the stoichiometric apatites along the (0 0 1) plane did not vary as much as what was observed for the (1 0 0) plane. The crystallite size did not vary at a value of *ca.* 26 nm, except for SrAp-100 leaded (31 nm).

An essentially similar trend was observed in case of the deficient apatites. The crystallite size of deficient solids increased consistently from 7 nm to 13 nm along (1 0 0) plane when the Sr content is increased from 0 mol.% (Dap) to 100 mol.% (SrDap-100). In (0 0 1) plane, the crystallite size was initially found to decrease from 22 nm to 19 nm with increasing Sr content from 0 mol.% (Dap) to 50 mol.% (SrDap-50) and then increased to 27 nm when Sr substitution reached 100 mol.% in SrDap-100.

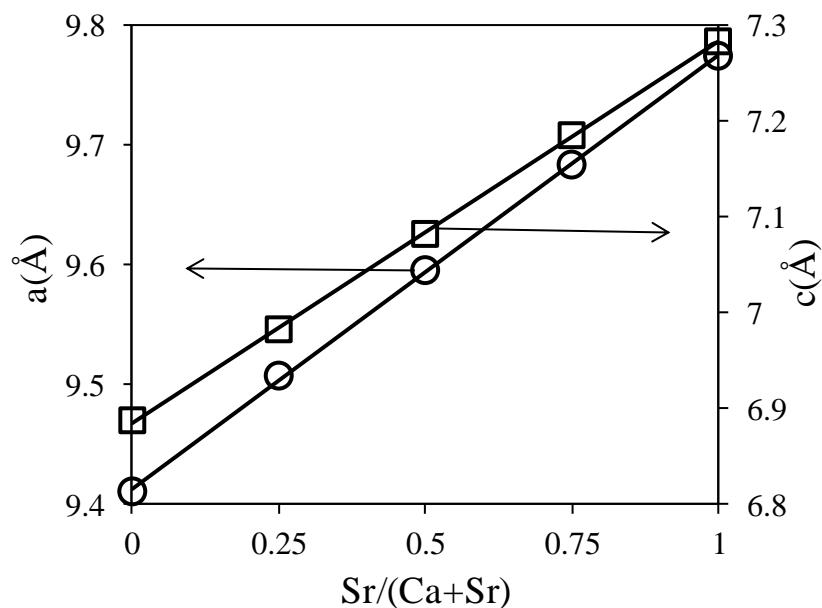


Figure 4-6 Variation in the *a* and *c* cell parameters with the Sr content in stoichiometric apatites.

The lower length/thickness ratio of Sr apatites compared to Ca apatites suggests that the crystallites of Sr substituted apatites turn to be more spherical than Ca apatites (Table 4-2). In stoichiometric apatites, this length/thickness ratio tended to decrease from 3.2 to 1.5

with increase in Sr content from HAp to SrAp-75 and then increased slightly to 2.2 with further increase in Sr content in SrAp-100. This implies that the crystallite turn to be almost spherical with increase in Sr content and SrAp-75 crystallites should be more spherical than all other apatites. The length/thickness ratio was found to vary in a similar manner for deficient apatites as that for stoichiometric apatites.

The decrease in surface area of the Sr apatites compared to the Ca apatites can be explained by the increased crystallite size with Sr substitution as determined by Rietveld refinement. Since the variation in crystallite size is inconsistent between (1 0 0) and (0 0 1), we have correlated the length/thickness ratio to the surface area (Figure 4-7). Thus, the decrease in surface area of the stoichiometric apatites from HAp to SrAp-75 and the further increase in surface area in SrAp-100 are in rather good agreement with length/thickness ratio obtained from Rietveld refinement.

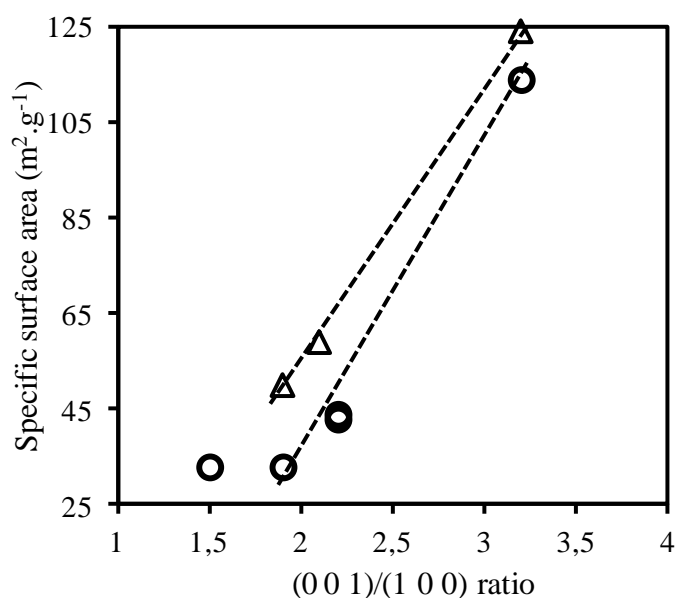


Figure 4-7 Specific surface area as a function of the (0 0 1)/(1 0 0) ratio (open circles represents the stoichiometric apatites and triangles the deficient apatites).

4.2.1.3 Scanning electron microscopy (SEM)

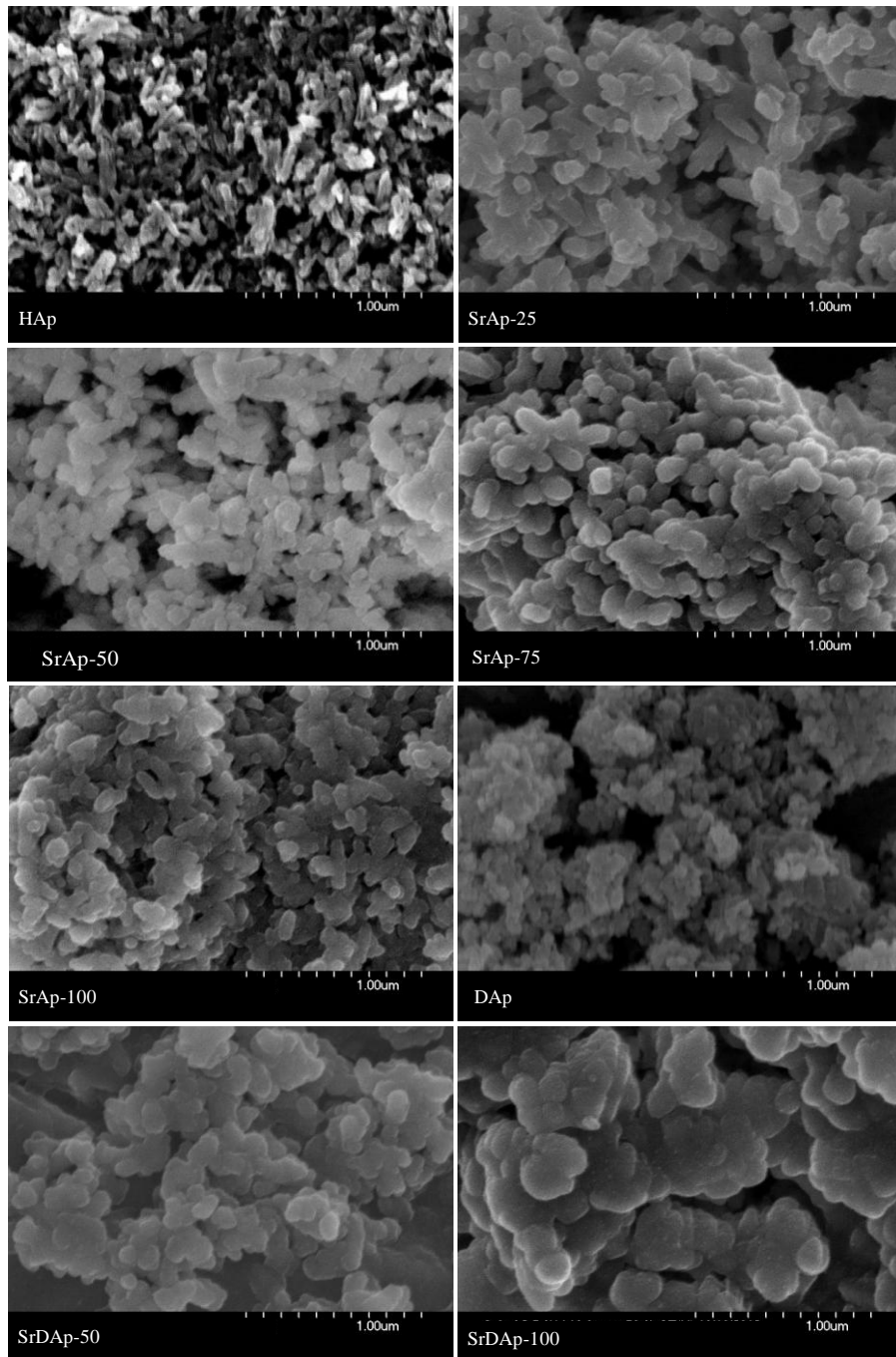


Figure 4-8 SEM images of the calcined apatites taken at a 50k magnification.

To compare the crystallites shape of the prepared solids with their grain shape, SEM pictures were taken (Figure 4-8). The SEM images clearly show that the grain size of the Sr-free apatites (HAp and Dap) is much lower compared to that of the Sr-containing

apatites. Considering the stoichiometric Sr apatites, the particles were rod or capsule-shaped agglomerates in SrAp-25, SrAp-50 and SrAp-100 and turned to a more spherical shape in SrAp-75. Thus, the grain shapes obtained from SEM images is well related with the crystallites shape deduced from Rietveld refinement. For example, the crystallite and grain shape of SrAp-75 were found spherical. The grain shape of the Sr-deficient apatites SrDAP-50 and SrDAP-100 is spherical, with larger grains compared to the stoichiometric apatites.

4.2.1.4 ICP & XPS to determine elemental composition

Table 4-3 shows the atomic composition of the calcined apatite solids determined by elemental analysis. The (Ca + Sr)/P ratio of the stoichiometric apatites are in rather good in agreement with the molar ratio of the solutions (1.67) used during the synthesis. Only SrAp-75 solid exhibited a slightly lower (Ca + Sr)/P ratio of 1.65. For deficient apatites, the (Ca + Sr)/P ratios of the prepared solids are higher than that of the ratio taken during the synthesis. For a (Ca + Sr)/P molar ratio of 0.9 in the solutions, we obtained deficient solids with ratios in the range of 1.61 to 1.62, thus approaching the stoichiometry.

Table 4-3 Elemental and surface composition of apatite solids calcined at 400°C.

| Solids | ICP | | | XPS | | |
|-----------|----------------|----------------|---------------------|----------------|----------------|---------------------|
| | Ca/P (at.%) | Sr/P (at.%) | (Ca+Sr)/P (at.%) | Ca/P (at.%) | Sr/P (at.%) | (Ca+Sr)/P (at.%) |
| HAp | 1.69 | - | 1.69 | 1.27 | - | 1.27 |
| SrAp-25 | 1.27 | 0.41 | 1.68 | 0.92 | 0.52 | 1.44 |
| SrAp-50 | 0.85 | 0.83 | 1.68 | 0.64 | 0.98 | 1.62 |
| SrAp-75 | 0.44 | 1.21 | 1.65 | 0.29 | 1.51 | 1.80 |
| SrAp-100 | - | 1.69 | 1.69 | - | 2.10 | 2.10 |
| DAP | 1.62 | - | 1.62 | 1.19 | - | 1.19 |
| SrDAP-50 | 0.81 | 0.80 | 1.61 | 0.59 | 0.97 | 1.56 |
| SrDAP-100 | - | 1.61 | 1.61 | - | 1.91 | 1.91 |

The surface composition of all the apatites determined by XPS is given in Table 4-3. Since an overlap of the Sr3d and the P2p photopeaks was observed in XPS, the surface

compositions were determined using Ca2p, Sr3p3/2 and P2s photopeaks (Figure 4-9). Moreover an overlap of C1s and Sr3p1/2 photopeaks was observed in stoichiometric and deficient strontium substituted apatites. Therefore P2s photopeak was used as reference since the binding energy value of P2s remained constant at 299.5eV for HAp and Dap samples. For all the apatites, the binding energy of Ca2p, Sr3p3/2 and O1s peaks thus lies in the range of 347.3-347.6 eV, 269.1-269.3 eV and 531.0-531.3 eV, respectively.

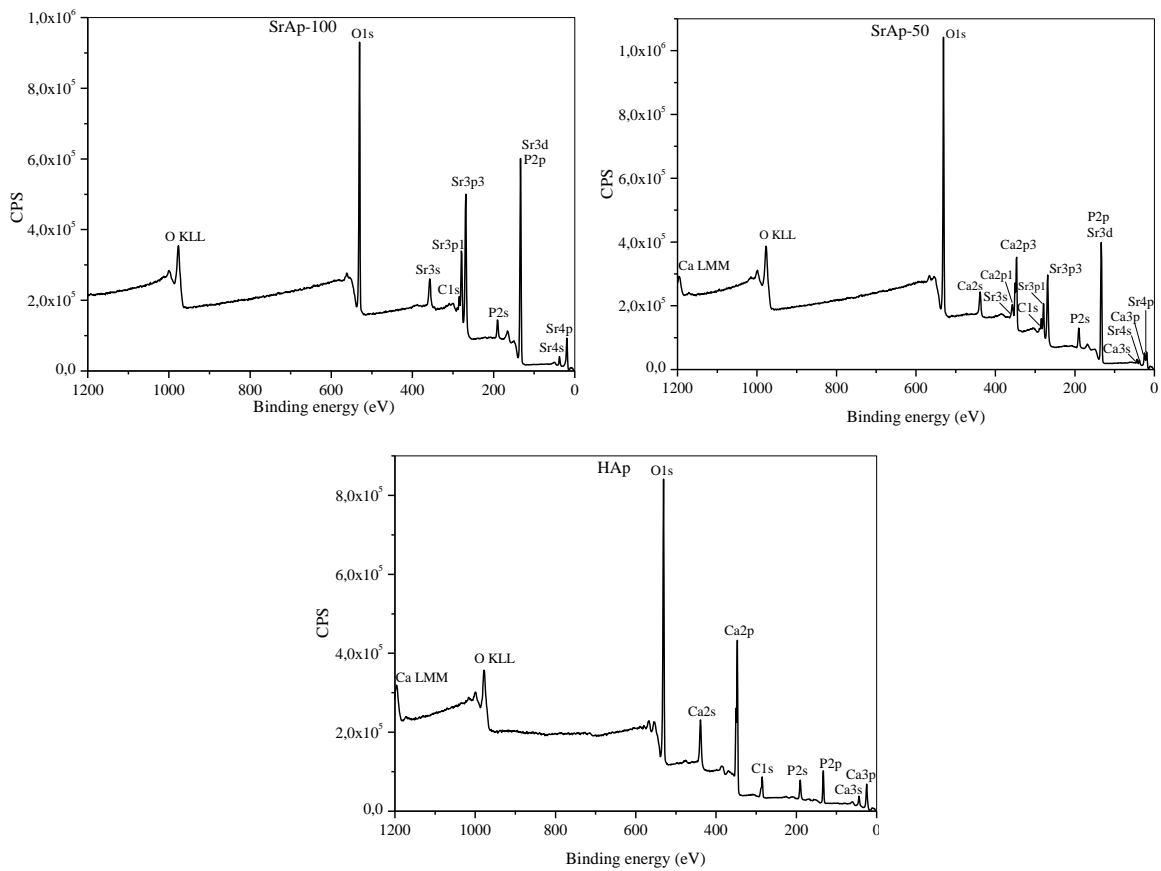


Figure 4-9 XPS spectra of SrAp-100, SrAp-50 and HAp.

The surface (Ca + Sr)/P ratio of stoichiometric and deficient apatites increased with increase in the Sr substitution, though the (Ca + Sr)/P bulk ratio remained almost unchanged [Figure 4-10(a)]. For all apatites with 0% to 50% of Sr substitution, the surface (Ca + Sr)/P ratio was found to be lower compared to bulk (Ca + Sr)/P ratio. Above 50% Sr substitution, the surface (Ca + Sr)/P ratio exceeds the bulk ratio. It is because up to a Sr substitution of 50%, more phosphate groups are exposed to the surface than Ca and/or Sr

compared to the bulk, whereas for apatites with more than 50% Sr substitution, more Ca and/or Sr are exposed to the surface than phosphate groups compared to the bulk. Moreover, the Ca/P surface ratio was always lower than the bulk Ca/P ratio but the Sr/P surface ratio was higher than the bulk Sr/P ratio [Figure 4-10(b) & (c)]. This confirms that, irrespective of the Sr content in the apatites, Sr atoms are more exposed to surface than phosphate groups, whereas the Ca is less exposed to the surface than the phosphate groups compared to the bulk. These observations are good in agreement with a previous report that revealed high surface Sr/P ratios in apatite solids compared with the bulk ratios [1]. The larger size of Sr^{2+} cation (ionic radius = 0.118 nm) compared to Ca^{2+} cation (ionic radius = 0.100 nm) may be the reason for this increased surface exposure of Sr. Furthermore, it can explain the decrease in the surface exposure of both calcium and phosphate groups in Sr-substituted apatites.

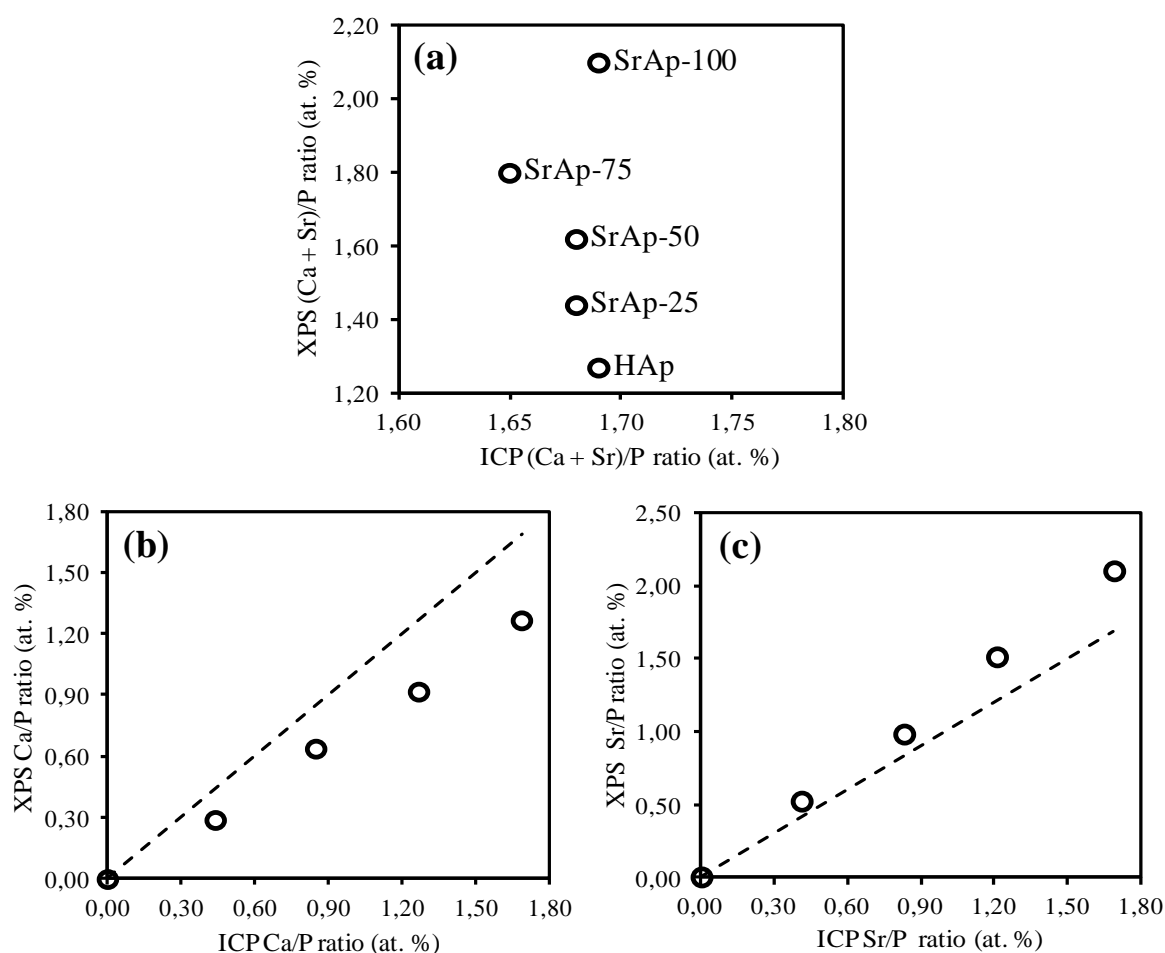


Figure 4-10 (a) (Ca + Sr)/P ratio determined by XPS as a function of (Ca + Sr)/P ratio by ICP, (b) Ca/P ratio determined by XPS as a function of Ca/P ratio by ICP and (c) Sr/P ratio determined by XPS as a function of Sr/P ratio by ICP in the stoichiometric apatites.

4.2.1.5 Low energy ion scattering (LEIS)

To verify the effect of Sr substitution on distribution of the first atomic layer, HAp (0 mol.% Sr), SrAp-50 (50 mol.% Sr) and SrAp-100 (100 mol.% Sr) were chosen for LEIS analysis (Figure 4-11). In all the solids, an O peak was observed at 1230 eV and a weaker peak due to P was also observed at 1880 eV. However, this latter seems to overlap the background signal resulting from the contribution of a uniform distribution of lighter atoms (H, C & O). The presence of P peak was confirmed using $\text{NH}_4\text{H}_2\text{PO}_4$ precursor as explained in Chapter 3 (section 3.2.1.4.2). A peak due to Ca was observed in HAp and SrAp-50, at around 2100 eV. The peak due to Sr was observed for SrAp-50 and SrAp-100 at around 2560 eV.

Considering HAp, the Ca ions and O ions were more exposed on the first atomic layer. This observation contradicts with the results obtained by XPS for HAp that showed a lower Ca/P ratio (compared to bulk) due to more P (phosphate) exposure (Table 4-3). However, it is worth noting that the LEIS technique only probes the uppermost atomic layer of the samples, while XPS gives information on the composition along a depth of a few nanometers. In contrast, no such contradiction was observed in the case of SrAp-100 that showed more Sr exposure compared to P, in both XPS and LEIS. In SrAp-50 (thus with 50 mol.% Ca and 50 mol.% Sr), Ca and Sr ions are more exposed to the first atomic layer compared to P. A direct prediction on the surface exposure of Ca and Sr ions is not possible only from their relative peak intensity, as the peak intensity depends on certain parameter like atomic mass. However, a semi-quantitative calculation in SrAp-50 (based on the 100% Ca and 100% Sr samples) has shown that more Ca ions are exposed compared to Sr ions, with a roughly estimated factor of 1.4. This is in contradiction with the XPS results: SrAp-50 exhibited a higher Sr/P ratio than the Ca/P ratio (see Table 4-3). This clearly shows that, along a depth of around 10 nanometers corresponding to XPS depth analysis, the Sr ions are more abundant than the Ca ions, but considering only the uppermost atomic layer, more Ca ions are exposed than Sr ions.

Since the results obtained from Rietveld refinements have shown that the crystallite growth is more pronounced along [0 0 1] or in the *c*-axis direction, the Ca^{2+} and/or Sr^{2+} ions should be more exposed along the *c*-axis, that is, on *ac* and *bc* planes.

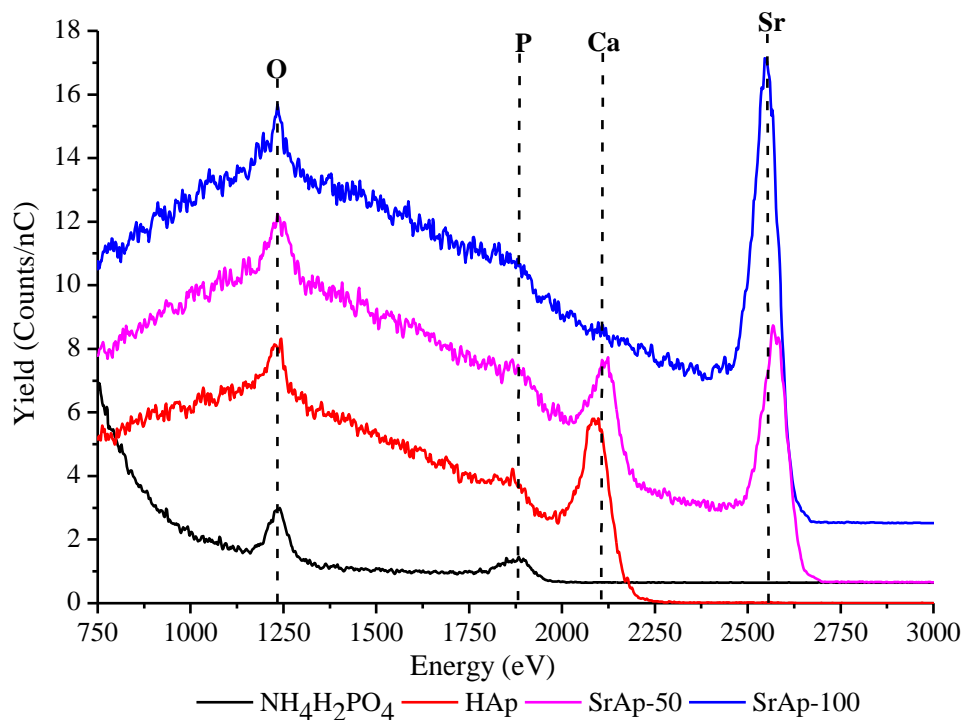


Figure 4-11 LEIS spectra of apatite solids

4.2.1.6 Infrared spectra of the solids

Figure 4-12 shows two domains of the same infra red spectra for all the apatite solids focused on two regions, namely $3000\text{-}3700\text{ cm}^{-1}$ and $1700\text{-}400\text{ cm}^{-1}$. The vibrational band in the range $3000\text{-}3700\text{ cm}^{-1}$ is observed in all the apatites due the presence of adsorbed and constitutive water molecules [4]. A sharp band at 3572 cm^{-1} is observed for Sr-free apatites (HAp and DAp) that can be assigned to structural OH group. The intensity of this peak decreased in Sr-substituted apatites compared to Sr-free apatites, as previously reported [5]. SrAp-25 exhibited OH band at the same position (3572 cm^{-1}) as observed in Sr-free apatites. When the Sr substitution was further increased to SrAp-50 and SrAp-75, the intensity of the OH band diminished accompanied by the band broadening. A close observation of the OH band in SrAp-75 revealed the presence of two low intense peaks, the first one at 3572 cm^{-1} , and the second one at 3592 cm^{-1} . This is good in agreement with previous reports that have shown the OH band split is due to the variation in the strength of O-H bond attached to both Ca and substituted Sr ions in the Ca (II) triangle sites [5,6]. This band was completely upshifted to 3592 cm^{-1} in 100 % Sr substituted apatites SrAp-

100 and SrDAp-100. The above observation indicates the substitution of Ca ions by Sr ions from the Ca (II) sites, especially for Sr substitutions of above 50 mol%.

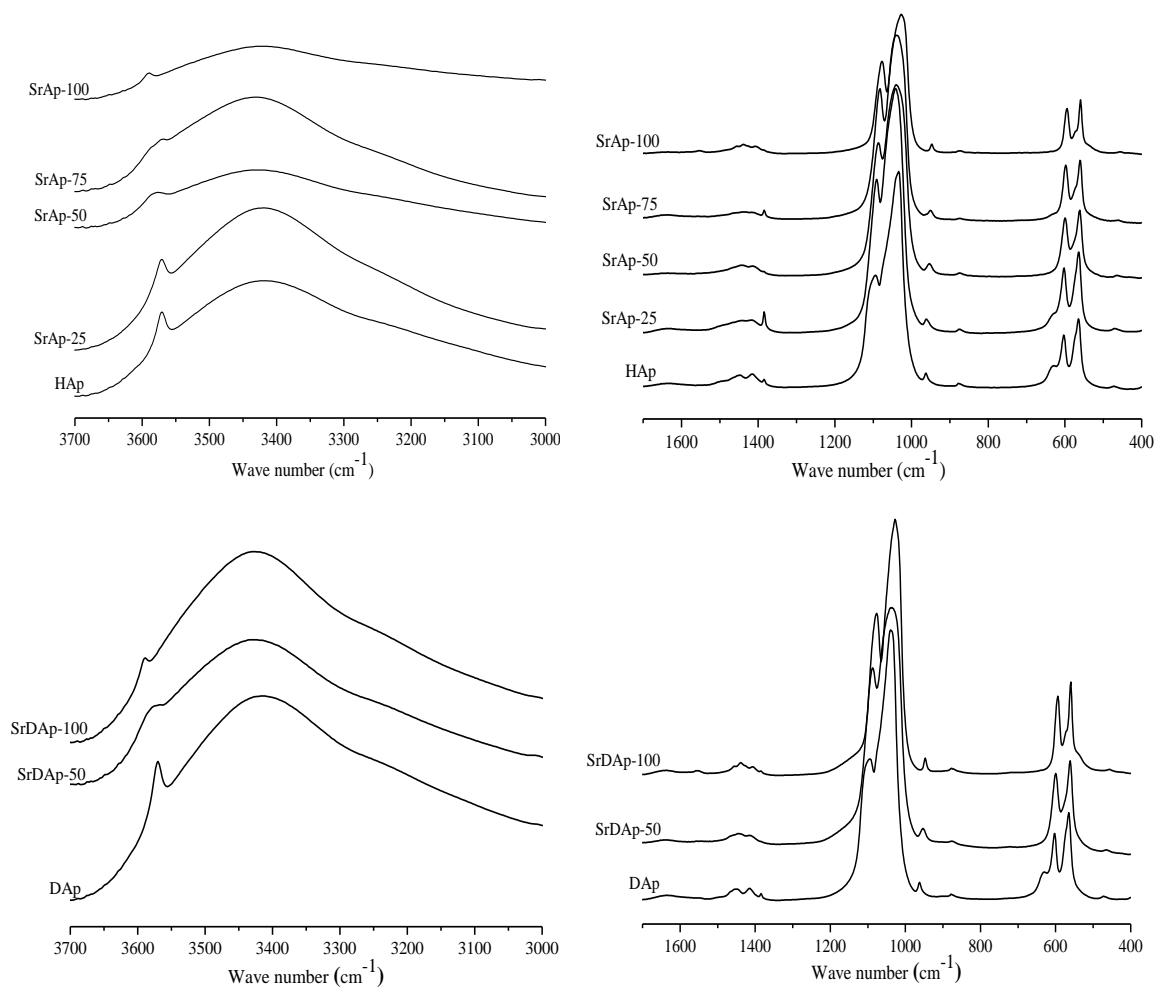


Figure 4-12 Infra-red spectra of the stoichiometric and the deficient apatites calcined at 400°C.

An OH libration band was observed at around 630 cm^{-1} for Ca apatites and the intensity of this band also decreased with increase in Sr content. This band is absent for Sr apatites with Sr content above 50 mol%. This decrease in intensity of all OH modes of vibration in Sr apatites compared with Ca apatites resulted from the decrease in stronger hydrogen bond interactions between OH and PO_4 groups due to Sr substitution. B.O. Fowler reported that polarizing power of Sr (1.59) is lower than Ca (2.04) and hence the polarization of OH^- ions decreased with Sr substitution [5]. This decrease in polarization

in Sr apatites in turn decrease the tendency of OH⁻ to form hydrogen bond with PO₄³⁻ groups resulting in decrease in OH band intensity. Since the OH⁻ ions are located at the centre of Ca (II) triangles, this observation once again confirms the substitution of Ca (II) ions by Sr ions. In addition all the above observations also point to the fact that the absence or the reduced intensity of OH⁻ bands especially in stoichiometric apatites is not due to the deficiency in OH⁻ groups but due to the changes in environment of OH⁻ ions due to Sr substitution.

The PO₄ vibrational modes for Ca apatites are observed at 565 cm⁻¹, 605 cm⁻¹, 963 cm⁻¹ and 1030 – 1100 cm⁻¹ [7]. The infrared absorption bands due to phosphate groups shifted to lower wave numbers on increasing strontium content in apatites as previously reported [3]. In addition the peaks at 1460 cm⁻¹ and 1419 cm⁻¹ are attributable to CO₃²⁻ [4]. A peak at 1350 cm⁻¹ is observed for some solids (SrAp-25 & SrAp-75) due to the nitrate impurity from the precursors used for the synthesis [8].

4.3.1.7 Raman spectra of solids

Figure 4-13 shows the Raman spectra of the stoichiometric apatites and deficient apatites. As shown in the figure, four peaks were observed for all solids, which are characteristic of hydroxyapatites. In the case of HAp, these peaks appeared at 960 cm⁻¹ (ν_1 PO₄³⁻ mode), 400 – 460 cm⁻¹ (ν_2 PO₄³⁻ mode), 1010 – 1100 cm⁻¹ (ν_3 PO₄³⁻ mode) and 570 – 620 cm⁻¹ (ν_4 PO₄³⁻ mode), which is good in agreement with previous reports [9,10].

By increasing the Sr content from 0 mol% to 100 mol%, a down shift was observed for all the aforementioned PO₄³⁻ vibration modes. For example, this is more evident for ν_1 mode that has shown a linear down shift from 960 cm⁻¹ in HAp to 944 cm⁻¹ in SrAp-100 with increase in the Sr content (Figure 4-14 : circles). This linear relation reveals that the shift of PO₄³⁻ ν_1 mode is due to the changes in the PO₄³⁻ environment with increase in Sr substitution. This also reveals that Sr is substituting the Ca to form a single apatite phase, since Sr substitution did not show any additional peak in Raman spectra. Similar trends were observed in the Raman spectra of the deficient apatites (Figure 4-14 : triangles).

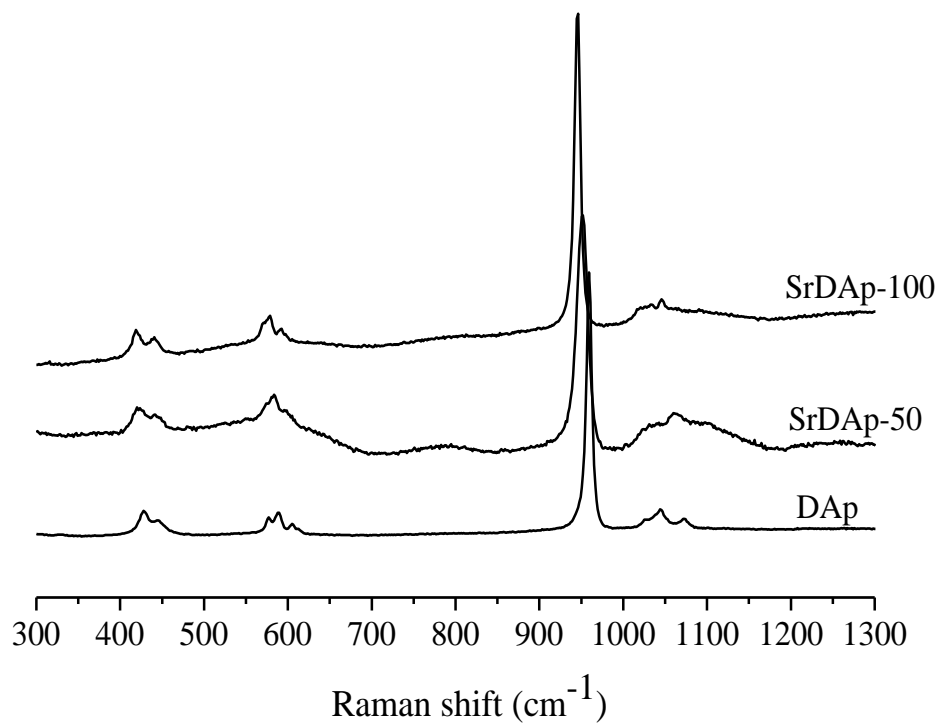
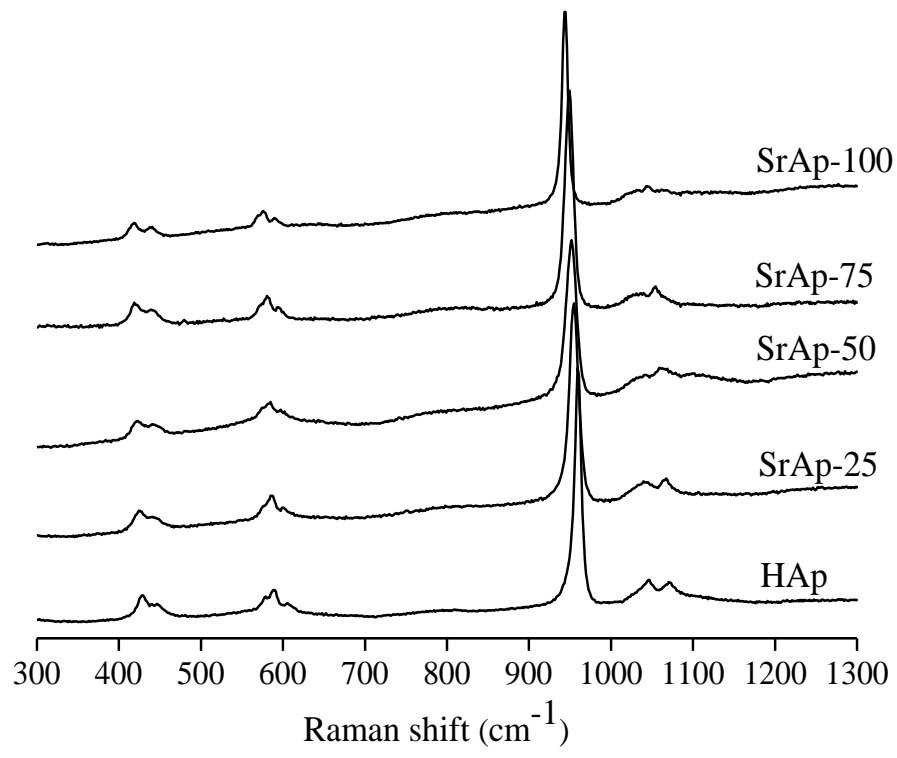


Figure 4-13 FT-Raman spectra of the calcined stoichiometric and deficient apatites.

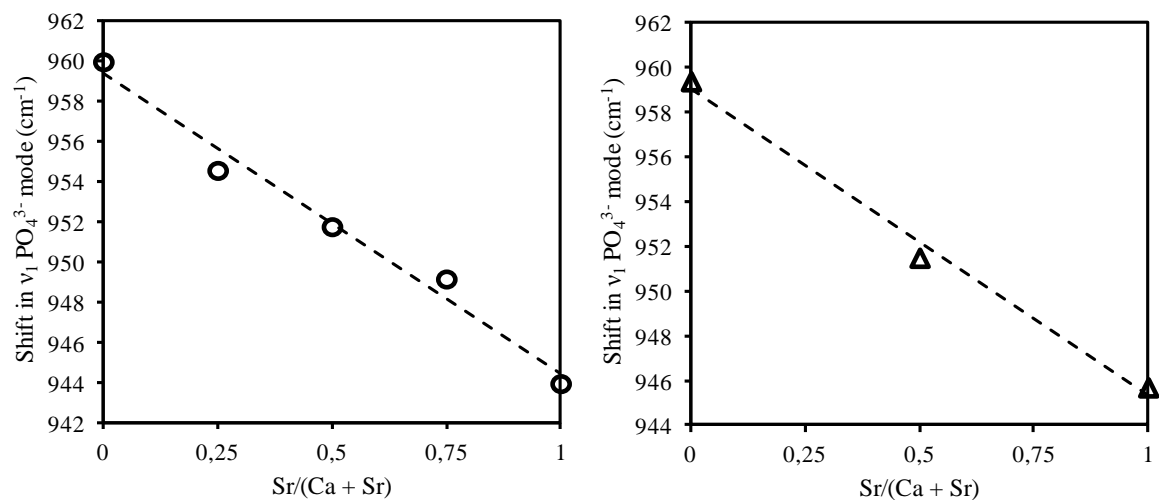


Figure 4-14 Shift in PO_4^{3-} ν_1 mode as a function of Sr substitution (open circles represents the stoichiometric apatites and triangles the deficient apatites)

4.2.1.8 TPD- NH_3 and TPD- CO_2

Acid and basic properties of the different samples, evaluated respectively using TPD- NH_3 and TPD- CO_2 experiments, are given in table 4-4.

Table 4-4 Acid-base properties of apatite solids determined by NH_3 -TPD & CO_2 -TPD experiments

| Catalysts | Number of acid sites ($\mu\text{mol.g}^{-1}$) | Acid sites density ($\mu\text{mol.m}^{-2}$) | Number of basic sites ($\mu\text{mol.g}^{-1}$) | Basic sites density ($\mu\text{mol.m}^{-2}$) | Ratio of number of acid sites to basic sites (R_{AB}) |
|-----------|---|---|--|--|---|
| HAp | 114.58 | 1.01 | 15.10 | 0.130 | 7.6 |
| SrAp-25 | 21.50 | 0.50 | 3.69 | 0.086 | 5.8 |
| SrAp-50 | 15.84 | 0.48 | 3.34 | 0.101 | 4.7 |
| SrAp-75 | 14.52 | 0.44 | 3.34 | 0.101 | 4.3 |
| SrAp-100 | 25.08 | 0.57 | 6.21 | 0.141 | 4.0 |
| DAp | 143.40 | 1.16 | 6.20 | 0.050 | 23.1 |
| SrDAp-50 | 28.0 | 0.56 | 1.29 | 0.026 | 21.7 |
| SrDAp-100 | 34.8 | 0.59 | 1.91 | 0.032 | 18.2 |

The amount of acid sites was larger in the deficient apatites compared to their stoichiometric counterparts having similar Sr substitutions (Table 4-4). This result is good in agreement with previous report [11]. In stoichiometric apatites, the number of acid sites tended to decrease from $1.01 \mu\text{mol.m}^{-2}$ to $0.44 \mu\text{mol.m}^{-2}$ with the increase in the Sr substitution from HAp to SrAp-75 and then increased to $0.57 \mu\text{mol.m}^{-2}$ with further increase in Sr content to SrAp-100. A similar trend was observed for deficient apatites. The Ca^{2+} ions generally behave as acid sites in Sr-free apatites and when these Ca^{2+} ions are substituted by larger Sr^{2+} ions, the number of acid sites per square meter can decrease. This might be the reason for decrease in acid sites with increase in Sr substitution, though it cannot explain the higher acid sites density observed for the 100% Sr substituted samples (SrAp-100 and SrDAp-100).

The basic site density of stoichiometric apatites decreased from $0.130 \mu\text{mol.m}^{-2}$ to $0.086 \mu\text{mol.m}^{-2}$ with increase in Sr content from HAp to SrAp-25 (Table 4-4). Further increase in Sr content to 50 mol% increased the basic site density from $0.086 \mu\text{mol.m}^{-2}$ to $0.101 \mu\text{mol.m}^{-2}$ and remains unchanged for SrAp-75. For SrAp-100 the basic site density was found to be $0.141 \mu\text{mol.m}^{-2}$, which is higher than other apatites. Deficient apatites possess lower basic sites density compared to their stoichiometric counterparts. The amount of basic sites in deficient apatites decreased from $0.050 \mu\text{mol.m}^{-2}$ to $0.026 \mu\text{mol.m}^{-2}$ with an increase in Sr substitution from 0 mol % (DAp) to 50 mol % (SrDAp-50) Sr substitution and then increased slightly to $0.032 \mu\text{mol.m}^{-2}$ for further increase in Sr content to 100 mol % (SrDAp-100).

Increase in Sr substitution was expected to increase the basic site density, but values from stoichiometric and deficient apatites do not reflect this trend. The first reason may be due to small deviations resulted from the underestimated integration (the end of CO_2 -TPD curves for the Sr based samples did not return to the base line). Secondly, the basicity of the apatite can be different for the Sr substituting in the Ca(I) sites and in the Ca(II) sites. Indeed the basicity of an atom is well known to increase with increase in its coordination number. In hydroxyapatite Ca(I) is coordinated to 9 O atoms and Ca(II) is coordinated to 7 O atoms. Hence Sr atoms substituting for Ca(I) sites will possess more basicity compared to Sr atoms substituting Ca(II) sites. These two sites are not necessary equally substituted by strontium which can thus cause an inconsistent trend in basicity with Sr substitution.

Since both the acid and the base sites are required for the Guerbet reaction catalyzed by the apatites, the ratio of number acid to basic sites (R_{AB}) can be a useful parameter for our studies. Deficient apatites are known to be highly acidic in nature compared to stoichiometric apatites [11]. This was clearly observed in case of deficient apatite DAp that possess large number of acid sites than stoichiometric HAp. But strontium deficient apatites SrDAp-50 and SrDAp-100 which are supposed to be more acidic in behaviour than stoichiometric apatites have less number of acid sites compared to stoichiometric HAp. However the R_{AB} value was found to be higher for all deficient apatites compared to their stoichiometric counterparts showing their relative dominant acidic behaviour of deficient apatites over stoichiometric solids (Table 4-4). Also for stoichiometric apatites, the R_{AB} value tended to decrease sharply with increase in Sr substitution up to 50 mol% and then slowly for Sr substitutions above 50 mol% (Figure 4-15). This decrease in R_{AB} value is an indirect representation of relative increase in the predominance of basic sites over acid sites with increase in Sr substitution. Similarly a rather linear decrease in R_{AB} with Sr substitution is observed for deficient apatites (Figure 4-15).

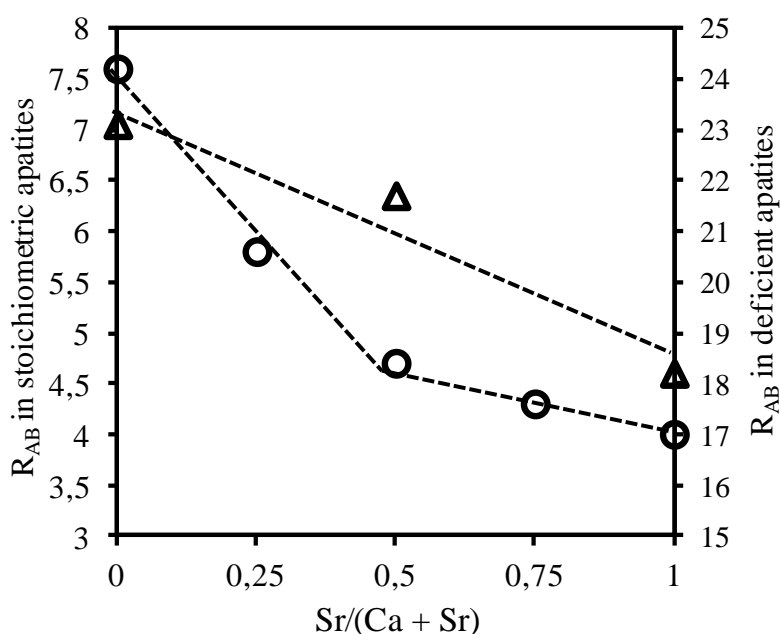


Figure 4-15 Variation in the ratio of number of acid sites to basic sites (R_{AB}) with Sr substitution in stoichiometric apatites (represented by open circles) and in deficient apatites (represented by open triangles).

Figure 4-16 shows the CO₂ desorption curves of stoichiometric and deficient apatites. Three desorption peaks were clearly observed in stoichiometric apatites at temperatures of around 125°C, 190°C and 330°C which may be due to the presence of weak, medium and strong basic sites. The peak at 330°C due to stronger basic sites was not observed for deficient apatites. So we can assume that this peak is due to the lattice OH⁻ groups in the apatite structure that lacks in deficient apatites resulting from the removal of OH⁻ groups for the charge compensation due to Ca deficiency [11,12]. The intensity of peaks due to medium basic sites was more pronounced than the weak basic sites in Sr apatites. Moreover in stoichiometric apatites, increase in Sr substitution from 0 mo% to 75 mol% resulted in the consistent decrease in the intensity of the peak due to weak basic site. Further increase in Sr content to 100% resulted in the increase in the intensity of this peak.

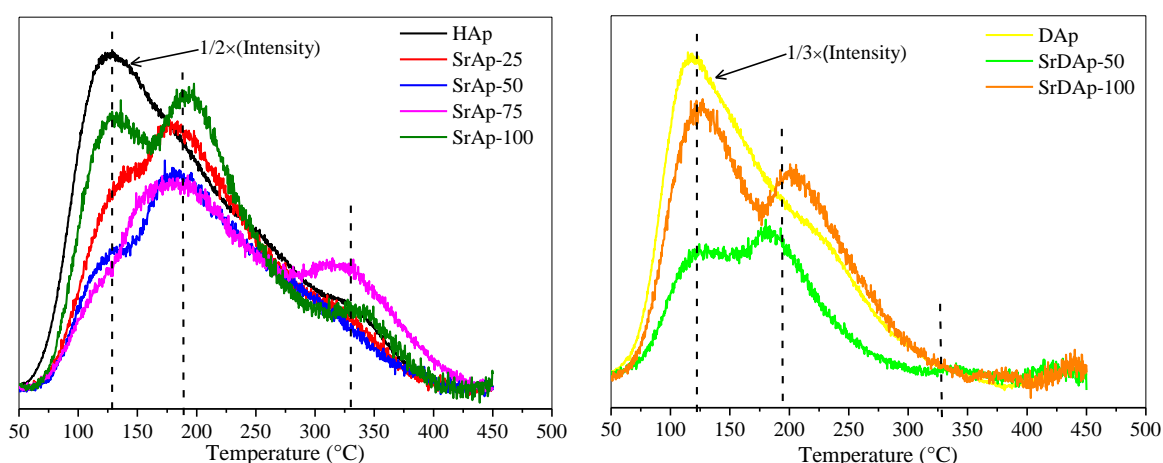


Figure 4-16 TPD-CO₂ curves of stoichiometric and deficient apatites (Intensity of HAp & DAp reduced and base line subtracted)

As a conclusion to this part, acid-base behaviour of the apatites was found to vary by varying the Sr substitution. The ratio of number of acid sites to basic sites (R_{AB}) decreased with increase in Sr substitution thereby revealing the increase in predominant basic behaviour with increase in Sr substitution. Deficient apatites possess higher R_{AB} ratio showing their higher predominant acidic behaviour compared to stoichiometric apatites. Moreover the strength of the apatites was found to vary by varying the Sr substitution. Hence varying the Sr content allowed in modulating both density and strength of acid and basic sites.

4.3.1.9 Isopropanol test

Isopropanol decomposition to propylene and acetone was performed over all apatites to evaluate the acid-base property of the solids. Isopropanol can be transformed to propylene by dehydration over the acid sites and to acetone by dehydrogenation over the basic sites. Figure 4-17 and Figure 4-18 show the selectivity to propylene and acetone respectively at 20% conversion of *isopropanol*.

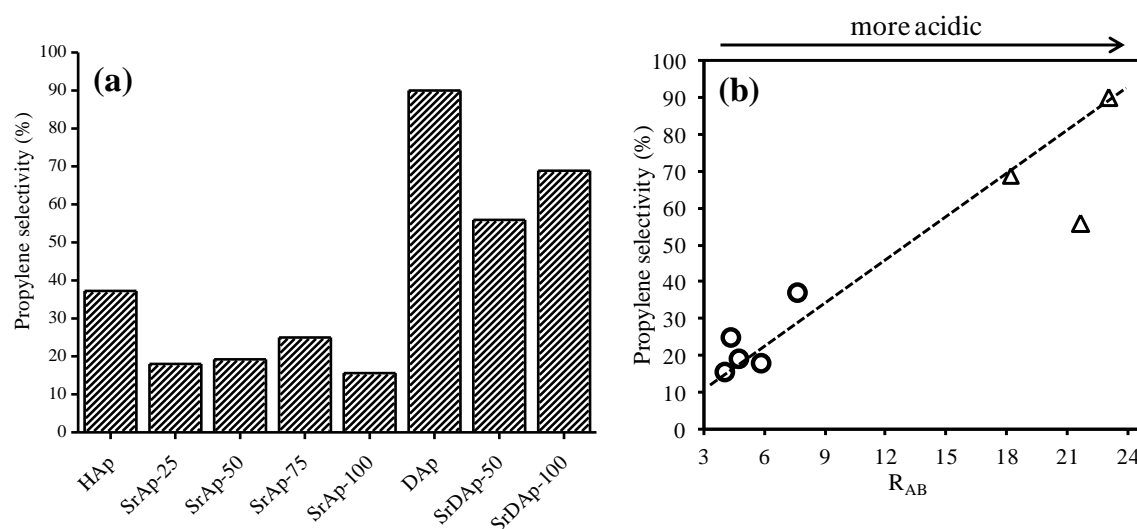


Figure 4-17 (a) *Isopropanol* decomposition to propylene over apatite catalysts at 20% conversion (Catalyst amount = 0.1 g, He flow = 25 mL.min⁻¹, saturator temperature = 10°C); (b) Plot of propylene selectivity as a function of ratio of number of acid sites to basic sites (R_{AB}). (Open circles represents the stoichiometric apatites and open triangles the deficient apatites).

Figure 4-17(a) shows that propylene selectivity over stoichiometric apatites decreased from 37.2 % to 18 % with increase in Sr content from HAp to SrAp-25. This is good in agreement with the TPD-NH₃ results where HAp possess very high amount of acid sites (114.58 $\mu\text{mol.g}^{-1}$) compared to other Sr-substituted stoichiometric apatites. Further increase in Sr content in stoichiometric apatites did not vary much the propylene selectivity. This reveals that variation in the number of acid sites between 15 $\mu\text{mol.g}^{-1}$ and 25 $\mu\text{mol.g}^{-1}$ had no significant effect on propylene selectivity in stoichiometric apatites. In the case of deficient apatites, Sr-free deficient apatite (DAp) was more selective to propylene than Sr substituted deficient apatites. The propylene selectivity over deficient

apatites decreased from 90 % to 55.9 %, when Sr content is increased respectively from 0 % in DAp to 50% in SrDAp-50. Further increase in Sr content to 100% in SrDAp-100 increased the propylene selectivity to 69%. These observations are good in agreement with the TPD-NH₃ results. However it is worth to note that the propylene selectivity increased from around 20% in Sr-substituted stoichiometric apatites to about 60% in Sr-substituted deficient apatites though there is not much difference in the number of acid sites (Table 4-4). Therefore this increase in propylene selectivity could be explained by the increase in strength of acid sites. Indeed the comparison of TPD-NH₃ curves have shown an extension of the desorption curves at higher temperatures for the deficient apatites (Figure 4-18), explaining by the presence of stronger acid sites.

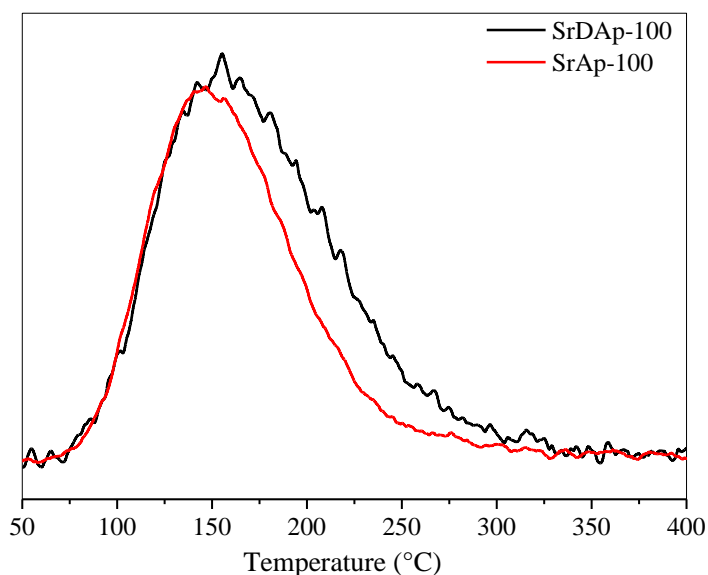


Figure 4-18 Comparison of TPD-NH₃ curves of SrAp-100 and SrDAp-100 samples

As abovementioned, since the ratio of number of acid sites to basic sites (R_{AB}) is a good parameter to verify the predominance of acid and basic behaviour of the apatite catalysts, the correlation between R_{AB} and propylene selectivity was investigated [Figure 4-17(b)]. The propylene selectivity was found to increase rather linearly with increase in R_{AB} . Stoichiometric apatites with lower R_{AB} were less selective to propylene thereby showing their lower acidic behaviour compared to the deficient apatites. In contrast the deficient apatites with higher R_{AB} value have shown higher selectivity to propylene confirming their

higher acidic behaviour. This can, in addition to the presence of stronger sites, explain why the Sr-substituted deficient apatites (eg. SrDAP-100) are more selective to propylene than Sr-substituted stoichiometric apatites (eg. SrAp-100) though the number of acid sites did not varied much.

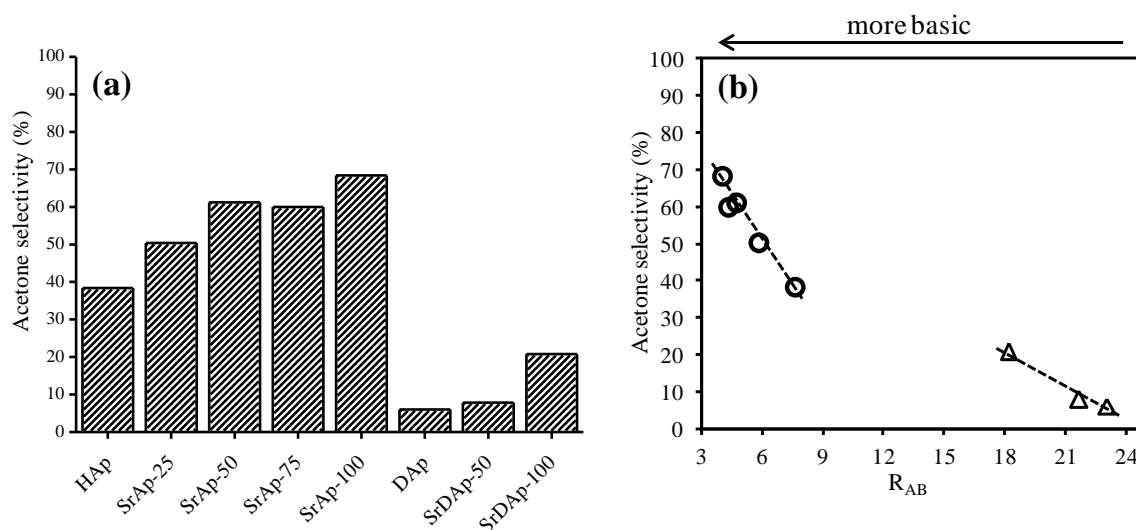


Figure 4-18 (a) *Isopropanol* decomposition to acetone over apatite catalysts at 20% conversion (Catalyst amount = 0.1 g, He flow = 25 mL.min⁻¹, saturator temperature = 10°C); (b) Plot of acetone selectivity as a function of ratio of number of acid sites to basic sites (R_{AB}). (Open circles represents the stoichiometric apatites and open triangles the deficient apatites).

Acetone formation from *isopropanol* decomposition over stoichiometric apatites tended to increase from 38.4 % to 68.4 % with increase in Sr content respectively from 0 mol % (HAp) to 100 mol % (SrAp-100) except for SrAp-75 which has shown similar acetone selectivity as SrAp-50 [Figure 4-18(a)]. Similar to stoichiometric apatites, acetone formation over deficient apatites increased from 6 % to 20.8 % with increase in Sr content from 0 % in DAp to 100 % in SrDAP-100. These observations are good in agreement with TPD-CO₂ results showing the increase in basic sites with Sr substitution. Though the Sr-free apatites HAp and DAp possess more number of basic sites compared to Sr-substituted apatites, they have shown lower selectivity to acetone. This discrepancy can be then explained using the R_{AB} parameter hereafter.

If we consider the R_{AB} ratio, the acetone selectivity was found to increase linearly with decrease in R_{AB} for stoichiometric and deficient apatites [Figure 4-18(b)]. This clearly shows that the acetone selectivity increases with increase in the predominant basic behaviour, since the lower R_{AB} value is an indirect representation of the relative predominance of basic behaviour in apatite catalysts. Hence the higher R_{AB} value and lower basic behaviour can explain why Sr-free apatites HAp and DAp were less selective to acetone compared to other Sr-substituted apatites though HAp and DAp possess larger number of basic sites. Furthermore a sharp increase in acetone selectivity with decrease in R_{AB} was clearly observed for stoichiometric apatites compared to deficient apatites. We suppose this sharp increase in the stoichiometric apatites is due to the presence of stronger basic sites which can promote the dehydrogenation of propanol to acetone, these stronger basic sites being absent in deficient apatites (see Figure 4-16).

Hence we could conclude that it is not only the amount of sites but also the strength of the sites in the apatites that affect the selectivity towards the acetone and propylene.

4.2.2 Catalytic reaction

4.2.2.1 Guerbet reaction products observed at iso-conversion

Table 4-5 Selectivity to Guerbet reaction products at 13% of ethanol conversion.

| | HAp | SrAp-25 | SrAp-50 | SrAp-75 | SrAp-100 | DAp | SrDAp-50 | SrDAp-100 |
|-----------------------------|-----|---------|---------|---------|----------|------|----------|-----------|
| Ethylene | 2.4 | 4 | 3.5 | 4.1 | 1.7 | 4.5 | 43 | 32.2 |
| Acetaldehyde | 10 | 11 | 15.7 | 7.5 | 9.1 | 6.5 | 14.2 | 20.2 |
| Butanol | 50 | 51 | 47.8 | 52 | 63.2 | 49 | 11.4 | 16 |
| C4-C8 alcohols ^a | 18 | 5.5 | 7.4 | 8 | 13.2 | 16 | 2 | 3 |
| Total alcohols ^b | 68 | 56.5 | 55.2 | 60 | 76.4 | 65 | 13.4 | 19 |
| Dienes ^c | 1.6 | 5.8 | 5 | 4 | 2.7 | 3.5 | 1.6 | 2.6 |
| Diethylether | 4 | 3.5 | 1.7 | 3.2 | 2 | 5.3 | 9 | 7.6 |
| Others ^d | 14 | 19.2 | 18.9 | 21.2 | 8.1 | 15.2 | 18.8 | 18.4 |

^a2-buten-1-ol, 2-ethylbutanol, hexanol, 2-ethylhexanol, octanol

^bButanol and C4-C8 alcohols.

^c1,3-butadiene and C6-dienes

^dHigher aldehydes, higher alkenes, aromatics.

Table 4-5 shows the selectivity to the main products for the Guerbet reaction of ethanol over apatite catalysts at ethanol iso-conversion of 13%. This iso-conversion of ethanol was achieved by properly adjusting the temperature between 300°C and 400°C at GHSV's between 5000 mL.h⁻¹.g⁻¹ and 15000 mL.h⁻¹.g⁻¹. Butanol is one of the major products observed in the Guerbet reaction of ethanol over all the apatite catalysts, except deficient apatites SrDAp-50 and SrDAp-100. In SrDAp-50 and SrDAp-100, ethylene was formed as major product with the selectivity of 43% and 32.2% respectively which is good in agreement with isopropanol test. Selectivity towards butanol was found to be maximum over catalyst SrAp-100 (63.2%) compared to all other apatite catalysts. Noticeable amount of acetaldehyde, the dehydrogenation product of ethanol, was also produced over all the catalysts. Diethylether was also formed by the dehydration of ethanol over all the catalysts and its formation is slightly higher over deficient apatites compared to stoichiometric apatites. Small quantity of dienes was also observed over all the catalysts. Other compounds include higher aldehydes, higher alkenes and trace amount of aromatics, which are formed by uncontrolled consecutive reaction over the various sites present at the surface of the solids.

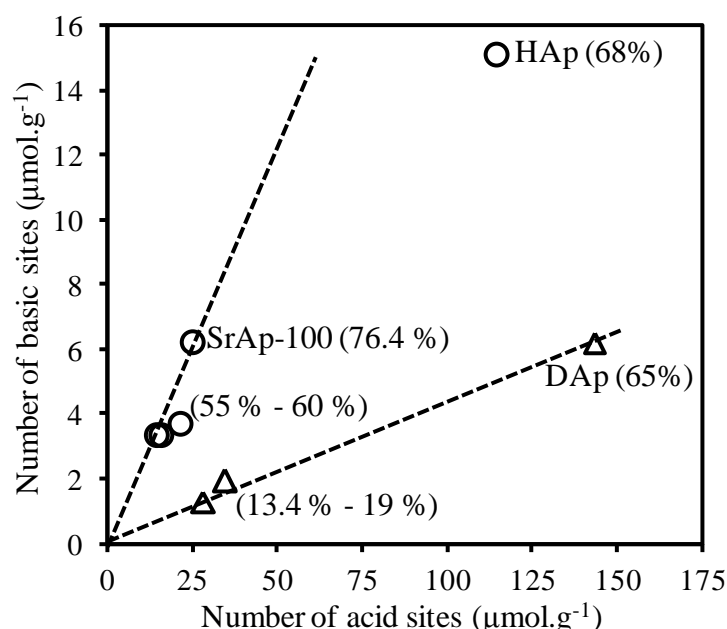


Figure 4-19 Number of basic sites as a function of number of acid sites. Selectivity to total alcohols is given in brackets near to the symbols (Open circles represents the stoichiometric apatites and open triangles the deficient apatites).

Plot of number of basic sites as a function of number of basic sites for the apatite catalysts is shown in Figure 4-19. A dashed line is plotted starting from origin and passing through the Sr substituted stoichiometric apatites. The stoichiometric apatites SrAp-25, SrAp-50 and SrAp-75 possess almost similar amount of acid and basic sites, have shown similar total alcohols selectivity in the range between 55% - 60% (Figure 4-19). The total alcohols selectivity increased to a maximum of 76.4% in SrAp-100, which have shown a slight increase in the number of acid sites and the number of basic sites than the aforementioned stoichiometric Sr substituted apatites. This clearly shows that small variation in the number of basic and acid sites can have a big influence on the product distribution in Guerbet reaction.

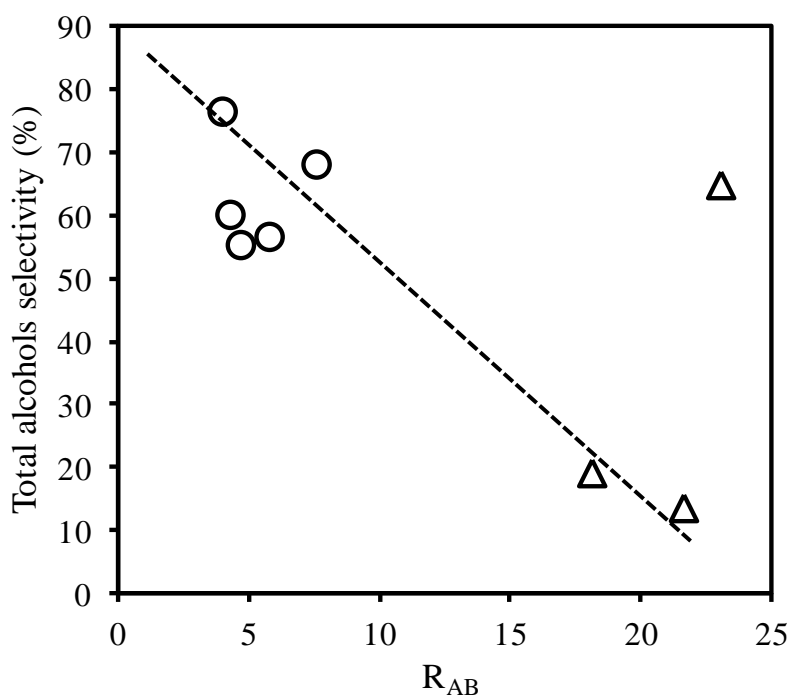


Figure 4-20 Plot of total alcohols selectivity as a function of the ratio of number of acid sites to basic sites (Open circles represents the stoichiometric apatites and open triangles the deficient apatites).

HAp deviates from the linearity of stoichiometric apatites since HAp have large number of acid and basic sites compared to other stoichiometric apatites. However HAp was still selective (68%) towards total alcohols due to simultaneous increase of both acid and basic sites thus maintaining a compromise between these antagonist sites. The above

observation clearly shows that it is not only the number of acid and basic sites but their ratio (R_{AB}) that mainly influences the total alcohols selectivity. The total alcohols selectivity was found to decrease rather linearly with increase in R_{AB} (Figure 4-20). This is also an indirect representation that the stoichiometric catalysts with relatively predominant basic behavior (lower R_{AB} value) than deficient catalysts are more selective to total alcohols.

DAP has shown total alcohols selectivity of 65% even though they possess higher R_{AB} value (predominant acid behavior) compared to other catalysts and deviates from the linear trend (Figure 4-20). This is supposedly due to the large number of basic sites ($6.20 \mu\text{mol.g}^{-1}$) in DAP compared to other deficient apatites SrDAP-50 ($1.29 \mu\text{mol.g}^{-1}$) and SrDAP-100 ($1.91 \mu\text{mol.g}^{-1}$).

As a conclusion to this part, both acid and basic sites together had a big influence on the total alcohols selectivity. Total alcohol selectivity was higher over stoichiometric apatites which have lower R_{AB} ratio and predominant basic behavior compared to deficient apatites. Hence the stoichiometric apatite SrAp-100 (100 mol% Sr substituted) with an optimum value of $R_{AB} = 4.0$ was found to be more selective to total alcohols compared to all other apatites. This optimum value of 4 in Sr substituted apatite is thus close but slightly lower compared to the optimum R_{AB} value of 4.8 observed in Sr-free apatites in chapter 3. Also it was found that Sr-free apatites HAp and DAP despite of their high R_{AB} values have shown higher total alcohols selectivity after SrAp-100. This is supposedly due to their large number of basic sites and higher specific surface area compared to Sr substituted apatites.

4.2.2.2 Guerbet reaction: Optimization of experimental conditions

As mentioned in chapter 3 (section 3.2.2.2), the main aim of the optimization study is to have maximum ethanol conversion and higher alcohols yields. Therefore the ethanol reaction was performed at different temperatures and GHSVs to attain optimal conditions and to reach the abovementioned objective.

Table 4-6 Ethanol conversion and products yield over apatite catalysts at GHSV = 5000 mL.h⁻¹.g⁻¹

| | GHSV = 5000 mL.h ⁻¹ .g ⁻¹ | | | | | | | |
|-----------------------|---|---------|---------|---------|----------|-------|----------|-----------|
| | HAp | SrAp-25 | SrAp-50 | SrAp-75 | SrAp-100 | DAp | SrDAp-50 | SrDAp-100 |
| Conversion at | | | | | | | | |
| 300°C | 13.5 | 5.3 | 5.5 | 4.8 | 4.3 | 14 | 4.2 | 5 |
| 350°C | 32 | 17.5 | 13.7 | 11 | 13.1 | 27 | 10.3 | 11.2 |
| 400°C | 64.6 | 32.1 | 23 | 25.5 | 22.3 | 61.8 | 26.2 | 25.1 |
| Yield at 300°C | | | | | | | | |
| Alkenes | | | | | | | | |
| Ethylene | 0.32 | 0.06 | 0.07 | 0.11 | 0.02 | 0.63 | 0.63 | 0.41 |
| Aldehydes | | | | | | | | |
| Acetaldehyde | 1.82 | 0.49 | 1.00 | 0.49 | 0.49 | 0.88 | 1.01 | 0.95 |
| Butanal | - | 0.01 | 0.01 | 0.01 | 0.02 | - | - | - |
| Dienes | | | | | | | | |
| Butadiene | 0.16 | 0.07 | 0.04 | 0.06 | 0.02 | 0.28 | 0.04 | 0.04 |
| C6 dienes | 0.05 | - | - | - | - | 0.13 | - | - |
| Alcohols | | | | | | | | |
| Butanol | 6.80 | 3.70 | 3.33 | 3.49 | 3.22 | 6.86 | 0.76 | 1.77 |
| Butenol | 0.41 | 0.48 | 0.44 | 0.24 | 0.19 | 0.21 | 0.57 | 0.60 |
| C6-C8 alcohols | 1.78 | 0.15 | 0.14 | 0.14 | 0.21 | 1.81 | 0.08 | 0.21 |
| Diethylether | 0.61 | 0.03 | 0.13 | 0.04 | 0.04 | 0.70 | 0.29 | 0.16 |
| Aromatics | - | 0.02 | 0.03 | 0.01 | 0.03 | - | 0.02 | 0.03 |
| Yield at 350°C | | | | | | | | |
| Alkenes | | | | | | | | |
| Ethylene | 1.60 | 0.53 | 0.48 | 0.67 | 0.22 | 2.65 | 3.24 | 2.36 |
| Butene | 0.67 | 0.07 | 0.07 | 0.04 | 0.05 | 0.27 | 0.04 | 0.06 |
| Hexene | 0.16 | - | - | - | - | 0.05 | - | - |
| Aldehydes | | | | | | | | |
| Acetaldehyde | 2.56 | 1.07 | 2.15 | 0.83 | 1.19 | 0.76 | 1.75 | 1.81 |
| Butanal | 0.26 | 0.05 | 0.07 | 0.04 | 0.10 | - | 0.02 | 0.03 |
| Dienes | | | | | | | | |
| Butadiene | 1.18 | 0.67 | 0.41 | 0.35 | 0.20 | 1.43 | 0.34 | 0.32 |
| C6 dienes | 0.58 | 0.32 | 0.27 | 0.18 | 0.16 | 0.68 | 0.12 | 0.11 |
| Alcohols | | | | | | | | |
| Butanol | 17.57 | 9.47 | 6.41 | 5.72 | 8.28 | 14.45 | 1.47 | 2.41 |
| Butenol | 0.10 | 0.49 | 0.45 | 0.39 | 0.55 | 0.16 | 0.31 | 0.45 |
| C6-C8 alcohols | 4.48 | 1.58 | 0.56 | 0.50 | 1.18 | 2.70 | 0.12 | 0.22 |
| Diethylether | 1.18 | 0.40 | 0.23 | 0.35 | 0.26 | 1.62 | 0.77 | 0.56 |
| Aromatics | - | 0.12 | 0.14 | 0.06 | 0.21 | - | 0.05 | 0.09 |
| Yield at 400°C | | | | | | | | |
| Alkenes | | | | | | | | |
| Ethylene | 11.31 | 5.30 | 3.93 | 5.41 | 2.07 | 36.59 | 17.11 | 13.96 |
| Butene | 2.78 | 0.87 | 0.48 | 0.54 | 0.36 | 2.97 | 0.10 | 0.25 |
| Hexene | 2.71 | 0.16 | 0.05 | 0.08 | 0.04 | 0.31 | - | - |
| Aldehydes | | | | | | | | |
| Acetaldehyde | 3.10 | 0.96 | 2.62 | 0.97 | 1.61 | 1.92 | 1.60 | 2.38 |
| Butanal | 0.78 | 0.10 | 0.18 | 0.10 | 0.33 | - | 0.05 | 0.13 |
| Hexanal | - | - | - | - | 0.02 | - | - | - |
| Dienes | | | | | | | | |
| Butadiene | 5.30 | 3.05 | 2.42 | 2.14 | 0.94 | 2.35 | 0.89 | 1.00 |
| C6 dienes | 3.23 | 0.80 | 0.46 | 0.59 | 0.49 | 0.74 | 0.31 | 0.33 |
| Alcohols | | | | | | | | |
| Butanol | 21.32 | 14.00 | 7.25 | 10.46 | 10.79 | 6.18 | 1.05 | 1.81 |
| Butenol | 0.19 | 0.22 | 0.35 | 0.31 | 0.45 | 0.12 | 0.13 | 0.25 |
| C6-C8 alcohols | 3.04 | 1.61 | 0.92 | 0.79 | 2.61 | 0.19 | 0.10 | 0.13 |
| Diethylether | 1.94 | 1.09 | 1.01 | 0.77 | 0.45 | 5.25 | 2.49 | 1.91 |
| Aromatics | 0.39 | 0.48 | 0.32 | 0.31 | 0.56 | 0.31 | 0.21 | 0.25 |

Tables 4-6 and 4-7 show the ethanol conversion and various product distributions at different temperatures and GHSVs. The reaction products mainly consisted of alkenes, aldehydes, higher alcohols, dienes, diethylether and trace amount of aromatics. Nature of products indicated that there are no cleavage and decomposition mechanisms involved in the Guerbet reaction of ethanol over apatite catalysts.

Table 4-7 Ethanol conversion and products yield over apatite catalysts at GHSV = 15000 mL.h⁻¹g⁻¹

| | GHSV=15000mL.h ⁻¹ g ⁻¹ | | | | | | | |
|-----------------------------|--|---------|---------|---------|----------|-------|----------|-----------|
| | HAp | SrAp-25 | SrAp-50 | SrAp-75 | SrAp-100 | DAp | SrDAp-50 | SrDAp-100 |
| Conversion at | | | | | | | | |
| 300°C | 4.5 | 3.5 | 3.8 | 3 | 3.4 | 4.2 | 3.3 | 3.7 |
| 350°C | 11 | 6.2 | 6.3 | 4.8 | 6.2 | 10.4 | 5.1 | 6 |
| 400°C | 33 | 15.7 | 12.2 | 11.5 | 12.5 | 32 | 13.6 | 13 |
| Selectivity at 400°C | | | | | | | | |
| Alkenes | | | | | | | | |
| Ethylene | 5.28 | 1.63 | 1.13 | 1.41 | 0.69 | 12.80 | 7.21 | 5.49 |
| Butene | 1.06 | 0.19 | 0.07 | 0.12 | 0.10 | 0.80 | 0.03 | 0.05 |
| Hexene | 0.30 | 0.05 | - | 0.02 | - | 0.10 | - | - |
| Aldehydes | | | | | | | | |
| Acetaldehyde | 2.08 | 1.26 | 2.67 | 1.28 | 1.89 | 2.50 | 1.93 | 2.63 |
| Butanal | 0.26 | 0.06 | 0.09 | 0.06 | 0.18 | 0.10 | 0.03 | 0.04 |
| Dienes | | | | | | | | |
| Butadiene | 2.74 | 0.94 | 0.65 | 0.55 | 0.30 | 3.26 | 0.18 | 0.27 |
| C6 dienes | 1.16 | 0.28 | 0.12 | 0.15 | 0.15 | 0.48 | 0.04 | 0.07 |
| Alcohols | | | | | | | | |
| Butanol | 14.19 | 7.61 | 4.11 | 4.92 | 6.54 | 7.84 | 0.19 | 0.78 |
| Butenol | 0.23 | 0.24 | 0.61 | 0.23 | 0.38 | 0.13 | 0.05 | 0.08 |
| C6-C8 alcohols | 2.48 | 0.47 | 0.22 | 0.16 | 0.68 | 0.74 | - | - |
| Diethylether | | | | | | | | |
| | 0.99 | 0.55 | 0.55 | 0.38 | 0.35 | 2.56 | 1.22 | 0.98 |
| Aromatics | | | | | | | | |
| | 0.10 | 0.09 | 0.09 | 0.05 | 0.15 | 0.06 | 0.04 | 0.05 |

The ethanol conversion at 400°C and at the two different GHSVs (namely, 5000 mL.h⁻¹g⁻¹ and 15000 mL.h⁻¹g⁻¹, obtained using 0.2 g and 0.6 g of catalyst, respectively) are shown in Figure 4-21.

For all the apatite catalysts, ethanol conversion was found to increase with the decrease in the GHSV from 15000 mL.h⁻¹g⁻¹ to 5000 mL.h⁻¹g⁻¹. This is as expected due to the increase in the ethanol contact time with decrease in the GHSV. Furthermore at the same GHSV of 15000 mL.h⁻¹g⁻¹ (grey filled symbols), Sr-free and Sr-substituted apatites have shown different ethanol conversions. Sr-free apatites HAp and Dap exhibited an ethanol

conversion of around 32% compared to Sr-substituted apatites which showed ethanol conversion of around 13%. The higher ethanol conversion in HAp and DAp can be correlated to their larger surface areas ($\sim 120 \text{ m}^2.\text{g}^{-1}$) compared to Sr-substituted apatites ($\sim 45 \text{ m}^2.\text{g}^{-1}$) (see the dashed lines in Figure 4-21).

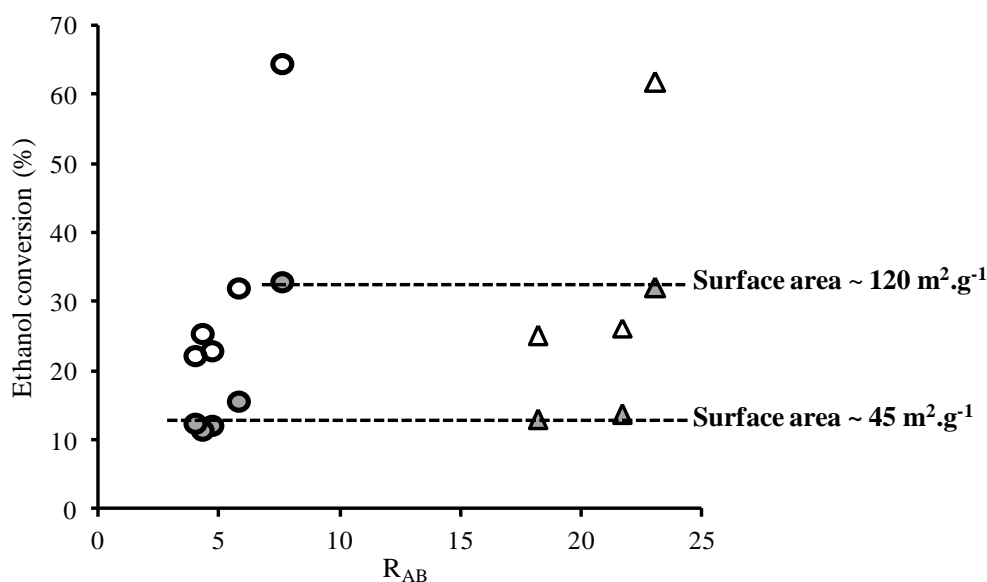


Figure 4-21 Ethanol conversion as a function of number of acid sites to basic sites at 400°C; GHSV = 5000 mL.h⁻¹.g⁻¹ (grey filled symbols) and GHSV = 50000 mL.h⁻¹.g⁻¹ (open symbols). (Circles represent the stoichiometric apatites and triangles the deficient apatites).

Similar trend in ethanol conversion is observed also at GHSV = 5000 mL.h⁻¹.g⁻¹ (open symbols). As aforementioned, since our aim is to have maximum ethanol conversion and total alcohol yields following studies were performed at GHSV = 5000 mL.h⁻¹.g⁻¹.

In the stoichiometric apatites except HAp, yield towards total alcohols yield was found to increase with increase in temperature from 300°C to 400°C [Figure 4-22(a)]. When the temperature was increased above 400°C, the formation of alkenes and aromatics become pronounced, which in turn reduced the total alcohols yield (data not shown). In HAp total alcohols yield increased from 9% to 22% with increase in temperature from 300°C to 400°C and remained almost unchanged with further increase in temperature to 400°C. This is due to the slightly higher acidic behavior in HAp compared to other stoichiometric apatites which become more pronounced at higher temperature leading to ethanol

dehydration to ethylene (a competitive side reaction to Guerbet reaction) as explained in chapter 3 (section 3.2.2.2).

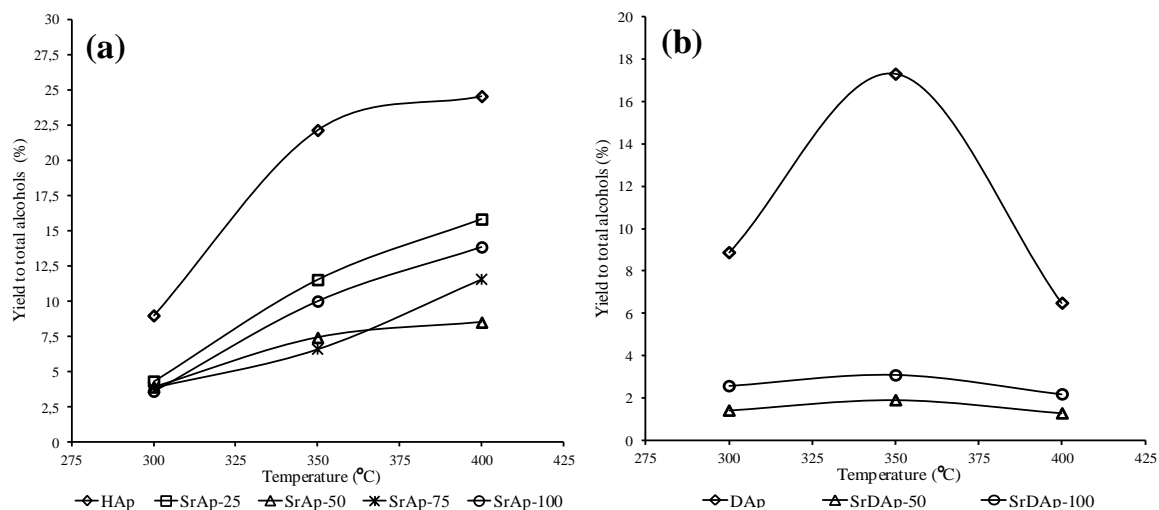


Figure 4-22 Influence of temperature towards total alcohols yield (GHSV = 5000 mL.h⁻¹.g⁻¹) in (a) stoichiometric apatites and (b) deficient apatites.

Considering deficient apatites Sr-substituted SrDAP-50 and SrDAP-100, the total alcohols yield remained very low and temperature had no influence towards total alcohols yield [Figure 4-22(b)]. Whereas in case of Sr-free apatite DAP the total alcohols yield increased from 9% to 17.3% with increase in the temperature from 300°C to 350°C and then decreased to 6.5% with further increase in temperature to 400°C. This decrease in total alcohol yield is due to the highly acidic behavior of DAP compared to other apatites that resulted in dehydration of ethanol to ethylene as explained in chapter 3 (section 3.2.2.2). Hence 400°C was found to be an optimal temperature for the production of total alcohols over all apatite catalysts except deficient apatite DAP.

In order to have an insight of the direct influence of R_{AB} ratio on the ethanol conversion and products yield, the intrinsic reaction rate of ethanol conversion (Figure 4-23) and products formation (Figure 4-24), respectively, has been calculated at the optimal conditions of 400°C and GHSV = 5000 mL.h⁻¹.g⁻¹. In this way the variation in specific surface area of the different apatite catalysts was not taken into account.

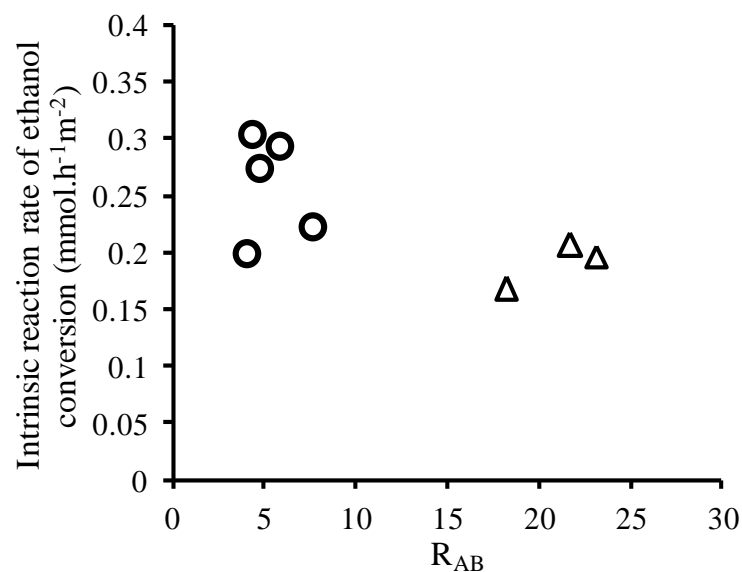


Figure 4-23 Plot of intrinsic reaction rate of ethanol conversion as a function of ratio of acid sites to basic sites (Circles represent the stoichiometric apatites and triangles the deficient apatites).

In both stoichiometric and deficient apatites, the intrinsic reaction rate of ethanol conversion did not vary much with increase in R_{AB} and no particular correlation was observed between the R_{AB} and intrinsic reaction rate of ethanol (Figure 4-23). We can conclude that it is not R_{AB} but the specific surface area of the apatites that significantly impacts the ethanol conversion (see Figure 4-21).

Intrinsic reaction rate of total alcohol production tended to decrease in a rather linear manner with increase in R_{AB} [Figure 4-24(a)]. The figure clearly shows that total alcohol production was favoured over stoichiometric apatites with lower R_{AB} value (ie; with predominant basic behaviour) compared to deficient apatites. The intrinsic reaction rate of total alcohol production is much lower in deficient apatites due to their higher R_{AB} value (predominant acidic behaviour). This observation is in good agreement with the iso-conversion results that showed a linear decrease in total alcohols selectivity with increase in R_{AB} (see Figure 4-20).

Figure 4-24(b) clearly shows that the intrinsic reaction rate of ethylene production increased rather linearly with increase in R_{AB} . As expected ethylene production was found to be higher over the deficient apatites with higher R_{AB} value (ie; with predominant acidic behaviour). This result is in good agreement with the *isopropanol* test where the propylene selectivity tended to increase with increase in R_{AB} (see Figure 4-17).

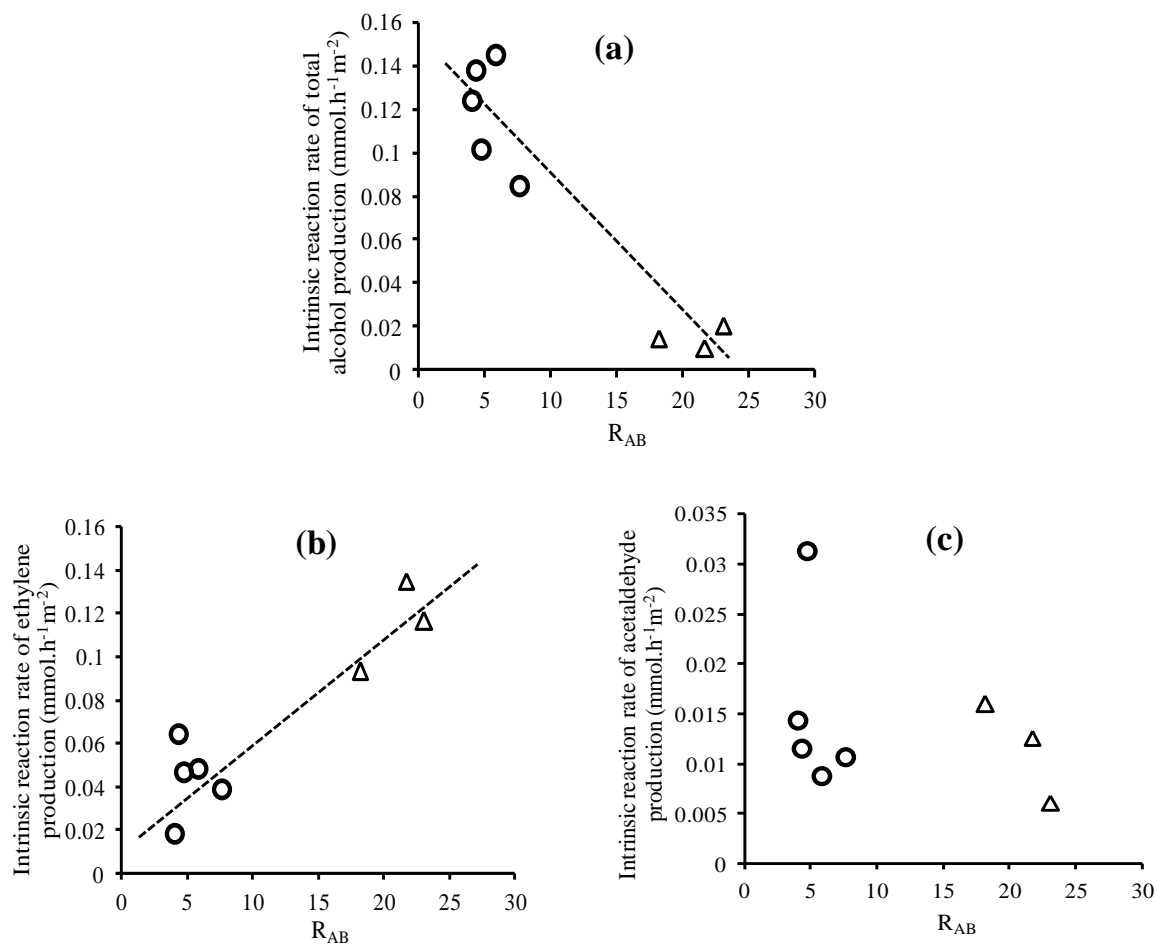


Figure 4-24 Plots of (a) intrinsic reaction rate of total alcohols as a function of R_{AB} , (b) intrinsic reaction rate of ethylene as a function of R_{AB} and (c) intrinsic reaction rate of acetaldehyde as a function of R_{AB} (Circles represent the stoichiometric apatites and triangles the deficient apatites).

Furthermore the intrinsic reaction rate of acetaldehyde production [Figure 4-24(c)] did not show any direct correlation with R_{AB} . This is because acetaldehyde is an intermediate in the Guerbet reaction cycle that can further undergo transformation to form heavier products. So there is chance of underestimation in dehydrogenation property of the catalysts taking into account only the acetaldehyde production as explained previously in chapter 3.

4.3 Conclusions

Sr-substituted stoichiometric and deficient apatites were successfully synthesized with varying Sr content. The surface areas determined by BET nitrogen adsorption

measurement have shown that even a small quantity of Sr substitution drastically reduced the surface area of the hydroxyapatite solids. The pore volume, pore diameter and BET surface area of the apatites exhibited a similar trend with the variation in Sr substitution. Unit cell parameters 'a' and 'c' determined by the Rietveld refinement were found to increase linearly with increase in Sr substitution. Anisotropic crystallite shape investigated by Rietveld refinement is in good agreement with the grain shapes observed in SEM. The surface (Ca + Sr)/P ratio of all apatite solids increased with increase in the Sr substitution, though the (Ca + Sr)/P bulk ratio remained almost unchanged. We found that this is especially due to the surface enrichment of larger Sr²⁺ ions compared to Ca²⁺ ions. Combining the results obtained from XRD refinement and LEIS we could propose that the Ca²⁺ and/or Sr²⁺ ions are more exposed along the c-axis, that is, on ac and bc planes. The substitution of Ca(II) sites by Sr was identified by Infrared spectroscopy. Raman spectra of the apatites have shown a linear down shift of the peaks with increase in Sr substitution confirming the replacement of Ca by Sr atoms. The ratio of number of acid sites to basic sites (R_{AB}) determined by TPD-NH₃ and TPD-CO₂ was found to decrease linearly with increase in Sr substitution which is an indirect representation of increase in the relative predominance of basic sites with Sr content. The deficient apatites exhibited higher R_{AB} value indicating their predominant acidic behaviour compared to stoichiometric apatites. The acid-base behaviour determined by *isopropanol* test was found to be in good agreement with the acid-base properties (R_{AB}) obtained directly from the TPD-NH₃ and TPD-CO₂ experiments.

Guerbet reaction of ethanol was further carried out and the products were analyzed at iso-conversion of ethanol. We found that the selectivity to Guerbet products was not simply related to acid sites or basic sites but related to both antagonist sites and hence the ratio of number of acid sites to basic sites (R_{AB}). Stoichiometric 100 mol% Sr substituted apatite (SrAp-100) with an optimal R_{AB} value of 4 was found to be highly selective to total alcohols compared to other apatites. Moreover the selectivity to total alcohols decreased rather linearly with increase in R_{AB} value indicating that too much acidic behavior is not favorable for the production of the Guerbet alcohols. However HAp and DAp apatites have shown sufficient total alcohols selectivity though they possess higher R_{AB} values. This is supposedly due to their large number of basic sites and higher specific surface area compared to other Sr substituted apatites.

Further optimization of reaction conditions like temperature and GHSV have shown that among the different conditions we employed, the temperature of 400°C and GHSV = 5000 mL.h⁻¹g⁻¹ allowed having maximum ethanol conversion and yield to total alcohols. In contrast to the iso-conversion studies where Sr substituted SrAp-100 apatite was more selective to total alcohols, the yield to total alcohols was more over HAp mainly due to its higher ethanol conversion compared to Sr substituted catalysts. Moreover the study of variation in intrinsic reaction rate of ethanol conversion with R_{AB} showed that R_{AB} did not affect much the ethanol conversion, underlining the key role of specific surface area in the ethanol conversion. The intrinsic reaction rate of total alcohol production tended to decrease rather linearly with increase in R_{AB} which is in good agreement with iso-conversion studies. Furthermore the intrinsic reaction rate of ethylene production increased linearly with increase in R_{AB} which is a similar trend as observed between the propylene selectivity and R_{AB} in the *isopropanol* test.

-
- [1] S. Ogo, A. Onda, Y. Iwasa, K. Hara, A. Fukuoka, K. Yanagisawa, 1-Butanol synthesis from ethanol over strontium phosphate hydroxyapatite catalysts with various Sr/P ratios, *Journal of Catalysis*, vol 296 (2012) p. 24-30.
- [2] M. D. O'Donnell, Y. Fredholm, A. de Rouffignac, R. G. Hill, Structural analysis of a series of strontium-substituted apatites, *Acta Biomaterialia*, vol 4 (2008) p. 1455-1464.
- [3] A. Bigi, E. Boanini, C. Capuccini, and M. Gazzano, Strontium-substituted hydroxyapatite nanocrystals, *Inorganica Chimica Acta*, vol 360 (2007) p. 1009-1016.
- [4] C. Lamonier, J.-F. Lamonier, B. Aellach, A. Ezzamarty, J. Leglise, Specific tuning of acid/base sites in apatite materials to enhance their methanol thiolation catalytic performances, *Catalysis Today*, vol 164 (2011) p. 124-130.
- [5] B.O. Fowler, Infrared studies of apatites II. Preparation of normal and isotopically substituted calcium, strontium, and barium hydroxyapatites and spectra-structure-composition correlations, *Inorganic Chemistry*, vol 13 (1974) p. 207-214.
- [6] C. Wei, H. Zhiliang, L. Yu, H. Qianjun, Preparation and characterization of a novel solid base catalyst hydroxyapatite loaded with strontium, *Catalysis Communications*, vol 9 (2008) p. 516-521.
- [7] G. Bonel, Contribution a l'étude de la carbonatation des apatites. I. Synthèse et étude des propriétés physico-chimiques des apatites carbonatées du type A, *Annali di Chimica*, vol 7 (1972) p. 65-88.
- [8] F.A. Miller, C.H. Wilkins, Infrared Spectra and Characteristic Frequencies of Inorganic Ions, *Analytical Chemistry*, vol 28 (1952) p. 1253-1294.
- [9] C.C. Silva, A.G. Pinheiro, M.A.R. Miranda, J.C. Góes, A.S.B. Sombra, Structural properties of hydroxyapatite obtained by mechanosynthesis, *Solid State Sciences*, vol 5 (2003) p. 553-558.
- [10] G. Penel, G. Leroy, C. Rey, E. Bres, MicroRaman spectral study of the PO₄ and CO₃ vibrational modes in synthetic and biological apatites, *Calcified Tissue International*, vol 63, (1998) p. 475-481.
- [11] T. Tsuchida, J. Kubo, T. Yoshioka, S. Sakuma, T. Takeguchi, W. Ueda, Reaction of ethanol over hydroxyapatite affected by Ca/P ratio of catalyst, *Journal of Catalysis*, vol 259 (2008) p. 183-189.
- [12] S.J. Joris, C.H. Amberg, Nature of deficiency in nonstoichiometric hydroxyapatites I. Catalytic activity of calcium and strontium hydroxyapatites, *Journal of Physical Chemistry*, vol 75 (1971) p. 3167-3171.

General Conclusions and Perspectives

The aim of this thesis was to synthesis higher alcohols from ethanol through Guerbet reaction using hydroxyapatite-based catalysts. From the literature review we noticed that many heterogeneous catalysts like metal oxides, mixed metal oxides, hydrotalcites, hydroxyapatites etc...were employed for the gas phase Guerbet reaction of ethanol. We have chosen hydroxyapatites $[\text{Ca}_{10}(\text{PO}_4)_6(\text{OH})_2]$ among all the aforementioned catalysts since they possess both the acid sites and the basic sites in their structure, which is the main requirement for the Guerbet reaction. Furthermore these acid-base sites in hydroxyapatite solids can be tuned accordingly, both by varying the Ca/P ratio and by the substitution of the Ca^{2+} cations and $\text{PO}_4^{3-}/\text{OH}^-$ anions. Hence our study was mainly divided into two parts:

In the first part (chapter 3) hydroxyapatites with different Ca/P ratio or carbonate content synthesized by precipitation method, was screened in the Guerbet reaction of ethanol after deep characterization of the solids. The characterization has been performed to study the structural, textural and acid-base properties of the prepared solids. It was found that carbonate content increased linearly with increase in the Ca/P ratio. Rietveld refinement and SEM analysis showed that morphology of the apatite solids was found to vary by varying the carbonate content. Global tentative formulae for the apatites were deduced taking into account the amount and type of CO_3^{2-} substitution using XRD refinement and TGA. By using the LEIS technique along with the XRD refinement results, we proposed that Ca^{2+} are more exposed along the 0 0 1 direction on the ac and bc planes. The acid-base properties were found to vary by varying the carbonate content. We found that in the apatite solids HPO_4^{2-} species behave as Brønsted acid sites, and Ca^{2+} or OH^- vacancies as Lewis acid sites. Deficient and stoichiometric apatites with lower Ca/P ratio or carbonate content have shown pronounced acidic behaviour compared to other apatites with higher carbonate content. Further correlation study between the Guerbet reaction results and the characterization results showed that the amount, the strength and the nature of the acid-base properties affects each step in the Guerbet reaction. We found that the best ratio between the number of acid sites to the number of basic sites was 5, to attain maximum selectivity to higher alcohols over hydroxyapatite catalysts. A

scheme of Guerbet reaction cycle was then proposed taking into account all the above observations.

The second part (chapter 4) dealt with synthesis and characterization of the strontium substituted apatites followed by the screening of the apatites in the Guerbet reaction of ethanol. We found that the structural, textural and acid-base properties varied by varying the Sr substitution in the apatites. The surface area of the apatite solids drastically decreased even with small amount of Sr substitution. Unit cell parameters and crystallite size were found to increase with increase in Sr substitution in the apatites. A correlation existed between the crystallite shape and grain shape of the apatite solids. The surface (Ca + Sr)/P ratio of all apatite solids varied from the bulk (Ca + Sr)/P ratio and it was found that surface (Ca + Sr)/P ratio increased with increase in Sr substitution due to surface enrichment of larger Sr^{2+} ions compared to Ca^{2+} ions. The ratio of number of acid sites to number of basic sites (R_{AB}) showed that increase in Sr substitution resulted in an increase of basic behaviour of apatites. The R_{AB} value and isopropanol test showed that the deficient apatites possess more acidic behaviour than stoichiometric apatites. The selectivity to total alcohols decreased rather linearly with increase in R_{AB} value and 100 mol.% Sr substituted stoichiometric apatite with an optimal R_{AB} value of 4 was highly selective to total alcohols compared to all other apatites. Further optimization of reaction conditions showed that the yield to total alcohols was more over Sr-free stoichiometric apatite due to its higher specific surface area. The intrinsic reaction rate of total alcohol production tended to decrease rather linearly with increase in R_{AB} . This confirmed that the increase in basic behaviour in Sr apatites favors the Guerbet alcohol production. The apatites with higher R_{AB} value and hence the predominant acidic behavior was found to favor the ethylene production.

Our studies helped to have some insights on the number, strength and nature of acid-base sites in the hydroxyapatite-based catalysts which are involved in the Guerbet reaction cycle. Future research can be done for the back optimization of the catalysts by precisely tuning the acid-base sites. This will be then useful to have a control over the competitive side reactions like dehydration and to obtain maximum yield to desired Guerbet alcohols. Furthermore the above observations can be also applied to many other organic reactions like the Michael addition, the Knoevenagel condensation, the Friedel-Crafts reaction etc...that demands the acid-base sites in the hydroxyapatite catalysts.

It is known that besides the acid-base properties, the redox properties of the catalysts can also have an influence on the Guerbet reaction. We have synthesized and characterized copper containing hydroxyapatite and preliminary tests have shown that more aromatics are formed at higher temperature. So our future research will be oriented to optimize the Guerbet reaction conditions using the transition metal containing hydroxyapatite catalysts. Similar to the tuning of acid-base properties of the apatite solids, it can be interesting to tune the pores of the apatite solids by using template assisted synthesis and then screen them both in the liquid phase and in the gas phase Guerbet reaction.

Annexes

- Annexe 1 : X-ray diffraction (XRD)
- Annexe 2 : Fourier Transform Infrared spectroscopy (FTIR)
- Annexe 3 : Raman spectroscopy
- Annexe 4 : Nuclear Magnetic Resonance (NMR) spectroscopy
- Annexe 5 : X-ray photoelectron spectroscopy (XPS)
- Annexe 6 : Low-energy ion scattering (LEIS)
- Annexe 7 : Inductively coupled plasma (ICP)
- Annexe 8 : Scanning electron microscopy (SEM)
- Annexe 9 : Porosity measurements by nitrogen adsorption (BET)
- Annexe 10 : Temperature-Programmed Desorption (TPD)
- Annexe 11 : Thermogravimetry & Differential thermal analysis (TGA/DTA)

Annexe 1 X-ray diffraction (XRD)

XRD is one of the main techniques employed by solid-state chemists for the characterization of crystalline solids and to determine their structure. X-ray diffraction results from the interaction between X-rays and charged particles, mainly electrons of atoms in the solids according to Rayleigh scattering. Each crystalline solid has a unique characteristic X-ray powder pattern resulting from its unique atomic architecture. These patterns can thus behave as fingerprints for the identification of solid phases. Depending on the atomic arrangement, interferences between the scattered rays are constructive if the path difference between two rays differs by an integral number of wavelengths (Figure A-1).

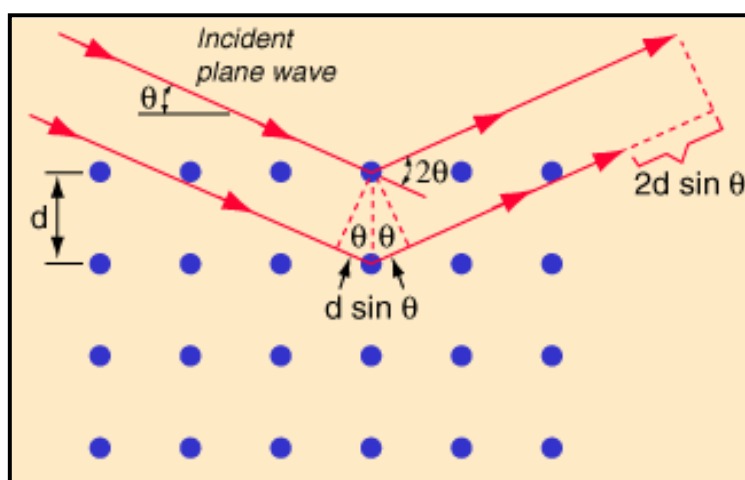


Figure A-1 Schematic representation of diffraction of X-rays by crystallographic planes.

The Bragg's law explains the conditions for constructive interference in certain directions and the production of diffracted scattered X-rays:

$$n\lambda = 2d \sin\theta$$

where n is an integer, λ is the wavelength of the radiation, d is the space between two crystallographic planes, and θ is the angle between the X-ray and the plane [1].

Unit cell parameter (a_0) of a cubic lattice can be determined by the following equation: $a_0 = d_{hkl} \sqrt{(h^2 + k^2 + l^2)}$, where d = distance between two consecutive parallel lattice planes having Miller indices h , k and l . From the diffraction patterns, phase purity, unit cell parameters, degree of crystallinity can be determined [2,3]. X-ray diffraction's peak gives an additional indication on crystallite size and possible microstrains in the sample. It has been widely used to characterize supported metal crystallites in the nanoscale. The average size of the nanoparticles can be estimated using the Debye-Scherrer equation:

$$D = k\lambda / \beta \cos \theta$$

where D = thickness of the nanocrystal, k is a constant (it is equal to 1 when the integral width of Bragg peak is used and 0.89 when the Full Width at Half Maximum is used), λ = wavelength of X-rays, β = width at half maximum of reflection at Bragg's angle 2θ [4].

So, through X-ray spectra, one can spot and examine any kind of crystalline matter. The quality of the obtained result depends on the degree of crystallinity. Usually, an X-ray diffractometer consists of a X-ray generator, a goniometer, a sample holder, and a X-ray detector, such as photographic film or a movable proportional counter. X-ray tubes are mostly used to generate X-rays, which produce X-rays by bombarding a metal target with high energy electrons (10-100 keV) that kick out the core electrons. Thus, an electron in an outer shell fills the hole in the inner shell and emits an X-ray photon. Two well-known metal targets are Mo and Cu, which have strong $K\alpha$ X-ray emissions at 0.71073 and 1.5418 Å, respectively. The secondary lines (*e.g.* $K\beta$ lines) other than the main line are partially suppressed by using a crystal monochromator or by an energy filtering material with an adsorption edge between $K\alpha$ and $K\beta$ wavelengths. For example Ni is used as a filter material to filter Cu $K\beta$ lines.

Annexe 2 Fourier Transform Infrared spectroscopy (FTIR)

FTIR is a technique based on the vibrations of the atoms within a molecule. For a molecule to show infrared (IR) absorption bands, it should possess a permanent dipole moment. When a molecule, which possesses permanent dipole vibrates, the permanent dipole interacts with the oscillating electric field of the incident infrared radiation. So, for a molecule to be IR active there must be a change in the dipole moment of the molecule

during the time of vibration. An infrared spectrum is obtained by passing the radiation through samples, which are IR active and measuring the absorbed fraction of the incident radiation with a particular energy. The energy at which any peak in an IR spectrum appears corresponds to the frequency of a vibration of a part of the sample molecule [5,6]. Each interatomic bond will vibrate in several different motions (stretching or bending) so that the individual bonds can absorb more than one IR frequency. Stretching vibrations usually give rise to stronger peaks compared to bending modes, but the weaker bending modes of absorptions are important for distinguishing similar types of bonds. The energy corresponding to these vibrations lies in the infrared region ($4000\text{--}400\text{ cm}^{-1}$) of the electromagnetic spectrum. The term Fourier transform (FT) refers to a development in which the data are collected and converted from an interference pattern to an infrared absorption spectrum that is like a molecular "fingerprint" [7].

An IR spectrometer usually consists of a source, a monochromator and a detector or receptor. In general, for all the IR sources, the radiant energy is low and lies in the far infrared region. Then, to obtain sufficient energy, the slit width of the source has to be considerably opened resulting in a decrease in resolution. There must be some kind of device in between the source and the detector to analyse the radiation, so that intensity can be evaluated for each wavelength resolution element. Generally, there are two types of such devices, monochromators and interferometers. Monochromators are used in dispersive instruments, and interferometers employed in Fourier transform instruments. A prism or a diffraction grating is used in a monochromator to separate the components of polychromatic radiation. The function of a grating is to offer monochromatic radiation from a radiation, which is composed of many wavelengths. A diffraction grating contains many equally spaced slits, which diffract light by interference. There are basically two types of diffraction gratings, the transmission and the reflectance types. The final part of an IR spectrometer is the detector. The IR measures the energy of the radiation from the IR source that passes through the sample. The major function of detector is to convert radiation energy into electrical energy that can be generated to process a spectrum [5]. The basic components of an FTIR spectrometer are shown schematically in Figure A-2.

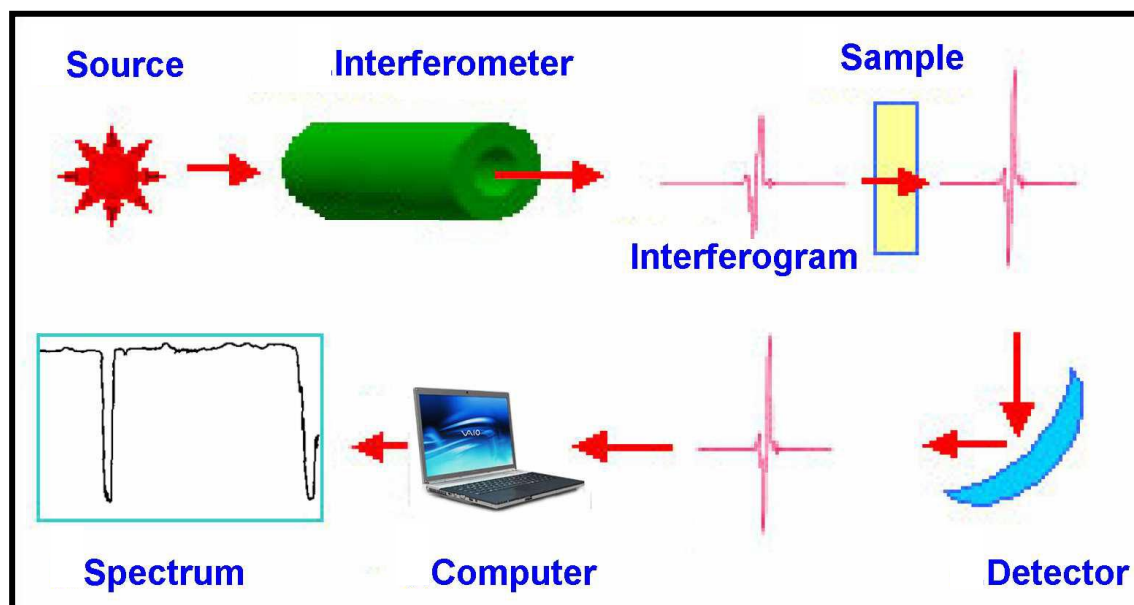


Figure A-2 Schematic diagram of Infra red spectrometer.

Annexe 3 Raman Spectroscopy

Raman spectroscopy is a spectroscopic technique used to study vibrational, rotational, and other low-frequency modes in a system. It relies on inelastic scattering, or Raman scattering, of monochromatic light, usually from a laser in the visible, near infrared, or near ultraviolet range [8,9]. Raman is an important technique for characterisation of solid materials similar to the IR spectroscopy. Raman spectroscopy has been widely employed compared to other similar spectroscopic techniques because of its higher resolution, its versatility and simplicity in terms of sample handling and the possibility of acquisition of the whole spectra (4000 to 10 cm^{-1}) with the same instrument. IR and Raman spectra analyses are based on the same vibrational behaviour of the molecule but they are not exact replicas because the selection rules and relative band intensities vary in many cases.

Raman spectra originate in the electronic polarization caused by UV or visible light. If a molecule is irradiated by monochromatic light of frequency ' ν ' having electric field strength ' E ', because of the electronic polarisation induced in the molecules by the incident light, it shows an induced dipole moment ' p ' that, at low E values, can be expressed as:

$$P = \alpha E$$

where ' α ' is the polarizability tensor [5].

There are three types of dispersed radiations: (1) Elastic scattering also known as Rayleigh scattering has the same wavelength as that of the source, (2) Anti-Stokes Raman scattering, which has a larger frequency than that of absorbed source/photon and, finally, (3) Stokes Raman scattering, which has a lower frequency than that of the absorbed photons. The polarizability of the molecule, the source intensity, the concentration of active groups are the main factors governing the intensity of a Raman band. The Raman intensities are directly proportional to the concentration of active species present in the materials like catalysts. Raman lines are also called Raman shifts designated as $\Delta\nu$ in cm^{-1} , and are independent of the excitation wavelength.

All the Raman spectrometers consist of basically of four units, namely a source, sample optics, a monochromator, and a detector/electronics/recorder system [10,11]. The basic setup is outlined in Figure A-3.

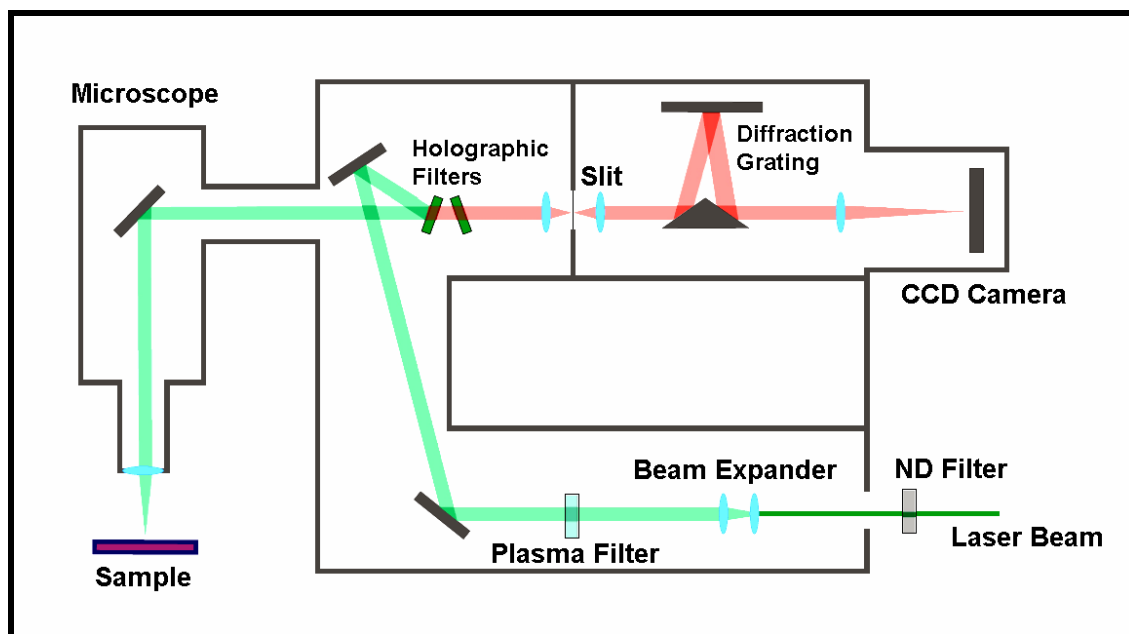


Figure A-3 Schematic illustration of Raman spectrometer [5]

Annexe 4 Nuclear Magnetic Resonance (NMR) spectroscopy

Matter is made of atoms which are composed of electrons and nuclei. The nucleus has four important physical properties: mass, electric charge, magnetism and spin and hence interacts with magnetic fields like a small magnet. This property is called nuclear magnetism. Moreover the nucleus has intrinsic angular momentum, which is known as spin. The properties of nuclear magnetism and spin have almost no effect on the physical and chemical properties of the matter. However, these two properties and their interactions represent very powerful tools for investigating the microscopic and internal structures of objects without disturbing them, being the essential principle of NMR spectroscopy.

Atomic nuclei containing odd number of protons and/or neutrons possess a nuclear spin $I \neq 0$ and consequently a magnetic moment $\mu = \gamma \hbar I$ (γ = gyromagnetic ratio, \hbar = Planck's constant divided by 2π). These nuclei when placed in a magnetic field of strength B_0 , results in quantized orientations of the nuclear magnetic moments due to Zeeman interaction [12]. The nucleus can adopt $(2I + 1)$ Eigen states with energies $E(m) = -m\gamma\hbar B_0$, where $m = (I, I-1, \dots, -I)$. Transitions between neighboring energy states ($\Delta m = \pm 1$) can be induced by electromagnetic radiation (energy $E = h\nu$) of frequency $\nu_0 = \gamma B_0/2\pi$.

The chemical shift interaction resulting from secondary local magnetic fields is induced by the interaction of the electrons surrounding the nucleus. This induced local field opposes the supplied magnetic field B_0 and hence shields the nucleus under observation. The shielding is spatially anisotropic due to the non spherical electron distribution around the nucleus [13]. Following Maxwell's equations this rotating magnetic field is associated by an oscillating electric field. If a wire coil is placed close to the sample, the rotating transverse magnetic field induces an oscillating electric current inside the coil that can be measured by using a radiofrequency detector. The oscillating electric current induced by the transverse magnetization is called the NMR signal or free-induction decay (FID). The NMR spectrometer is a device capable of registering an FID signal and by Fourier transformation of the FID to obtain the NMR spectrum.

At the beginning, NMR was a low-sensitivity technique because of the small population difference between energy levels and the low abundance and low gyromagnetic ratio of many nuclei. These features generate small signals which are difficult to distinguish from

the spectral noise. With the advent of sophisticated solid-state NMR techniques, it has become possible to obtain NMR spectra of solids with spectral resolution comparable to that of liquids [14]. Modern high-resolution solid-state NMR spectroscopy allows to elucidate the chemical and structural environment of several atoms (*e.g.* ^{13}C , ^{27}Al , ^{29}Si , ^{31}P , ^{51}V *etc.*) in a solid matrix like that of porous materials [15].

Annexe 5 X-ray photoelectron spectroscopy (XPS)

XPS is a commonly used surface sensitive analysis technique that operates under ultra-high vacuum. When the sample surface is irradiated with electromagnetic radiation with a $h\nu$ energy, it emits electrons from the valence or core levels of surface or near surface atoms because of the photoelectric effect [16]. The kinetic energies of ejected photoelectrons are not only characteristic of the atoms, but can also provide information on the chemical states of those surface atoms from which they are emitted [17].

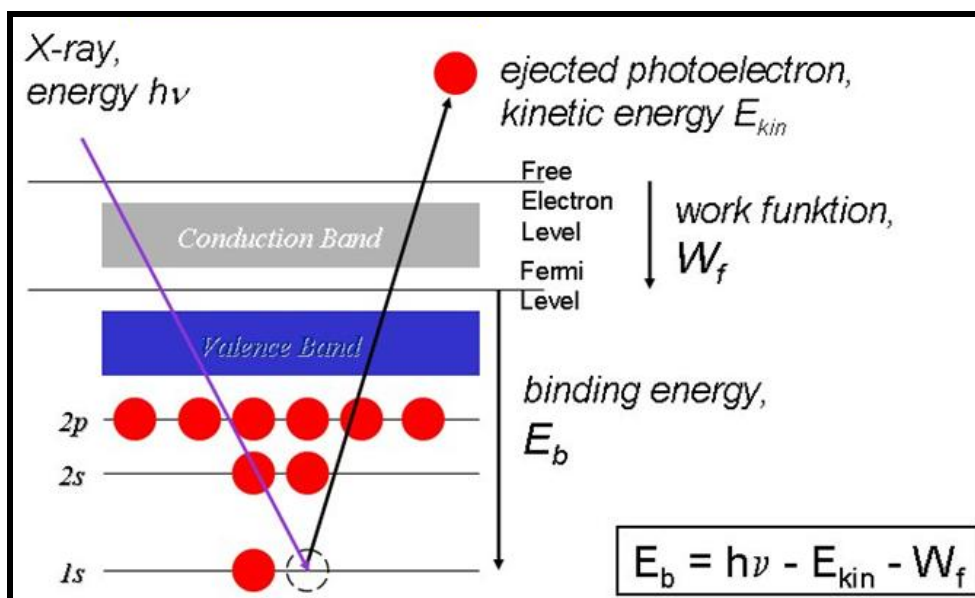


Figure A-4 Mechanism of photoelectron emission in XPS.

Figure A-4 shows the basic process of photoelectron emission involved in XPS. During irradiation, electrons are emitted from surface atoms only if the energy of the X-rays is

larger than a critical energy known as the surface work function (W_f). Work function is the energy required to excite an electron from its valence orbital to the continuum. In case of electrons that are emitted from inner orbitals, the electrons have to overcome also the binding energy, which further reduces the kinetic energy of the emitted electrons [18]. Therefore, the kinetic energy of an ejected electron will be equal to the energy of the incident X-rays minus the work function, minus the binding energy of the electron. An analyser is usually employed to measure the kinetic energy of ejected photoelectrons in XPS. The kinetic energy thus recorded is transformed into a binding energy for the specific atomic orbital of an electron. Because each element has a unique set of energy levels, they also possess a unique set of binding energies for electrons present in these levels. The binding energy can be described by using the following equation:

$$E_B = h\nu - W_f - E_K$$

Where, E_B = electron binding energy (eV)

h = Planck's constant (eV.s)

ν = frequency of incident X-rays (s^{-1})

E_K = kinetic energy of electron (eV)

W_f = surface work function (eV)

For a given element, a small variation in the position of corresponding photoelectron peaks result from small shifts in core energy levels associated with the oxidation state and bonding of the atoms. These variations in peak positions are typically in the order of 1-5 eV and can thus be detected with no trouble by most of the XPS spectrometers having energy resolutions of 0.1-0.2 eV [17].

The most commonly used source of X-rays is a sample consisting of Mg or Al. X-rays are emitted when electrons from a cathode produce ionization of the inner levels of these elements. The energy of $K\alpha$ emission for Al is 1.487 keV with a width of 1 eV and for Mg it has energy of 1.254 keV with a width of 0.8 eV. A plot of the number of detected electrons per energy interval versus their kinetic energy gives rise to an XPS spectrum.

A reference for binding energies is necessary in order to have a reproducible analysis. In solids, the binding energy is the energy that we have to provide to an electron to excite it to

a Fermi level. To have a good calibration of the lines, binding energy must be zero in the Fermi level of metal, and this is the level with maximum kinetic energy in the XPS spectrum. However, in practice, it is acquired by fixing the position of a known line of a certain element. In case of insulators, the loss of electrons results in the shift of the lines to greater E_B . Hence, the calibration is done by fixing the line from the 1s of the C, which is also a part of the surface contamination.

The XPS technique can analyse only the outer surface (1-10 nm) of a sample. This is because emitted photoelectrons lose kinetic energy as they travel through the sample and only photoelectrons from outermost layers of the sample have enough escape path or lifetime to reach the detector.

Annexe 6 Low-energy ion scattering (LEIS)

Low-energy ion scattering also referred to as ion scattering spectroscopy (ISS) is the surface sensitive counterpart of the Rutherford back scattering (RBS) technique [19,20,21]. LEIS involve directing a stream of ions at a surface and making observations of the positions, velocities, and energies of the ions that have interacted with the surface. Generally, the beam of ions used is noble gas ions such as helium and neon with energy between 0.1 and 10 keV and is exclusively sensitive to the outer surface layers. Data that are thus collected can be used to deduce information about the analysed material, such as the relative positions of atoms in a surface lattice and the elemental identity of those atoms. The reason for the favourable surface sensitivity of this technique is twofold [21]:

- The incident ion gets neutralized inside the solid. For example, 1 keV He^+ ions have 99% probability to undergo neutralization while passing through one layer of substrate atoms. Hence, the majority of ions must have scattered off from the outermost layer before reaching the detector;
- An electrostatic analyser is employed for the detection of low-energy particles. As a result, only ions can be detected and backscattered neutrals are not measured.

When an ion closely approaches the surface, an electron from the valence band may neutralize the ion by jumping to the empty state of the ion. The energy reached during this process equals the ionization potential of the primary ion minus the binding energy of the

target electron and target atom can use this energy to release other electron from the valence band. The whole process is two-centre Auger transition, which is the main route for the neutralization of an ion close to a surface. Auger electron may possess maximum energy of $(1-\varphi)$, where φ is the work function. Another type of neutralization known as resonance neutralization occurs through a resonant process, in which an electron from the sample tunnels to the empty state of the ion, which should then be at about the same energy. This neutralization is more likely to happen if the electron affinity of the ion is somewhat larger than the work function of the sample.

During collision of ion with the target surface, the low-energy ion does not penetrate the target atom so deeply. As a result of this, the ion feels the attenuated repulsion by the positive nucleus of the target atom because of the screening of nucleus by electrons. An approximately correct potential for the interaction is the following modified Coulomb potential:

$$V(r) = \frac{Z_{ion}eZe}{r} \times \frac{0.885a_0}{2r(\sqrt{Z_{ion}} + \sqrt{Z})^{2/3}}$$

$$= V_{Coulomb}(r).screening\ function$$

where a_0 is the Bohr radius of an atom, Z is the charge of electron, and Z_{ion} is the charge of the ion. The screening function becomes less useful at small r values, as it does not yield the true Coulomb potential inside the K-shell, and for this range Moliere approximation should be used [19].

The LEIS technique retains its excellent surface sensitivity due to the high neutralization probability of the rare gases. The fraction of He^+ ions that exists without being neutralized after undergoing a single collision is only between 10^{-4} and 10^{-2} . This indicates that the probability of the He^+ ions to return as an ion is practically zero, after penetrating the surface. However, there is a finite probability for the backscattered neutral He atom existing in ionized state after leaving the sample surface and as a result of this, LEIS spectrum retains some information on the state of the sample below its surface [21].

Generally, a beam of helium ions is employed for LEIS experiments. When a catalyst contains heavier elements, it is better to use neon ions to better distinguish between the elements, but the elements with a mass smaller than neon cannot be detected in that case.

The fact that LEIS gives quantitative information about the outer layer composition of the multi-component materials makes it an extremely powerful tool for surface characterization of the catalysts. The LEIS instrument used in our studies are shown in Figure A-5

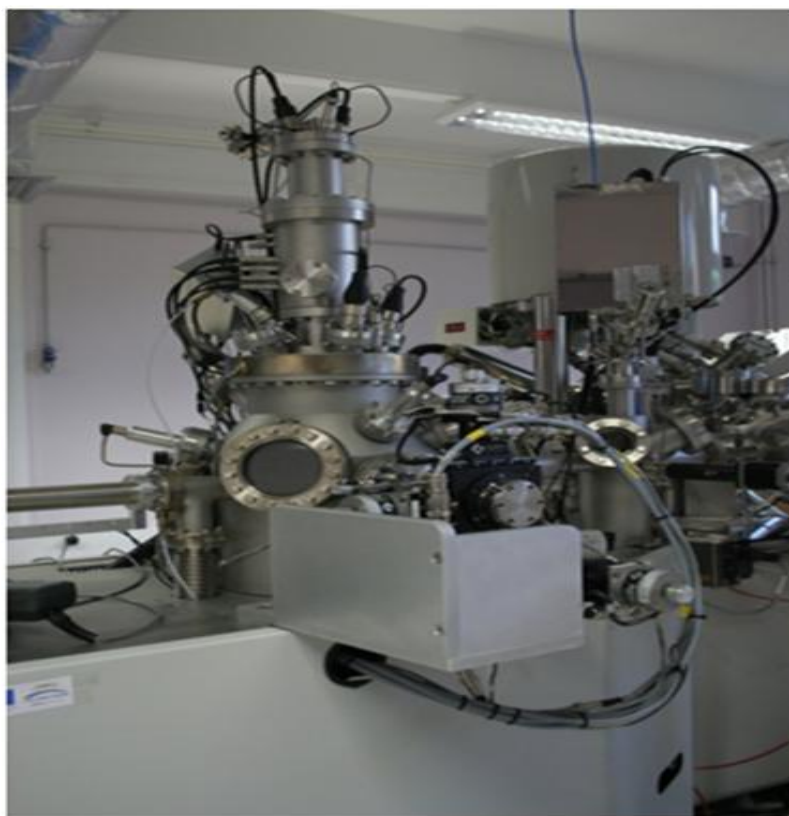


Figure A-5 LEIS instrument used for our studies.

Annexe 7 Inductively coupled plasma (ICP)

ICP is argon plasma maintained by the interaction of an RF field and ionized argon gas. The ICP can achieve temperatures as high as 10,000 K, and the sample experience temperatures between 5,500 K and 8,000 K. These temperatures enable complete atomization of the elements in a sample, minimizing chemical interference effects [22,23].

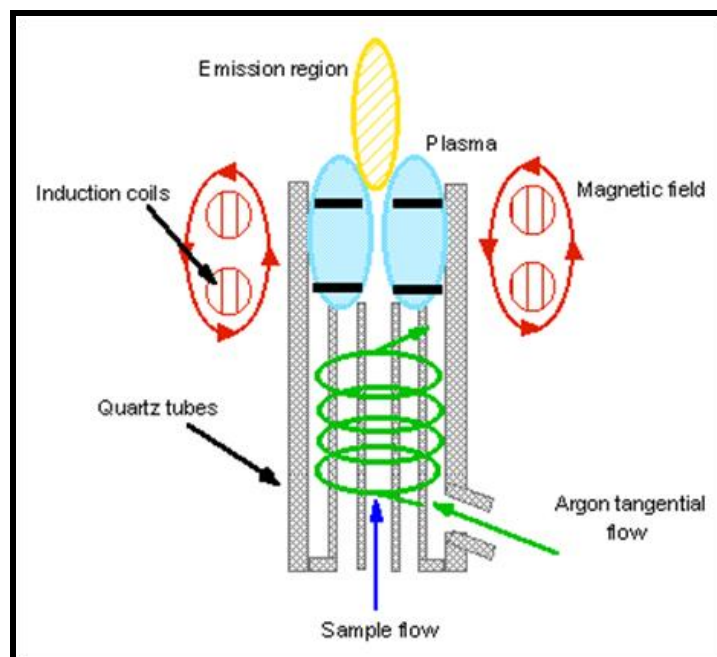


Figure A-6 Schematic cross-section of an ICP torch.

The plasma is formed by flowing tangentially stream of argon gas between two quartz tubes, as shown in Figure A-6. An oscillating magnetic field is formed when a radio-frequency (RF) power is applied through the coil. The plasma is formed when the argon is made conductive by exposing it to an electrical discharge, which creates seed electrons and ions. The charged particles (electrons and ions) are forced to flow in a closed annular path inside the induced magnetic field. When they are allowed to couple with the RF field, heating occurs resulting in additional ionization. The process immediately takes place and the plasma expands to its full dimensions. The plasma has a circular, “doughnut” shape when viewed axially from the end and the sample is injected as an aerosol through the centre of the doughnut [23]. This characteristic of the ICP limits the sample to a narrow region that can provide an optically thin emission source and a chemically inert atmosphere. If the liquids are directly injected into the plasma, it would either extinguish the plasma or cause the atoms to be improperly desolvated, making excitation and emission less efficient. A nebulizer is generally used to avoid this problem, which converts the liquid stream into an aerosol consisting of particles that are 1–10 μm in diameter. Sometimes argon is also used as a carrier gas for the sample. Depending upon the detectors used, the ICP is generally classified into two variations:

1) *Inductively coupled plasma-atomic emission spectroscopy (ICP-AES)*

ICP-AES also referred to as inductively coupled plasma-optical emission spectroscopy (ICP-OES) is the measurement of the light emitted by the elements in a sample that is introduced into an ICP source. The elemental concentration in the unknown sample is determined by comparing the measured emission intensities and the intensities of standards whose concentration are known. The light emitted from an ICP can be viewed radially or axially. Axial viewing enables reaching better detection limits, by as much as a factor of 10, than those attained through radial viewing.

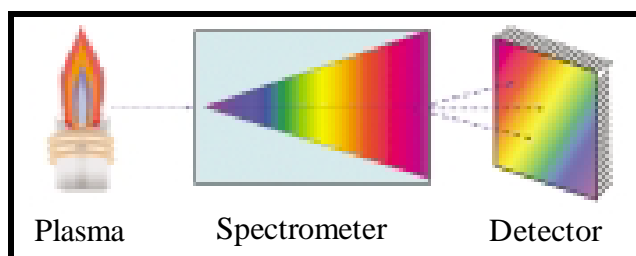


Figure A-7 Simplified drawing of a basic ICP-AES system.

The optical system used for ICP-AES contains a monochromator that helps focusing the desired wavelengths to the detector by separating the individual wavelengths of light (Figure A-7). Older types of ICP-AES systems used a series of photomultiplier tubes to determine pre-selected wavelengths, which can lead to much longer analysis times. In modern ICP-OES systems, solid-state detectors based on charge-coupled devices (CCD) are used, providing very flexible systems and eliminating the need for large numbers of single photomultiplier detectors. Interferences that take place in ICP-AES are generally compensated by the selection of an alternate wavelength or by employing inter-element correction factors (IECs) or more sophisticated techniques like multi-component spectral fitting (MSF) [24].

2) *Inductively coupled plasma- mass spectrometry (ICP-MS)*

As the name implies, ICP-MS is the synergistic combination of inductively coupled plasma with a mass spectrometer. ICP-MS makes use of the ability of the argon ICP to efficiently

generate singly charged ions from the elemental species within a sample, by directing these ions into the mass spectrometer. The function of the mass spectrometer is similar to that of the monochromator in an ICP-AES system. In ICP-MS, the mass spectrometer separates the ions introduced from the ICP according to their mass-to-charge ratio rather than separating light according to its wavelength. Ions of the selected mass-to-charge ratio are directed to a detector, which resolves the number of ions present (Figure A-8). Usually, a quadrupole mass spectrometer is employed due to its ease-of-use, robustness and speed.

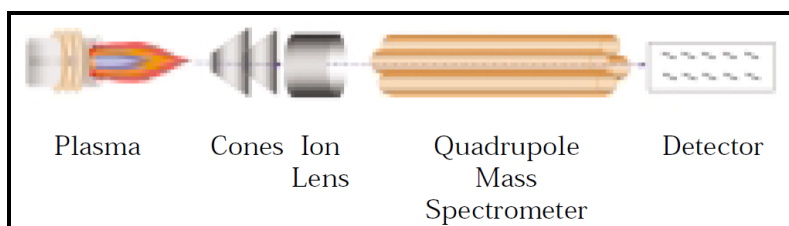


Figure A-8 Simplified drawing of a basic ICP-MS system.

ICP-MS combines the multi element capabilities of ICP techniques with exceptional detection limits and is also one of the few analytical techniques that enable the quantification of elemental isotopic concentrations and ratios. However, due to the fact that the sample components are actually introduced into the instrument, there are some limitations to introduce sample matrix into the ICP-MS. For routine operation and maximum stability of ICP-MS systems, the total dissolved solids content of a sample should be below 0.2%. Interferences can occur in ICP-MS like in ICP-AES, but, due to the spectral simplicity, most of the interferences are easily predictable. Interferences can be eliminated by using an alternate mass to determine an element or by proper selection of sample-preparation techniques [24].

Annexe 8 Scanning electron microscopy (SEM)

The SEM is a microscope that uses electrons instead of light to produce a magnified image, especially of objects having dimensions smaller than the wavelengths of visible light, with

a linear magnification of nearly a million (10^6). An electron microscope creates a three dimensional image on a cathode ray tube by focusing a beam of electrons across an object and reading both the electrons scattered by the object and the secondary electrons produced by it. An image is produced by bombarding a sample with a beam of high-energy electrons using high-powered indirect microscope. The electrons emitted from the sample are then scanned to produce a magnified image, which aids in examining the structure, relief and morphology of the materials. The SEM also has a great depth of field in addition to its great magnification. SEM can also analyse the X-rays produced by the target as a result of its bombardment with electrons. Since each element in the periodic table has its own X-ray spectrum, SEM is also used to determine the elemental composition of the samples [25].

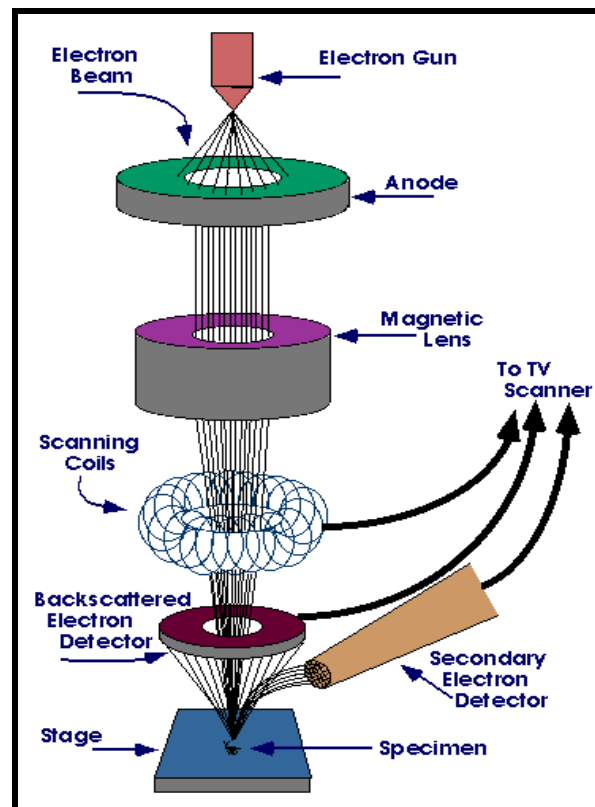


Figure A-9 Schematic representation of SEM.

The surface topography, microstructure, and chemistry of metallic and nonmetallic specimens can be examined by SEM using higher magnifications in the range of 50 to $\sim 100,000\times$, with a resolution limit $< 10\text{ nm}$ and a depth of focus up to several μm . In

SEM, after irradiation of the specimen by an electron beam, the data on the specimen are carried by secondary electrons coming from the surface layer of thickness ~ 5 nm and by backscattered electrons emitted from the volume of linear size ~ 0.5 μm . SEM is frequently used for studying fracture surfaces due to its higher depth of focus [26,27].

When the accelerated electrons that bear significant amount of kinetic energy are incident on a solid sample, they get decelerated, and the energy is dissipated as an array of signals produced by electron-sample interactions (Figure A-9). These signals consist of secondary electrons, backscattered electrons (BSE), diffracted backscattered electrons (EBSD), photons, visible light and heat. SEM images are produced by secondary electrons and the backscattered electrons are used to determine crystal structures and mineral orientations. Photons are characteristic X-rays produced for each element in a mineral excited by the electron beam and hence used for elemental analysis. Since the X-rays produced by electron interactions do not lead to volume loss of the sample, it is possible to analyse the same materials repeatedly. Therefore, SEM analysis is considered to be non-destructive. The schematic diagram of SEM is shown in Figure 11, demonstrating the interaction of the electron beam with a sample producing secondary, reflected electrons, X-rays, etc. The radiation emitted by the sample is transformed into electrical signals depending on the type of the detector. These signals after amplification are used to modulate a cathode-ray tube display where an image of the sample surface is formed [25].

Annexe 9 Porosity measurements by nitrogen adsorption (BET)

Adsorption is an enrichment of a substance in the vicinity of an interface when the surface of solid is immersed in or exposed to liquid or gas substances [28]. Adsorption techniques are usually employed to study the surface and textural properties of materials such as powders, pigments and porous solids like clays and membranes. Gas adsorption, especially nitrogen adsorption analysis, is one of major techniques in field of catalysis for determining the surface area and pore size distribution of a wide range of porous materials [29]. In 1881, Chappuis and Kayser introduced the terms ‘adsorption’ and ‘isothermal curve’, which were applied to study the adsorption measurements at a constant temperature [30,31]. Brunauer *et al.* introduced the BET theory, which is a well-known technique for determining the surface area of porous materials [32]. They determined the surface area of

an iron synthetic ammonia catalyst by employing the adsorption of nitrogen at lower temperature.

After adsorption at a given equilibrium pressure, if the amount of gas adsorbed and the amount desorbed are not coinciding, it results in an adsorption hysteresis. The relationship that exists between the amount adsorbed and the equilibrium pressure at constant temperature is known as the adsorption isotherm. Generally, there are two kinds of adsorptions: physisorption or physical adsorption that involves the van der Waals interactions and chemisorptions or chemical adsorption in which the adsorbent and adsorbate molecules are linked by a chemical bonding. Dubinin *et al.* (1960) identified three types of pores in activated carbons, *i.e.*, the pores with different width: micropores, mesopores, and macropores [33,34]. IUPAC classified pores according to their width [35,36]:

- Pores of widths exceeding about 50 nm are called macropores;
- Pores with widths between 2 nm and 50 nm are called mesopores;
- Pores of widths not exceeding about 2 nm are called micropores.

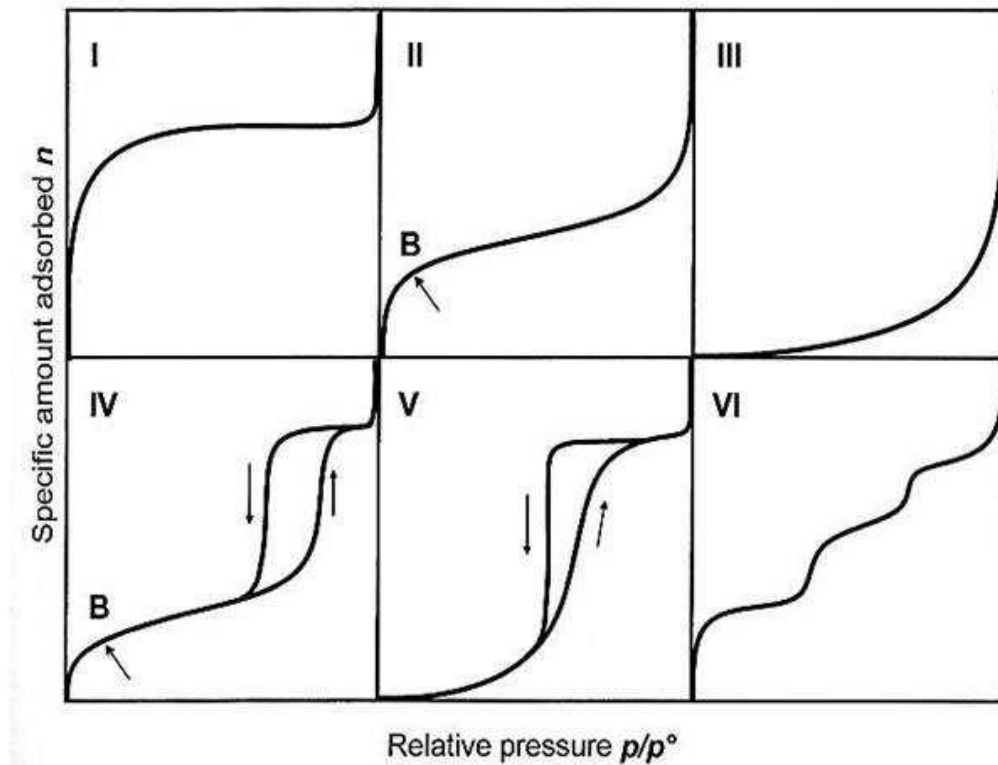


Figure A-10 Six types of isotherms according to IUPAC classification.

Adsorption isotherms have a variety of forms and can be grouped into one of six types according to the IUPAC classification. Figure A-10 shows the six types of isotherms applicable for the adsorption of a single component gas, and is very useful for the study of porous materials [28].

Type 1 by its concave shape indicates the existence of a limited range of pore size and is a characteristic of microporous solids. The Type II isotherm is related to non-porous and macroporous adsorbents, which enables the monolayer multi-layer adsorption at high values of relative pressure (P/P^0). Type III is typical for weak adsorbent-adsorbate interactions and is not common. Hysteresis loops in Type IV isotherms signifies the capillary condensation, which govern the filling and emptying of pores. The IUPAC further classified Type IV into four types of hysteresis loops namely H1, H2, H3 and H4. Type V isotherm is convex shaped and similar to Type III, which is due to the mechanism of pore filling and emptying by capillary condensation. Type VI isotherm is a result of layer-by-layer adsorption on a highly uniform surface.

Although there are some theoretical limitations, the Brunauer-Emmett-Teller (BET) method continues to be the most widely used method for the determination of surface area, pore volumes and pore size distributions of porous solids from N_2 physisorption isotherm data. The BET equation can be represented as follows:

$$\frac{p}{v(p^0 - p)} = \frac{1}{v_m c} + \frac{(c - 1)}{v_m c} \frac{p}{p^0}$$

where v = volume of N_2 adsorbed by the sample under pressure p , p^0 = saturated vapor pressure at the same temperature, v_m = volume of N_2 adsorbed when the surface is covered with a unimolecular layer, and c = constant for a given adsorbate [32]. The equation indicates that the plot of $\frac{p}{v(p^0 - p)}$ versus $\frac{p}{p^0}$ must be linear, and from the intercept $\frac{1}{v_m c}$ and slope $\frac{(c-1)}{v_m c}$, the values of useful and c can be determined as follows: $v_m = (\text{slope} + \text{intercept})^{-1}$. Hence the specific surface area (S) of a sample can be determined as follows: $S = \frac{N_0 v_m A}{22414m}$, where N_0 = Avogadro number, m = amount of solid adsorbent, A = cross-section of the gas molecules (16.2 \AA^2 for N_2), and S is expressed in $\text{cm}^2 \text{ g}^{-1}$ unit.

A number of computational procedures exist for the derivation of pore size distribution of mesoporous samples from physisorption isotherms. Most common and accepted one among them is the Barrett-Joyner-Halenda (BJH) model, which is based on speculative emptying of the pores by a stepwise reduction of p/p^0 , and allowance being made for the contraction of the multilayer in those pores already emptied by the condensate [37].

Annexe 10 Temperature-Programmed Desorption (TPD)

Temperature-Programmed Desorption (TPD) is one of the most widely used techniques to characterize the chemical behaviour of the catalyst surfaces. When molecules come in contact with a surface they adsorb onto it by forming a chemical bond with the surface, thereby minimizing their energy. The binding energy depends on the adsorbent and adsorbate and is different for different combinations of adsorbates and surfaces. If the surface is heated, a particular point is reached at which the energy gets transferred to the adsorbed species and causes it to desorb. The temperature at which this desorption happens is known as the desorption temperature. Thus, TPD provides information regarding the binding energy. Pumping capacity to provide high vacuum is an important criterion in TPD because pumping speed should be high enough to prevent the re-adsorption of the desorbed species back onto the surface. If the pumping speed is sufficiently high, re-adsorption may be ignored and relative rate of desorption can now be defined as the change in adsorbate coverage per unit of time [21,38,39].

Temperature Programmed Desorption of ammonia (TPD-NH₃)

Ammonia is a very basic molecule and can thus be used to probe the acid sites present in the solid catalysts. Its small molecular size permits ammonia to penetrate into all the pores of a solid and is also capable of titrating weak acid sites of catalysts. TPD-NH₃ is a widely used method for characterization of acid sites number and strength in solid acids due to the simplicity of this technique. TPD-NH₃ is generally carried out in three steps, first step being outgassing of the catalysts by increasing the temperature to a particular point in the presence of an inert gas flow. After the sample is kept at this temperature for a few hours, it is naturally cooled down and saturated by adsorption using basic probe molecule NH₃. Finally desorption of NH₃ is performed by ramping the temperature in a flow of inert gas.

Thermal conductivity detector (TCD) and mass spectrometer (MS) are generally used to monitor the desorbed NH_3 species. During the entire experiment, the inert gas flow is maintained to avoid the error in the quantification due to physisorbed NH_3 .

Temperature Programmed Desorption of carbon dioxide (TPD- CO_2)

TPD- CO_2 is a technique commonly used to measure the number and strength of basic sites. Here, CO_2 was used as a probe molecule to probe the basic sites in the catalysts. The strength and the amount of basic sites are reflected by the desorption temperature and the peak area in a TPD plot, respectively. However, it is hard to express the strength in a definite scale and to count the number of sites quantitatively. So, relative strengths and relative quantity of basic sites on the different catalysts are estimated by carrying out the TPD experiments under the same conditions. If the TPD plot gives a sharp peak, the heat of adsorption can be estimated. The TPD- CO_2 was generally performed in three steps as in the case of TPD of ammonia, that is, outgassing, adsorption of CO_2 molecule and desorption of CO_2 by raising the temperature.

Annexe 11 Thermogravimetry & Differential thermal analysis (TGA/DTA)

TGA is a technique in which the changes in mass of a sample are monitored as a function of temperature or time while the sample specimen is subjected to a controlled temperature program in a controlled atmosphere. A TGA comprises of a sample pan supported by a precision balance and the pan resides in a furnace that can be heated or cooled during the experiment. During TGA, the sample placed in the thermobalance is subjected to programmed heating and cooling cycles using the furnace and mass change of the sample accompanied by various physical and chemical processes is monitored [40,41]. A sample purge gas is always there to control the sample environment during the analysis. The purge gas is normally an inert gas that flows over the sample and leaves the furnace through an exhaust. In order to acquire precise experimental results, TGA is calibrated depending on the type of experimental set-up applied. Two types of calibration generally employed in thermo gravimetry are temperature and weight calibration.

DTA provide information about exothermic or endothermic transformations occurring in a material relative to an inert reference, as a function of temperature and time. DTA is mainly employed to study phenomena such as transition, chemical reaction, adsorption, crystallisation, melting, and sublimation that take place in the specimen. It is also possible to determine kinetic parameters and the heat of reaction using DTA [42].

Two cells are generally used in DTA, one containing the sample specimen and the other a reference material, which is thermally inert. Both the sample and the reference placed in alumina crucibles are simultaneously subjected to heating and cooling inside the furnace in a controlled atmosphere. The difference in temperature that occurs between the sample and the reference is measured while both are subjected to the same temperature programming [40,42,43].

-
- [1] W.H. Bragg, W.L. Bragg, *The Crystalline State*, McMillan, New York, vol 1 (1949).
- [2] S. Biz, M.L. Occelli, Synthesis and Characterization of Mesoporous Materials, *Catalysis Reviews: Science and Engineering*, vol 40 (1998), p. 329-407.
- [3] G. Bergeret, Handbook of Heterogeneous Catalysis, (G. Ertl, H. Knozinger, J. Weitkamp, eds) *Wiley-VCH*, Weinheim, vol 2 (1997) p. 464.
- [4] R.C. Rau, *Advances in X-Ray Analysis*, (W. M. Mueller, Sir Isaac Pitman and Sons, eds), London, vol 5 (1962) p. 104.
- [5] <http://www.tdx.cat/bitstream/handle/10803/2743/Tol1222.pdf?sequence=2>.
- [6] B. Stuart, Modern Infrared Spectroscopy, *John Wiley & Sons Ltd*, West Sussex, England, (1996) p. 1.
- [7] P.R. Griffiths, J.A. De Haseth, Fourier Transform Infrared Spectrometry, *John Wiley and Sons, Inc.*, New York, (1986).
- [8] D.J. Gardiner, Practical Raman spectroscopy, *Springer-Verlag*. ISBN 978-0-387-50254-0 (1989).
- [9] http://en.wikipedia.org/wiki/Raman_spectroscopy#cite_note-Gardiner-0.
- [10] D.A. Long, *Raman Spectroscopy*, (McGraw-Hill International Book Company, 1221 Ave. of the Americas, New York, NY), The United States (1977).
- [11] B.P. Straughan, S. Walker, *Spectroscopy*, Chapman and Hall, London, vol 2 (1976).
- [12] F.A. Rushworth, D.P. Tunstall, *Nuclear Magnetic Resonance*, Gordon and Breach Science, Publishers Ltd., London, (1973).
- [13] W.W. Paudler, Nuclear Magnetic Resonance: General Concepts and Applications, *John Wiley and Sons Inc.*, New York, (1987).
- [14] M. Mehring, High Resolution NMR Spectroscopy in Solids, *Springer-Verlag*, Berlin, (1976).
- [15] G. Engelhardt, D. Michel, High-Resolution Solid-State NMR of Silicates and Zeolites, *John Wiley and Sons Ltd.*, Chichester, (1987).
- [16] J.F. Moulder, W.F. Stickle, P.E. Sobol, K.D. Bomben, J. Chastain (editor), Handbook of X-ray photoelectron spectroscopy, 2nd Edition, ISBN: 0962702625, *Perkin Elmer Corporation*, Minnesota (1992).
- [17] [http://www.chm.bris.ac.uk/pt/diamond/lithesis/Chapter 3.pdf](http://www.chm.bris.ac.uk/pt/diamond/lithesis/Chapter%203.pdf).

-
- [18] C.D. Wagner, W.M. Riggs, L.E. Davis, J.F. Mulder, G.E. Muilenburg (Editor), Handbook of X-ray photoelectron spectroscopy, 1st Edition, ISBN: 0962702621, *Perkin Elmer Corporation*, Minnesota (1979).
- [19] L.C. Feldman, J.W. Mayer, *Fundamentals of Surface and Thin Film Analysis*, North Holland, New York (1986).
- [20] H.H. Brongersma, G.C. van Leerdam, Fundamental Aspects of Heterogeneous Catalysis Studied by Particle Beams, *NATO ASI Series B, Physics*, Plenum, New York, vol 265 (1991) p. 283.
- [21] J.W. Niemantsverdriet, Spectroscopy in Catalysis: An Introduction, 3rd edition, ISBN: 9783527316519, *Wiley-VCH*, (2007) p. 112.
- [22] R.H. Wendt, V.A. Fassel, Induction coupled plasma spectrometric excitation source, *Analytical Chemistry*, vol 37 (1965) p. 920-922.
- [23] H. Haraguchi, T. Hasegawa, M. Abdullah, Inductively coupled plasmas in analytical atomic spectrometry: excitation mechanisms and analytical feasibilities, *Pure and Applied Chemistry*, vol 60 (1988) p. 685-696.
- [24] http://www.d.umn.edu/~jevans1/chem4242_s12/PS_3/GDE_InorganicAnalysis_from_pe.pdf.
- [25] http://shodhganga.inflibnet.ac.in/bitstream/10603/710/8/08_chapter2.pdf.
- [26] G. Lawes, Scanning Electron Microscopy And X-Ray Microanalysis, *John Wiley and Sons Ltd.*, Chichester, (1987).
- [27] D.E. Newbury, D.C. Joy, P. Echlin, C.E. Fiori, J.I. Goldstein, Advanced Scanning Electron Microscopy and X-Ray Microanalysis, *Plenum Press*, New York (1986).
- [28] F. Rouquerol, J. Rouquerol, K. Sing, Adsorption by Powders and Porous Solids: Principles, methodology and Applications, *Academic press* (1999).
- [29] I. O. Evbuomwan, The Structural Characterisation of Porous Media for use as model Reservoir Rocks, Adsorbents and Catalysts; *A thesis submitted to University of Bath*, (2009).
- [30] Kayser, H., Wiedermann's, *Annual Review of Physical Chemistry*, vol 14 (1881) p. 451.
- [31] R.I. Masel, Principles of adsorption and reaction on solid surfaces, *Wiley-IEEE*, ISBN 0471303925, 97804713039 (1996).
- [32] S. Brunauer, P.H. Emmett, E. Teller, Adsorption of Gases in Multimolecular Layers, *Journal of American Chemical Society*, vol 60 (1938).p. 309-319.

-
- [33] M.M. Dubinin, The Potential Theory of Adsorption of Gases and Vapors for Adsorbents with Energetically Nonuniform Surfaces, *Chemical Reviews*, vol 60 (1960) p. 235–241.
- [34] M.M. Dubinin, Water vapor adsorption and the microporous structures of carbonaceous adsorbents, *Carbon*, vol 18 (1980) p. 355-364.
- [35] S.J. Gregg, K.S.W. Sing, *Adsorption, Surface Area and Porosity*. 2nd editioned (1982).
- [36] K.S.W. Sing, Reporting physisorption data for gas/solid systems with special reference to the determination of surface area and porosity, *Pure and Applied Chemistry*, vol 57 (1985) p. 603-619.
- [37] E.P. Barrett, L.G. Joyner, P.P. Halenda, The Determination of Pore Volume and Area Distributions in Porous Substances I Computations from Nitrogen Isotherms, *Journal of American Chemical Society*, vol 73 (1951) 373-380.
- [38] J.L. Falconer, J.A. Schwartz, Temperature-Programmed Desorption and Reaction: Applications to Supported Catalysts, *Catalysis Reviews: Science and Engineering*, vol 25 (1983) p. 141-227.
- [39] D. A King, Thermal desorption from metal surfaces: A review, *Surface Science*, vol 47 (1975) p. 384-402.
- [40] C.J. Keatch, D. Dollimore, *An introduction to thermogravimetry*, 2nd Ed., London: Heyden (1975).
- [41] Comprehensive handbook of Calorimetry & Thermal Analysis, *J. Wiley & Sons Ltd.*, The Atrium, Southern Gate, Chichester, West Sussex, England (2004).
- [42] A.J. Ellett, Oxygen Permeation and Thermo-Chemical Stability of Oxygen Separation Membrane Materials for the Oxyfuel Process, *PhD thesis*, RWTH Aachen (2009).
- [43] Michio Sorai ed. in chief, Comprehensive handbook of calorimetry and thermal analysis, New York, NY: *Wiley* (2004).